Novel photonic phenomena in nanostructured material systems with applications and Mid-range efficient insensitive Wireless Energy-Transfer

by

Aristeidis Karalis

Dipl., National Technical University of Athens, Greece (2001)
M.Sc., Massachusetts Institute of Technology, U.S.A. (2003)

Submitted to the Department of Electrical Engineering and Computer Science
in partial fulfillment of the requirements for the degree of

Doctor of Science in Electrical Engineering

at the

MASSACHUSETTS INSTITUTE OF TECHNOLOGY

June 2008

© Massachusetts Institute of Technology 2008. All rights reserved.

Author .....
Department of Electrical Engineering and Computer Science
May 23, 2008

Certified by .....
John D. Joannopoulos
Francis Wright Davis Professor of Physics
Thesis Supervisor

Accepted by .....
Terry P. Orlando
Professor of Electrical Engineering and Computer Science
Chairman, Department Committee on Graduate Students

MASSACHUSETTS INSTITUTE OF TECHNOLOGY
JUL 0 1 2008
LIBRARIES

ARCHIVES

Novel photonic phenomena in nanostructured material systems with applications and Mid-range efficient insensitive Wireless Energy-Transfer

by

Aristeidis Karalis

Submitted to the Department of Electrical Engineering and Computer Science
on May 23, 2008, in partial fulfillment of the
requirements for the degree of
Doctor of Science in Electrical Engineering

Abstract

A set of novel mechanisms for the manipulation of light in the nanoscale is provided. In the class of all-dielectric material systems, techniques for the suppression of radiative loss from incomplete-photonic-bandgap structures are developed: the cancellation of radiation channeled into discrete modes of the substrate, for resonant small-modal-volume cavities with patterned substrates, and the broadband mode-matching across the coupling interface, for large-bandwidth butt-coupled devices. Moreover, a hybrid plasmonic-dielectric material platform is introduced, able to localize light counterintuitively in low-index regions, by employing the unique subwavelength and cutoff properties of polaritonic waves, and to support dispersionless (to unusually-high orders) broadband-slow or stopped subwavelength light, by utilizing a simple planar multilayered dielectric structure. This platform can achieve a significant reduction in all (temporal, spatial and energy) light-scales and could enable compact and efficient optical buffers and active devices.

A method for mid-range efficient and insensitive wireless energy-transfer is proposed. A condition of 'strong coupling' of resonances is identified as necessary and sufficient for efficient energy-exchange, and is shown to be satisfied at mid-range distances by carefully-designed high-Q subwavelength resonances of realistic systems both theoretically and experimentally, in the latter case by powering a 60W light-bulb wirelessly across a 2m-distance using two 60cm-diameter resonant objects and with 45% efficiency. A technique for further efficiency enhancement and radiation suppression is suggested, based on employing destructive interference between the coupled-objects' radiated far-fields. The scheme is also found fairly insensitive to the near-presence of extraneous objects, especially when utilizing the special class of magneto-quasi-static resonances. Applications of the proposed wireless-powering method can be found in both the macro- and micro-worlds, and range among industrial, technological, medical, consumer and more.

Thesis Supervisor: John D. Joannopoulos
Title: Francis Wright Davis Professor of Physics

To my sister Νάγια

" Ό,τι έχουμε η αγάπη "

Acknowledgments

It has been a blessing for me to have had Prof. John Joannopoulos as my advisor on the doctorate degree. He is an inspiring scientist, with academic accomplishments that few people have and will ever achieve in the history of science and with phenomenal international acclaim. He is an amazing teacher, from fundamental theory to numerical calculations to writing papers and, in general, how to approach science and academia: almost every time I meet with him, I feel that I have learned something. But most importantly to me, he is an advisor that cares for his students, often putting their interest and well-being higher than his own, and he has shown this care to me repeatedly over the course of my degree in multiple ways. Finally, he is a great man, I would say the definition of a 'gentleman', and he sets a personal example to all of us in all life aspects. Thank you, John, for everything. You are the best!

A significant portion of my thesis, with highlight the Wireless Energy-Transfer project, was inspired, shared with me and led by Prof. Marin Soljačić, and most of the credits for the work done in this thesis are owed to him. I am deeply grateful to Marin for giving me the opportunity to work on his wonderful ideas. He is also the reason that I got the chance to live amazing experiences: academic, enterpreneurial and more. Our collaboration has been marked by a series of unforgettable joyful moments, of which I expect many more to come in the future. He is a great leader and teacher. Thanks Marin!

I was lucky to have as my officemate for my first doctorate year Prof. Steven G. Johnson. I learned innumerable things from him, which clearly helped me throughout my degree. He also advised me in the projects in this thesis relating to photonic-crystal structures. Thanks Steven, it is always great collaborating and chatting with you!

I would like to thank Prof. Erich Ippen and Prof. Franz Kaertner for accepting to be on my committee and putting up with my disorganized timing, and for all the useful conversations I have had with them throughout my years at MIT so far!

I am grateful to all the group members that have played a role throughout my doctorate degree: Alex, for being a great officemate and friend; Milos (from my old group), for the always extremely fun and useful conversations; Peter and Ardavan, for helping me especially with computer issues, often at critical times; Andre and Rafif, for the excellent collaboration on projects; and, in general, the entire ab-initio group for the discussions, the laughthers

and the support.

All of the past years at MIT would have been impossible, if it weren't for the support of my friends. Here in Boston: Andrea, Costas, Maria, Katerina, Luigi, Jenn, Areti, Mari, Niky, Eliza, Magda, Apostolos, Anna & Ramin, La Cúpula, Peter, Ali, and so many more it is impossible to list here. Thank you all for the help, the wonderful moments and the love you have offered me! And in Greece: Alexis, Giannis, Giorgos, Miltos, Michalis, Basilis, Baggelis, Andreas, and more more more, thank you all for being my eternal friends!

Finally, I owe not only this accomplishment, but everything I have achieved so far in my life, as a scientist, as a person, as a friend, as everything, to my amazing parents. Thank you from the bottom of the heart that you gave me. I love you more than anything, and will stand by you no matter what difficulties may the road bring and no matter what decisions you may ever take. I will try to live up to what you taught me to be, and be a good man. Anything you may ever need, now we have a doctor in the family!

Contents

I Novel photonic phenomena in nanostructured material systems with applications **27**

1 Introduction **29**

1.1 Background 29

1.2 Outline 31

2 High-radiation-Q small-modal-volume Dielectric-Photonic-Crystal (DPC) resonant cavities [1] **35**

2.1 High-Q cavities by discrete-mode cancellation mechanism 36

2.2 Discrete-mode cancellation for realistic systems 38

3 Low-radiation-loss butt-coupled Dielectric-Photonic-Crystal (DPC) broadband mirrors **43**

3.1 Formulation of the problem and preview of the final solution 46

3.2 Optimization for dimensions of the crystal in the horizontal plane of periodicity 48

3.2.1 Bloch modes of infinite photonic-crystal slab 48

3.2.2 Reflectivity of semi-infinite photonic-crystal-slab mirror 55

3.3 Optimization for dimensions of the crystal in the vertical direction of layer growth 59

3.4 Optimization for the material set comprising the crystal 63

4 Subwavelength and low-index-confined light in Surface-Plasmon-Polaritonic (SPP) systems [2] **69**

4.1 Subwavelength light-propagation in SPP systems 70

4.2 Low-index light-confinement mechanism by SPP effective-index guiding 72
4.2.1 Linear waveguides 72
4.2.2 Cavities 75

5 Dispersionless broadband-slow or stopped light in Surface-PlasmonoDielectric-Polaritonic (SPDP) systems [2, 3] 77

5.1 Broadband-slow or stopped light-guiding mechanism by layered SPDP systems 78
5.1.1 Planar waveguides 78
5.1.2 Linear waveguides 80
5.1.3 Cavities 82
5.2 Slow-light dispersion-manipulation mechanism by multilayered SPDP systems 83
5.2.1 Planar waveguides 83
5.3 High-order group-velocity-dispersion (GVD) cancellation mechanism by multilayered SPDP systems 84
5.3.1 Planar waveguides 84
5.3.2 Linear waveguides 89
5.3.3 Cavities 90
5.4 High-order attenuation-dispersion (AD) cancellation in multilayered SPDP systems 91
5.5 Applications 92
5.5.1 Delay lines 93
5.5.2 Active devices 94
5.6 Practical limitations 96
5.6.1 Material losses 96
5.6.2 Broadband coupling 97
5.7 Extensions 97

6 Conclusion 99

II Mid-range efficient insensitive Wireless Energy-Transfer 101

7 Introduction 103

8 Efficiency at mid-range transfer distances [4] 107

8.1 Efficient energy-transfer by 'strongly coupled' resonances 107

8.1.1 Finite-amount energy-transfer efficiency 107

8.1.2 Finite-rate energy-transfer (power) efficiency 111

8.2 'Strong coupling' at mid-range distances for realistic systems 114

8.2.1 Dielectric resonators 116

8.2.1.1 Dielectric disks 116

8.2.2 Metallic resonators 123

8.2.2.1 Capacitively-loaded conducting loops 125

8.2.2.2 Inductively-loaded conducting rods 132

8.2.2.3 Self-resonant conducting coils [5] 135

8.3 Experimental demonstration of mid-range efficient energy-transfer [5] 141

9 Efficiency enhancement and radiation suppression 147

9.1 Efficiency enhancement by far-field interference 147

9.1.1 Finite-amount energy-transfer efficiency 147

9.1.2 Finite-rate energy-transfer (power) efficiency 149

9.2 Far-field interference at mid-range distances for realistic systems 152

9.2.1 Dielectric resonators 153

9.2.1.1 Dielectric disks 153

9.2.2 Metallic resonators 158

9.2.2.1 Capacitively-loaded conducting loops 158

10 Insensitivity to near-presence of extraneous objects 163

10.1 Insensitive energy-transfer by robust lifetime and coupling of resonances . . . 163

10.2 Robust lifetime and coupling of resonances in the near-presence of extraneous objects 166

10.2.1 Dielectric resonators 170

10.2.1.1 Dielectric disks 170

10.2.2 Metallic resonators 173

10.2.2.1 Capacitively-loaded conducting loops 173

10.2.2.2 Self-resonant conducting coils [5] 174

11 Conclusion **179**

11.1 Mobility and versatility 179

11.2 Applications 180

11.3 Future directions 181

III Appendices **183**

12 Coupled-Mode Theory in electromagnetism **185**

12.1 Derivation of coupled equations and coupling coefficients 185

12.2 Prediction of radiative far-field interference 189

12.2.1 Coupled and interfering dielectric disks 192

Bibliography **195**

List of Figures

2-1 (a) Photonic-crystal slab microcavity, (b) Monorail microcavity, (c) Two-dimensional model of the cavities for the region in the vicinity of the defect. . 36

2-2 Results for $n_{core} = 3.35$, $n_{clad} = 3.17$, $d = 680nm$, $\Lambda = 320nm$, $w_a = 150nm$ and $w_{off} = 125nm$. (a) Q total, Q of guided mode, Q of continuum and $V/\left(\lambda/n_{def}\right)^2$ vs. n_{def} (w_{def} is adjusted so that λ=1.55μm); (b)-(d) Resonant field at certain values of n_{def}. 40

2-3 Results for $n_{core} = 3.45$, $n_{clad} = 1.45$, $d = 1\mu m$, $\Lambda = 300nm$, $w_a = 100nm$ and $w_{off} = 100nm$. (a) Q total, Q of guided mode, Q of continuum and $V/\left(\lambda/n_{def}\right)^2$ vs. n_{def}; (b)-(f) Resonant field at certain values of n_{def}. 41

3-1 (a) Photonic-crystal-slab mirror, (b) Photonic-crystal-monorail mirror, and (c) two-dimensional model of the mirrors based on their vertical cross-sections at their symmetry planes. 45

3-2 Minimized maximum radiation loss from the semi-infinite mirror of Figure 3-1(c), over a $B = 10\%$ bandwidth and under the fabrication limitations $AR = 5$, $w_{\mathrm{a}}^{\mathrm{min}} = w_{\mathrm{g}}^{\mathrm{min}} = 0.05\lambda_{\mathrm{o}}$, as a function of the core and substrate dielectric permittivities, where $\Delta\epsilon = \epsilon_{\mathrm{core}} - \epsilon_{\mathrm{clad}}$. 49

3-3 Bloch-mode wavevector K for a stack of alternated layers of refractive indices $n_{\mathrm{g}} = 3$, $n_{\mathrm{a}} = 1$ as a function of (a) their widths w_{g}, w_{a} and the wavelength λ inside the first photonic bandgap, and (b) the wavelength λ for the arbitrary choice of the widths $w_{\mathrm{g}} = 0.3\lambda_{\mathrm{o}}/n_{\mathrm{g}}$, $w_{\mathrm{a}} = 0.2\lambda_{\mathrm{o}}/n_{\mathrm{a}}$. 51

3-4 Fundamental-Bloch-mode wavevector K for a photonic-crystal slab consisting of an array of rectangular rods of $\epsilon_{\text{core}} = 12$ and thickness $d_{\text{core}} = 0.136\lambda_{\text{o}}$ suspended in air ($\epsilon_{\text{clad}} = 1$) (effective refractive indices $n_{\text{g}} = 2.764$, $n_{\text{a}} = 1$) as a function of (a) the widths of the rods w_{g} and the air holes w_{a} at the wavelength λ_{o} inside the first photonic bandgap, and (b) the wavelength λ for the arbitrary choice of the widths $w_{\text{g}} = 0.35\lambda_{\text{o}}/n_{\text{g}}$, $w_{\text{a}} = 0.25\lambda_{\text{o}}/n_{\text{a}}$. (The discreteness of the modes in the light cone (grey shaded area) is due to the necessary imposition of boundary walls for simulation purposes. Notice how the fundamental Bloch mode couples to the light cone at $\lambda_{\text{o}}/\lambda = 1.2036$, which coincides with the upper edge of the bandgap.) 53

3-5 Fundamental-Bloch-mode electric-field patterns for the rods-in-air photonic-crystal slab of Figure 3-4(b) at the (a) low-frequency edge $\lambda_{\text{o}}/\lambda = 0.6973$ and (b) high-frequency edge $\lambda_{\text{o}}/\lambda = 1.2036$ of the photonic bandgap. (Notice how the coupling to the light cone delocalizes transversely the field pattern in (b)). 54

3-6 Reflectivity from the rods-in-air photonic-crystal-slab mirror of Figure 3-4 as a function of (a) the widths of the rods w_{g} and the air holes w_{a} at the wavelength λ_{o} inside the first photonic bandgap, and (b) the wavelength λ for the arbitrary choice of the widths $w_{\text{g}} = 0.35\lambda_{\text{o}}/n_{\text{g}}$, $w_{\text{a}} = 0.25\lambda_{\text{o}}/n_{\text{a}}$ (black curve) from Figure 3-4(b), and the optimal choice of the widths $w_{\text{g}} = 0.4045\lambda_{\text{o}}/n_{\text{g}}$, $w_{\text{a}} = 0.05\lambda_{\text{o}}/n_{\text{a}}$ (green curve). The red lines in (a) indicate the fabrication limitations from Eq.(3.6) for the choice of the operation point $\{w_{\text{g}}, w_{\text{a}}\}$ at λ_{o}. 56

3-7 Electric-field pattern of reflection from the rods-in-air photonic-crystal-slab mirror of Figure 3-4(b) at the wavelength λ_{o} 57

3-8 Maximum radiation loss from the semi-infinite mirror of Fig. 3-1(c) with optimized in-plane dimensions w_{g} and w_{a}, over a $B = 10\%$ bandwidth and under the fabrication limitations $AR = 5$, $w_{\text{a}}^{\text{min}} = w_{\text{g}}^{\text{min}} = 0.05\lambda_{\text{o}}$, as a function of the thickness of the core d_{core} and the etch depth of the air hole d_{etch}. (a) $ratio = 0$, (b) $ratio = 0.5$ and (i) $\epsilon_{\text{core}} = 12$, $\epsilon_{\text{clad}} = 2$, (ii) $\epsilon_{\text{core}} = 12$, $\epsilon_{\text{clad}} = 6$, (iii) $\epsilon_{\text{core}} = 12$, $\epsilon_{\text{clad}} = 11$. The red lines indicate the etch-depth limits below which the hole cannot narrow any more. 61

3-9 Maximum radiation loss from the semi-infinite mirror of Fig. 3-1(c) with optimized in-plane dimensions w_g and w_a and core thickness d_{core}, over a $B = 10\%$ bandwidth and under the fabrication limitations $AR = 5$, $w_a^{min} = w_g^{min} = 0.05\lambda_o$, as a function of the placement of the core *ratio* and the etch depth of the air hole d_{etch}. (i) $\epsilon_{core} = 12$, $\epsilon_{clad} = 2$, (ii) $\epsilon_{core} = 12$, $\epsilon_{clad} = 6$, (iii) $\epsilon_{core} = 12$, $\epsilon_{clad} = 11$. The red lines indicate the etch-depth limits below which the hole cannot narrow any more. 63

3-10 Optimized reflectivity from the semi-infinite mirror of Fig. 3-1(c), over a $B = 10\%$ bandwidth and under the fabrication limitations $AR = 5$, $w_a^{min} = w_g^{min} = 0.05\lambda_o$, as a function of the wavelength λ for three choices from Fig. 3-2 for the core and cladding dielectric constants 65

3-11 Optimal in-plane dimensions (a) w_g/w_g^{min}, (b) w_a/w_a^{min} that minimize the radiation loss from the semi-infinite mirror of Fig. 3-1(c) to the values shown in Fig. 3-2, as a function of the core and substrate dielectric permittivities, where $\Delta\epsilon = \epsilon_{core} - \epsilon_{clad}$. 67

4-1 $\omega - k$ diagrams (solid curves) for conventional Surface-Plasmon-Polariton structures (insets $A - B$) with $\epsilon_{hi} = 4$ and $\epsilon_{low} = 1$ (air). The light lines $\omega/\omega_p = \sqrt{\epsilon}\cdot k/k_p$ ("vertical" dashed lines) and the cutoff frequencies $\omega_c(\epsilon)/\omega_p = 1/\sqrt{1+\epsilon}$ (horizontal dashed lines) are shown. 71

4-2 $\omega - \beta$ diagrams (red curves calculated via the effective-index method) for SPP-based waveguide structures (insets (i)) with $w/\lambda_p = 0.25$. (a) Effective-index-guiding mechanism: SPP B (from Figure 4-1) of the central vertical slice (thick solid black curve) and the ϵ_{hi} light line (dashed black curve) limit the region where fully confined modes can exist. (b) Regular index-guiding mechanism: SPP A and the vertical cladding-guided mode define the modal region. The H_x component of the first two modes at (a) $\omega/\omega_p = 0.705$ and (b) $\omega/\omega_p = 0.444$ is shown (insets (ii)-(iii) calculated via a finite-difference frequency-domain eigenmode solver). 74

5-1 $\omega-k$ diagrams (solid curves) for layered Surface-Plasmono-Dielectric-Polaritonic structures (insets $A-D$) with $\epsilon_{\mathrm{hi}}=4$ and $\epsilon_{\mathrm{low}}=1$ (air). Layer thicknesses $d/\lambda_p=0.015$, 0.02 and 0.025 are used for C and D (solid+dotted curves). The light lines $\omega/\omega_p=\sqrt{\epsilon}\cdot k/k_p$ ("vertical" dashed lines) and the cutoff frequencies $\omega_c(\epsilon)/\omega_p=1/\sqrt{1+\epsilon}$ (horizontal dashed lines) are shown. 79

5-2 $\omega-\beta$ diagrams (red curves calculated via the effective-index method) for SPDP-based waveguide structures (insets (i)) with $w/\lambda_p=0.25$ and $d/\lambda_p=0.02$. (a) SPDP D (from Figure 5-1) of the central vertical slice (thick solid black curves) and the ϵ_{hi} light line (dashed black curve) limit the region where fully confined modes can exist. (b) SPDPs C and B define the modal region. The H_x component of the first two modes at (a) $\omega/\omega_p=0.65$ and (b) $\omega/\omega_p=0.47$ is shown (insets (ii)-(iii) calculated via a finite-difference frequency-domain eigenmode solver). 81

5-3 (Taken from Ref.[86]) (a) Schematic of a 2d plasmon-cavity structure, like the one in Figure 5-2 but with a symmetry plane. (b) Q-enhancement as a function of the length L of the cavity. (Data was calculated with mode expansion method CAMFR [53].) 82

5-4 (i) $\omega-k$ dispersion diagram (designed to resemble 'MIT') for the plasmonic-dielectric layered structure shown in the inset with $\epsilon=1$, $\epsilon_{\mathrm{i}}=\{4,\ 1,\ 10,\ 1,\ 10,\ 1.7,\ 1,\ 10,\ 1.7\}$, $d_{\mathrm{i}}/\lambda_{\mathrm{p}}=\{10^{-2},\ 10^{-3},\ 5\cdot10^{-5},\ 4\cdot10^{-6},\ 3.5\cdot10^{-7},\ 5\cdot10^{-8},\ 2.4\cdot10^{-11},\ 4\cdot10^{-12},\ 6\cdot10^{-13}\}$ (from top to bottom) and $\epsilon_\infty=1$. (ii) [solid and dashed lines denote that the quantity plotted logarithmically is positive and negative respectively] (black line) $v_{\mathrm{g}}-k$ group-velocity dispersion diagram for the same structure (namely first derivative of (i)): note the apparent scaling $\max|v_{\mathrm{g}}|\sim 1/k$. (orange line) $\alpha-k$ attenuation dispersion diagram for the same structure with an added loss factor $\gamma/\omega_{\mathrm{p}}=10^{-4}$: note the apparent scaling $\min|\alpha|\sim k$, and that, away from the special points of zero group velocity and for subwavelength wavevectors, $\alpha\cdot v_{\mathrm{g}}=\gamma/2$ independently of wavevector (and thus frequency). $k_{\mathrm{p}}=\omega_{\mathrm{p}}/c=2\pi/\lambda_{\mathrm{p}}$. 85

5-5 (i) $\omega - k$ dispersion diagrams for plasmonic-dielectric layered structures with $\epsilon = \epsilon_\infty = 1$ and (a) $\epsilon_i = \{4, 1, 4, 1\}$, $d_i/\lambda_p = \{0.0200162, 0.00501101, 0.0086219, 0.0023344\}$, (b) $\epsilon_i = \{4, 1, 4, 1, 4\}$, $d_i/\lambda_p = \{0.02002878, 0.008302923, 0.01069271, 0.00349443, 0.004515306\}$: note the extremely linear regime around (a) $\omega_o/\omega_p = 0.5645$, $k_o/k_p = 13.4$, (b) $\omega_o/\omega_p = 0.5135$, $k_o/k_p = 11.5$. (ii) (all lines except orange) $\omega - D_{k,n}$ group-velocity dispersion (gvd) diagrams for the same structures (namely derivatives of (i)): plotted logarithmically in the main box and linearly in the inset, note that gvd orders $n = 2 ... N$ are cancelled at ω_o (dotted line), where (a) $v_{go}/c = D_{k,1}^{-1} = D_{\omega,1} = 0.0032 > 0$, $N = 4$, $D_{k,5} = 2.11 \cdot 10^8 \Rightarrow D_{\omega,5} = -2.24 \cdot 10^{-7}$, (b) $v_{go}/c = D_{k,1}^{-1} = D_{\omega,1} = -0.0020 < 0$, $N = 5$, $D_{k,6} = 3.16 \cdot 10^{11} \Rightarrow D_{\omega,6} = -3.96 \cdot 10^{-8}$, and thus the inset depicts the Eq.(5.1)-type behavior. (orange line) $\omega - \alpha$ attenuation dispersion (atd) diagrams for the same structures with an added loss factor $\gamma/\omega_p = 10^{-4}$: note that, throughout the plotted frequency regime, $\alpha \cdot v_g = \gamma/2$ independently of frequency (and thus wavevector) and therefore $D_{\alpha,n-1} = D_{k,n} \cdot \gamma/2\omega_p$ implying that atd orders $n - 1 = 1 ... N - 1$ are also cancelled at ω_o. 87

5-6 (i) $\omega - k$ dispersion diagram for a plasmonic-dielectric layered structure with $\epsilon = \epsilon_\infty = 1$ and (a) $\epsilon_i = \{4, 1, 4, 1, 4\}$, $d_i/\lambda_p = \{0.03805142, 0.001163696, 0.021089836, 0.00016090557, 0.004449584\}$: note the extremely linear regime around $\omega_o/\omega_p = 0.4513$, $k_o/k_p = 11.3$. (ii) (all lines except orange) $D_{\omega,n} - k$ group-velocity dispersion (gvd) diagrams for the same structure (namely derivatives of (i)): plotted logarithmically in the main box and linearly in the inset, note that gvd orders $n = 2 ... N$ are cancelled at k_o (dotted line), where $v_{go}/c = D_{\omega,1} = 0$, $N = 4$, $D_{\omega,5} = -6.46 \cdot 10^{-8}$, and thus the inset depicts the Eq. (5.2)-type behavior. (orange line) $\Gamma - k$ attenuation dispersion diagram for the same structure with an added loss factor $\gamma/\omega_p = 10^{-4}$: note that, for large enough wavevectors, $\Gamma = \gamma/2$ independently of wavevector. 88

5-7 (i) $\omega - \beta$ dispersion diagram for the plasmonic-dielectric layered waveguide structure shown in the inset with $\epsilon = \epsilon_c = 5$, $\epsilon_i = \{2, 5, 2, 5, 1.75, 5\}$, $d_i/\lambda_p = \{0.0066136, 0.0170872, 0.0021628, 0.008271, 0.000923, 0.000333\}$, $w/\lambda_p = 0.1$ and $\epsilon_\infty = 1$: note the extremely linear regime around $\omega_o/\omega_p = 0.449$, $\beta_o/k_p = 15.3$; using a finite-element calculation (at ω_o giving $\beta_o/k_p \approx 15.48$), the associated transverse modal profile is plotted in the inset for the H-component parallel to the plasmonic interface. (ii) $\omega - D_{\beta,n}$ group-velocity (gvd) dispersion diagrams for the same structure (namely derivatives of (i)): note that gvd orders $n = 2 ... N$ are cancelled at ω_o (dotted line), where $v_{go}/c = D_{\beta,1}^{-1} = D_{\omega,1} = 0.001 > 0$, $N = 5$, $D_{\beta,6} = 1.82 \cdot 10^{12} \Rightarrow D_{\omega,6} = -1.66 \cdot 10^{-9}$, and thus the inset depicts the Eq.(5.1)-type behavior. 90

8-1 (a,b) Efficiency of power transmission η_P for (a) $U = 1$ and (b) $U = 3$, as a function of the frequency detuning D_o and for different values of the loading rate U_o. (c) Optimal (for zero detuning and under conditions of impedance matching) efficiency for energy transfer and power transmission, as a function of the coupling-to-loss figure-of-merit U. 110

8-2 *Main plot.* A 2d high-ϵ disk of radius r (shown in yellow) surrounded by air, along with the electric field (with polarization pointing out of the page, from FEFD simulation) of its resonant 'whispering-gallery' mode superimposed (shown in red/white/blue in regions of positive/zero/negative field respectively). *Side plot.* Radial plot of the electric field of the mode shown in the main plot (basically a cross-section of the main plot). Note that in air (radius/$r > 1$) the field follows a Hankel-function form, with an initial exponential-like regime (with long tails compared to the small disk size), followed by the oscillatory/radiation regime (whose presence means that energy is slowly leaking out of the disk). 118

8-3 (a) Analytical SV results for the wavelength and absorption, radiation and total loss rates Q, for three different m values of subwavelength resonant modes of a dielectric disk, when varying its ϵ in the range $250 \geq \epsilon \geq 35$. Note that disk-material loss-tangent $\tan\delta = 6 \cdot 10^{-6}\epsilon - 2 \cdot 10^{-4}$ was used. (b) Relative Q error between analytical SV and numerical FEFD calculations of part (a). 119

8-4 System of two same 2d high-ϵ disks of radius r for medium-distance D coupling between them, along with the electric field (from FEFD simulation) of the normal mode, which is an even superposition of the single-disk modes of Figure 8-2, superimposed. Note that there is also a normal mode (not shown), which is an odd superposition of the single-disk modes of Figure 8-2. 120

8-5 CMT results for (a) the coupling rate Q_κ and (b) the coupling-to-loss figure-of-merit U, for three different m values of subwavelength resonant modes of two same dielectric disks at distance $D/r = 5$ (and also a couple more distances for $m = 2$), when varying their ϵ in the range $250 \geq \epsilon \geq 35$. (c) Relative U error between CMT and numerical FEFD calculations of part (b). 121

8-6 CMT results for (a) the coupling rate Q_κ and (b) the coupling-to-loss figure-of-merit U, for the two subwavelength resonant modes shown in Table 8.1 of two same dielectric disks, as a function of their distance D. (c) Relative U error between CMT and numerical FEFD calculations of part (b). 122

8-7 A conducting loop of radius r, connected to a pair of d-spaced parallel plates surrounded by air, along with a slice of the magnetic field (component parallel to the axis of the circular loop, from FEFD simulation) of their resonant mode superimposed. 126

8-8 (a) Analytical Circuit-theory (CT) results for the frequency and absorption, radiation and total loss rates Q, for the subwavelength modes of three different loops, when varying their loading capacitance. Note that for conducting material copper ($\sigma = 5.998107$S/m) was used. (b) Relative Q error between the analytical CT and numerical FEFD calculations of part (a). 127

8-9 System of two same conducting loops, connected to parallel plates for medium-distance D coupling between them, along with a slice of the magnetic field (from FEFD simulation) of the even normal mode superimposed. Note that there is also an odd normal mode (not shown). 130

8-10 Numerical CT results for (a) the coupling rate Q_κ and (b) the coupling-to-loss figure-of-merit U, for the three subwavelength resonant modes shown in Table 8.2 of two same loops, as function of their distance D. 131

8-11 A conducting rod of half-length h, connected at its center to a coil and surrounded by air. 134

8-12 Analytical Circuit-Theory (CT) results for the frequency and absorption, radiation and total loss rates Q, for the subwavelength modes of three different rods, when varying their loading inductance. Note that a Brooks inductor was assumed and for conducting material copper ($\sigma = 5.998107$S/m) was used. 134

8-13 Numerical CT results (a) the coupling rate Q_κ and (b) the coupling-to-loss figure-of-merit U, for the three subwavelength resonant modes shown in Table 8.2 of two same rods, as function of their distance D. 136

8-14 A self-resonant coil of radius r and height h with N turns of conducting wire surrounded by air. (a) Shown from a FEFD simulation along with a slice of the magnetic field (component parallel to axis of the coil). (b) Photograph of one of the actual coils built for the experiments, held together by styrofoam blocks and suspended from the ceiling with fishing wire. 137

8-15 Analytical Circuit-Theory (CT) results for the frequency and absorption, radiation and total loss rates Q, for the subwavelength modes of two different self-resonant coils, when varying their number of turns N. Note that for conducting material copper ($\sigma = 5.998107$S/m) was used. *Inset.* Dependence of self-resonant frequency on N. 138

8-16 System of two self-resonant coils for medium-distance D coupling between them, along with the magnetic field (from FEFD simulation) of the normal mode, which is an odd superposition of the single-coil modes of Figure 8-14. . 140

8-17 Numerical CT results for the electric and magnetic coupling rate Q_κ as a function of the self-resonant frequency (due to variation of N), for the modes shown in Figure 8-15 of two same coils, at the *same* distance $D_e = 1.3$m between their *edges*. 140

8-18 Theoretical CT and experimental results (a) the coupling rate Q_κ and (b) the coupling-to-loss figure-of-merit U, for the resonant modes shown in Table 8.4 of the two same self-resonant coils, as function of their distance D. 142

8-19 Schematic of the experimental setup used for wireless power transmission. s, d are the source, device self-resonant coils, coupled inductively respectively at rate κ_s, κ_d to a power supply circuit (Colpitts oscillator) and to a resistive load (light bulb). 142

8-20 Theoretical CT, from experimental measurements of κ and from experimental measurements of currents results for the transmission efficiency T, for the resonant modes shown in Table 8.4 of two same self-resonant coils, as function of their distance D. 144

8-21 Photograph (from two different angles) of the experimental system achieving transmission of 60W with $\sim 45\%$ efficiency across 2m distance between two 60cm-diameter self-resonant coils. 146

9-1 (a,b) Efficiency of power transmission η_P for (a) $U = 1$, $V = 0.5$ and (b) $U = 3$, $V = 0.5$, as a function of the frequency detuning D_o and for different values of the loading rate U_o. (The dotted lines show, for comparison, the results when there is no interference, as shown in Figure 8-1(a,b).) (c,d) Optimal (for optimal detuning and under conditions of impedance matching) efficiency for energy transfer (only in (c)) and power transmission, as a function of the coupling-to-loss figure-of-merit U and the interference-to-loss figure-of-merit V. 150

9-2 Antenna Theory (AT) results for the interference (a) factor Q_Ξ and (b) figure-of-merit $|V|$, as a function of frequency, for the exact same parameters as in Figure 8-5. (c) Relative V error between AT and numerical FEFD calculations of part (b). 154

9-3 Results for the overall power transmission as a function of frequency, for the same set of resonant modes and distances as in Figures 8-5 and 9-2, based on the predictions including interference (solid lines) and without interference just from U (dotted lines). 155

9-4 (a) Frequencies, where U and T are maximized, as a function of the transfer distance between the disks highlighted in bold in Table 8.1. (b) Efficiencies achieved at the frequencies of (a) and, in inset, the enhancement ratio of the optimal (by definition) for peak frequency of T versus the achievable at the peak frequencies of U. (c) The D-parametrized path of the transmission efficiency for the frequency choices of (a) on the $U - V$ efficiency map. 156

9-5 Results for the power radiated as a function of the transfer distance at resonant frequency ω_* (red curve of Figure 9-4(a)), when the operating frequency is detuned (solid black line), when it is not (solid red line) and when there is no interference whatsoever (dashed red line). In the inset, we show the corresponing radiation suppression factors. 158

9-6 Results for the overall power transmission as a function of frequency, for the same set of resonant modes and distances as in Figures 8-5 and 9-2, based on the predictions including interference (solid lines) and without interference just from U (dotted lines). 159

9-7 (a) Frequencies, where U and T are maximized, as a function of the transfer distance between the loops highlighted in bold in Table 8.2. (b) Efficiencies achieved at the frequencies of (a) and, in inset, the enhancement ratio of the optimal (by definition) for peak frequency of T versus the achievable at the peak frequencies of U. (c) The D-parametrized path of the transmission efficiency for the frequency choices of (a) on the $U - V$ efficiency map. 160

9-8 Results for the power radiated as a function of the transfer distance at resonant frequency ω_* (red curve of Figure 9-7(a)), when the operating frequency is detuned (solid black line), when it is not (solid red line) and when there is no interference whatsoever (dashed red line). In the inset, we show the corresponing radiation suppression factors. 161

10-1 (e) Deterioration factor J of Q for a disk mode in the presence of (a,b) a large wall w of $\epsilon = 2.5 + 0.05i$ (typical for daily materials) and (c,d) a small square human muscle m of $\epsilon = 49 + 16i$ (appropriate in the GHz regime) and side $2r$, as a function of the edge-to-edge distance $D_{(w,m)}$ and for two different positionings compared to the disk: (a,c) along the direction of minimum field and (b,d) along the direction of maximum field. 171

10-2 Deterioration factors (f) J_κ of Q_κ and (g) $J * J_\kappa$ of U for two coupled disk modes in the presence of (a) a large wall w of $\epsilon = 2.5 + 0.05i$ and thichness $2r$ between the disks, (b) two walls, one behind each disk at distance r , (c) a small square human muscle m of $\epsilon = 49 + 16i$ and side $2r$ between the disks, and (d) two muscles, one behind each disk at distance r. 172

10-3 Deterioration factor J of Q for a loop mode in the presence of a human muscle m of $\epsilon = 185 + 1230i$ (appropriate in the MHz regime) and dimensions $25\text{cm} \times 25\text{cm} \times 1.5\text{m}$, as a function of the edge-to-edge distance $D_{(m)}$ between the muscle and the capacitor. 174

10-4 Photograph of the experimental system, with and without an obstruction in the line-of-sight of the self-resonator coils, while achieving transmission of 60W across 2m distance. There is no visible difference in the brightness of the light-bulb. 176

10-5 Photograph of the experimental system, with the entire research team between the self-resonant coils, while achieving transmission of 60W across 2m distance. All the members of the team are smiling! 177

11-1 Photograph of another experimental setup, where 15W are being delivered to a load on a 50cm-diameter coil across 2m distance, from a source hidden behind a board. 182

12-1 Results for the real and imaginary parts of the complex frequency splitting of the two normal modes of the system of two coupled 2d disks with the properties in Table 12.1 as a function of their distance D, using three methods: CMT calculation for κ and Ξ, CMT calculation for κ and analytical antenna-theory prediction for Ξ, and numerical FEFD calculations. 194

List of Tables

8.1 Analytical SV and (in parentheses) numerical FEFD results for two of the modes shown in Figure 8-3, close to the frequencies where Q respectively peaks for each m. (The specific disk-mode highlighted with **bold** in the table corresponds to the one plotted in Figure 8-2.) 118

8.2 Analytical CT and (in parentheses) numerical FEFD results for the modes of the three loops shown in Figure 8-8, close to the frequencies where Q respectively peaks. (The specific loop-mode highlighted with **bold** in the table corresponds to the one plotted in Figure 8-2.) 128

8.3 Analytical CT results for the modes of the three rods shown in Figure 8-12, close to the frequencies where Q respectively peaks. 133

8.4 Numerical CT and experimental results for the resonant mode of the coil shown in Figure 8-14. Note the discrepancy in Q due to the fact that copper ($\sigma = 5.998107\text{S/m}$) was assumed for the simulations, while the experimental conductor was measured to have lower conductivity. 139

12.1 Analytical SV (and in parentheses numerical FEFD) results for the wavelength and absorption, radiation and total loss rates, for two different subwavelength-disk resonant modes. Note that disk-material loss-tangent $\tan\delta = 6 \cdot 10^{-6}\epsilon - 2 \cdot 10^{-4}$ was used. 192

Part I

Novel photonic phenomena in nanostructured material systems with applications

Chapter 1

Introduction

1.1 Background

One fundamental aspect of optical technology has always been the quest for the perfect photonic platform to guide, confine and, in general, manipulate light. Ideally, one would like to have a system that supports light propagation in waveguides with subwavelength modal size, controllable (with special interest lately on slow [6]) group velocity and very small (radiation and absorption) attenuation, both devoid of frequency dispersion [7]; and light confinement in cavities with subwavelength modal volumes and very small (radiation and absorption) loss. If this were possible, temporally and spatially tiny wavepackets would propagate down these waveguides at desirable (e.g. slow) speed without changing shape but only with extremely-slowly and uniformly decreasing size; and spatially tiny light-drops would stay trapped inside these cavities for extremely long times. In theory, passive components for routing, filtering and (de)multiplexing broadband signals would operate almost losslessly, and active components for switching, amplifying and frequency converting would require minimal energy down to single-photon levels, and all of the above on a very small footprint. Therefore, very-large-scale-integrated all-optical communication and computing chips would be readily manufacturable. Such a platform is not yet known to exist in nature, as none of the existing ones can achieve simultaneously all of the above attributes, but at most only a subset. However, large-scale efforts continue and great advances are witnessed every year in the realm of nanophotonic technology.

Along the search for the ideal photonic platform, one needs to consider both the material selection and the geometric/structural design. For guiding light, the traditional material

options are dielectric and metallic materials. Their fundamental difference is that dielectric materials allow light to propagate through them, while metals do not. Therefore, the mechanism they employ to confine light is different: dielectrics use the so-called 'index-guiding', where light traveling inside a high-index dielectric is reflected on its interface with lower-index surrounding materials and thus stays trapped inside the body of the dielectric (as is the case in optical fibers and waveguides); metals reflect all light up to visible, namely they exhibit a 'gap', and thus use the so-called 'gap-guiding', where light is simply traveling inside a hollow metallic structure (as is the case in microwave waveguides). However, once we consider a geometrical variation of the structural material properties, by adding periodicity to form Dielectric Photonic Crystals (DPC) [8, 9] and MetalloDielectric Photonic Crystals (MDPC) [10], these complex structures can now have, at different frequency regimes both passband and bandgap behavior, and therefore can be used respectively either as a guiding core or as a confining cladding. Interestingly, there exists though one more guiding mechanism, that of trapping light on the surface between a 'pass' material structure (dielectric, DPC, MDPC) and a 'gap' material structure (metal, DPC, MDPC).

Based on this categorization, let us now examine the advantages and disadvantages of the existing photonic platforms, with respect to the criteria stated earlier. All-dielectric uniform integrated photonic structures [11] are the most fundamental and robust existing systems, due to their simplicity and low absorption loss; however, they suffer from radiation loss at structural discontinuities, especially when forced to maintain modal volumes on the order of the wavelength. This problem is resolved by DPCs [12], which, by definition, do not allow light to escape and can thus be essentially lossless; they require though very high fabricational complexity and have thus not yet really been put to practice. An intermediate all-dielectric compromise in complexity and radiation-loss are the incomplete-photonic-bandgap structures [13, 14], namely ones that in some directions light is blocked by gap-guiding and in the rest via index-guiding; this has slowly started to play a role, as it can be designed to combine the benefits from its limiting cases. Nevertheless, all-dielectric structures have some fundamental limitations they cannot overcome: they cannot enable highly subwavelength operation, as very large refractive indices are not available in the optical, and, basically for the same reason, they cannot support slow light over a large frequency bandwidth (an increasingly important concept for nanophotonics [15]), rather they exhibit an upper limit in the so-called 'bandwidth-delay product' [16].

Hollow metallic structures, such as those used in the microwave, are by construction radiation free (same as photonic crystals), but metals suffer from increased absorption losses in the optical (and this is why optical fibers were invented in the first place) and are still limited by the free-space wavelength. MDPC systems can actually be extremely subwavelength, but, since periodicity limits the maximum possible wavevector, this subwavelength operation is achieved only at very low frequencies; it is precisely this regime of operation that we simply call 'electronics'.

For a system with highly-subwavelength performance and with the possibility of having slow light over arbitrarily large frequency bandwidth in the optical, the photonic platform fundamentally should be able to support light of arbitrarily large wavevectors and this is attainable only by exploiting bulk or surface polaritons in plasmonic [17, 18] or other resonant-material (e.g. atomic, excitonic, phononic [19, 20]) structures. Unfortunately, since this behavior typically happens close to a material resonance, it is associated with heavy absorption losses and the bandwidth of operation is limited. Enforcing a quantum coherent coupling of more than one such resonances (such as in electromagnetically-induced transparency [21]) can at least lead to absorption-free subwavelength and extremely slow- [22, 23, 24, 25] or stopped-light [26, 27, 28] performance, even though narrow band.

Finally, the one problem that is commonly shared among all existing photonic systems is modal dispersion, forced by both the materials and the geometries, and can typically be cancelled only to the lowest order, because it is difficult to control.

1.2 Outline

In this part of my thesis, the work has been focused on two of the most promising material platforms described above:

Incomplete-bandgap all-dielectric photonic structures are very promising in achieving, to a satisfying extent and with simplicity, what complete-bandgap photonic-crystal structures can do, perfectly but intricately, by suppressing radiation only into the one-dimensional line or two-dimensional plane of the patterned structure, provided they can be designed to not suffer significant out-of-line or out-of-plane losses. Thus the development of mechanisms to suppress this radiation is needed.

Some such mechanisms have been demonstrated for the case of resonant cavities and in-

clude the delocalization mechanism [29], where essentially the modal volume is compromised, either in the in-plane or out-of-plane direction, to achieve a high Q, and the cancellation mechanism [30], where the near-field resonant pattern is designed to be orthogonal to the dominant dipole moment of radiation; once coupling to this moment is cancelled, the total radiation is suppressed and a significant enhancement in Q is achieved, without sacrificing modal volume. In Chapter 1, we have extended this cancellation mechanism to the case of patterned substrates, by noting that, in these cases, radiation is channeled into the substrate via discrete guided or leaky modes, to which coupling can be forbidden using the same orthogonality principle as for the free-space multipoles, and thus again a significant enhancement in Q is accomplished.

In the case of non-resonant components, it is essential that radiation loss at discontinuities is kept low over a large frequency bandwidth, if this platform is to be used for high-speed photonic signals. Under special symmetries [31, 32] this can be achieved even in the absence of a complete photonic bandgap, but the required structures are still not easily amenable to fabrication. Instead, an optimization procedure is required over the system parameters. Some of these parameters have been examined in the past, in particular the differential index-contrast of the core and the cladding materials [33, 34] and the etched-hole depth in the case of substrates [35, 36], however, a thorough and global optimization procedure has not been undertaken and is the topic of Chapter 2, where we have used the particular example of lossless reflection from a butt-coupled semi-infinite mirror for our optimization. The results indicate that considering a broader parameter-space is important, and that both traditionally used high-index-contrast and low-index-contrast platforms are optimal, depending on the particular application at hand.

Surface plasmon-polaritonic structures have also been of such great interest lately that an entire field, called 'plasmonics', has been developed for their study. It is exactly their ability to guide and trap light in highly subwavelength volumes that makes them so appealing, at a time when demand for integration density and sensing resolution is increasing.

Typically, making waveguides in plasmonics consists of using a very thin metallic wire with light running on its surface [37, 38, 39, 40, 41], but other configurations, such as channel plasmon polaritons [42, 43] have also been used. In Chapter 3, we introduce a new guiding mechanism, with which light can counter-intuitively be localized inside the region of a low-index material, when this is adjacent to a high-index material extending to infinity. This is

a surprising result, because only as part of a photonic crystal is a high-index material known to allow such confinement. But it is the special subwavelength guiding ability of plasmon polaritons that enables this mechanism.

Finally, given the increased interest in slow light, which could enhance the performance of active and switching devices by reducing their power requirement and/or substantially reducing their size [15], plasmonics have received some attention due to the very slow group velocity they enable near the surface resonance. However, as with all other system based on resonances, the frequency bandwidth has been limited. In Chapter 4, we introduce a new hybrid Surface-PlasmonoDielectric-Polaritonic (SPDP) platform that, not only can support slow light over a very large frequency range, but it actually provides a large enough number of degrees-of-freedom to manipulate its dispersion at will, to the extent that group-velocity dispersion and attenuation dispersion can be cancelled at the same time to unprecedently high orders. This platform will be shown to have great applications in optical delay lines and active devices.

Chapter 2

High-radiation-Q small-modal-volume Dielectric-Photonic-Crystal (DPC) resonant cavities [1]

A critical component of optical devices is a resonant cavity, characterized by its radiation loss (or lifetime Q) and its modal volume V. Without a complete photonic bandgap [12] or special symmetries [32], cavities normally have intrinsic losses. However, incomplete-gap systems, e.g. combining index guiding with 1D/2D bandgaps [13], are of widespread interest because they are easily fabricated. Here, we focus on systems where the periodic pattern extends into the substrate (and superstrate), with either high or low vertical index contrast, such as those shown in Figures 2-1(a,b). In the case of a *uniform* substrate (e.g. a bridge [44] or membrane [45] suspended in air), a strong peak in Q can be achieved without modifying V by forcing a cancellation of a multipole term in the radiated far field [30] or, in a related way, by cancelling dominant Fourier components in the near field [46, 45, 47, 48]—the key feature, we argue, being a qualitative change in the far-field/Fourier pattern. We show that this cancellation mechanism is substantially modified by a *patterned* substrate, because the radiation is no longer purely a continuum: it can be dominated by discrete guided or leaky modes propagating vertically in the central unpatterned region of the cladding (Figure 2-1(c)). In this case, which applies to arbitrary index-contrast substrates, one forces an orthogonality of the near field with such a discrete mode, resulting in a peak in Q. Again, no sacrifice in modal volume V is needed, in contrast to previous works, which have

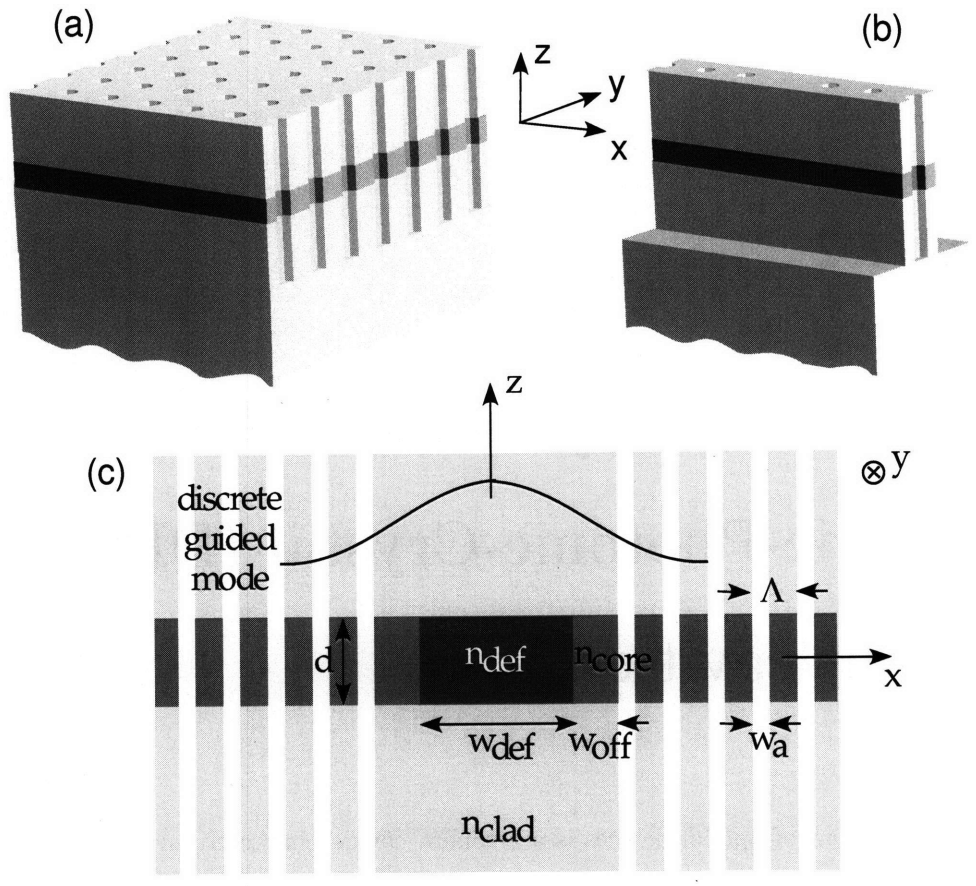


Figure 2-1: (a) Photonic-crystal slab microcavity, (b) Monorail microcavity, (c) Two-dimensional model of the cavities for the region in the vicinity of the defect.

shown how to increase Q by delocalizing the mode either horizontally [29] or vertically [49]. In this letter, we first describe the general mathematical foundations for all such cancellation mechanisms (with guided, leaky, and continuum modes), and then give two 2D example systems (with high and low index contrast) illustrating a factor of 10 increase in Q. Improvement of the same order is expected in 3D, since similar gains were demonstrated in 3D for multipole-based cancellations [30].

2.1 High-Q cavities by discrete-mode cancellation mechanism

Consider, as examples, the integrated cavities shown in Figures 2-1(a,b). If the resonant near field does not "see" the solid substrate and air superstrate, these can be ignored. This is true if the array of holes is etched deep enough through the high-index slab, so that they cover at least the decay length of the waveguide mode [49]. Labelling the vertical out-of-plane

direction as z, the effective patterned cladding can now be thought of as a multilayered waveguide along z, which at the resonant frequency ω supports a complete set of modes (with dependence $e^{i\beta z - i\omega t}$), that consists of a continuous spectrum and possibly discrete index- and bandgap-guided modes. Those propagating in z (real β) fall inside the radiation cone and thus contribute to the total loss, while the evanescent ones (complex β) do not. The mode profiles for the transverse to z field components will be $\vec{e}_n(x,y)$, $\vec{h}_n(x,y)$ for the discrete and $\vec{e}(\beta;x,y)$, $\vec{h}(\beta;x,y)$ for the continuum. Having ignored the solid substrate and air superstrate and dropping the x,y dependence for simplicity, the field outside the cavity can be written as [50]

$$\begin{bmatrix} \vec{E}_t(\vec{r}) \\ \vec{H}_t(\vec{r}) \end{bmatrix} = \sum_n c_n \begin{bmatrix} \vec{e}_n \\ \vec{h}_n \end{bmatrix} e^{i\beta_n z} + \int_\beta c(\beta) \begin{bmatrix} \vec{e}(\beta) \\ \vec{h}(\beta) \end{bmatrix} e^{i\beta z} d\beta \,. \tag{2.1}$$

If this complete set of modes is orthonormalized so that

$$\begin{aligned} \tfrac{1}{4}\int_{xy} \left[\vec{e}_n^* \times \vec{h}_m + \vec{e}_m \times \vec{h}_n^*\right] \cdot \hat{z}\, dxdy &= \delta_{mn} \\ \tfrac{1}{4}\int_{xy} \left[\vec{e}(\beta)\times\vec{h}(\beta') + \vec{e}(\beta')\times\vec{h}^*(\beta)\right] \cdot \hat{z}\, dxdy &= \delta(\beta-\beta') \,, \end{aligned} \tag{2.2}$$

then the total power radiated will be (for any z)

$$P = \frac{1}{2} Re\left[\int_{xy} \vec{E}_t \times \vec{H}_t^* \cdot \hat{z}\, dxdy\right] = \sum_{n:\beta_n\, real} |c_n|^2 + \int_{\beta\ real} |c(\beta)|^2 d\beta \,, \tag{2.3}$$

namely an incoherent sum of discrete terms and a continuum. If the stored energy inside the cavity is $U = \int u dV$, with $u = \frac{1}{2}\epsilon \left|\vec{E}\right|^2$ the energy density, then the two major figures of merit that characterize a resonant cavity are the quality factor Q [11] and the modal volume V [51]:

$$Q^{-1} = \frac{P}{\omega U} = \sum_{n:\beta_n\, real} Q_n^{-1} + \int_{\beta\ real} Q^{-1}(\beta)\, d\beta \tag{2.4}$$

$$V = U/max(u) \,, \tag{2.5}$$

where the introduced individual factors $Q_n^{-1} = |c_n|^2 / \omega U$ and $Q^{-1}(\beta) = |c(\beta)|^2 / \omega U$ contribute independently to the total Q. For a low loss cavity, Q must be large, while a small modal volume is usually desired.

Depending on the design, the discrete terms in (2.3) may often carry a significant portion of the total radiated power, so that Q is limited by some Q_n, as seen below. In that

case, a significant increase in Q can be achieved by cancelling the corresponding expansion coefficients. These are determined by the near-field pattern $\vec{E}_{t0}(x,y)=\vec{E}_t(x,y,z=0)$ and $\vec{H}_{t0}(x,y)=\vec{H}_t(x,y,z=0)$:

$$\begin{bmatrix} c_n \\ c(\beta) \end{bmatrix} = \frac{1}{4}\int_{xy} \left\{ \begin{bmatrix} \vec{e}_n \\ \vec{e}(\beta) \end{bmatrix}^* \times \vec{H}_{t0} + \vec{E}_{t0} \times \begin{bmatrix} \vec{h}_n \\ \vec{h}(\beta) \end{bmatrix}^* \right\} \cdot \hat{z}\, dxdy\,. \tag{2.6}$$

Cancellation of a c_n can be achieved by forcing the near field to be orthogonal to its associated mode by proper design of the defect, for example by tuning its dielectric constant or shape. Similarly, an elimination of a mode $c(\beta)$ within the continuum can be imposed again through (2.6). In any case, cancellation of an eigenmode of this generalized-Fourier type basis set for the near field implies, according to Fraunhofer diffraction theory, a corresponding nodal direction in the far field.

The multilayered waveguide formed by the patterned cladding might also support discrete modes of the "leaky" type. Their contribution to the radiated field associated with the continuum can be made evident by applying a Steepest Descent approximation to (2.1) for some angle of observation. If then leaky wave poles $\widetilde{\beta}_m$ are crossed during the deformation of the integration path in the complex β-plane, Eq.(2.1) becomes [52]

$$\begin{bmatrix} \vec{E}_t(\vec{r}) \\ \vec{H}_t(\vec{r}) \end{bmatrix} \approx \sum_n c_n \begin{bmatrix} \vec{e}_n \\ \vec{h}_n \end{bmatrix} e^{i\beta_n z} + \sum_m \widetilde{c}_m \begin{bmatrix} \widetilde{\vec{e}}_m \\ \widetilde{\vec{h}}_m \end{bmatrix} e^{i\widetilde{\beta}_m z} + \int_{SD\ path} [...]\, d\beta\,. \tag{2.7}$$

Since leaky modes do not belong to a complete orthogonal set, relations of the form (2.3) or (2.4) cannot be rigorously written. Still, cancelling a discrete coefficient $\widetilde{c}_m$ in the expansion (2.7) should result in an increase of the radiation Q, if the associated leaky wave carries a significant portion of the field radiated within the continuum.

Just like the free-space cancellations [30], such a discrete-mode cancellation involves only small changes in the near-field pattern in order to force the orthogonality relation, and it does not rely on delocalization. Modal volume can thus be kept small and nearly constant.

2.2 Discrete-mode cancellation for realistic systems

To illustrate the principles above, the simplified 2D model of Figure 2-1(c) was used to describe the region in the vicinity of the cavities in Figures 2-1(a,b). TE (y-polarized)

modes were examined using an eigenmode expansion method [53]. A periodic array of deep air-grooves is etched all the way through a single-mode symmetric slab waveguide, opening a bandgap in the x direction. A defect is then introduced by making one waveguide section longer. The resonant field will leak power vertically out of the cavity. To study the effects of defect variations on radiation loss, we vary the index n_{def} of a part of the waveguide core (Figure 2-1(c)), while simultaneously adjusting its length w_{def}, so as to keep the resonant wavelength fixed - maintaining a fixed position in the gap is critical so as to preserve the localization and not confuse the cancellation and delocalization mechanisms for improving Q.

For a low index-contrast InP/GaInAsP ($n=3.35/3.17$) waveguide with a bandgap in the 1.205-1.949μm range, a typical field plot for the 2^{nd} order (two nodes in the defect) resonance at $\lambda = 1.55\mu m$ is shown in Figure 2-2(b). The majority of the radiation loss is index-confined in the central region to a discrete, vertically propagating, guided mode, while some of the extended modes $\vec{e}(\beta; x)e^{i\beta z}$ have been removed by the bandgap. For $n_{def}=3.29$ the guided mode is cancelled (Figures 2-2(a,c)) with a corresponding factor of 10 increase in total Q, and the peak limited only by the continuum to $Q \approx 58,000$. Moreover, the modal volume is almost independent of the tuning and very small, on the order of $0.28\,(\lambda/n_{def})^2$ (Figure 2-2(a)).

A high index-contrast Si/SiO_2 ($n=3.45/1.45$) waveguide with a 1.205-1.651μm bandgap has, for the same resonance at $\lambda = 1.55\mu m$, a field pattern like in Figure 2-3(b). Due to the smaller cladding index variation (air-SiO_2) the discrete guided mode is now less confined, and its contribution to radiated power is no longer dominant, but is similar to that of the continuum. Two equally prominent cancellations are now present: one of the discrete eigenmode type presented in this paper, at $n_{def}=3.142$ (Figures 2-3(a,c)) and one of the multipole type [30] at $n_{def}=3.221$ (Figures 2-3(a,e)). The total Q is maximized to $Q \approx 21,000$ midway, at $n_{def} = 3.18$ (Figures 2-3(a,d)). The null in the far-field pattern is sweeping in angle from the vertical z to the horizontal x direction as the tuning parameter n_{def} is varied and a different discrete or extended mode is cancelled. The modal volume is again roughly constant, and even smaller than before at $0.11\,(\lambda/n_{def})^2$ (Figure 2-3(a)).

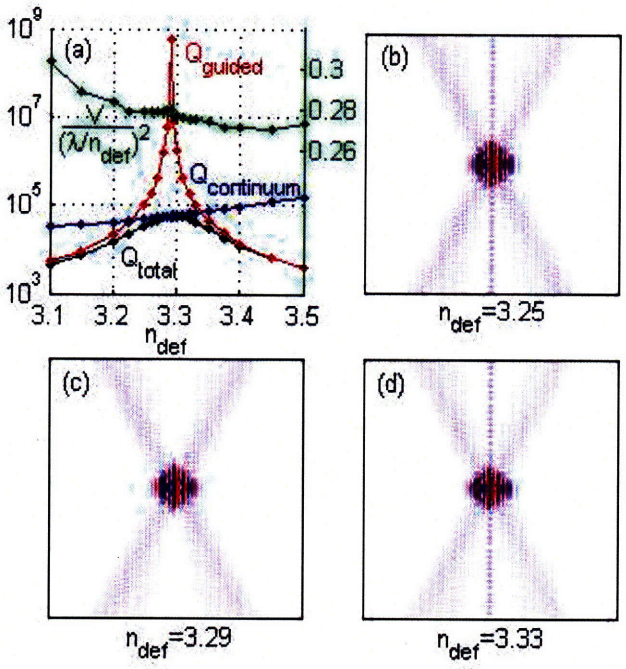


Figure 2-2: Results for $n_{core} = 3.35$, $n_{clad} = 3.17$, $d = 680nm$, $\Lambda = 320nm$, $w_a = 150nm$ and $w_{off} = 125nm$. (a) Q total, Q of guided mode, Q of continuum and $V/(\lambda/n_{def})^2$ vs. n_{def} (w_{def} is adjusted so that $\lambda = 1.55\mu m$); (b)-(d) Resonant field at certain values of n_{def}.

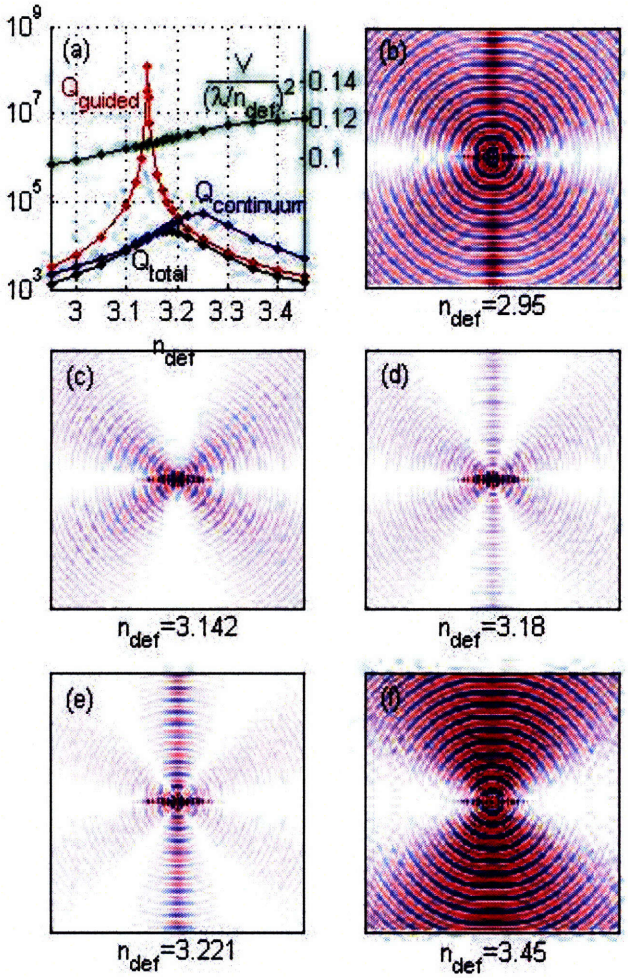


Figure 2-3: Results for $n_{core} = 3.45$, $n_{clad} = 1.45$, $d = 1\mu m$, $\Lambda = 300nm$, $w_a = 100nm$ and $w_{off} = 100nm$. (a) Q total, Q of guided mode, Q of continuum and $V/\left(\lambda/n_{def}\right)^2$ vs. n_{def}; (b)-(f) Resonant field at certain values of n_{def}.

Chapter 3

Low-radiation-loss butt-coupled Dielectric-Photonic-Crystal (DPC) broadband mirrors

Another important component of integrated optical systems is an all-dielectric mirror, characterized by its reflectivity, radiation loss and frequency bandwidth. A challenging problem of current technology is the design of such mirrors with very low loss over large bandwidths. In the presence of a complete photonic bandgap [8, 9, 12] or special symmetries [31, 32] radiation losses can be completely suppressed in three-dimensional structures, but the fabrication of the required geometries is very demanding and has not yet been demonstrated satisfactorily. On the contrary, incomplete-photonic-bandgap systems, namely ones that partly rely also on the index-guiding mechanism to confine light [13, 14], are presently straightforward to implement, and one could anticipate that they might be sufficient in terms of losses and dominate the future photonic technology, based on recent experimental results on such photonic-crystal-slab cavities of extremely high-Q [54, 55, 56]. For a given material selection and geometry of the photonic crystal, in order to achieve this performance for resonant cavities, the *defect* design procedure consists of choosing a mode of a favorable symmetry [46] and then applying the delocalization [29] and cancellation [30, 1] mechanisms to further optimize Q, the latter of which was analyzed in Chapter 2. These techniques rely on the resonant nature of the electromagnetic field and are thus not applicable in the case of mirrors, where loss must be minimized over a large frequency bandwidth. Instead, the materials and

the geometry of the *crystal* themselves need to be properly designed. For structures such as those shown in Figures 3-1(a) and 3-1(b), the main parameters under investigation so far have been the core-substrate refractive-index differential contrast [33, 34] and the hole depth [35, 36]. Here, we treat this problem with much more generality and show that a larger parameter space must be considered to fully optimize for the radiation loss, such as the exact refractive-indices of the materials (and not only their differential contrast) and the in-plane dimensions and periodicity of the holes. We derive specific design rules and provide theoretical explanations for the physical mechanisms that underlie the improvement. The design guidelines presented should apply to all incomplete-gap devices (resulting, for example, in further improvement in cavity-Q and reduced-loss waveguide bends) and should be considered, when choosing the photonic-crystal-slab platform of an integrated optical system.

To motivate the importance of low-loss broadband integrated mirrors, consider the example of a certain class of channel add-drop filters, where one channel is dropped from a photonic-crystal or grating cavity and the through channels are simply reflected and redirected to an exit port. A system that consists of many such drop units (each appropriate for a different wavelength) cannot afford consecutive losses for the through channels that are not even being processed, and thus the reflectivity of the cavity needs to be as close to unity as possible for all the off-resonance wavelengths that cover the entire bandwidth of the incoming multiplexed signal.

In our following analysis, we first give in Section 3.1 a description of the photonic-crystal-slab mirror structure under consideration and the formulation of the optimization problem, along with a preview of the final result of minimized radiation loss upon reflection as a function of the core and substrate dielectric constants. In Section 3.2, we proceed in discussing the design rules for the dimensions of the crystal in the horizontal plane of the periodicity, while in Section 3.3 those for the dimensions in the vertical direction of layer growth. The variation of losses with the choice of materials is then further discussed in detail in Section 3.4, and conclusions are drawn pertaining to complete design rules for incomplete-gap photonic systems.

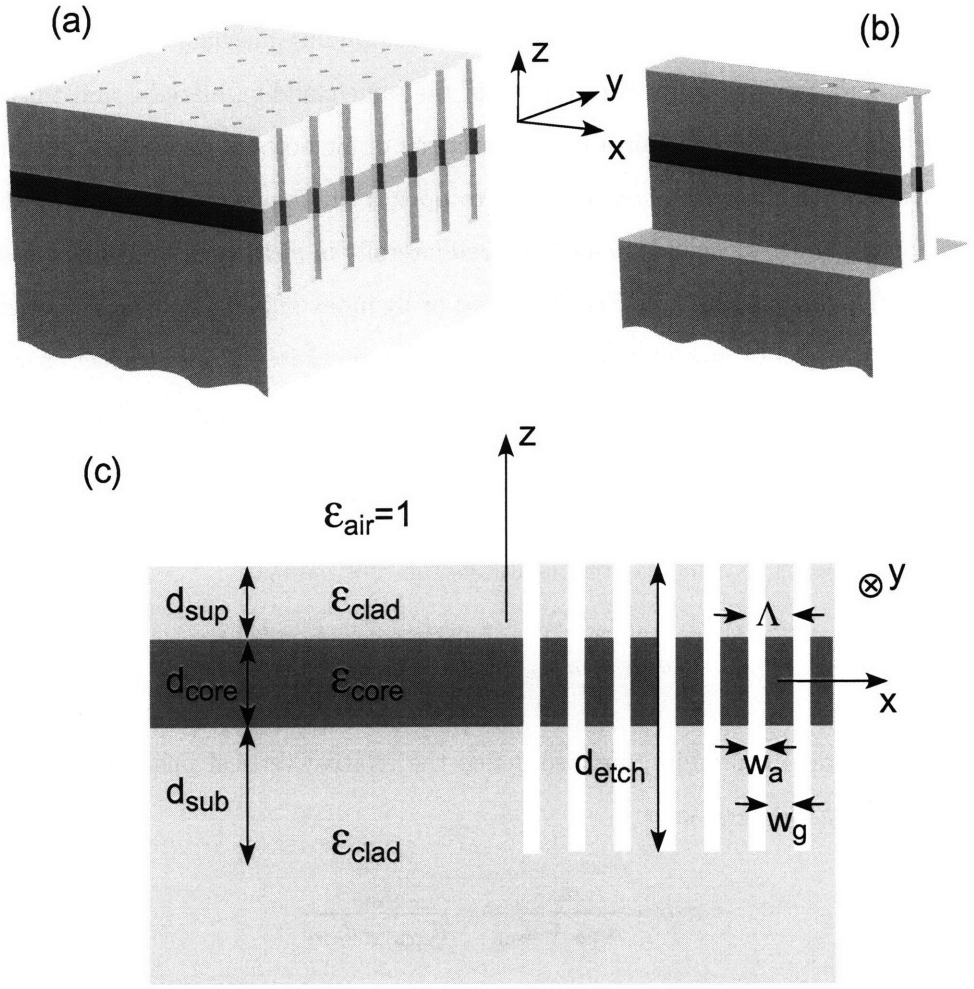


Figure 3-1: (a) Photonic-crystal-slab mirror, (b) Photonic-crystal-monorail mirror, and (c) two-dimensional model of the mirrors based on their vertical cross-sections at their symmetry planes.

3.1 Formulation of the problem and preview of the final solution

The most common and fabrication-wise realistic geometries of incomplete-photonic-bandgap devices are photonic-crystal slabs [57] and monorails [58], as shown in Figures 3-1(a) and (b). The core layer of dielectric permittivity ϵ_{core} and thickness d_{core} is deposited on top of a substrate of lower permittivity ϵ_{clad}, for the index-guiding mechanism inside the core to be enabled, and perhaps a superstrate layer of the same cladding material and thickness d_{sup} separates the core from the air above.[1] An array of air holes of depth d_{etch}, diameter w_{a} and periodicity Λ is then etched, in order to open a photonic bandgap in the axial x direction of an incoming waveguide mode, confined laterally in y either by the same bandgap (photonic-crystal-slab waveguide of Figure 3-1(a)) or by index guiding (monorail waveguide of Figure 3-1(b)). It is of our interest to study and suppress losses upon reflection of the mentioned waveguide mode onto itself from the formed mirrors over a prescribed frequency bandwidth $B = \Delta\lambda/\lambda_{\text{o}}$, where λ_{o} is the central wavelength. It has been shown [35, 36] that these losses are severe unless the holes are perforated all the way through the core layer, thus we will assume henceforth that this is always the case, namely

$$d_{\text{etch}} \geq d_{\text{core}} + d_{\text{sup}} \geq d_{\text{core}}. \tag{3.1}$$

Given this geometrical constraint, we also define the relative vertical position of the core layer to the hole by the parameter

$$ratio = \frac{d_{\text{sup}}}{d_{\text{sup}} + d_{\text{sub}}} = \frac{d_{\text{sup}}}{d_{\text{etch}} - d_{\text{core}}}. \tag{3.2}$$

Note that the class of structures contained in the above description is very broad and general. For example, membranes [57] and bridges [58] suspended in air are a subcase for $\epsilon_{\text{clad}} = 1$, and in that case the parameters d_{etch} (under condition (3.1)) and *ratio* lose any real physical significance.

In Section 3.2 we show that the lost power is produced and radiated only from the interface $x = 0$ that breaks the axial symmetry of the otherwise translationally invariant

[1] We believe that the assumption of the same material for the superstrate layer is a justified one, since, if the presence of this layer is beneficial at all, it will be so only by preserving the vertical symmetry of the waveguide and this presupposes same materials for the sub- and superstrates.

waveguide and mirror segments. Therefore, increasing the length of the mirror does not affect this loss L but only drives transmission T to zero. Since only the former is of interest to us, we will assume for simplicity that the periodic mirrors are semi-infinite, so then transmission is exactly zero

$$T = 0 \Leftrightarrow R + L = 1 \tag{3.3}$$

and thus the loss L at a given wavelength can be obtained by just looking at the mirror reflectivity R for the incident waveguide mode.

For simplicity, we choose to analyze an equivalent two-dimensional system (shown in Figure 3-1(c)), that of the $x - z$ cross-section at the symmetry plane of the systems in Figures 3-1(a) and (b). All the important physics stays the same in three dimensions (apart from an exception mentioned in Section 3.3), so the final design rules will be applicable to the 3d structures too. Unless certain restrictions are imposed, the problem of minimizing radiation loss over the bandwidth B for this mirror geometry has a trivial solution in 2d. By taking the core thickness d_{core} and hole depth d_{etch} go to infinity, the structure is asymptotically vertically (in z) invariant and therefore the incident mode is just a plane wave that couples only to itself upon reflection, and thus loss is identically zero through Eq.(3.3). Let us, then, apply the restriction of single-mode (sm) operation for the waveguide, up to the shortest wavelength $\lambda_{min} = \lambda_{\text{o}}\,(1 - B/2)$ of the bandwidth B of interest, namely

$$d_{\text{core}} \leq d_{\text{sm}} = d_{\text{sym}} \left[1 + \frac{1}{\pi} \tan^{-1} \left(\frac{C}{1 + \pi C d_{\text{sup}}/d_{\text{sym}}} \right) \right] \tag{3.4}$$

where $C = \sqrt{\Delta\epsilon_{\text{c}}/\Delta\epsilon} = \sqrt{(\epsilon_{\text{clad}} - 1)\,/\,(\epsilon_{\text{core}} - \epsilon_{\text{clad}})}$, and $d_{\text{sym}} = \lambda_{\text{min}}/\left(2\sqrt{\Delta\epsilon}\right)$ is the single-mode limit for a symmetric ($C = 0$ or $d_{\text{sup}} = \infty$) version of the two-dimensional waveguide of Figure 3-1(c). This condition still does not bound the transverse dimensions, since the core-cladding refractive-index contrast $\Delta\epsilon$ can be arbitrarily small. This bound comes from considering the limitations that current fabrication techniques impose, and it is exactly these that make the optimization problem a nontrivial one. In particular, holes with small disorder can only be made up to a certain aspect ratio AR of their depth over their width, namely

$$d_{\text{etch}}/w_{\text{a}} \leq AR, \tag{3.5}$$

and this limits d_{etch}, and d_{core} through Eq.(3.1). In addition, there is a smallest feature size

for each lithographic technique available and this will be incorporated here by restrictions on the widths of the air holes and the surrounding dielectric pattern, namely

$$w_{\mathrm{a}} \geq w_{\mathrm{a}}^{\mathrm{min}} \text{ and } w_{\mathrm{g}} \geq w_{\mathrm{g}}^{\mathrm{min}}. \tag{3.6}$$

Now, given the specifications for the operating bandwidth $\{\lambda_{\mathrm{o}},\ B\}$ and the fabrication limitations $\left\{AR,\ w_{\mathrm{a}}^{\mathrm{min}},\ w_{\mathrm{g}}^{\mathrm{min}}\right\}$, the minimization of the maximum radiation loss throughout the range $[\lambda_{\mathrm{o}}\,(1-B/2)\,,\ \lambda_{\mathrm{o}}\,(1+B/2)]$, in terms of $\{w_{\mathrm{g}},\ w_{\mathrm{a}},\ d_{\mathrm{core}},\ d_{\mathrm{etch}},\ ratio\}$ for the geometry of Fig. 3-1(c) and under the conditions (3.1),(3.4),(3.5) and (3.6), is a well-posed problem and one of great practical interest, as we explained in the introduction of Section 3.

The numerical solution of this problem has been obtained using the electromagnetic simulation package CAMFR [53] that is based on bounding the computational domain with walls enforced with a perfectly-marched-layer (PML) boundary condition, and then applying the eigenmode-expansion and mode-matching methods at a given frequency. The simulations led to some numerical error, which is mainly due to singularities of the solution at the edge of the Brillouin zone and does not affect the qualitative conclusions of the analysis; a very soft averaging has been applied to mitigate this numerical error in subsequent plots.

Figure 3-2 shows the final solution of the minimized maximum radiation loss within a $B = 10\%$ bandwidth for different choices of the core and cladding materials. It can be seen that radiation loss is low for high-index-contrast air-membrane- or air-bridge-type structures and for the low-index-contrast but overall high-index structures. From the plot it is now obvious that indeed solely the index contrast is not a sufficient parameter to characterize radiation losses. The optimization procedure, the physical interpretation and the consequences of this result are the subjects of the subsequent Sections.

3.2 Optimization for dimensions of the crystal in the horizontal plane of periodicity

3.2.1 Bloch modes of infinite photonic-crystal slab

To understand the behavior of a semi-infinite photonic-crystal slab as a mirror, when this operates inside the bandgap, it is first necessary to comprehend the nature of the solutions for the infinite crystal in this frequency regime. These are Bloch modes, which are evanescent

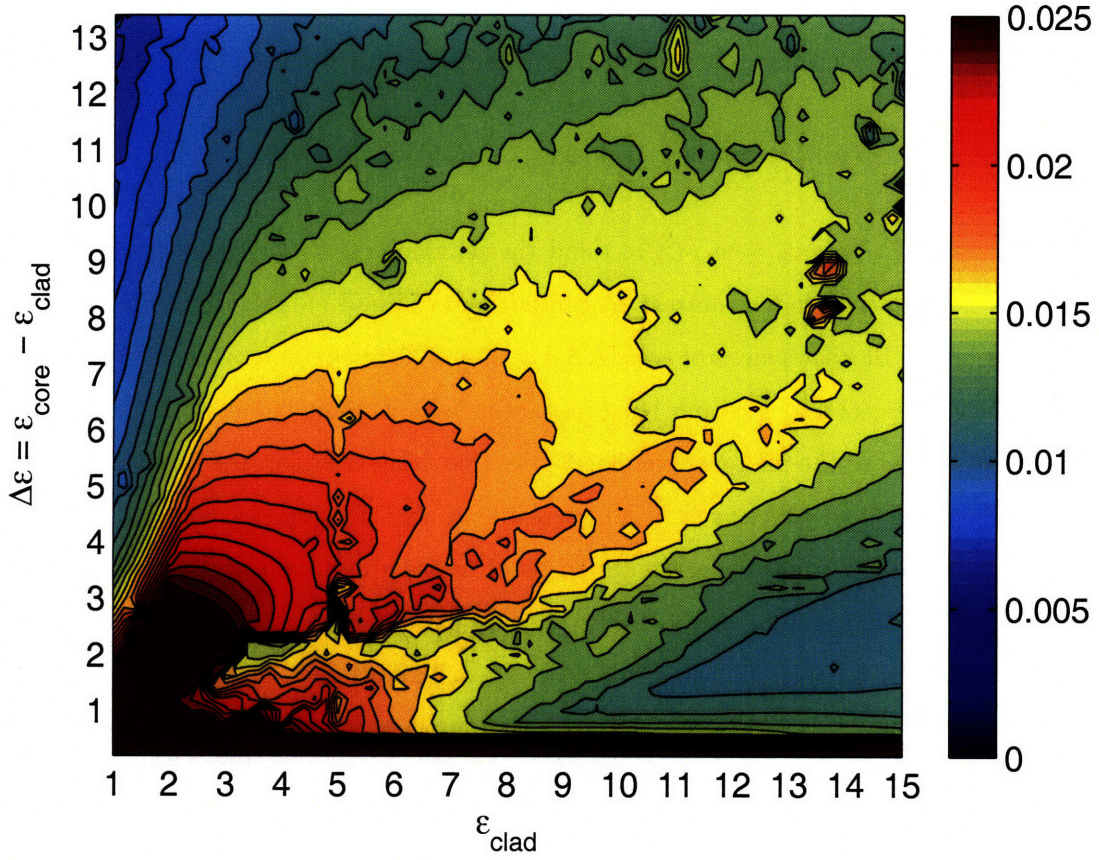


Figure 3-2: Minimized maximum radiation loss from the semi-infinite mirror of Figure 3-1(c), over a $B = 10\%$ bandwidth and under the fabrication limitations $AR = 5$, $w_{\mathrm{a}}^{\mathrm{min}} = w_{\mathrm{g}}^{\mathrm{min}} = 0.05\lambda_{\mathrm{o}}$, as a function of the core and substrate dielectric permittivities, where $\Delta\epsilon = \epsilon_{\mathrm{core}} - \epsilon_{\mathrm{clad}}$.

inside the photonic gap, and their longtitudinal and transverse field profiles along with their wavelength dependence are of interest to us, because they are related, as we shall see, to the amount of radiation loss produced upon reflection.

Before analyzing the two-dimensional case relevant to Figure 3-1(c), it will be useful to review the Bloch mode solutions for a one-dimensional infinite stack of alternated dielectric layers. If the high and low refractive indices of the two layers are respectively n_g and n_a, and their widths w_g and w_a (with $w_g + w_a = \Lambda$ the period), then the Bloch eigenvalue K at wavelength λ and for no transverse variation of the field (normal incidence) is given by [59]

$$\cos(K\Lambda) = \cos(2\pi z_g)\cos(2\pi z_a) - P\sin(2\pi z_g)\sin(2\pi z_a), \tag{3.7}$$

where $z_g = w_g/(\lambda/n_g)$, $z_a = w_a/(\lambda/n_a)$ and the parameter $P = (n_g/n_a + n_a/n_g)/2 > 1$ quantifies the refractive-index contrast. A contour plot of Eq.(3.7) is shown in Figure 3-3(a) for values of the Bloch wavevector $|\cos(K\Lambda)| > 1 \Leftrightarrow K\Lambda = m\pi + i\alpha$ with $m = 1$, which lead to the evanescent Bloch modes lying inside the first photonic bandgap (namely empty regions correspond to the photonic bands). Notice that from this plot, the dependence of K on w_g and w_a at a fixed wavelength λ_o can be read, but also, if w_g and w_a are fixed, then one wavelength λ_o defines a particular operation point in the graph, and then the dependence of K on any wavelength λ can be read from the straight line that passes through this point and the origin and is depicted in Figure 3-3(b). As well known, and obvious from Figure 3-3(a), the size of the gap and the decay rate α are maxima for a quarter-wave-layer stack and increase with the index contrast P. Finally, the Bloch eigenmodes have most of their electromagnetic energy stored inside the high-index layer at the lower-frequency gap edge and in the low-index layer at the higher-frequency gap edge [12]. This property will have an important impact, when we later characterize losses in two-dimensional mirrors.

In the case of photonic-crystal slabs of the forms shown in Figure 3-1(c), the Bloch modes have been studied in the past [60, 13]. They can be either discrete bounded modes (exponentially decaying as $|z| \to \infty$) or a continuum of delocalized modes known as the light cone. The bounded modes are based on index-guiding and are localized inside the highermost-index (core) region, therefore their ω vs k dispersion curve lies below the light-cone continuum of modes, which are extended in the lower-index claddings (air and substrate). This holds even at the Brillouin zone edge resulting in photonic gaps for the discrete modes that are

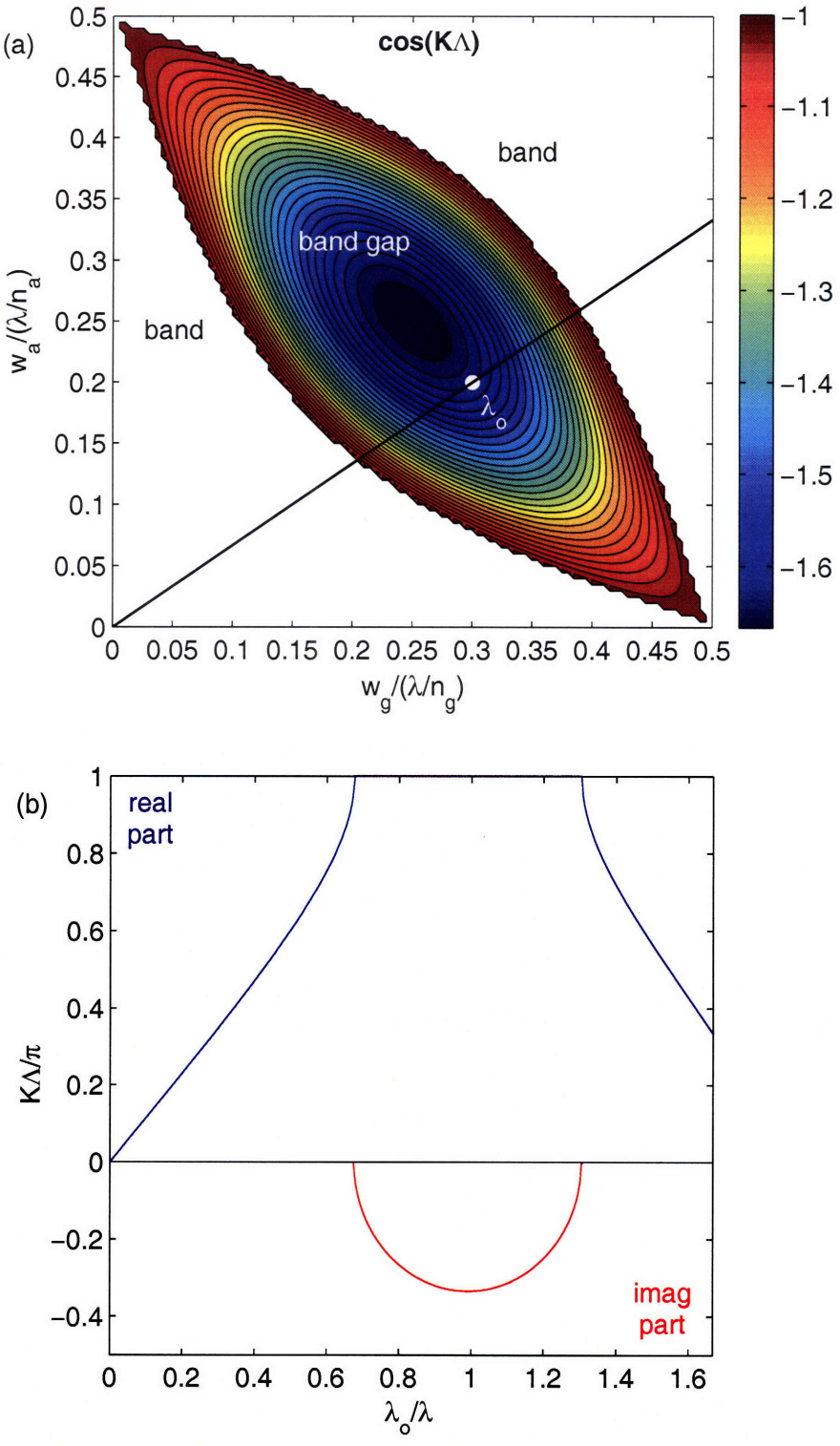


Figure 3-3: Bloch-mode wavevector K for a stack of alternated layers of refractive indices $n_g = 3$, $n_a = 1$ as a function of (a) their widths w_g, w_a and the wavelength λ inside the first photonic bandgap, and (b) the wavelength λ for the arbitrary choice of the widths $w_g = 0.3\lambda_o/n_g$, $w_a = 0.2\lambda_o/n_a$.

at least partly below the light cone, and support thus evanescent in x Bloch modes that are still bounded in z. Under the single-mode condition (3.4) there will normally be only one such gap under the light cone, and this is the regime where this periodic structure can operate as a low-loss photonic-crystal-slab mirror. Due to the folding of the bands, the discrete mode couples to the continuum at some frequency, which lies inside or above the gap, and turns into a complex discrete mode. In the vicinity of the coupling, the Bloch mode field pattern has features of both localization inside the core and delocalization throughout the claddings.[2] Again, the Bloch eigenmodes in the photonic gap have most of their energy stored inside the high-index regions at the lower-frequency edge and in the low-index regions at the higher-frequency edge [60].

To illustrate the above principles, we examine the simplest example of membranes and bridges in air ($\epsilon_{\text{clad}} = 1$), which corresponds to just rectangular rods in free space for the two-dimensional case relevant to Figure 3-1(c). The unit cell of this periodic structure can be thought, to first order, as a one-dimensional stack of alternated layers of effective refractive indices n_{g}, the effective index of the single guided mode of the unpatterned slab waveguide, and $n_{\text{a}} = 1$, since the air hole is infinitely deep. This motivates us to make again a contour plot (Figure 3-4(a)) of the exact (from CAMFR simulations) Bloch wavevector $\cos(K\Lambda)$ for the lowest-order Bloch mode with $w_{\text{g}}/(\lambda_{\text{o}}/n_{\text{g}})$ and $w_{\text{a}}/(\lambda_{\text{o}}/n_{\text{a}})$ at a fixed wavelength λ_{o} and inside the region that is identified as the first gap. If w_{g} and w_{a} are fixed, the wavelength dependence (Figure 3-4(b)) is now only approximately quantitatively, but well qualitatively, represented by the straight line that passes through the λ_{o}-operation point and the origin. In this case, the gap lies always below the light-cone continuum (grey shaded area): for small hole diameters the discrete mode meets and couples to the light cone within the second Brillouin zone, namely within the second band above the first gap, while for large hole diameters the coupling point, which identifies the beginning of the light cone, coincides with the upper gap edge (Figures 3-4(a,b)).[3] The Bloch modes at the two different edges of

[2]It can be shown [60], however, that inside the second Brillouin zone the complex discrete mode is still proper (lies in the proper Riemann sheet, namely the delocalized portion of the field is still exponentially decaying as $|z| \to \infty$), even though it lies above the light cone, and turns improper (leaky, lying in the improper Riemann sheet, exponentially increasing as $|z| \to \infty$) only upon entering the third Brillouin zone. One should not be confused, though, to deduce that conventional photonic-crystal-slab waveguide modes can exist above the light cone, since these proper complex modes do not carry power.

[3]Note also that at the second Brillouin zone edge the imaginary part of the wavevector necessarily goes to zero before the discrete complex mode turns leaky, as it enters the third Brillouin zone [60]. This improper branch of the solution is not apparent in Fig. 3-4(b), because such leaky solutions do not exist for problems with bounded domains such as the one used in our simulations.

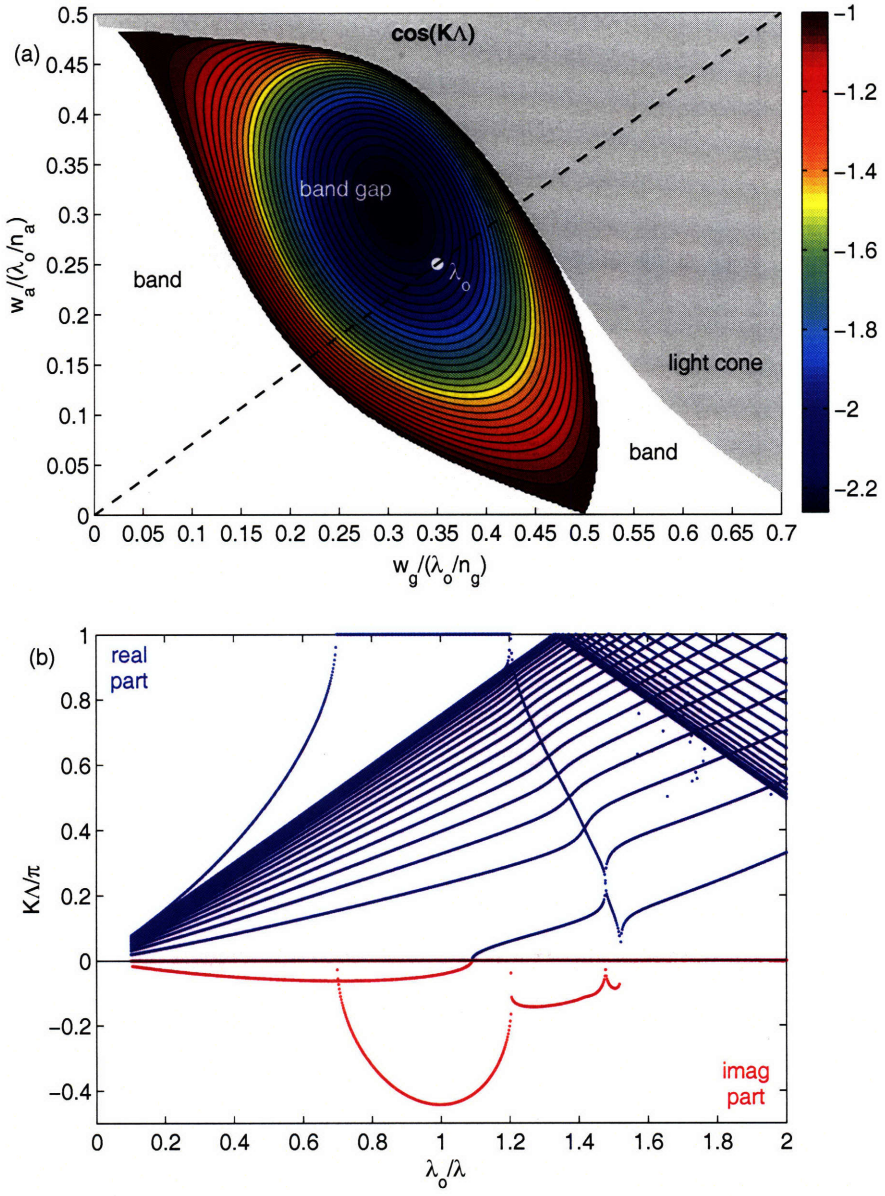


Figure 3-4: Fundamental-Bloch-mode wavevector K for a photonic-crystal slab consisting of an array of rectangular rods of $\epsilon_{\text{core}} = 12$ and thickness $d_{\text{core}} = 0.136\lambda_o$ suspended in air ($\epsilon_{\text{clad}} = 1$) (effective refractive indices $n_g = 2.764$, $n_a = 1$) as a function of (a) the widths of the rods w_g and the air holes w_a at the wavelength λ_o inside the first photonic bandgap, and (b) the wavelength λ for the arbitrary choice of the widths $w_g = 0.35\lambda_o/n_g$, $w_a = 0.25\lambda_o/n_a$. (The discreteness of the modes in the light cone (grey shaded area) is due to the necessary imposition of boundary walls for simulation purposes. Notice how the fundamental Bloch mode couples to the light cone at $\lambda_o/\lambda = 1.2036$, which coincides with the upper edge of the bandgap.)

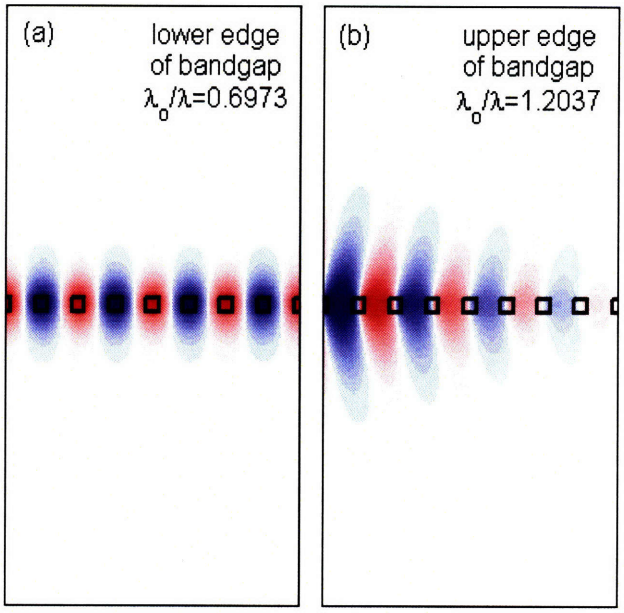


Figure 3-5: Fundamental-Bloch-mode electric-field patterns for the rods-in-air photonic-crystal slab of Figure 3-4(b) at the (a) low-frequency edge $\lambda_o/\lambda = 0.6973$ and (b) high-frequency edge $\lambda_o/\lambda = 1.2036$ of the photonic bandgap. (Notice how the coupling to the light cone delocalizes transversely the field pattern in (b)).

the gap are depicted in Figures 3-5(a) and (b). At the lower edge (a), the mode is indeed localized close to the axis of the high-index rods and mostly inside them, having a node in the air hole, while at the upper edge (b), it extends in the surrounding air due to coupling to the light cone and is localized more inside the hole, having a node in the rod.

When there is a substrate and the holes are deep enough that they can be considered infinite, the situtation is more complicated, since the modes of the continuum, extended inside the periodically patterned substrate, exhibit themselves a gap too. Therefore, the coupling of the discrete mode and the light cone modes happens within both their gaps and a splitting is observed in the imaginary part of their wavevectors. This coupling point is closer to the lower edge of the discrete mode gap the wider the air holes are and the smaller the core-substrate index contrast is. The stronger coupling expresses itself also in the Bloch-mode field patterns that start extending into the substrate for even lower frequencies within the gap. Finally, it is important to remember that the states of the continuum that lie inside a gap cannot carry power.

3.2.2 Reflectivity of semi-infinite photonic-crystal-slab mirror

Having the knowledge of the form of the Bloch eigenvalues and eigenstates in different regimes of the discrete mode gap of a photonic-crystal slab, we can proceed to examine and explain the sources of the radiation loss upon reflection from such a semi-infinite mirror.

Inside the photonic gap, the radiative loss of a semi-infinite photonic-crystal-slab mirror is, through Eq.(3.3), equal to the complement of its reflectivity, for which the numerical results are plotted in Figure 3-6 for the same system of rectangular rods in air, presented in Figure 3-4 and in the same format. The reflectivity is seen to be larger in the lower gap-edge and decreasing for higher frequencies. Furthermore, it increases as the air-hole diameter w_a gets smaller, reaching 100% at the obvious limit that the holes vanish and the gap shrinks to zero. The black curve in Figure 3-6(b) (corresponding approximately to the dashed black line in Figure 3-6(a)) demonstrates that the naive choice of operation point close to the quarter-wave equivalent can lead to huge losses within the bandwidth of interest. Similar conclusions for the loss dependence on frequency and hole width were derived numerically for the case when a substrate is present, as in Figure 3-1, and for several values of the substrate refractive index.

Theoretically, the mode-matching principle can be used to explain the above described variation of reflectivity (and therefore loss) with frequency and the dimensions of the photonic-crystal slab in the horizontal plane of the periodicity:

From one viewpoint, one considers the set of eigenmodes for the incoming waveguide ($x < 0$ in Figure 3-1) and the set of Bloch eigenmodes for the semi-infinite photonic-crystal slab ($x > 0$). It was seen previously that the fundamental mode of an infinite photonic-crystal slab is discrete and vertically (in z) bounded within the first two Brillouin zones, including the frequency range of its gap located at the first Brillouin zone boundary. This means that such an infinite periodic structure would not radiate by itself, even inside this gap. Thus, all the radiation upon reflection of a waveguide mode from the semi-infinite version of this periodic structure is produced only at their interface ($x = 0$ plane) that breaks the translational symmetry (in x) of the entire system. This is justified by the point-like radiation pattern, shown in Figure 3-7, produced upon reflection of the incoming waveguide mode. By matching the two sets of modes on each side of the critical interface, one can quantify the reflectivity and loss.

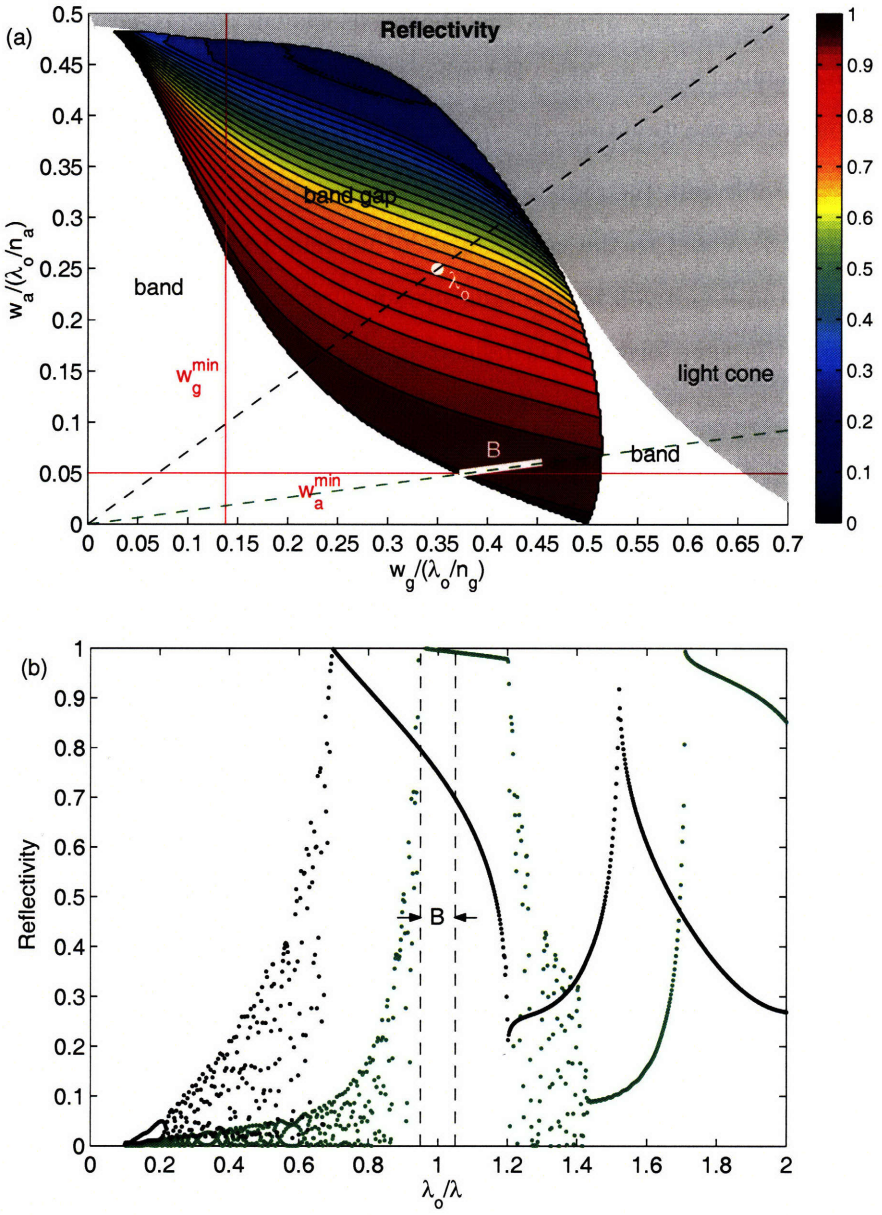


Figure 3-6: Reflectivity from the rods-in-air photonic-crystal-slab mirror of Figure 3-4 as a function of (a) the widths of the rods w_g and the air holes w_a at the wavelength λ_o inside the first photonic bandgap, and (b) the wavelength λ for the arbitrary choice of the widths $w_g = 0.35\lambda_o/n_g$, $w_a = 0.25\lambda_o/n_a$ (black curve) from Figure 3-4(b), and the optimal choice of the widths $w_g = 0.4045\lambda_o/n_g$, $w_a = 0.05\lambda_o/n_a$ (green curve). The red lines in (a) indicate the fabrication limitations from Eq.(3.6) for the choice of the operation point $\{w_g, w_a\}$ at λ_o.

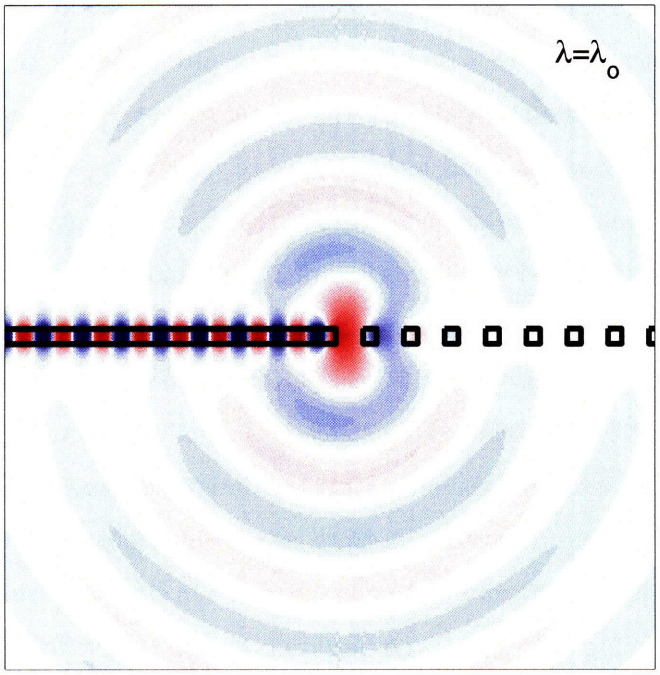


Figure 3-7: Electric-field pattern of reflection from the rods-in-air photonic-crystal-slab mirror of Figure 3-4(b) at the wavelength λ_o .

Under certain symmetry conditions [31, 32] the same-order modes of both sides of the structure can have exactly the same transverse profile, so that the fundamental waveguide mode matches perfectly on the $x = 0$ plane to the evanescent (lying in the gap) fundamental Bloch mode of the mirror. Thus the incident mode will couple only to this Bloch mode and not to higher-order ones, and, since this does not carry power, perfect reflection into the same backward waveguide mode will occur. This is exactly the case also for the one-dimensional stacks of alternated layers discussed previously, where the modes are plane waves, and reflection is always perfect.

In general, such symmetries are not present, so there is a mismatch between the two fundamental modes (quantified by their overlap integral $\eta \neq 1$) and the incident waveguide mode couples also to higher-order modes both in the forward and backward directions. Under the single-mode assumption, these higher-order modes are extended ones and, provided they can carry power, they lead to radiation loss, which originates, as we said, from the $x = 0$ interface. For the overlying air and for uniform substrates, as in Figures 3-4-3-7, all extended modes within the light cone carry power and then the reflectivity has been shown to be approximately equal to $R \approx \eta^2$ [61], namely it is determined mostly by the mismatch of the

two fundamental modes. This explains the variation of the reflectivity in Figure 3-6 in two ways [62]: First, since the Bloch mode of the semi-infinite mirror is more localized inside the dielectric pattern at the low gap-edge, the field does not "see" much of the air hole, especially if this is narrow, and thus looks transversely more like the incoming waveguide mode (Figure 3-5(a)), leading to strong reflection; the opposite longtitudinal localization of the field happens at the upper gap-edge (Figure 3-5(b)) and thus radiation loss is higher. Second, as frequency or w_a increases, the fundamental Bloch mode comes closer to the light cone, so coupling to it increases and the field pattern of this Bloch mode gets delocalized off the core (Figure 3-5(b)), becoming thus greatly dissimilar transversely to the incoming waveguide mode; this again translates to higher radiation loss upon reflection. When the array of holes penetrates deep into the substrate, as we said, a gap opens also for some of the extended states of this periodically patterned cladding. In that case, since these states do not carry power, coupling to them does not lead to radiation loss, so the simple model above breaks and the coupling to more than just the fundamental evanescent Bloch mode needs to be accounted for. Still, the two arguments above can be used again to qualitatively explain how reflectivity changes with the wavelength and the in-plane dimensions of the crystal.

From a different viewpoint, often called the Fourier-space picture, one considers the set of eigenmodes supported by the z-invariant regions exactly above ($z > d_{\text{core}}/2$) and below ($z < -d_{\text{core}}/2$) the core layer. The continuous-wave total standing wave pattern of reflection inside the core layer ($|z| < d_{\text{core}}/2$) couples to these modes, and then radiation loss arises from those modes propagating to $z \to \pm\infty$. For air and uniform substrates these are simply the modes lying inside the radiation cone of these materials, and, clearly, localization of the standing wave pattern inside the core material, either due to small air holes or due to operation at the lower gap-edge, implies that the Fourier transform of this field pattern in x has little k_x-wavevector content inside this radiation cone, and thus that the system suffers small radiation loss. The conclusion is therefore similar to that of the first viewpoint, as expected. For patterned substrates the situation is more complicated, since some radiative modes are removed due to the presence of a bandgap in the substrate, but still coupling to the remaining radiative modes is again reduced with strong field localization inside the core. Basically, this second viewpoint uses a 90°-rotated frame compared to the first one, but follows the same mode-matching principles. Such an approach has been followed in the past also for cavities for radiation into free space [46, 30] and for radiation into deeply patterned

substrates, as was seen in Chapter 2.

Therefore, the design rules that emerge from the analysis of this paragraph are that, for given $\{d_{\text{core}},\, d_{\text{etch}},\, ratio\}$, the operation point $\{w_{\text{g}},\, w_{\text{a}}\}$ should be chosen so that the longest wavelength $\lambda_{\max} = \lambda_{\text{o}}\,(1 + B/2)$ within the bandwidth B of interest is placed at the almost lossfree low gap-edge (lge) and that the hole diameter w_{a} is as small as possible, making sure that the fabrication limitations (3.5) and (3.6), depicted in Figure 3-6(a) with red lines, are not violated and the bandwidth B actually fits inside the gap. This choice can be written in mathematical terms as

$$w_{\text{g}} = \max\left\{w_{\text{g}}^{\min},\, w_{\text{g}} : \lambda_{\max} = \text{lge}\right\}, \tag{3.8}$$

$$w_{\text{a}} = \max\left\{w_{\text{a}}^{\min},\, \frac{d_{\text{etch}}}{AR},\, w_{\text{a}} : \text{gap} = B\right\} \tag{3.9}$$

and corresponds qualitatively to placing the desired frequency bandwidth as shown with a white stripe on Figure 3-6(a), where for air substrate d_{etch} lacks physical significance and thus $w_{\text{a}} = w_{\text{a}}^{\min}$ is the optimal choice, assuming for this choice the associated gap is also large enough. We implement these design rules in our numerical computations and the resulting green curve in Figure 3-6(b) (corresponding approximately to the dashed green line in Figure 3-6(a)) shows the tremendous improvement one gets in terms of losses within the specified $B = 10\%$ bandwidth (white stripe in Figure 3-6(a)); notice that, even for such a narrow etching, the periodic perturbation is indeed large enough to open a 23% gap due to the strong $n_{\text{g}} - n_{\text{a}}$ index contrast. Actually, the requirement in (3.9) that entire bandwidth B fits inside the gap can be absorbed into the optimization over the etch depth d_{etch}, so we will not worry about explicitly satisfying this requirement in subsequent calculations.

3.3 Optimization for dimensions of the crystal in the vertical direction of layer growth

Having set, through appropriate design rules, the dimensions $\{w_{\text{g}},\, w_{\text{a}}\}$ of the photonic-crystal-slab mirror in the plane of the periodicity as a function of the dimensions $\{d_{\text{core}},\, d_{\text{etch}},\, ratio\}$ in the vertical direction, we now need to optimize also in terms of these latter parameters, and we proceed in this Section in giving more design criteria for these too.

For two different placements of the core layer relative to the hole, (a) a symmetric one

($ratio = 0.5$) and (b) a completely asymmetric one ($ratio = 0$), and for three different material selections (i)-(iii), in Fig. 3-8 we make a contour plot of the maximum mirror loss within the bandwidth of interest B as a function of d_{etch} and d_{core}, where at each point Eq. (3.8) and (3.9 - except for ensuring a large enough gap) have been applied to optimize w_{g} and w_{a}. Based on the conclusions of Section 3.2, reflectivity is usually a monotonically decreasing function of frequency inside the gap and thus this maximal loss within B is usually expected to be that at the shortest wavelength λ_{min}; however, for extra safety, here we take the plotted maximal loss within B to be the maximum of the losses at λ_{min}, λ_{o} and λ_{max}, which is reasonable, since, in any case, reflectivity never has an oscillatory behavior inside the gap. Both d_{etch} and d_{core} have been normalized to the critical core thickness $d_{\text{asym}} = d_{\text{sym}}\left(1 + \frac{1}{\pi}\tan^{-1} C\right)$, up to which (from Eq. 3.4) the asymmetric superstrate-free ($d_{\text{sup}} = 0$) version of the two-dimensional waveguide of Fig. 3-1(c) stays single-mode inside the entire bandwidth B. For etch depths smaller than this limit ($d_{\text{etch}} < d_{\text{asym}}$) we plot only for values for which condition (3.1), that the hole fully perforates the core, is not violated, while for larger etch depths ($d_{\text{etch}} > d_{\text{asym}}$) the single-mode limit (3.4) imposes a maximum value for the allowed core thickness, which is always $d_{\text{sm}} \leq d_{\text{asym}}$. (The equality holds, as d_{etch} is increased, when either the slab waveguide stays without a superstrate layer, because $ratio = 0 \Rightarrow d_{\text{sup}} = 0$, or in the trivial case $\epsilon_{\text{clad}} = 1 \Rightarrow C = 0$.)

The results in Fig. 3-8 first of all show that the loss upon reflection is minimal always for the largest possible thickness of the core layer, and in general increases with decreasing d_{core}. This should not be surprising for two reasons: First, shrinking the core brings closer to the light cone the fundamental modes of both the uniform waveguide (n_{g} decreases) and the periodic mirror, so the latter has features of coupling to extended modes (Fig. 3-5(b)) and has thus a greatly dissimilar transverse profile compared to the former, leading to radiation. Second, as d_{core} gets smaller, n_{g} decreases, so also the $n_{\text{g}} - n_{\text{a}}$ contrast reduces, thus the gap width shrinks, and therefore the optimal d_{etch} increases, in order to push w_{a} through Eq. (3.9) closer to the quarter-wave-equivalent operation point, where the wider gap can accomodate the bandwidth B; increasing w_{a} though implies, as we know, increased losses. Remember, after all, from Section 3.1 that an infinitely wide core, accompanied by an infinitely deep hole, lead asymptotically to a one-dimensional structure that is exactly lossless. All the above considerations lead to the conclusion that the core layer must always have the maximum possible thickness for the system to be single-mode within the bandwidth

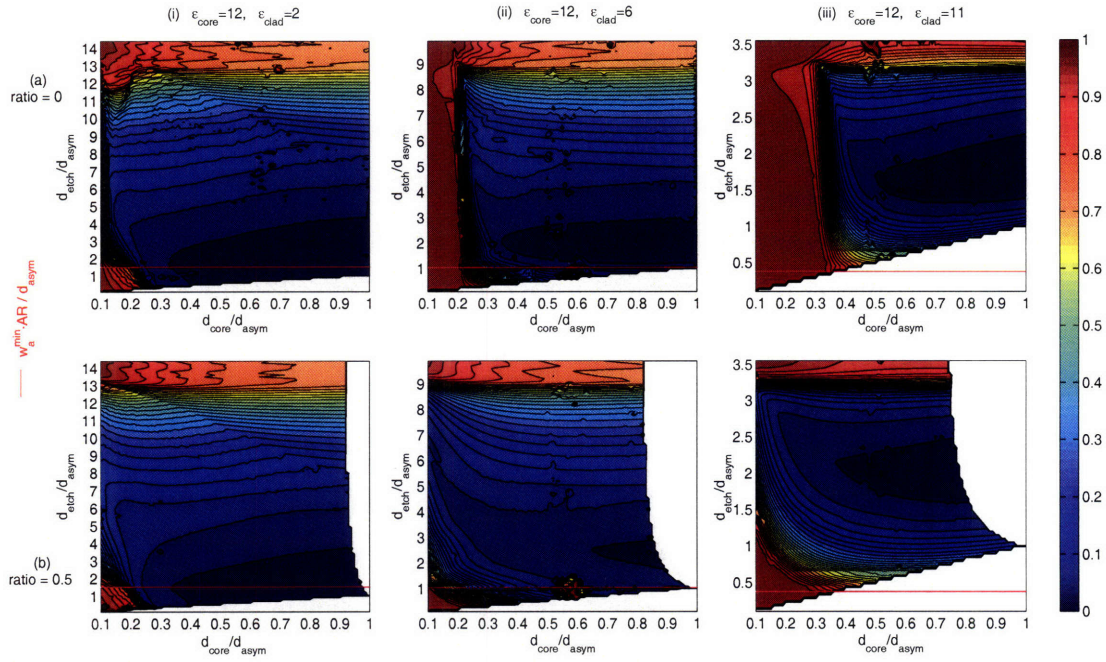


Figure 3-8: Maximum radiation loss from the semi-infinite mirror of Fig. 3-1(c) with optimized in-plane dimensions w_{g} and w_{a}, over a $B = 10\%$ bandwidth and under the fabrication limitations $AR = 5$, $w_{\mathrm{a}}^{\mathrm{min}} = w_{\mathrm{g}}^{\mathrm{min}} = 0.05\lambda_{\mathrm{o}}$, as a function of the thickness of the core d_{core} and the etch depth of the air hole d_{etch}. (a) $ratio = 0$, (b) $ratio = 0.5$ and (i) $\epsilon_{\mathrm{core}} = 12$, $\epsilon_{\mathrm{clad}} = 2$, (ii) $\epsilon_{\mathrm{core}} = 12$, $\epsilon_{\mathrm{clad}} = 6$, (iii) $\epsilon_{\mathrm{core}} = 12$, $\epsilon_{\mathrm{clad}} = 11$. The red lines indicate the etch-depth limits below which the hole cannot narrow any more.

of operation, so instead of Eq. (3.4) we demand

$$d_{\text{core}} = d_{\text{sm}}. \tag{3.10}$$

Regarding the optimal hole etch-depth d_{etch}, first of all, within our optimization algorithm it affects mathematically through Eq. (3.9) the hole width and, through this, the gap size (see comment in last sentence of Section 3.2); therefore, note that the optimal etch depth will always be $w_{\text{a}} \geq w_{\text{a}}^{\min} \Rightarrow d_{\text{etch}} \geq w_{\text{a}}^{\min} AR$ (this limit is shown with a red line in Figs. 3-8 and 3-9). Now, for $\epsilon_{\text{clad}} = 1$, this is the only effect of the parameter d_{etch} and, since we want the hole to be narrow, the optimal d_{etch} is expected to be small ($d_{\text{etch}} = w_{\text{a}}^{\min} AR$, if B fits in the gap, as in the example of Fig. 3-6 shown in green). This applies in general to low-index claddings through analytic continuation of the result of the optimization problem. On the other hand, as the substrate index of refraction gets higher, the radiation is channeled predominantly into it due to the higher local density of states there. The presence of a deep hole in the substrate is then significant, since the periodicity removes some of the extended states in the substrate (by opening a gap) reducing thus the radiation. As the hole depth increases, a larger part of the exponential tail of the incident waveguide mode samples the periodicity, and the reduction in radiation is stronger [36]. However, when the entire near field is covered by the hole, the improvement is not significant with further etching. The two competing effects suggest that there is an optimal d_{etch} for minimum radiation, which has to be determined numerically. This numerical minimization will automatically satisfy also the requirement that entire bandwidth B fits inside the gap, since otherwise $\lambda_{\min}$ would fall inside the second passband (Brillouin zone) and loss there would be huge, which is far from optimum.

Because of the benefits of a thick core layer and a deep hole, it turns out usually that the optimal $d_{\text{etch}} \geq d_{\text{asym}}$. In this regime we plot then again in Fig. 3-9 the mirror loss as a function of d_{etch} and *ratio* for the same systems (i)-(iii) as in Fig. 3-8, where now the condition (3.10) has also been imposed. The result, for all choices of the parameter set $\{\lambda_{\text{o}},\ B,\ AR,\ w_{\text{a}}^{\min},\ w_{\text{g}}^{\min}\}$ and the materials we tried, is that radiation loss upon reflection is minimal for *ratio* ≈ 0, namely for a slab waveguide without a superstrate layer. The explanation is very similar to arguments stated earlier. A given hole depth should all be exploited to inhibit the radiation that is predominantly channeled into the substrate. Adding

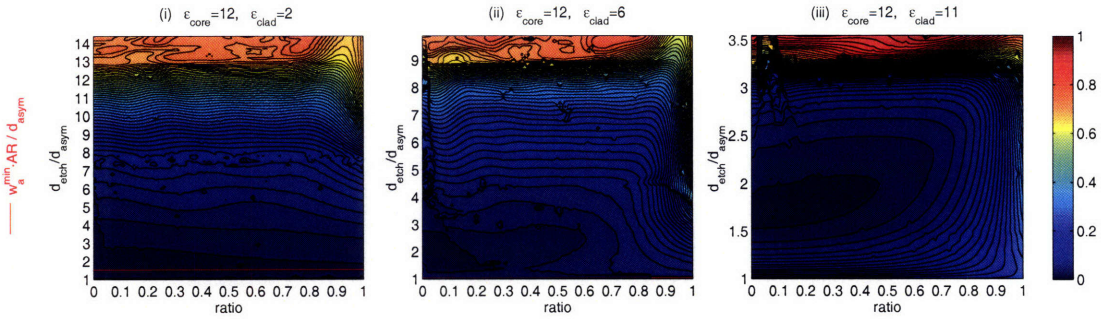


Figure 3-9: Maximum radiation loss from the semi-infinite mirror of Fig. 3-1(c) with optimized in-plane dimensions w_g and w_a and core thickness d_{core}, over a $B = 10\%$ bandwidth and under the fabrication limitations $AR = 5$, $w_a^{min} = w_g^{min} = 0.05\lambda_o$, as a function of the placement of the core *ratio* and the etch depth of the air hole d_{etch}. (i) $\epsilon_{core} = 12$, $\epsilon_{clad} = 2$, (ii) $\epsilon_{core} = 12$, $\epsilon_{clad} = 6$, (iii) $\epsilon_{core} = 12$, $\epsilon_{clad} = 11$. The red lines indicate the etch-depth limits below which the hole cannot narrow any more.

a superstrate layer would only utilize part of the hole depth to keep the core away from the overlying air, into which radiation is small anyway. An advantage would only come from symmetry considerations, namely a symmetric slab waveguide has half the radiation modes it can couple to (only the even or odd) than an asymmetric one. But this principle would become applicable only for a very deep hole, namely for good fabricating capabilities of large aspect-ratio (AR) holes. Note here that asymmetry might have another disadvantage that shows up only in three-dimensional structures. There are actually two fundamental waveguide modes with opposite polarizations in 3d. For a symmetric configuration these have opposite parity and cannot couple. Instead, asymmetry can lead to undesirable effects, such as reflection to the wrong waveguide mode. Then, the optimal value for *ratio* may be nonzero, but it will never be greater than 0.5, for the same reasons explained before. For the two-dimesional structure examined in the present work, however, we can quite safely apply the design rule

$$ratio = 0. \tag{3.11}$$

3.4 Optimization for the material set comprising the crystal

For a given material set for the core and the claddings of the structures presented in Fig. 3-1, the design rules (3.9),(3.8) and (3.10),(3.11) have simplified the problem of minimizing radiation loss upon reflection from a photonic-crystal-slab mirror into optimization with respect to the single parameter d_{etch}, as discussed in Section 3.3. Carrying through this

procedure for different $\{\epsilon_{\text{core}}, \epsilon_{\text{clad}}\}$ pairs, we have gotten the end result, already shown in Fig. 3-2, of minimal possible loss for different materials. Also in Fig. 3-10 we show the variation of the optimized reflectivity with frequency for three such pairs (corresponding to three points in Fig. 3-2). From these two plots, it is obvious that following our proposed design rules can indeed lead to a tremendous suppression of radiation loss (less than $0.1dB$) over the large required frequency bandwidth. In addition, Fig. 3-2 leads to the significant conclusion that, to make a good integrated optical mirror, the refractive-index contrast is very important not only in terms of the difference $\Delta\epsilon = \epsilon_{\text{core}} - \epsilon_{\text{clad}} > 0$ but also in terms of the ratio $R\epsilon = \epsilon_{\text{core}}/\epsilon_{\text{clad}} > 1$. In particular, lowest-loss mirrors are those for which

$$\Delta\epsilon,\ R\epsilon \gg 1, \tag{3.12}$$

usually called high-index-contrast systems, such as silicon-on-insulator (SOI) or suspended in air devices, and those for which

$$\Delta\epsilon \to 0,\ R\epsilon \to 1, \tag{3.13}$$

usually called low-index-contrast systems, such as the ones based on the AlGaAs material compounds.

The reasons that these two material sets are appropriate for low-loss broadband mirrors are quite opposite. The high-index-contrast systems base their success on strong localization of the field inside the high-index core: in the first mode-matching viewpoint, the fundamental evanescent Bloch mode then "sees" the air hole enough to open a large enough gap, but not too much, so it bears strong resemblance to the incident waveguide mode, inhibiting therefore coupling to radiation; in the second viewpoint (Fourier-space picture), the total field pattern has most Fourier components at large wavevectors and small content lying inside the radiation cone of the low-index cladding, thus radiation loss is small. On the contrary, for low-index-contrast systems, the high reflectivity is achieved through transverse delocalization: the incident waveguide mode is spread out into the air and substrate, and, if the holes are deep enough to cover its evanescent tails, the structure starts resembling the one-dimensional stack of layers, known to be lossless.

In choosing between the two suggested platforms - a source of considerable debate in the integrated optics community - two important additional factors need to be considered:

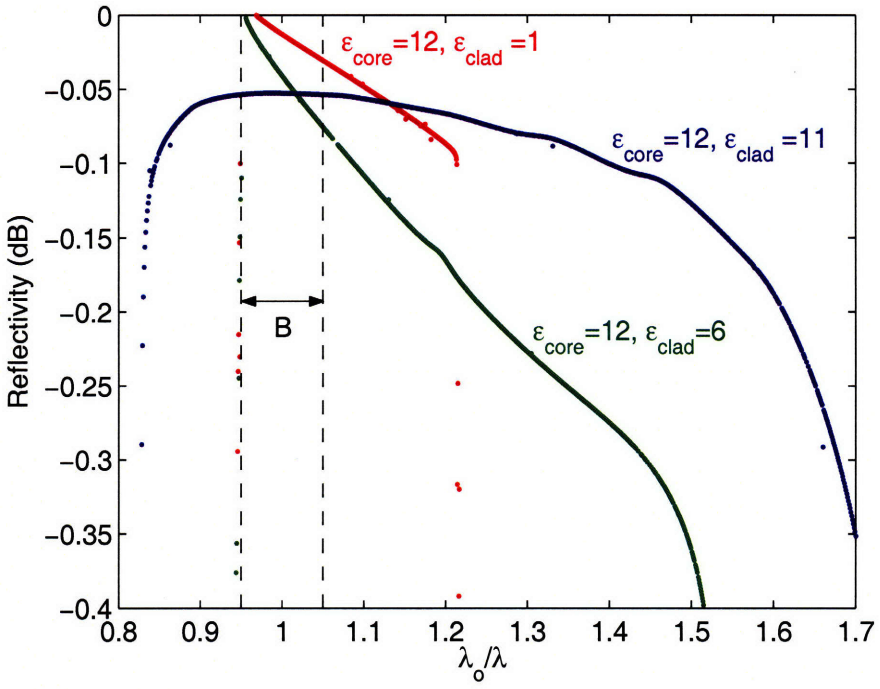


Figure 3-10: Optimized reflectivity from the semi-infinite mirror of Fig. 3-1(c), over a $B = 10\%$ bandwidth and under the fabrication limitations $AR = 5$, $w_a^{min} = w_g^{min} = 0.05\lambda_o$, as a function of the wavelength λ for three choices from Fig. 3-2 for the core and cladding dielectric constants .

field localization and sensitivity to surface roughness. The amount of power scattered into radiation from surface roughness increases with the strength of the field at the site of the roughness, so strong field localization is expected to lead to larger sensitivity to disorder. Therefore, based on the discussion in the previous paragraph, it can be inferred that the choice of platform depends on the particular device under consideration. For example, for nonlinear devices, where the nonlinearity is enhanced by strong field localization, the high-index-contrast platform (3.12) is more suitable, while for passive devices, where localization is not a requirement, the low-index-contrast platform (3.13) should work better due to its insensitivity to disorder from fabrication and its flat response over extremely large frequency bandwidths (see Fig. 3-10).

It is also important to understand how different restrictions, imposed by fabrication, limit the performance of the two material systems. To see this, the contour plots Fig. 3-11(a) and (b) show w_{g} and w_{a} respectively for the optimal results of Fig. 3-2. Where these widths are clamped to their minimum possible values given in (3.6), they inhibit the radiation loss to be suppressed even further, since w_{g} and w_{a} would optimally like to be even smaller in these regions of Fig. 3-11, as can be inferred from analytic continuation. Therefore, it can be seen that the high-index-contrast systems (3.12) are limited by the finite lithographic resolution $w_{\mathrm{a}}^{\mathrm{min}}$ in etching holes, while the low-index-contrast systems (3.13) are limited by the minimal feature size of the remaining dielectric pattern $w_{\mathrm{g}}^{\mathrm{min}}$ and the maximal fabricatable aspect ratio AR of the air holes. As lithographic techniques improve, the loss levels for incomplete-photonic-bandgap-based integrated systems will thus be further reduced.

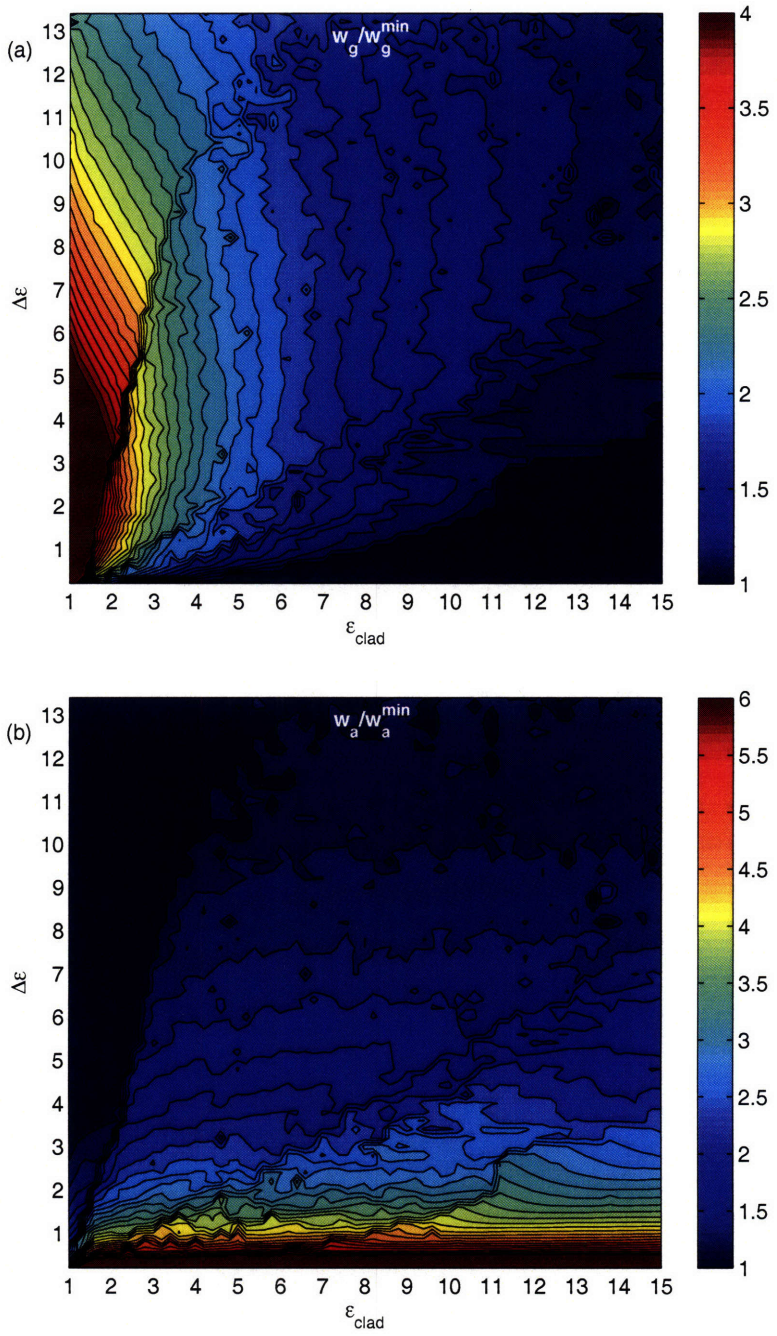


Figure 3-11: Optimal in-plane dimensions (a) $w_{\mathrm{g}}/w_{\mathrm{g}}^{\mathrm{min}}$, (b) $w_{\mathrm{a}}/w_{\mathrm{a}}^{\mathrm{min}}$ that minimize the radiation loss from the semi-infinite mirror of Fig. 3-1(c) to the values shown in Fig. 3-2, as a function of the core and substrate dielectric permittivities, where $\Delta\epsilon = \epsilon_{\mathrm{core}} - \epsilon_{\mathrm{clad}}$.

Chapter 4

Subwavelength and low-index-confined light in Surface-Plasmon-Polaritonic (SPP) systems [2]

Precise control of the properties of light propagation and localization has always been of great importance in the world of optics. All-dielectric photonic and photonic-crystal systems have reached an amazing level of maturity and performance, being nowadays able to support very fast signals, with very low loss and on a minimal wavelength-sized footprint, by utilizing various elaborated mechanisms, such as the ones presented in Chapters 2 and 3. However, the desire to always push the technological edge even further necessitates the investigation of different material systems too, as these all-dielectric structures do have their limitations. For example, the constant need for compactness and increase in spatial resolution has made the confinement of light in subwavelength-size regions a very desirable attribute for modern nanophotonics. This property cannot be accomplished by all-dielectric structures, which are limited by the highest refractive index available, however, such compact light-guidance has been accomplished by exploring surface plasmon-polariton modes [17, 18] into designing waveguides, by using conductors of finite cross-section [37, 38, 39, 40, 63, 41, 42, 43, 64], combinations of surface plasmons with bandgaps [65], or coupled-metallic-nanoparticle chains [66, 67]. Therefore, this type of structures has acquired increased interest lately, and inves-

tigation of its capabilities is definitely due.

One challenging goal in photonics has always been to guide light through air in the presence of higher-refractive-index dielectric media, since light tends to localize itself mostly in these high-index regions. So far, photonic bandgaps [12] and other index-guiding-based mechanisms [68] have been ways to address this issue. In this Chapter, we introduce a new class of axially uniform surface-plasmon-polariton waveguides, employing a new mechanism to accomplish light-confinement in a low-index region when surrounded by high-index materials, without a photonic bandgap. They are implemented on a simple flat conducting surface of large extent, and rely on a nonperiodic dielectric distribution on top of this substrate to generate transversely confined guided modes. The new mechanism for confining much more field in the low-index rather than in the adjacent high-index region is based on the relative dispersive characteristics of different surface-plasmon-polariton modes present in these structures, and is applicable within a finite frequency regime that abides to certain cutoff conditions.

4.1 Subwavelength light-propagation in SPP systems

Surface-Plasmon-Polaritons (SPP) are well known [17, 18] electromagnetic waves that propagate along the interface between a plasmonic material (e.g. metal) and a single dielectric material of permittivities ϵ_p and ϵ. A SPP exists only for TM polarization (magnetic field parallel to the interface) and its ω-$\mathbf{k}$ dispersion relation is $k \equiv |\mathbf{k}| = \omega/c \cdot \sqrt{\epsilon \cdot \epsilon_p(\omega) / (\epsilon + \epsilon_p(\omega))}$, where $\mathbf{k}$ is in the plane of two-dimensional (2d) translational symmetry. For example, assuming for now lossless materials and using the Drude model $\epsilon_p(\omega) = \epsilon_\infty - \omega_p^2/\omega^2$, where ϵ_∞ is the permittivity at very high frequencies and ω_p is the bulk plasma frequency, the condition $\epsilon_p < -\epsilon < 0$ for propagation leads to a high-frequency cutoff at $\omega_c(\epsilon) = \omega_p/\sqrt{\epsilon_\infty + \epsilon}$, to which the SPP asymptotes for large wavevectors k, as it is then tightly confined on the interface, while the SPP asymptotes to the light-line of the dielectric $k = \omega/c \cdot \sqrt{\epsilon}$ for small wavevectors k, as it then extends far into the dielectric. The dispersion relation is shown by curves A, B in Figure 4-1 for two different dielectric materials ($\epsilon_{hi} > \epsilon_{low}$ in insets A, B). Clearly, this polaritonic light exhibits the desired extremely subwavelength propagation, in the frequency regime just below the cutoff frequency of surface resonance.

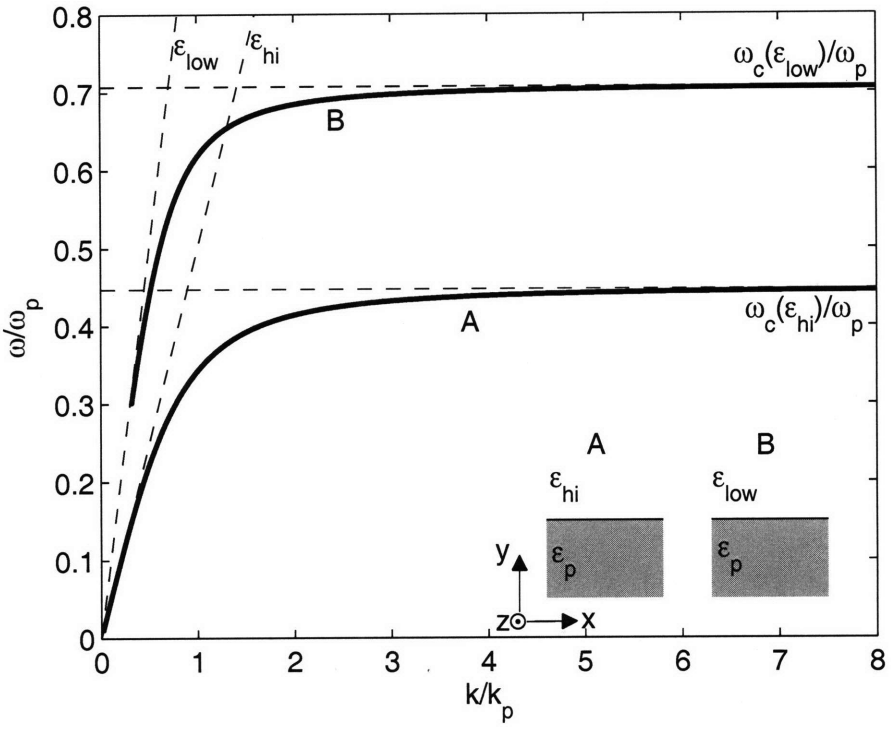


Figure 4-1: $\omega - k$ diagrams (solid curves) for conventional Surface-Plasmon-Polariton structures (insets $A - B$) with $\epsilon_{\text{hi}} = 4$ and $\epsilon_{\text{low}} = 1$ (air). The light lines $\omega/\omega_p = \sqrt{\epsilon} \cdot k/k_p$ ("vertical" dashed lines) and the cutoff frequencies $\omega_c(\epsilon)/\omega_p = 1/\sqrt{1+\epsilon}$ (horizontal dashed lines) are shown.

4.2 Low-index light-confinement mechanism by SPP effective-index guiding

4.2.1 Linear waveguides

The SPP waveguides discussed in the previous Section are vertically (along y) confined, but infinitely extended in the $x-z$ plane of propagation. We would like to design linear, axially uniform waveguides that can support modes guided along z (with $exp\,(i\beta z - i\omega t)$ dependence), but confined also in the lateral x direction. Consider, for the $x-y$ cross-section of such a waveguide, a semi-infinite vertical slab of width w and permittivity ϵ_{low}, placed on top of the semi-infinite space of conducting medium ϵ_p, and surrounded by a higher-index medium ϵ_{hi}, as shown in inset (i) of Figure 4-2(a). If we divide this waveguide cross-section in three vertical slices, then the central slice has an average dielectric permittivity lower than that of the exterior slices. Thus, one might expect that light confinement in x is not possible, by invoking the common index-guiding mechanism. However, we now show that this structure, devoid of a photonic bandgap or a finite-sized conductor, supports well-defined guided modes with the desired property of having much more energy stored inside the ϵ_{low} slab rather than the neighboring ϵ_{hi} space. The central slice, if examined individually being uniform in $x-z$, supports the SPP B from Figure 4-1, which lies in the $\omega-k$ plane above the SPP A, supported by the high-index outer slices. Let now SPP B travel inside the plasma-ϵ_{low} slice at a small angle with the z axis (namely with a large $k_z = \beta$ component of its total wavevector k_B). Then, upon incidence on the ϵ_{hi} boundary (uniform in z), it couples to A only for frequencies below $\omega_c\,(\epsilon_{\text{hi}})$, in which case, in order to preserve β phase-matching along z, A has to radiate outwards in x (since $\beta < k_B < k_A \Rightarrow k_{x,A}^2 = k_A^2 - \beta^2 > 0$), excluding indeed the possibility for existence of confined guided modes. However, above this cutoff the SPP mode A disappears, and the lowest order mode of the outer slices that can lead to radiation laterally or vertically becomes just the first mode within the continuum described by the ϵ_{hi} light line. This line now lies above the SPP B ($\omega/c \cdot \sqrt{\epsilon_{\text{hi}}} < k_B$) for a *narrow* frequency range below $\omega_c\,(\epsilon_{\text{low}})$, so B can now couple only to decaying modes inside the high-index side claddings. Thus in this frequency regime fully transversely confined guided modes can exist, with propagation constants β between the ϵ_{hi} light line and B, and with a significant part of the energy stored inside the low-index core. To our knowledge, this is a new guiding mechanism that is enabled by the unique cutoff properties of SPP

subwavelength modes.

A simple method to quickly obtain an estimate for the propagation constants β_n of the guided modes is the effective index method [50]: each i^{th} vertical slice is replaced by a homogeneous dielectric layer of refractive index equal to the effective index ($n_{\text{eff},i} = k_i/(\omega/c)$) of the lowest order mode (k_i, $\phi_i(y)$) supported within this slice; the complicated cross-section of the waveguide thus gets reduced into a simpler but approximately equivalent dielectric layered structure, whose modes can be easily found, making sure that the most appropriate polarization of the fields is used. The method is most accurate, when the transverse profiles $\phi_i(y)$ of these lowest order modes are nearly the same, so that the couplings to higher order modes can be safely ignored. To implement the method for the structure of Figure 4-2(a), the effective indices of the SPPs B and A should be used respectively for the central and outer layers of the resulting symmetric slab waveguide, while the E-field is chosen to be polarized along y, since B and A are TM polarized with the H-field in the $x-z$ plane. The resulting dispersion curves are shown in Figure 4-2(a). An infinite number of modes is found just below the $\omega = \omega_c(\epsilon_{\text{low}})$ cutoff line, since in that frequency region $k \to \infty$ for curve B, so the effective slab waveguide is one with an infinite index-contrast, which indeed supports an infinite number of modes inside its core. The effective-index method is within 1% accuracy for the fundamental mode by comparison to 'exact' (but technically difficult) simulations with a Finite-Difference Frequency-Domain (FDFD) eigenmode solver for a few frequencies. The exact TM-like H_x component of the first two modes is shown in insets (ii) and (iii), and is indeed found to be two orders of magnitude larger than the TE-like components.

For completeness, let us examine also the case where the values of the dielectrics for the structure presented in Figure 4-2(a) are interchanged, leading to that in inset (i) of Figure 4-2(b). The existence of modes is less surprising for this configuration, since it does follow the simple index-guiding intuition and doesn't rely on the presently introduced mechanism. The effective index method can again be employed using for the central slice the SPPs A and for the outer slices the SPP B, yielding the results shown in Figure 4-2(b). The FDFD fundamental mode (insets (ii)) is again at most 1% away from this estimate. Note that for Figure 4-2(b) the conserved wavenumber β must be larger than that of the mode supported by the $\epsilon_{\text{low}} - \epsilon_{\text{hi}} - \epsilon_{\text{low}}$ waveguide standing vertically on top of the substrate, for the field to couple only to decaying modes in y.

An important lesson is that the index-guiding mechanism rigorously relates to appropri-

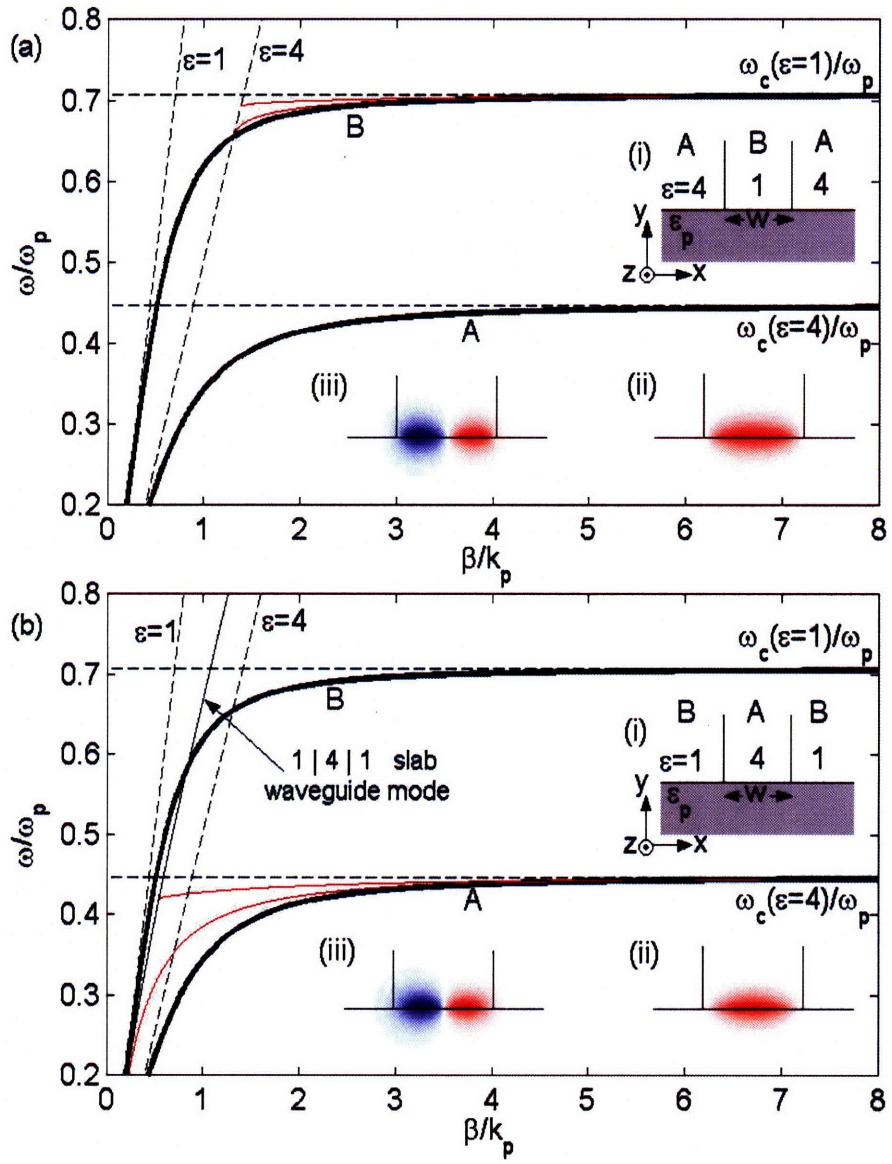


Figure 4-2: $\omega - \beta$ diagrams (red curves calculated via the effective-index method) for SPP-based waveguide structures (insets (i)) with $w/\lambda_p = 0.25$. (a) Effective-index-guiding mechanism: SPP B (from Figure 4-1) of the central vertical slice (thick solid black curve) and the ϵ_{hi} light line (dashed black curve) limit the region where fully confined modes can exist. (b) Regular index-guiding mechanism: SPP A and the vertical cladding-guided mode define the modal region. The H_x component of the first two modes at (a) $\omega/\omega_p = 0.705$ and (b) $\omega/\omega_p = 0.444$ is shown (insets (ii)-(iii) calculated via a finite-difference frequency-domain eigenmode solver).

ate effective and not actual material indices. In all-dielectric structures the two follow the same trend, but this is not the case always in the presence of metals, allowing for the design of what are basically *Surface-Plasmon-Polariton Effective-Index-Guiding* waveguides, like the ones above. Note, also, that care should be taken, when searching for guided modes of such structures, in that the correct way to interpret the concept that the dispersion line of a mode lies *above* or *below* another is to compare their effective indices $n_{\text{eff}} = ck/\omega$ at a *fixed frequency* ω and not the other way around, so perhaps the terms *left* and *right* respectively seem more appropriate.

4.2.2 Cavities

Once can easily imagine that this confinement mechanism can be used to implement light localization in subwavelength low-index (such as air) cavities. Consider, for example, again the structure of Figure 4-2(a), but view it not as a linear waveguide in the z direction, but simply a 2d cavity in the $x-y$ plane. Clearly, such a cavity will have a finite Q, because light of the form of an SPP B (from Figure 4-1), localized inside the center low-index ϵ_{low} region, will couple to the radiative modes to the *left* of the ϵ_{hi} light-line upon bouncing off the walls. However, this radiation loss is expected to be very small, since the SPP B is so subwavelength that its mode profile does not match those radiative modes. Therefore, high-radiative-Q and extremely subwavelength air cavities are made possible with this mechanism, and they can have great applications in nanotechnology, such as sensing and characterization of streams of nanoparticles flowing through the air-core cavity.

Chapter 5

Dispersionless broadband-slow or stopped light in Surface-PlasmonoDielectric-Polaritonic (SPDP) systems [2, 3]

There has been increased interest lately in the development of photonic systems that can slow down [22, 23, 24, 69, 70, 71, 72, 73, 25] or stop [26, 27, 28] light, as they could find great applications in all-optical buffers and switches for telecommunications and computing. However, for slow- and stopped-light systems, there is a limitation on their achievable so-called 'bandwidth-delay product' [16] and the major reason is modal dispersion [74, 75, 76, 77, 78, 79]. In fact, dispersion is a problem commonly shared among all existing photonic systems. This fact has thus motivated the recent invention of a few advanced dispersion-cancellation schemes, which make use of coupled geometric [80] or gain-material [81] resonances or a fine balance of dispersion with nonlinearities [82]. In this Chapter, we show that *layered* axially-uniform plasmonic-dielectric-hybrid waveguiding systems, which we will call Surface-PlasmonoDielectric-Polaritonic (SPDP), can guide broadband-slow or stopped and subwavelength light, and that such *multilayered* systems allow for a new physical mechanism, which enables their inherently-single-polarization surface-polaritonic modes to additionally have - for small positive, negative or zero group-velocity - the dispersion coefficients of simultaneously both the group velocity and the attenuation systematically

cancelled to unusually high orders, thus leading to the first linear passive system in nature, known to us, that essentially is dispersionless and breaks the 'bandwidth-delay product' limitation. Furthermore, they can also be tailored to invent a variety of novel intricate dispersion relations with multiple points of zero group velocity. The applications of this class of guiding systems in the technological realm of nanophotonics could be substantial, since they promise significant reduction in all (spatial, temporal and operational energy) device scales.

5.1 Broadband-slow or stopped light-guiding mechanism by layered SPDP systems

In this Section we will demonstrate that surface-plasmonic-polaritonic systems can uniquely support both very broadband slow light and also stopped light (namely having zero group-velocity), provided a thin layer of a dielectric material is deposited on top of the plasmonic substrate, whose presence modifies the surface resonance in a controllable way. We call these systems Surface-PlasmonoDielectric (SPDP), because the presence of the dielectric layer is essential for the physical mechanism. This phenomenon can find applications in ultra-compact broadband slow-light waveguides and nano-sized high-radiation-Q cavities.

5.1.1 Planar waveguides

Let us start our analysis from the basic planar SPP structure of Figure 4-1. Several extensions of this simple structure in the form of planar layers have been examined in the past [83, 84]. Instead, let us keep the plasmonic substrate $\epsilon_{\rm p}$ infinite and consider the case of a $\epsilon_{\rm hi}$-dielectric layer of thickness d inserted between this substrate and a $\epsilon_{\rm low}$-dielectric space (Fig. 5-1, inset C). The dispersion relation of the mode (curve C) is implicitly determined by $\tanh\left(u_{\rm hi}\epsilon_{\rm hi}d\right) = -\left(1+u_{\rm p}/u_{\rm low}\right)/\left(u_{\rm hi}/u_{\rm low}+u_{\rm p}/u_{\rm hi}\right)$, where $u_{\rm hi}=\epsilon_{\rm hi}^{-1}\sqrt{k^2-\omega^2/c^2\cdot\epsilon_{\rm hi}}$ and similarly for $u_{\rm low}$ and $u_{\rm p}$. The localization of the mode to the metal-$\epsilon_{\rm hi}$ interface increases with the wavevector k. Therefore, for low frequencies ω (and small k) this Surface-PlasmonoDielectric-Polariton (SPDP) mode has most of its energy stored in the outer dielectric $\epsilon_{\rm low}$, and does not 'see' much the $\epsilon_{\rm hi}$-dielectric layer, thus it asymptotes to a SPP on a $\epsilon_{\rm p}$-$\epsilon_{\rm low}$ interface (curve B), while in the limit of large k the SPDP mode is tightly confined on the $\epsilon_{\rm p}$-$\epsilon_{\rm hi}$ interface and doesn't 'see' much of the outside material, thus it asymptotes

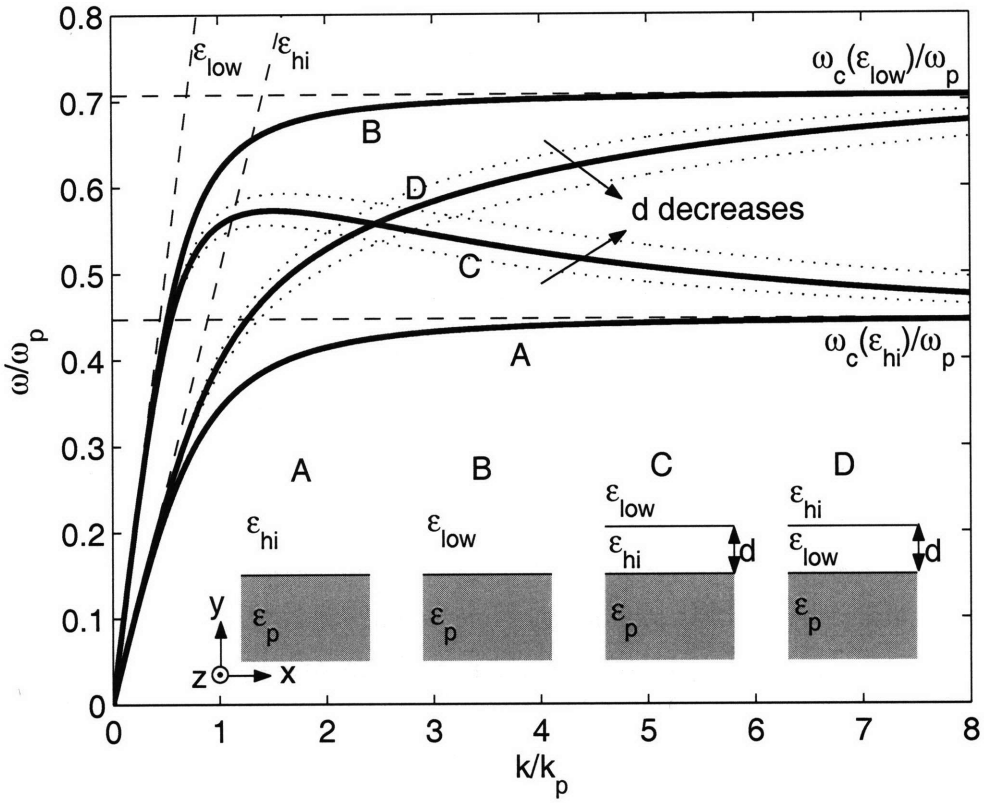


Figure 5-1: $\omega - k$ diagrams (solid curves) for layered Surface-Plasmono-Dielectric-Polaritonic structures (insets $A - D$) with $\epsilon_{\text{hi}} = 4$ and $\epsilon_{\text{low}} = 1$ (air). Layer thicknesses $d/\lambda_p = 0.015$, 0.02 and 0.025 are used for C and D (solid+dotted curves). The light lines $\omega/\omega_p = \sqrt{\epsilon} \cdot k/k_p$ ("vertical" dashed lines) and the cutoff frequencies $\omega_c(\epsilon)/\omega_p = 1/\sqrt{1+\epsilon}$ (horizontal dashed lines) are shown.

to a SPP on such a $\epsilon_{\rm p}$-$\epsilon_{\rm hi}$ interface (curve A). The smaller the thickness d, the higher the wavenumber k where this change in behavior happens, as depicted in Figure 5-1 with dotted curves. Furthermore, for d smaller than a certain threshold, since both the asymptotic low-k and high-k SPPs have positive group velocity and $\epsilon_{\rm hi} > \epsilon_{\rm low} \Rightarrow \omega_{\rm c}(\epsilon_{\rm hi}) < \omega_{\rm c}(\epsilon_{\rm low})$, the limiting k-regions must be connected through a regime of *negative* group velocity, with two boundaries of zero group velocity (zgv), one with negative curvature at a small $k_{\rm n}$ and one with positive curvature at a large $k_{\rm p} > k_{\rm n}$. Note that these boundaries are circles in the 2d $\mathbf{k}$-plane (projected as points in ω-k plots) and that Surface-Polaritonic systems are the only systems in nature with 2d continuous translational symmetry known so far to exhibit such zgv points at a non-zero wavevector. Similarly, if the two dielectric materials are interchanged (inset D), there still exists a vertically confined (namely exponentially decaying as $|y| \rightarrow \infty$) surface wave (curve D), which now has opposite asymptotic behavior from C in the two limits of low ω and high k values, so its group velocity is always *positive*.

A significant remark for both cases is that sufficiently decreasing the layer thickness can lead to arbitrarily small group velocity (negative or positive respectively) over the *entire large bandwidth* $\left[\ \omega_c(\epsilon_{\rm hi}),\ \ \omega_c(\epsilon_{\rm low})\ \right]$. This is a unique physical property for layered plasmonic systems, since any other known system that can support very low group velocities (such as electromagnetically induced transparency or a photonic crystal) does so only within a narrow frequency band. This striking attribute of unlimited 'frequency bandwidth over group velocity' ratio carries over immediately to linear plasmonic waveguides, such as the ones discussed below.

5.1.2 Linear waveguides

In order to construct now linear waveguides with the same interesting properties of the planar SPDP modes C, D of Figure 5-1, the same effective-index guiding mechanism presented in Section 4.2 can be used. Let us start from the structure of inset (i) in Figure 4-2, but let the central low-permittivity slab have a finite height d, as shown in inset (i) of Figure 5-2(a). This structure can be treated similarly, the only difference here being that the inner slice alone supports the SPDP D from Figure 5-1, which still lies to the left of SPP A for $\omega < \omega_c(\epsilon_{\rm hi})$, but to the right of the $\epsilon_{\rm hi}$ light line, the lowest order mode supported by the sides for $\omega_c(\epsilon_{\rm hi}) < \omega < \omega_c(\epsilon_{\rm low})$. Therefore, for a fixed frequency ω within this *broad* range, guided modes exist with wavenumbers β between the $\epsilon_{\rm hi}$ light line and D, since only in this

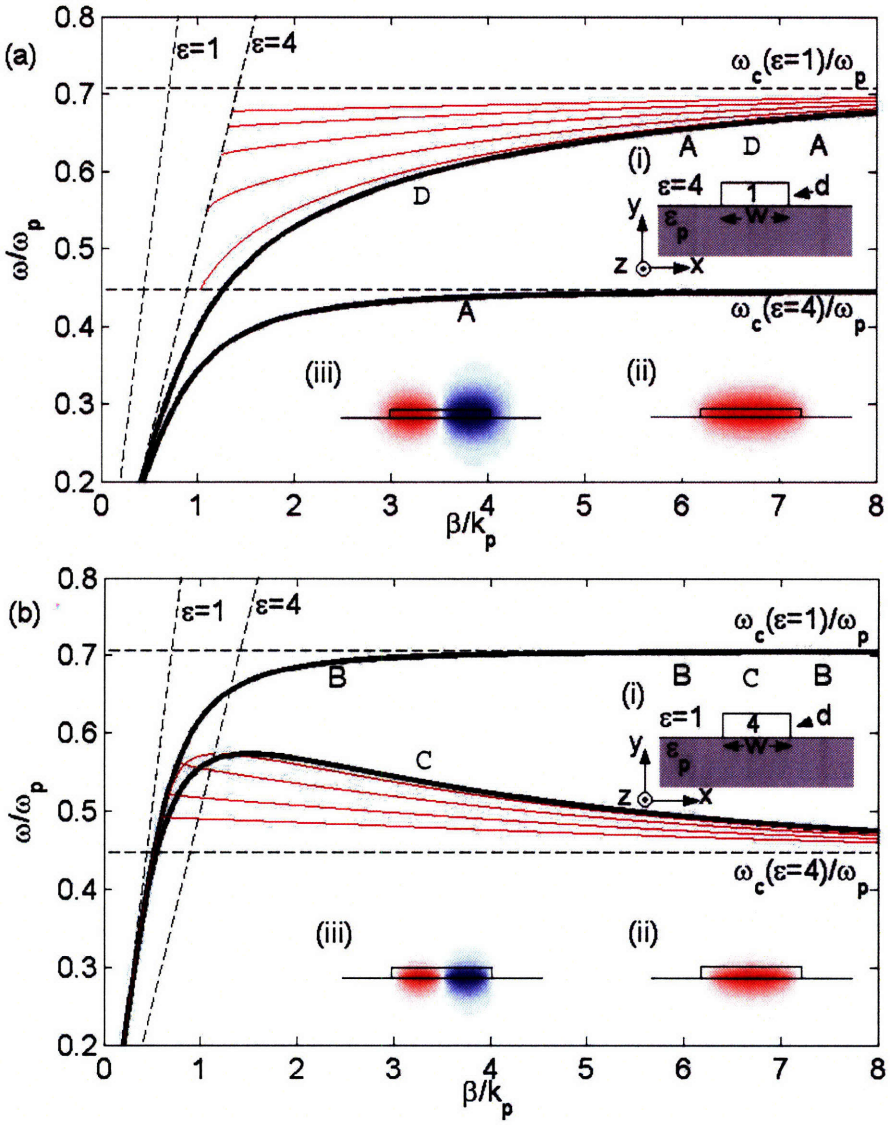


Figure 5-2: $\omega - \beta$ diagrams (red curves calculated via the effective-index method) for SPDP-based waveguide structures (insets (i)) with $w/\lambda_p = 0.25$ and $d/\lambda_p = 0.02$. (a) SPDP D (from Figure 5-1) of the central vertical slice (thick solid black curves) and the ϵ_{hi} light line (dashed black curve) limit the region where fully confined modes can exist. (b) SPDPs C and B define the modal region. The H_x component of the first two modes at (a) $\omega/\omega_p = 0.65$ and (b) $\omega/\omega_p = 0.47$ is shown (insets (ii)-(iii) calculated via a finite-difference frequency-domain eigenmode solver).

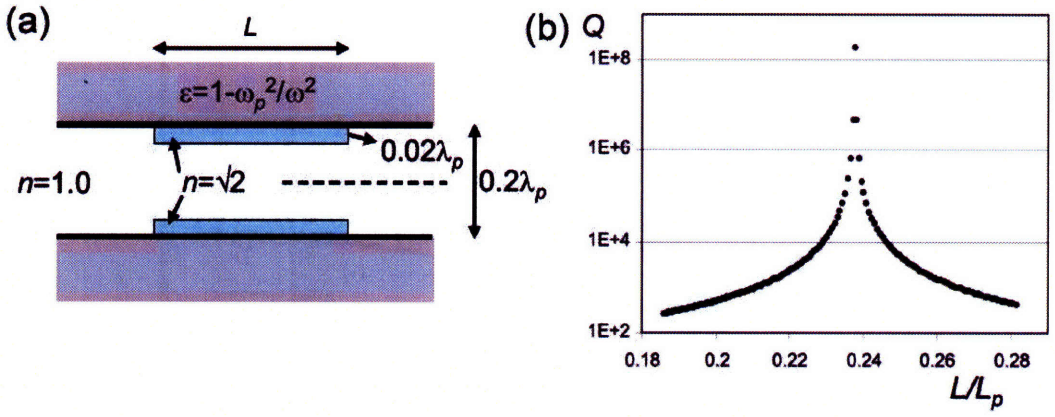


Figure 5-3: (Taken from Ref.[86]) (a) Schematic of a 2d plasmon-cavity structure, like the one in Figure 5-2 but with a symmetry plane. (b) Q-enhancement as a function of the length L of the cavity. (Data was calculated with mode expansion method CAMFR [53].)

regime the field is composed only by decaying modes in the outer regions. The effective index method indicates how the dispersion curves approximately look like (Figure 5-2(a)), while the FDFD modes are again shown in insets (ii) and (iii). The more intuitive case of a high-index finite-height d slab on top of the plasmonic substrate and surrounded by a lower-index material is shown in Figure 5-2(a). This mode maintains the interesting features of curve C in Figure 5-1, such as the existence of two zgv points, but with transverse localization provided by the linear waveguide.

Note that the most important characteristic of the SPDP modes in Figure 5-2 is that they accomplish exactly our desired goal of supporting slow light over an unusually large frequency bandwidth, while it is simultaneously subwavelength and can be guided inside a low-index region (such as air).

5.1.3 Cavities

The two unique points of zero group-velocity, exhibited by the SPDP mode of curve C in Figure 5-1 and that of Figure 5-2(b), at nonzero wavevectors k_{n} and k_{p}, whose location depends and can be designed solely by the choice of the thickness d, can be used to design enhanced-radiation-Q cavities of nanoscale size, using a mechanism that greatly relates to the one described in Chapter 2, since it is based on far-field destructive interference [85, 86]. In Figure 5-3 (taken from ref.[86]) this Q-enhancement is demonstrated.

5.2 Slow-light dispersion-manipulation mechanism by multilayered SPDP systems

Since the insertion of thin dielectric layers on plasmonic substrates led to a discovery of very interesting dispersive behavior of the associated SPDP modes, in this Section we will consider what happens if we extend this idea to an arbitrary number of thin dielectric layers. What we find is, that each one of these layers affects the surface resonance of the polaritonic mode and the associated interplay of the free charges inside the plasmonic material with the bound charges of the thim dielectric films leads to a system, that of multilayered SPDPs, with an incredible number of degrees-of-freedom for the manipulation of the polaritonic-mode dispersion at will. Very intricate and unique dispersion diagrams can be tailored this way, which would not be possible with any different system in nature known so far.

5.2.1 Planar waveguides

Let us start from the planar layered structure of inset C in Figure 5-1, and denote $\epsilon_{\text{low}} \rightarrow \epsilon$, $\epsilon_{\text{hi}} \rightarrow \epsilon_1$, $d \rightarrow d_1$, $k_{\text{n}} \rightarrow k_{\text{n,1}}$ and $k_{\text{p}} \rightarrow k_{\text{p,1}}$, since for a multilayered structure we will need an index that counts each layer. Now further insert, between the plasmonic substrate and the high-index ϵ_1-dielectric layer, another planar dielectric layer of permittivity $\epsilon_2 < \epsilon_1$ and thickness $d_2 < d_1$. This structure has never, to our knowledge, been analyzed before and behaves as follows: for small k, the behavior will not change, but, for large k, the SPDP mode must now asymptote to a SPP on a ϵ_{p}-ϵ_2 interface; since $\epsilon_2 < \epsilon_1 \Rightarrow \omega_{\text{c}}(\epsilon_2) > \omega_{\text{c}}(\epsilon_1)$, the large-$k_{\text{p,1}}$ zgv point will move to a smaller wavevector $k_{\text{p,2}} < k_{\text{p,1}}$ and two zgv points will remain at $\sim k_{\text{n,1}}$ and $k_{\text{p,2}}$, provided d_2 is small enough that $k_{\text{n,1}} < k_{\text{p,2}}$.

This process of inserting additional layers of smaller and smaller thickness $\{d_{\text{i}}\}$ of various dielectrics $\{\epsilon_{\text{i}}\}$ onto the plasmonic substrate can be continued arbitrarily. The general rules for the resulting SPDP modal dispersion relation upon insertion of the i^{th} layer are that always $\omega(k \rightarrow \infty) = \omega_{\text{c}}(\epsilon_{\text{i}})$ and typically (for smaller enough thicknesses $d_{\text{i}} < d_{\text{i}-1}$) the following occur: (A) $\epsilon_{\text{i}} < \epsilon_{\text{i}-1} < \epsilon_{\text{i}-2} \Rightarrow$ no new zgv point, (B) $\epsilon_{\text{i}} < \epsilon_{\text{i}-1} > \epsilon_{\text{i}-2} \Rightarrow$ no new zgv point and the large-$k_{\text{p,i}-1}$ zgv point moves to $k_{\text{p,i}}$ (where $k_{\text{n,i}-1} < k_{\text{p,i}} < k_{\text{p,i}-1}$), (C) $\epsilon_{\text{i}} > \epsilon_{\text{i}-1} < \epsilon_{\text{i}-2} \Rightarrow$ two new zgv points at $k_{\text{n,i}}$ and $k_{\text{p,i}} > k_{\text{n,i}}$, and (D) $\epsilon_{\text{i}} > \epsilon_{\text{i}-1} > \epsilon_{\text{i}-2} \Rightarrow$ either two new zgv points at $k_{\text{n,i}} > k_{\text{p,i}-1}$ and $k_{\text{p,i}} > k_{\text{n,i}}$, if d_{i} is really small, or no new zgv point and the large-$k_{\text{p,i}-1}$ zgv point moves to another large wavevector $k_{\text{p,i}}$, if d_{i} is

only a little smaller than d_{i-1}. These rules provide ample degrees of freedom to create very interesting dispersion relations with many zgv points. An example, which was calculated using a standard transfer-matrix method, is shown in Figure 5-4.

5.3 High-order group-velocity-dispersion (GVD) cancellation mechanism by multilayered SPDP systems

An even larger variety of exotic dispersion relations can be created, if we don't restrict the dielectric layers to be progressively thinner from top to bottom. One fascinating example is that of exceptionally-high-order cancellation of group-velocity dispersion for a broadband-slow or stopped subwavelength light mode. Linear waveguides and extremely-high-radiation-Q cavities can again be constructed.

5.3.1 Planar waveguides

To demonstrate how this gvd cancellation can be accomplished, let us use a structure of the type shown in Figure 5-4 as a starting point. Consider a small group velocity v_{go}, indicated in Figure 5-4(ii) by a dotted line, so that the function $v_g - v_{go}$ has several roots, depending on the chosen v_{go}; by then modifying the structure of Figure 5-4 so as to increase (decrease) the thicknesses of the bottom (top) layers, the roots of $v_g - v_{go}$ at large (small) wavevectors will now move to smaller (larger) wavevectors, and, with the appropriate choice of the thicknesses $\{d_i\}$, multiple (let's say N) of these roots can be forced to coincide at the same wavevector of intermediate value k_o and at frequency ω_o. Such a root of multiplicity N means that dispersion has been cancelled up to N^{th} order for the SPDP mode; locally its dispersion relation looks like

$$k - k_o = v_{go}^{-1}(\omega - \omega_o) + \frac{c^{-1}\omega_o^{-N}}{(N+1)!} D_{k,N+1}(\omega - \omega_o)^{N+1}, \tag{5.1}$$

or equivalently

$$\omega - \omega_o = v_{go}(k - k_o) + \frac{c^{N+1}\omega_o^{-N}}{(N+1)!} D_{\omega,N+1}(k - k_o)^{N+1}, \tag{5.2}$$

where $D_{k,n} \equiv \omega_o^{n-1} \frac{\partial^{n-1}}{\partial \omega^{n-1}} \left(\frac{\partial ck(\omega_o)}{\partial \omega} \right)$, $D_{\omega,n} \equiv \omega_o^{n-1} \frac{\partial^{n-1}}{\partial (ck)^{n-1}} \left(\frac{\partial \omega(k_o)}{\partial ck} \right)$ are the normalized dimensionless dispersion constants of n^{th} order, and, when all are zero up to N^{th} order as

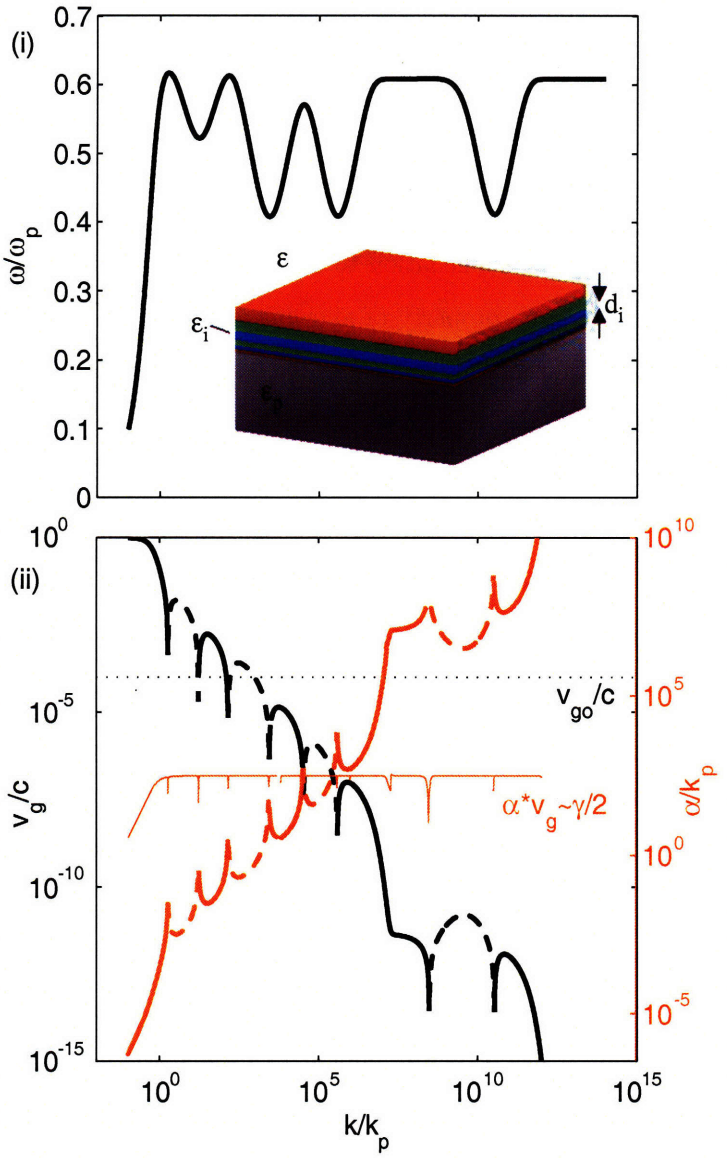


Figure 5-4: (i) $\omega - k$ dispersion diagram (designed to resemble 'MIT') for the plasmonic-dielectric layered structure shown in the inset with $\epsilon = 1$, $\epsilon_i = \{4, 1, 10, 1, 10, 1.7, 1, 10, 1.7\}$, $d_i/\lambda_p = \{10^{-2}, 10^{-3}, 5 \cdot 10^{-5}, 4 \cdot 10^{-6}, 3.5 \cdot 10^{-7}, 5 \cdot 10^{-8}, 2.4 \cdot 10^{-11}, 4 \cdot 10^{-12}, 6 \cdot 10^{-13}\}$ (from top to bottom) and $\epsilon_\infty = 1$. (ii) [solid and dashed lines denote that the quantity plotted logarithmically is positive and negative respectively] (black line) $v_g - k$ group-velocity dispersion diagram for the same structure (namely first derivative of (i)): note the apparent scaling $\max|v_g| \sim 1/k$. (orange line) $\alpha - k$ attenuation dispersion diagram for the same structure with an added loss factor $\gamma/\omega_p = 10^{-4}$: note the apparent scaling $\min|\alpha| \sim k$, and that, away from the special points of zero group velocity and for subwavelength wavevectors, $\alpha \cdot v_g = \gamma/2$ independently of wavevector (and thus frequency). $k_p = \omega_p/c = 2\pi/\lambda_p$.

in Eqs.(5.1) and (5.2), then $D_{\omega,\mathrm{N}+1}/D_{k,\mathrm{N}+1} = -(v_{\mathrm{go}}/c)^{\mathrm{N}+2}$. Examples for such high-order dispersion cancellation are given in Figures 5-5(a), 5-5(b) and 5-6 for three values of v_{go}: positive, negative and zero respectively. To our knowledge, there is no other system in nature, whose photonic dispersion relation can be such a long straight-line segment and which is not a plane-wave.

Plasmonic-dielectric layered material systems even allow the parameters ω_{o}, k_{o}, v_{go} and N of this phenomenal dispersion cancellation to be tailored at will, to a great extent:

• These systems have the unique property of allowing independent control of the temporal and spatial scales of their photonic modes: their dispersion curve must lie in the ω-k plane "allowed region" between the two curves for simple SPPs on a ϵ_{p}-min $\{\epsilon_{\mathrm{i}}, \epsilon\}$ interface and a ϵ_{p}-max $\{\epsilon_{\mathrm{i}}, \epsilon\}$ interface (in particular, $\omega_{\mathrm{c}}(\max\{\epsilon_{\mathrm{i}}, \epsilon\}) < \omega < \omega_{\mathrm{c}}(\min\{\epsilon_{\mathrm{i}}, \epsilon\})$ and $k > \omega/c \cdot \sqrt{\epsilon}$ in the subwavelength regime of interest); then ω_{o} can be dictated mainly by the proper choice of materials for the plasmonic substrate $\{\omega_{\mathrm{p}}, \epsilon_{\infty}\}$ and the dielectric layers $\{\epsilon_{\mathrm{i}}, \epsilon\}$, while k_{o}, quite independently, by the choice of the layer thicknesses $\{d_{\mathrm{i}}\}$. Similarly there is substantial freedom of choice for v_{go}, with the sole restriction, imposed by the general nature of plasmonic systems, that the maximum attainable $|v_{\mathrm{g}}|$ decreases rapidly as k increases, with an apparent scaling $\max|v_{\mathrm{g}}| \sim 1/k$ as can be seen from Figure 5-4(ii), namely the same scaling as for the phase velocity $v_{\mathrm{p}} = \omega/k$, which is typically though much larger ($v_{\mathrm{g}} \ll v_{\mathrm{p}}$) for these systems in the subwavelength regime.

• Given desired (and compatible under the above restriction) ω_{o}, k_{o} and v_{go}, the recipe for an N^{th} order dispersion cancellation is then as follows: Since the roots of the $v_{\mathrm{g}} - v_{\mathrm{go}}$ function are the essential tool of the cancellation mechanism, an oscillatory behavior of this function is needed and thus the choice of materials for the layers should be such that higher- and lower-index layers alternate (cases B and C discussed earlier), since each such pair of consecutive layers generates an additional oscillation with two zgv points (and hopefully, depending on the chosen v_{go}, two roots of $v_{\mathrm{g}} - v_{\mathrm{go}}$) at controllable ω- and k-values; therefore, with this design, a minimal number of $\approx$ N layers are needed for creating N roots of $v_{\mathrm{g}} - v_{\mathrm{go}}$, and then their N-fold coincidence can be accomplished at the desired frequency ω_{o} and subwavelength wavevector k_{o} by choosing and/or fine-tuning the parameters $\{\omega_{\mathrm{p}}, \epsilon_{\infty}, \epsilon_{\mathrm{i}}, \epsilon, d_{\mathrm{i}}\}$. In principle, one can keep adding pairs of layers to increase N and whether this can be increased arbitrarily depends on how rapid a change in group velocity within the dispersion curve does the plasmonic material system allow. Unfortunately, due to its complexity, the existence and

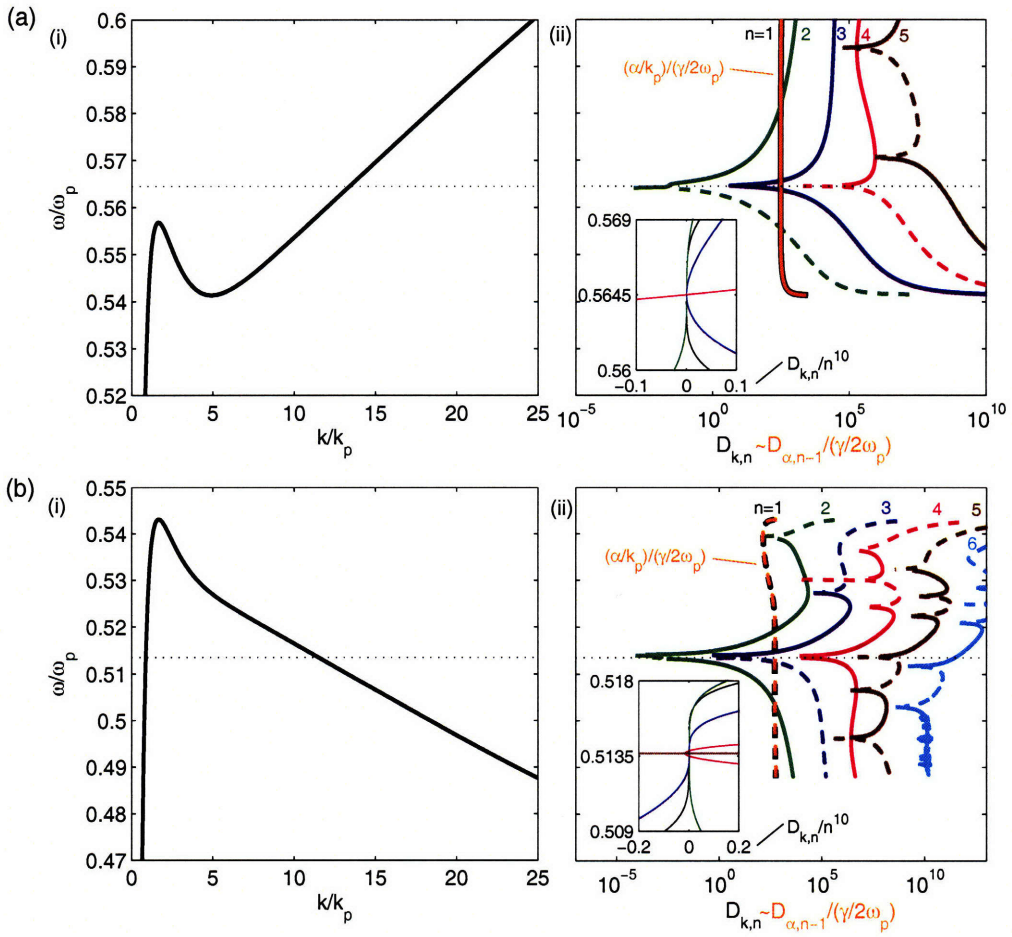


Figure 5-5: (i) $\omega - k$ dispersion diagrams for plasmonic-dielectric layered structures with $\epsilon = \epsilon_\infty = 1$ and (a) $\epsilon_\mathrm{i} = \{4, 1, 4, 1\}$, $d_\mathrm{i}/\lambda_\mathrm{p} = \{0.0200162, 0.00501101, 0.0086219, 0.0023344\}$, (b) $\epsilon_\mathrm{i} = \{4, 1, 4, 1, 4\}$, $d_\mathrm{i}/\lambda_\mathrm{p} = \{0.02002878, 0.008302923, 0.01069271, 0.00349443, 0.004515306\}$: note the extremely linear regime around (a) $\omega_\mathrm{o}/\omega_\mathrm{p} = 0.5645$, $k_\mathrm{o}/k_\mathrm{p} = 13.4$, (b) $\omega_\mathrm{o}/\omega_\mathrm{p} = 0.5135$, $k_\mathrm{o}/k_\mathrm{p} = 11.5$. (ii) (all lines except orange) $\omega - D_{k,\mathrm{n}}$ group-velocity dispersion (gvd) diagrams for the same structures (namely derivatives of (i)): plotted logarithmically in the main box and linearly in the inset, note that gvd orders $\mathrm{n} = 2 \ldots \mathrm{N}$ are cancelled at ω_o (dotted line), where (a) $v_{\mathrm{go}}/c = D_{k,1}^{-1} = D_{\omega,1} = 0.0032 > 0$, $\mathrm{N} = 4$, $D_{k,5} = 2.11 \cdot 10^8 \Rightarrow D_{\omega,5} = -2.24 \cdot 10^{-7}$, (b) $v_{\mathrm{go}}/c = D_{k,1}^{-1} = D_{\omega,1} = -0.0020 < 0$, $\mathrm{N} = 5$, $D_{k,6} = 3.16 \cdot 10^{11} \Rightarrow D_{\omega,6} = -3.96 \cdot 10^{-8}$, and thus the inset depicts the Eq.(5.1)-type behavior. (orange line) $\omega - \alpha$ attenuation dispersion (atd) diagrams for the same structures with an added loss factor $\gamma/\omega_\mathrm{p} = 10^{-4}$: note that, throughout the plotted frequency regime, $\alpha \cdot v_\mathrm{g} = \gamma/2$ independently of frequency (and thus wavevector) and therefore $D_{\alpha,\mathrm{n}-1} = D_{k,\mathrm{n}} \cdot \gamma/2\omega_\mathrm{p}$ implying that atd orders $\mathrm{n} - 1 = 1 \ldots \mathrm{N} - 1$ are also cancelled at ω_o.

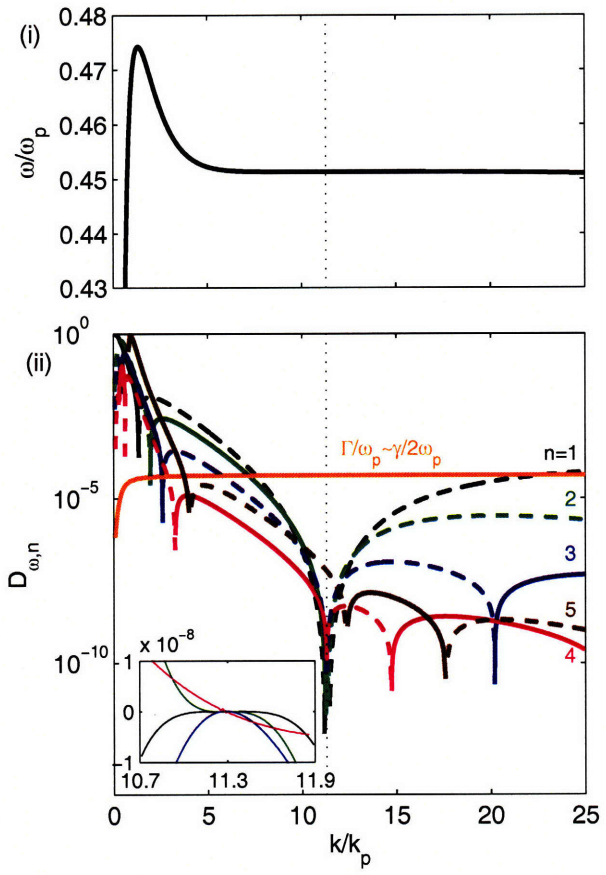


Figure 5-6: (i) $\omega - k$ dispersion diagram for a plasmonic-dielectric layered structure with $\epsilon = \epsilon_\infty = 1$ and (a) $\epsilon_i = \{4, 1, 4, 1, 4\}$, $d_i/\lambda_p = \{0.03805142, 0.001163696, 0.021089836, 0.00016090557, 0.004449584\}$: note the extremely linear regime around $\omega_o/\omega_p = 0.4513$, $k_o/k_p = 11.3$. (ii) (all lines except orange) $D_{\omega,n} - k$ group-velocity dispersion (gvd) diagrams for the same structure (namely derivatives of (i)): plotted logarithmically in the main box and linearly in the inset, note that gvd orders $n = 2 \ldots N$ are cancelled at k_o (dotted line), where $v_{go}/c = D_{\omega,1} = 0$, $N = 4$, $D_{\omega,5} = -6.46 \cdot 10^{-8}$, and thus the inset depicts the Eq. (5.2)-type behavior. (orange line) $\Gamma - k$ attenuation dispersion diagram for the same structure with an added loss factor $\gamma/\omega_p = 10^{-4}$: note that, for large enough wavevectors, $\Gamma = \gamma/2$ independently of wavevector.

estimation of such an upper limit on the achievable N remains an open theoretical question. We can simply argue that a larger N is easier to get as $|v_{go}|$ gets smaller and k_o increases, since a longer straight-line segment can then fit inside the "allowed region" in the ω-k plane described earlier or, seen differently from Figure 5-4(ii), $v_g - v_{go}$ can have more roots more easily. In practical applications though, this is not even an issue, since N does not need to be too large, as will be seen in examples later.

This scheme can very easily take into account also the potential material dispersion of the dielectrics, since this dispersion is much weaker than the strong geometric dispersion enforced by the design.

5.3.2 Linear waveguides

The currently proposed plasmonic-dielectric platform and the mechanisms to design complicated dispersion relations, which include many zgv points and/or extremely-high-order dispersion cancellation, can be extended to linear waveguides. Consider the suggested layered dielectric structure, on top of the plasmonic substrate, to be axially uniform in the waveguiding direction but to have finite width w in the transverse direction, being surrounded by a homogeneous dielectric of permittivity ϵ_c, as shown in the inset of Figure 5-7(i). Then, using again the effective-index method, described in detail in Section 4.2, we conclude that multiple guided modes exist, as long as the dispersion curve of the initial layered plasmonic structure of infinite width lies in the ω-k plane to the right of a SPP on a ϵ_p-ϵ_c interface. This condition can be satisfied for a wide range of permittivities ϵ_c, including at least $\epsilon_c \leq \min\{\epsilon_i, \epsilon\}$ and $\epsilon_c \geq \max\{\epsilon_i, \epsilon\}$ (e.g. for $\epsilon_c = \epsilon = 1$). Then, denoting β the conserved wavevector along the one-dimensional (1d) translationally-invariant guiding direction, the same manipulations as before (e.g. choosing and/or fine-tuning $\{\omega_p, \epsilon_\infty, \epsilon_i, \epsilon_c, \epsilon, d_i\}$ for an N^{th} order cancellation) can be implemented on the ω-β dispersion of the first few of these guided SPDP modes (typically the very first one), since it digresses only a little from that of the infinite-width structure. An example is shown in Figure 5-7: the structural parameters of the final design were calculated using the efficient but approximate semi-analytical effective-index method, however, finite-element [87] numerical calculations were also performed on the final structure to confirm the existence (the achievable discretization led to 1% convergence accuracy, not enough to also calculate dispersion coefficients) of the guided mode, shown in the inset of (i); note that guidance occurs, counter-intuitively, in the region

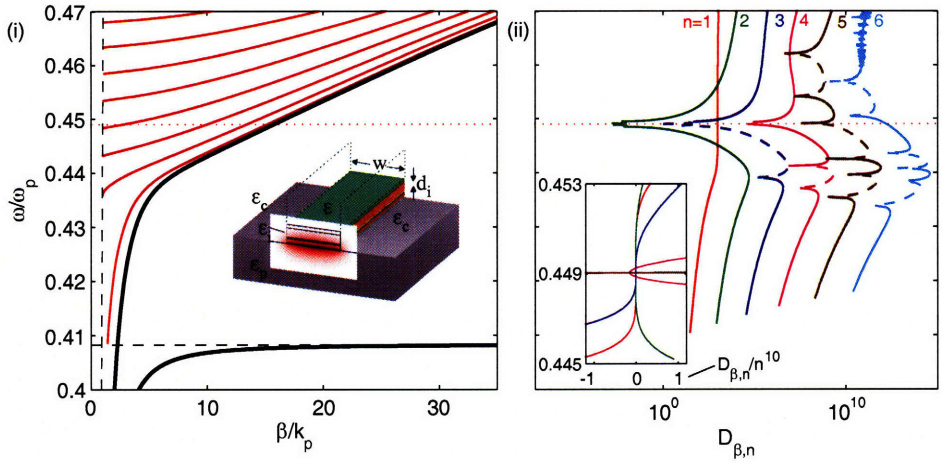


Figure 5-7: (i) $\omega - \beta$ dispersion diagram for the plasmonic-dielectric layered waveguide structure shown in the inset with $\epsilon = \epsilon_c = 5$, $\epsilon_i = \{2, 5, 2, 5, 1.75, 5\}$, $d_i/\lambda_p = \{0.0066136, 0.0170872, 0.0021628, 0.008271, 0.000923, 0.000333\}$, $w/\lambda_p = 0.1$ and $\epsilon_\infty = 1$: note the extremely linear regime around $\omega_o/\omega_p = 0.449$, $\beta_o/k_p = 15.3$; using a finite-element calculation (at ω_o giving $\beta_o/k_p \approx 15.48$), the associated transverse modal profile is plotted in the inset for the H-component parallel to the plasmonic interface. (ii) $\omega - D_{\beta,n}$ group-velocity (gvd) dispersion diagrams for the same structure (namely derivatives of (i)): note that gvd orders n = 2 ... N are cancelled at ω_o (dotted line), where $v_{go}/c = D_{\beta,1}^{-1} = D_{\omega,1} = 0.001 > 0$, N = 5, $D_{\beta,6} = 1.82 \cdot 10^{12} \Rightarrow D_{\omega,6} = -1.66 \cdot 10^{-9}$, and thus the inset depicts the Eq.(5.1)-type behavior.

of lower average dielectric permittivity using the mechanism developed in Chapter 4. Again, the method can take the weak material dispersion of the dielectrics into account, and similar considerations as before hold for the range of the simultaneously achievable ω_o, β_o, v_{go} and N.

5.3.3 Cavities

A very interesting behavior is expected, when these dispersion-cancelled waveguides are truncated to form subwavelength cavities with a length corresponding to the wavevector, at which cancellation has been achieved for the corresponding waveguide. In particular, the most interesting behavior should be seen, when making cavities out of zero group-velocity modes with such a high-order gvd cancellation, and this is a topic for future study.

In short, the radiation-Q enhancement observed for cavities at zgv points has been associated [86] with far-field interference between the two counterpropagating modes that result in the zgv point. As can be seen in Ref.[86], the coupling of these two modes results

into the existence of two different resonances, one with low and one with high radiation-Q. We believe that these two resonant modes must correspond to an even and an odd superposition of the counterpropagating waveguide modes, one of which has enhanced loss due to constructive far-field interference and the other is the interesting high-Q cavity mode. When now considering cavities out of our SPDP waveguides where multiple modes interfere to create a high-order zgv point, coupling and far-field interference between N such modes is expected to lead to N normal modes, of which one is a super-radiant and one is an extremely-high-Q sub-radiant state. The scaling of Q with N should follow general antenna-theory arguments and could be related to the associated density of states (calculated later in Eq.(5.9)) of the SPDP mode.

5.4 High-order attenuation-dispersion (AD) cancellation in multilayered SPDP systems

All plasmonic materials in reality exhibit absorption losses, whose effects on the suggested dispersion manipulation mechanisms need to be studied. For any material system, instrinsic absorption losses are usually quantified as losses-per-unit-distance α (also called 'propagation losses') or losses-per-unit-time Γ (related to the 'quality factors' $Q = \omega/2\Gamma$); for small loss, using the analyticity of the ω-k relation and the Cauchy-Riemann equation $\frac{\partial \mathrm{Im}k}{\partial \mathrm{Im}\omega} = \frac{\partial \mathrm{Re}k}{\partial \mathrm{Re}\omega} = 1/v_\mathrm{g}$, these relate by $\alpha \approx \frac{\partial \mathrm{Im}k}{\partial \mathrm{Im}\omega} \cdot \Gamma \Rightarrow \alpha v_\mathrm{g} \approx \Gamma$, so α is not a good measure in regimes close to zgv points, where 'propagation' lacks physical meaning and $\alpha \sim 1/v_\mathrm{g} \to \infty$ (see Figure 5-4(ii)), but Γ is more appropriate. Using accordingly the appropriate loss measure, the group-velocity dispersion-characteristics ($\mathrm{Re}\omega - \mathrm{Re}k$ relation) for light within a system remain almost unaffected in the presence of material absorption, its basic effect being just field attenuation. This means that, in particular for our proposed plasmonic-dielectric material structures, our dispersion manipulation and cancellation methods are still easily applicable in the presence of loss; this was also confirmed by simulations.

To account for absorption and calculate losses, we use the simple Drude model for plasmonic materials $\tilde{\epsilon}_\mathrm{p}(\omega) = \epsilon_\infty - \omega_\mathrm{p}^2/\left(\omega^2 + i\gamma\omega\right)$ (where the tilde denotes a complex quantity), which has the unique property that, for small γ/ω_p ($\sim 10^{-2}$ at room temperature for metals), $\tilde{\epsilon}_\mathrm{p}(\omega) \approx \epsilon_\mathrm{p}(\omega + i\gamma/2)$. Then, denoting as $n_\mathrm{p}(\omega) \equiv ck/\omega = c/v_\mathrm{p}$ the phase (effective) index and as $n_\mathrm{g}(\omega) \equiv c\frac{dk}{d\omega} = c/v_\mathrm{g} = n_\mathrm{p}(\omega) + \omega\frac{dn_\mathrm{p}(\omega)}{d\omega}$ the group index of a lossless plasmonic-

dielectric structure, when we add loss *only* to the plasmonic material as above, the complex propagation constant becomes $c\tilde{k} = \omega\tilde{n}_{\mathrm{p}}(\omega) \approx \omega n_{\mathrm{p}}(\omega + i\gamma/2) \approx \omega n_{\mathrm{p}}(\omega) + \omega\frac{dn_{\mathrm{p}}(\omega)}{d\omega} \cdot i\gamma/2$, namely $c\alpha \approx (n_{\mathrm{g}} - n_{\mathrm{p}})\gamma/2$ and, since $c\alpha \approx n_{\mathrm{g}}\Gamma$, we conclude that: in the small-k regime, where most of the light is localized outside the lossy plasmonic material and $n_{\mathrm{g}} \approx n_{\mathrm{p}} \Leftrightarrow v_{\mathrm{g}} \approx v_{\mathrm{p}}$, we naturally find $\alpha \approx \Gamma \approx 0$, while in the subwavelength large-k regime of interest, where there is strong light confinement inside the plasmonic material and typically $n_{\mathrm{g}} \gg n_{\mathrm{p}} \Leftrightarrow v_{\mathrm{g}} \ll v_{\mathrm{p}}$, as seen earlier, we get $\alpha v_{\mathrm{g}} \approx \Gamma \approx \gamma/2$, namely a constant independent of frequency and wavevector (see part (ii) of Figures 5-4, 5-5, 5-6). This has the remarkable implication that, at points ω_{o}, k_{o} where group-velocity dispersion (gvd) has been cancelled to N^{th} order ($D_{k,\mathrm{n}} = 0$ for $n = 2 \ldots \mathrm{N}$), also the attenuation dispersion (ad) has been cancelled to $(\mathrm{N}-1)^{\mathrm{th}}$ order ($D_{\alpha,\mathrm{n}} \equiv \omega_{\mathrm{o}}^{\mathrm{n}}\frac{\partial^{\mathrm{n}}}{\partial\omega^{\mathrm{n}}}\left(\frac{c\alpha(\omega_{\mathrm{o}})}{\omega_{\mathrm{p}}}\right) = \omega_{\mathrm{o}}^{\mathrm{n}}\frac{\partial^{\mathrm{n}}}{\partial\omega^{\mathrm{n}}}\left(\frac{\partial ck(\omega_{\mathrm{o}})}{\partial\omega}\right) \cdot \gamma/2\omega_{\mathrm{p}} = D_{k,\mathrm{n}+1} \cdot \gamma/2\omega_{\mathrm{p}} = 0$ for $n = 1 \ldots \mathrm{N}-1$) and thus the propagation loss rate can be written as

$$\alpha = \alpha_{\mathrm{o}} + \frac{c^{-1}\omega_{\mathrm{o}}^{-\mathrm{N}}\omega_{\mathrm{p}}}{\mathrm{N}!}D_{\alpha,\mathrm{N}}(\omega - \omega_{\mathrm{o}})^{\mathrm{N}}. \tag{5.3}$$

Finally, since these Surface-Polaritonic modes exist inherently only for a single (TM) polarization, they do not suffer from Polarization Mode Dispersion (pmd) [7] either. Clearly, this triple simultaneous dispersion cancellation is an amazing and unique feature of layered plasmonic-dielectric material structures. Its main consequence, discussed in detail below, is the freedom from all kinds of pulse-shape distortion in these systems.

5.5 Applications

The new class of systems presented in this Chapter has features that could greatly impact the field of nanophotonics by being able to shrink light in all (spatial, temporal and energy) scales. At the very high k-values close to ω_c the characteristic longtitudinal length and the transverse modal profile have sizes in the nanoscale, allowing for very high device compactness. The fact that the group velocity can become arbitrarily small by decreasing the core thickness is a very important attribute that can be used to significantly enhance nonlinearities or gain in devices, and thus to reduce their required operational power [88]. Furthermore, the amazing feature that this is achievable over a large bandwidth and with unusually-high-order gvd and ad cancellation (and devoid of pmd) implies that these waveguides can slow down and shrink ultrashort pulses without introducing distortion to them,

thereby allowing for exciting promises in the fields of ultrafast optics, optical memories and quantum computing [6]. Below, we will analyze in detail two particular of these applications, delay lines and active devices.

5.5.1 Delay lines

First of all, this material system can be designed to support slow and subwavelength propagation of short pulses that do not suffer any type of distortion (phase or amplitude) as they travel. This is a very important feature required for the design of very compact and efficient optical buffers and memory, for use in optical telecommunications and computing. The common figure-of-merit for the characterization of optical delay lines is the so-called 'bandwidth-delay product', which has been shown to be fundamentally limited by dispersion [74, 75, 76, 77, 78, 79]. Indeed, using the procedure in Ref.[7], we find that: after propagation on length L of a line with only gvd as in Eq.(5.1), Gaussian bit-pulses of initial width (standard deviation) $T_P(0)$, consisting of not-too-few ($\gg D_{\mathrm{k,N+2}}/D_{\mathrm{k,N+1}}$) optical cycles so that the $(\mathrm{N}+2)^{\mathrm{th}}$-order dispersion can be ignored, are broadened to width

$$T_P^2(L) = T_P^2(0) \cdot \left[1 + \left[\frac{D_{\mathrm{k,N+1}}(\omega_o L/c)}{(\omega_o T_P(0))^{\mathrm{N+1}}} s_{\mathrm{N+1}}\right]^2\right], \tag{5.4}$$

where $s_{\mathrm{N+1}} = \sqrt{(2\mathrm{N}-1)!!/(\mathrm{N}!)^2 - \mathrm{mod}(\mathrm{N}+1,2)/(\mathrm{N}!!)^2}/2^{\mathrm{N}}$, so, for bitrate $B = 1/T_B$, the optimal $T_P(0)$ and the maximum L for distortionless ($T_P(L)/T_B \leq 1/4$) propagation are

$$T_P(0)/T_B = \frac{1}{4}\sqrt{\frac{\mathrm{N}}{\mathrm{N}+1}} \tag{5.5}$$

$$L/\lambda_{\mathrm{o}} = \frac{S_{\mathrm{N+1}}(\omega_o T_B)^{\mathrm{N+1}}}{2\pi |D_{\mathrm{k,N+1}}|}, \tag{5.6}$$

where $S_{\mathrm{N+1}} = \sqrt{\mathrm{N}^{\mathrm{N}}/(\mathrm{N}+1)^{\mathrm{N+1}}} s_{\mathrm{N+1}}/2^{2\mathrm{N+2}}$, and then the figure-of-merit, expressed as the number M of bits that the line can store (namely the largest possible product of the bitrate B times the distortionless time delay $\tau = L/|v_{\mathrm{go}}|$), is

$$M = \tau/T_B = \frac{S_{\mathrm{N+1}}(\omega_o T_B)^{\mathrm{N}}}{|D_{\mathrm{k,N+1}}|(|v_{\mathrm{go}}|/c)}. \tag{5.7}$$

The huge benefit from having a delay line with a large N is obvious from Eq.(5.7), since even the shortest possible pulse has at least one optical-cycle duration ($\omega_o T_P \geq 2\pi \Rightarrow \omega_o T_B \geq 8\pi$) and by allowing for slightly broader pulses (smaller bitrate) the N-polynomial increase in M is then tremendous. Similarly, for a line with only ad as in Eq.(5.3), under the assumption $D_{\alpha,\mathrm{N}}\left(\omega_\mathrm{p} L/c\right)/\left(\omega_o T_P\left(0\right)\right)^\mathrm{N} \ll 1$, the leading-order contribution to pulse-broadening comes for N even ($\mathrm{N} = 2, 4, 6...$) and is

$$T_P^2\left(L\right) = T_P^2\left(0\right) \cdot \left[1 + \frac{D_{\alpha,\mathrm{N}}\left(\omega_\mathrm{p} L/c\right)}{\left(\omega_o T_P\left(0\right)\right)^\mathrm{N}} \mathrm{s}'_\mathrm{N}\right], \tag{5.8}$$

where $\mathrm{s}'_\mathrm{N} = \left[(\mathrm{N}-1)!!/\left(\mathrm{N}-1\right)!\right]/2^{\mathrm{N}-1}$, while for the combined effect of both gvd and ad mechanisms one needs to add the contributions from Eqs.(5.4) and (5.8), but then simple analytical formulas for L and M cannot be derived. To test the performance of our proposed plasmonic-dielectric structures, first note that, since $D_{\alpha,\mathrm{N}} = D_{k,\mathrm{N}+1} \cdot \gamma/2\omega_\mathrm{p}$ and $\gamma/\omega_\mathrm{p} \leq 10^{-2} \ll 1$, these structures are limited only by gvd for pulses of not-too-many ($\ll \omega_\mathrm{p}/\gamma$) optical cycles, namely ad can be ignored and Eqs.(5.6) and (5.7) provide safe performance estimates. Using then the results of Figures 5-5(a), 5-5(b) and 5-7, we find that these delay lines could, for example, hold respectively $\sim$ 63200, $\sim$ 61700 and $\sim$ 21400 undistorted bits of 50-optical-cycle pulses ($\sim$ 1Tbps at $\lambda_\mathrm{o} \equiv 2\pi c/\omega_\mathrm{o} = 1.3\mu$m using Eq.(5.5)) with line lengths of respectively $\sim 45200\lambda_\mathrm{o}$, $\sim 27000\lambda_\mathrm{o}$ and $\sim 4700\lambda_\mathrm{o}$, or that a $\sim$ 29Gbps at $\lambda_\mathrm{o} = 1.3\mu$m data-stream could travel undistorted (albeit *significantly* attenuated) on the delay line of Figure 5-7 all the way from Boston, USA to Bangkok, Thailand (13730km), the same distance as a typical fiber at this zero-dispersion wavelength [7], only with $\sim 10^3$ times slower speed! This slow-light performance is orders of magnitude better than what has been demonstrated ever before [77], thus we can claim that this material system essentially does not suffer from any practical limit on the 'bandwidth-delay product'.

5.5.2 Active devices

Furthermore, the presently proposed system could greatly enhance the performance of a large variety of active optical devices (nonlinear, electronic, thermal etc). The rate of the underlying interaction depends strongly on the number of the participating photonic states (as suggested for example by Fermi's Golden Rule [89]); therefore, if $\Delta\omega$ is the frequency bandwidth of the interaction, we will define here, as the figure-of-merit for a photonic structure,

the enhancement ratio M of the number of states within $\Delta\omega$ for this structure compared to a uniform medium, whose refractive index equals the effective index of the photonic structure at the center frequency of the interaction. Then, using the standard procedure [89] and accounting for only one polarization state, we find that: for a dispersion relation as in Eq.(5.2) with $v_{go} = 0$, the associated density of 1d and 2d Surface-Polaritonic states close to ω_o (in particular so that $k - k_o \ll k_o$) of a system with 1d-length L and 2d-area A respectively, is

$$g_{\{1d,2d\}}(\omega) = S\,\frac{\omega_o\,\{2L, k_o A\}}{2\pi c\,(N+1)}\left[\frac{(N+1)!}{\omega_o\,|D_{\omega,N+1}|}\right]^{\frac{1}{N+1}}\cdot|\omega-\omega_o|^{-\frac{N}{N+1}}\,, \tag{5.9}$$

where $S = |\mathrm{mod}\,(N,2) + \mathrm{sign}\,[D_{\omega,N+1}\cdot(\omega-\omega_o)]| \in \{0,1,2\}$. It can be seen from Eq.(5.9) that both 1d and 2d densities of states interestingly have the *same* frequency dependence, which for $N > 1$ exhibits a new type of singularity (not classified by van Hove [90]) and for $N \gg 1$ approaches the non-integrable $|\omega-\omega_o|^{-1}$, as $\omega \to \omega_o$. Therefore, by integrating Eq.(5.9) over $\Delta\omega$ and then dividing, for each dimensionality, by the well-known [89] number-of-states result (accounting for both polarizations) inside a uniform medium of the same dimensionality and index ck_o/ω_o, we find the enhancement factor

$$M = \frac{\omega_o}{ck_o}\left[\frac{(N+1)!}{2\,|D_{\omega,N+1}|}\right]^{\frac{1}{N+1}}\cdot\left(\frac{\omega_o}{\Delta\omega}\right)^{\frac{N}{N+1}}. \tag{5.10}$$

This result is again the *same* for both 1d and 2d, and shows that, as the interaction bandwidth $\Delta\omega/\omega_o \ll 1$ decreases, for a system with a large N the enhancement M can be extremely large. To test our proposed plasmonic-dielectric structures, first note that, for the specific case of a zgv mode there is, with certainty, no theoretical upper limit on N and dispersion can be cancelled to arbitrarily high order, since k_o can in theory be arbitrarily large, leading to an extraordinary straight-horizontal-line segment of arbitrary k-length as the associated ω-k dispersion curve. Using now the results of Figure 5-6, we find that the $\Delta\omega$-independent prefactor in Eq.(5.10) is ~ 2.5 and thus, for example, for atoms with typical due-to-collisions homogeneously-broadened linewidths $\Delta\omega/\omega_o \sim 10^{-8}$ [91], the figure-of-merit is $M \sim 6.2\cdot 10^6$, and the radiative lifetime of the atoms would be reduced approximately by this factor compared to that in a uniform medium, so even a dipole-forbidden transition could have a lifetime $\sim$ 200ps instead of its typical $\sim$ 1ms [91]! This enhancement is orders of magnitude better than for any other known translationally-invariant material system, and should therefore make the currently proposed plasmonic-dielectric platform a

strong candidate for future active devices, while it could possibly enable also a variety of novel applications.

5.6 Practical limitations

The practical limitations of the currently proposed plasmonic-dielectric structures need also to be discussed:

5.6.1 Material losses

The most significant problem of integrated plasmonic structures is absorption and scattering loss. Although attenuation dispersion induced by plasmonic-material-type absorption losses was shown earlier in this article to be cancellable, unfortunately, for metals in the optical frequency regime and at room temperatures $\gamma/\omega_p \approx 1/100$, so the attenuation rate itself is strong ($Q \approx 100$ in time or $\alpha \approx 10\log_{10}\left(c/\left|v_g\right| \cdot \pi/100\right)\ dB/\lambda_p$ in space, the latter increasing prohibitively with the wavevector, since $\min|\alpha| \approx (\gamma/2)\ /\max|v_g| \sim k$, as seen earlier and in Figure 5-4(ii)). These absorption losses of conducting materials stem from inellastic electron-scattering mechanisms, namely the predominant electron-phonon scattering, which can only be suppressed by cooling, and electron-electron scattering, which is negligible compared to the first at room temperatures. Additional loss mechanisms are those due to elastic electron-scattering, as from impurities or imperfections of the crystal, dictating the need for very clean samples, and from the metal-crystal boundaries, indicating the requirement for very low surface roughness and disorder. The latter is a significant cause also for photonic-scattering losses ($\sim 1/v_g$) and spurious reflections ($\sim 1/v_g^2$) [92], and is dictated by the fabrication tolerances.

Here lies the advantage of the currently presented PlasmonoDielectric system design, in that it involves only a large bulk and completely unpatterned metallic substrate, while the patterning is done in the dielectrics on top of it. Current atomic layer-by-layer deposition techniques (such as atomic layer deposition and molecular beam epitaxy) and nm-scale lithographic techniques (such as deep ultraviolet immersion lithography) are promising for high-quality mass-producible plasmonic structures with operation at not-too-large k-values, such as those in Figures 5-5, 5-6 and 5-7. Thus, devoid of surface roughness, boundary electron-scattering and photon-scattering could perhaps be minimized, making the loss limited only

to its intrinsic (electron-phonon) part, which can be decreased by lowering temperature.

With this assumption, by using again the Drude model $\epsilon_p(\omega) = 1 - \omega_p^2/(\omega^2 + i\gamma\omega)$ to account for losses, a calculation for the planarly layered structures of Figure 5-1 showed that their propagation characteristics stay intact up to large k-values, while absorption loss increases as group velocity decreases and temperature increases. Specifically, for copper ($\omega_p \simeq 5 \cdot 10^{15} rad/s$) at the frequency where the group velocity reaches $\simeq 0.1$c the loss is $\simeq 5.8 dB/\mu m$ at room temperature ($T = 300°\text{K} \Rightarrow \gamma \simeq 5 \cdot 10^{13} rad/s$) and much lower $\simeq 5.8 \cdot 10^{-4} dB/\mu m$ at liquid He temperature ($T = 4°\text{K} \Rightarrow \gamma \simeq 5 \cdot 10^{8} rad/s$) [93], while for $\simeq 0.01$c these numbers are $\simeq 72 dB/\mu m$ and $\simeq 72 \cdot 10^{-4} dB/\mu m$ for the two temperatures respectively.

Moreover, since slow light results in a significant reduction of the required device sizes [88], the overall suffered loss by a plasmonic device might still be in tolerable levels, even in room temperature, for certain applications.

5.6.2 Broadband coupling

Even under the assumption of perfect materials and geometry, there is also the issue of coupling light efficiently into such a broadband slow and subwavelength system, since any common material system would be highly k-mismatched. This problem could be addressed for positive-group-velocity slow structures by adiabatically tapering the dimensions of the layered structure, so as to always have dispersion cancellation at a fixed frequency, while adiabatically increasing group velocity, until it can be brought into broadband alignment with that of a regular-waveguide mode (the key requirement for all coupling mechanisms). For negative-group-velocity structures also adiabatic transitions in time would be required.

5.7 Extensions

The dispersion-manipulation methods presented so far here can be applied also to different geometries and material systems:

Even though this light-manipulation scheme was shown for rectangular waveguides on a plasmonic substrate, it should be applicable straightforwardly also to cylindrical or elliptical fibers with a plasmonic core.

Moreover, instead of many adjacent dielectric layers on a single plasmonic material, one

could also use one or many dielectrics $\{\epsilon_i\}$ on multiple adjacent plasmonic layers $\{\omega_{p,j}, \epsilon_{\infty,j}\}$ to vary the limiting $\omega_c = \omega_{p,j}/\sqrt{\epsilon_{\infty,j} + \epsilon_i}$ at will. In fact, instead of discrete layers, SPDP modes from continuous $\epsilon > 0$ and $\epsilon_p < 0$ distributions (stuck together on some interface) can, in principle, also be designed.

Finally, devices operating in lower frequency regimes can be designed by exploiting Surface-AtomDielectric-, ExcitonDielectric- or PhononDielectric-Polaritons on interfaces between dielectrics and materials with permittivities such as $\tilde{\epsilon}_p(\omega) = \epsilon_\infty - \omega_p^2/(\omega^2 - \omega_o^2 + i\gamma\omega)$, where ω_o is the atomic, excitonic or phononic resonance frequency. In this case, some of the above problems are mitigated, since these polaritonic materials usually exhibit smaller intrinsic losses (smaller γ/ω_p) and, at lower frequencies, also large k-values could translate to fabricatable devices with relatively small surface disorder.

Chapter 6

Conclusion

A set of guidelines has been provided for the design of low-radiation-loss platforms for integrated optical systems based on incomplete photonic bandgaps:

In the case of resonant cavities, where one often wishes to maintain a small modal volume but suppress radiative loss, when the guiding layer and the periodic pattern are built on top of a substrate, with the holes perforating deep into it, the resonant defect properties (its refractive index and size) can be designed so that the resonant frequency is at the center of the incomplete gap, for strongest in-plane localization, but the near-field pattern is orthogonal to the guided mode formed by the etched holes inside the substrate under the defect. Since this discrete guided more would be the dominant channel of radiation for this system, an enhancement of Q, typically to an order of magnitude is achievable.

For devices with a large desired operational bandwidth, such as a photonic-crystal-slab mirror, our analysis led to two different indications for preferred material sets and the associated geometry of the photonic crystal, such that defects therein, that break the translational symmetry, allow for building devices with small radiation loss over the entire frequency bandwidth.

The first option is a high-index-contrast system comprising of a high-index (e.g. Si) slab suspended in air or sitting on top of a very-low-index substrate (e.g. SOI), if that is necessary. The slab should have the largest thickness for single-mode operation within the bandwidth of interest. In forming a crystal, then, one should etch, all the way through the slab, the narrowest possible holes that can open a photonic bandgap of the necessary bandwidth B of the device. The spacing of the holes (namely the period) should finally be

chosen so that the specified bandwidth is placed close to the lower edge of the bandgap. This material set is mostly appropriate for devices where strong field localization is important.

The second option is a system of low index-contrast, in terms of both the difference and the ratio of the indices, namely one of a high-index slab deposited on top of a slightly-lower-index substrate (e.g. AlGaAs). Again, the core slab should be thick but support only one mode inside it. However, upon etching the air holes, their narrowness should now be compromised for their depth, since it is necessary that they reach far into the substrate. The size of the remaining dielectric pattern should though be as narrow as possible. This material system is appropriate for extremely large operational bandwidths and is expected to be less sensitive to geometrical roughness from fabrication.

As fabrication methods are constantly being improved, integrated optical systems based on incomplete photonic bandgaps will start playing a very significant role in photonic technology, since they can exhibit very small radiation loss over large frequency bandwidths, when carefully designed according to rules such as the above.

A hybrid plasmonodielectric material platform has been proposed, along with mechanisms to manipulate the flow of polaritonic light in the nanoscale:

The effective-index-guiding mechanism has been employed in association with the subwavelength nature of SPP modes to create waveguides that confine light in a low-index region, even though it is surrounded by a high index, by operating above the cutoff frequency of a SPP in that outer region.

It was shown that using a multilayered dielectric structure on top of a plasmonic substrate allows the design of optical waveguiding systems, in which the dispersion relation of slow subwavelength light can be tailored, by adjusting the refractive indices and the thicknesses of the thin layers, to exhibit a large variety of exotic behaviors, such as multiple zero-group-velocity points with intermediate regions of positive and negative group velocity or simultaneous cancellation of group-velocity and attenuation dispersion to extremely high orders for positive, negative or zero group velocity. Therefore, this platform attacks systematically a fundamental aspect of optical physics (dispersion), thus potentially enabling great technological achievements in nanophotonics (such as efficient and compact delay lines and active devices) or, at least, simply providing the fascinating ability to make light flow according to the lettering of one's own favorite word (MIT) ...

Part II

Mid-range efficient insensitive Wireless Energy-Transfer

Chapter 7

Introduction

In the early days of electromagnetism, before the electrical-wire grid was deployed, serious interest and effort was devoted (most notably by Nikola Tesla [94]) towards the development of schemes to transport energy over long distances without any carrier medium (namely wirelessly). These efforts appear to have met with little success. Rapid development of autonomous electronics of recent years (e.g. laptops, cell-phones, house-hold robots, that all typically rely on chemical energy storage) justifies revisiting investigation of this issue. Today, we face a different challenge than Tesla: since the existing electrical-wire grid carries energy almost everywhere, even a medium-range ($D_{\text{transfer}} \approx \text{few} \cdot L_{\text{device}}$, where D_{transfer} is the transfer distance and L_{device} is the characteristic size of the device) wireless energy-transfer would be quite useful for many applications.

The major criteria that characterize the performance of any method for wireless energy-transfer are: its efficiency as a function of the transfer distance, its sensitivity to the near-presence of extraneous objects and, then, given it can be at least mid-range efficient and insensitive, its ability to accommodate multiple and mobile devices. Omni-directional far-field (radiative) schemes [95], which work very well for information transfer, since they offer great receiver mobility and device-number and -type versatility, are not suitable for efficient energy-transfer, because a vast majority of energy is wasted into free space. Directed far-field (radiative) schemes (e.g. using lasers or highly-directional antennas) can be used for efficient energy-transfer even for long distances ($D_{\text{transfer}} \gg L_{\text{device}}$) and are thus useful for certain applications, but they require existence of line-of-sight uninterrupted by extraneous objects, to which such a high-power directive beam could potentially also cause hazard, and they lack

mobility and versatility, since a complicated tracking system for the mobile devices is needed and a separate beam for each one. Near-field (non-radiative) schemes are already widely used (e.g. in inductive electric transformers and in optical waveguide or cavity couplers), but are so far restricted to very close-range ($D_{\text{transfer}} \ll L_{\text{device}}$) energy-transfers [96, 97, 98, 99] or mid-range ($D_{\text{transfer}} \approx \text{few} \cdot L_{\text{device}}$) and mobile but very low-power ($\sim$ mW) inefficient energy-transfers [100]. Mid-range-efficient, insensitive, mobile and versatile wireless energy-transfer has not been accomplished yet, as can be confirmed by the lack of a technology for the wireless powering of the omni-present above-mentioned autonomous electronic devices.

Many of the existing schemes (and actually the most successful) are based on the well-known principle of resonant coupling, namely the fact that two same-frequency resonant objects tend to couple, while interacting weakly with other off-resonant environmental objects. In particular, in the case of resonant 'evanescent' coupling, where the coupling mechanism is mediated through the overlap of the non-radiative near-fields of the two objects, this well-known physics leads trivially to the result that energy can be efficiently coupled between objects in the extremely near field and thus has successfully been used for close-range energy-transfer (as in the schemes described above: optical couplers and resonant magnetic induction). However, it is far from obvious how this same physics performs at mid-range distances and, again, there is, to our knowledge, no work in the literature that demonstrates efficient energy-transfer for distances a few times larger that the largest dimension of both objects involved in the transfer.

In the present work, we propose a method for wireless energy-transfer that is also based on the principle of resonant coupling, but, in contrast to the existing schemes, we identify the criterion of 'strong coupling', namely of fast coupling-rate compared to all loss-rates, as the sole crucial requirement for efficient wireless energy-transfer, and, to achieve 'strong coupling' at mid-range distances, we investigate the feasibility of using long-lived oscillatory resonant modes, with localized slowly-decaying non-radiative field patterns. The physics of 'strong coupling' is also known but in very different areas (such as those of light-matter interactions [101]) and, when applied towards this particular application of wireless mid-range energy-transfer, to our knowledge for the first time, our theoretical, numerical and experimental analyses show that, provided the exchange system is carefully designed, this favorable strongly-coupled operating regime can indeed be achieved, so efficient mid-range wireless energy-exchange is made possible.

This scheme belongs to the class of schemes utilizing the near field to mediate the coupling, and, not only does it not rely on radiation, but it actually needs it minimized to the greatest possible extent, because it adds to the system losses and could also interfere with other communication systems. Towards this goal, we show that a system based on our proposed method for wireless power can be specially tailored to additionally employ destructive interference between the far-fields of the coupled resonators, in order to suppress the total radiation and also enhance the transfer efficiency even further.

Furthermore, since our proposed method is based on very sharp resonances, the selective property of the principle of resonance basically suggests that lots of energy can be transferred between two resonant objects, while suffering only modest transfer and dissipation of energy into extraneous non-resonant or off-resonant objects. Using the near field also implies that the transmitted power is not focused into a narrow beam, as is the case for radiation, but the power density spreads out and even wraps around random objects, and therefore, compared to radiative schemes, the same power transmission can be achieved without the need for line-of-sight and with smaller local fields, which is much safer. For the aspects of safety, we will additionally discuss the benefits of magnetic resonances, which achieve the coupling via magnetic fields, to which biological organisms are, to a great extent, immune. Therefore, this method is fairly insensitive to the near-presence of random objects and, reversely, does not cause significant interference to objects in the near or far field.

Finally, the omni-directional (but stationary, non-lossy) nature of the near field and its immunity to line-of-sight interruptions make this mechanism highly suitable for mobile wireless receivers. Multiple devices can also easily be accommodated for the same reason, but an additional mechanism is required for transferring the appropriate amounts of power to each device while maintaining a good overall efficiency.

The proposed method for wireless energy-transfer could have a large variety of possible applications. It could improve existing technologies by powering remotely devices that would otherwise either rely on finite-lifetime batteries, which are often also heavy, expensive and inefficient, or that are typically powered with wires, which limit though their performance by restricting their mobility and ease of use. More excitingly, it could enable new technologies by powering devices that can only be powered wirelessly, such as those hidden, embedded or buried inside something else, and to which thus there is limited or no access for recharging or replacing the battery. The method can be implemented in both the daily macroscopic

world and in the technological microworld, it relying on very general scalable physical laws and principles. In general, this method could reduce our current dependency on batteries and lead to the realization of the concept of wireless electricity.

Chapter 8

Efficiency at mid-range transfer distances [4]

The first task of the analysis is to determine up to which distances can our proposed method of wireless energy-transfer be efficient, the primary criterion for characterizing the method's performance. What are the necessary theoretical conditions for mid-range efficiency and can these conditions be satisfied for realistic materials systems and geometries?

8.1 Efficient energy-transfer by 'strongly coupled' resonances

Physically, one can make predictions on the energy-transfer efficiency by comparing the coupling and loss time scales of the system: if little energy has been lost by the time most energy has been coupled from one object to the other, then the transfer efficiency can be expected to be high. In this section, we show that indeed such a condition of 'strong coupling' is necessary and sufficient for efficient energy-transfer.

Different temporal schemes may be employed, depending on the application, to transfer energy between two resonant objects. Here we will consider two particularly simple but important schemes: a one-time finite-amount energy-transfer scheme and a continuous finite-rate energy-transfer (power) scheme.

8.1.1 Finite-amount energy-transfer efficiency

Let the source and device objects be 1, 2 respectively and their resonance eigemodes, which we will use for the energy exchange, have angular frequencies $\omega_{1,2}$, frequency-widths due

to intrinsic (absorption, radiation etc.) losses $\Gamma_{1,2}$ and (generally) vector fields $\mathbf{F}_{1,2}(\mathbf{r})$, normalized to unity energy. Once the two resonant objects are brought in proximity, they will interact and an appropriate analytical framework for modeling this resonant interaction is that of the well-known coupled-mode theory (CMT) [11]. In this picture, the field of the system of the two resonant objects 1, 2 is approximated by $\mathbf{F}(\mathbf{r},t) = a_1(t)\mathbf{F}_1(\mathbf{r}) + a_2(t)\mathbf{F}_2(\mathbf{r})$, where the field amplitudes $a_{1,2}(t)$ are defined so that $|a_{1,2}(t)|^2$ is equal to the energy stored inside the object 1, 2 respectively. Then, using $e^{-i\omega t}$ time dependence, the field amplitudes can be shown (see [11] and Appendix) to satisfy, to lowest order:

$$\begin{aligned} \frac{d}{dt}a_1(t) &= -i(\omega_1 - i\Gamma_1)a_1(t) + i\kappa_{11}a_1(t) + i\kappa_{12}a_2(t) \\ \frac{d}{dt}a_2(t) &= -i(\omega_2 - i\Gamma_2)a_2(t) + i\kappa_{21}a_1(t) + i\kappa_{22}a_2(t), \end{aligned} \tag{8.1}$$

where $\kappa_{11,22}$ are the shifts in each object's frequency due to the presence of the other, which are a second-order correction and can be absorbed into the eigenfrequencies by setting $\omega_{1,2} \rightarrow \omega_{1,2} - \kappa_{11,22}$, and $\kappa_{12,21}$ are the coupling coefficients, which from the reciprocity requirement of the system must satisfy $\kappa_{12} = \kappa_{21} \equiv \kappa$.

The normal modes of the combined system are found, by substituting $\left[\begin{array}{cc} a_1(t), & a_2(t) \end{array}\right] = \left[\begin{array}{cc} A_1, & A_2 \end{array}\right] e^{-i\tilde{\omega}t}$, to have complex frequencies

$$\tilde{\omega}_{\pm} = \frac{\omega_1 + \omega_2}{2} - i\frac{\Gamma_1 + \Gamma_2}{2} \pm \sqrt{\left(\frac{\omega_1 - \omega_2}{2} - i\frac{\Gamma_1 - \Gamma_2}{2}\right)^2 + \kappa^2}, \tag{8.2}$$

whose splitting we denote as $\delta_{E\pm} \equiv \tilde{\omega}_+ - \tilde{\omega}_-$. (Note that, at exact resonance $\omega_1 = \omega_2$ and for $\Gamma_1 = \Gamma_2$, $\delta_{E\pm} = 2\kappa$.)

Assume now that at time $t = 0$ the source object 1 has finite energy $|a_1(0)|^2$, while the device object has $|a_2(0)|^2 = 0$. Since the objects are coupled, energy will be transferred from 1 to 2. With these initial conditions, Eqs. (8.1) can be solved, predicting the evolution of the device field-amplitude to be

$$\frac{a_2(t)}{|a_1(0)|} = \frac{2\kappa}{\delta_{E\pm}}\sin(\delta_{E\pm}t)\cdot e^{-\frac{\Gamma_1+\Gamma_2}{2}t}, \tag{8.3}$$

which, at exact resonance $\omega_1 = \omega_2$ and in the special case $\Gamma_1 = \Gamma_2 \equiv \Gamma_o$, can be written as

$$\frac{a_2(T)}{|a_1(0)|} = \sin(UT) \cdot e^{-T}, \tag{8.4}$$

where $T \equiv \Gamma_o t$ and $U \equiv \kappa/\Gamma_o$. The energy-transfer efficiency will be $\eta_E \equiv |a_2(t)|^2 / |a_1(0)|^2$.

In practice, the system designer can adjust the duration of the coupling t at will. Then, in the special case $\Gamma_1 = \Gamma_2 \equiv \Gamma_o$, it can be inferred from Eq.(8.4) that the device energy (and thus efficiency η_E) is maximized for

$$T_* = \frac{\tan^{-1}(U)}{U}, \tag{8.5}$$

resulting in an optimal energy-transfer efficiency

$$\eta_{E*} \equiv \eta_E(T_*) = \frac{U^2}{1+U^2} \exp\left(-\frac{2\tan^{-1}U}{U}\right), \tag{8.6}$$

which is only a function of the coupling-to-loss ratio $U = \kappa/\Gamma_o$ and tends to unity when $U \gg 1$, as depicted in Figure 8-1(c). In general, also for $\Gamma_1 \neq \Gamma_2$, the energy transfer is nearly perfect, when the coupling rate is much faster than all loss rates ($\kappa/\Gamma_{1,2} \gg 1$).[1]

In a real wireless energy-transfer system, there must be some generator that will supply the energy to the source object and there normally would be some load that will consume the energy from the device. To incorporate such supply and consumption mechanisms into this temporal scheme, one can imagine that the generator is very briefly but very strongly coupled to the source at time $t = 0$ to almost instantaneously provide the energy, and the load is similarly very briefly but very strongly coupled to the device at time $t = t_*$ to almost instantaneously drain the energy. For a constant powering mechnism, at time $t = t_*$ also the generator can again be coupled to the source to feed a new amount of energy, and this process can be repeated periodically with a period t_*. This scheme bears then some similarities to active 'Q-switching' in laser cavities, where the laser pulse is allowed to exit the cavity only at certain periodic instants in time, when the cavity Q is switched to a small value.

[1]The CMT model is valid exactly for this optimal operational regime of well-defined resonances. Its range of applicability does not include very-close-distance coupling, since there the necessary condition $\kappa \ll \omega_{1,2}$ does not hold, but it is suitable for the medium-distance near-field coupling of interest. thus the use of this model is justified and the parameters κ, $\Gamma_{1,2}$ are well defined.

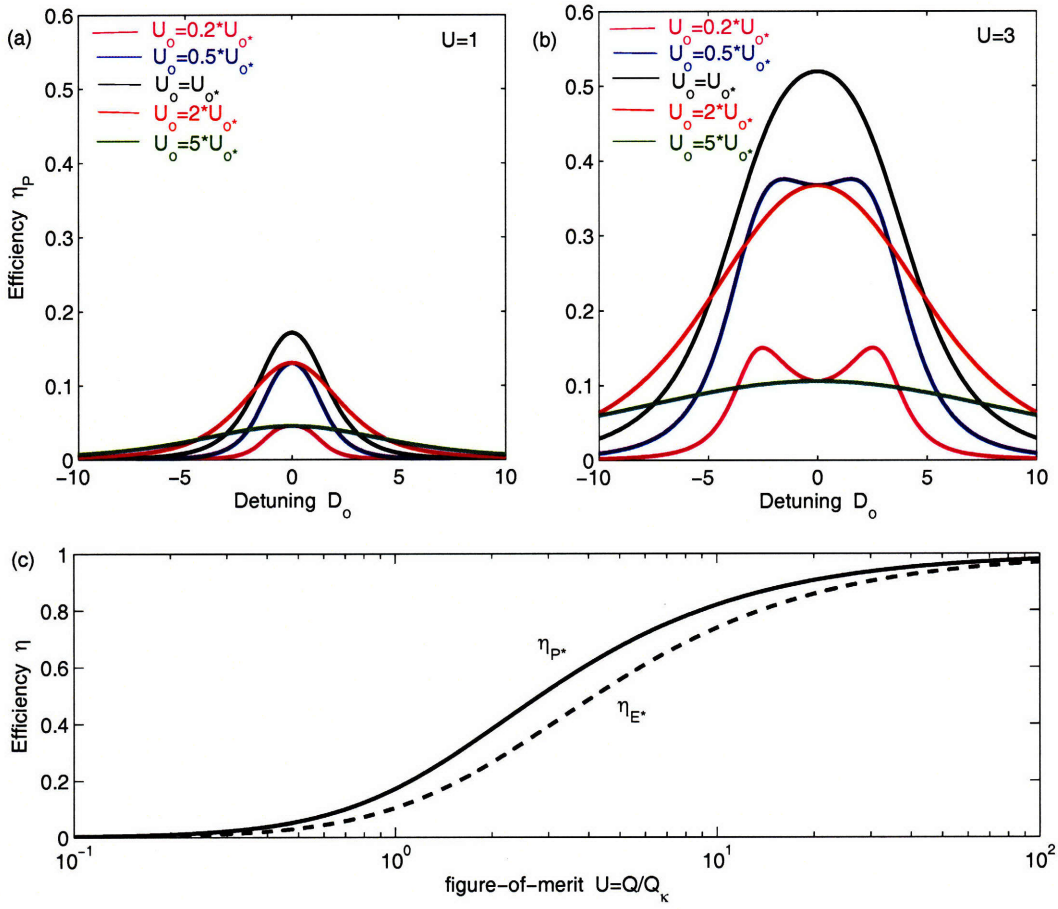


Figure 8-1: (a,b) Efficiency of power transmission η_P for (a) $U = 1$ and (b) $U = 3$, as a function of the frequency detuning D_o and for different values of the loading rate U_o. (c) Optimal (for zero detuning and under conditions of impedance matching) efficiency for energy transfer and power transmission, as a function of the coupling-to-loss figure-of-merit U.

8.1.2 Finite-rate energy-transfer (power) efficiency

Let the generator be continuously supplying energy to the source object 1 at a rate κ_1 and the load continuously draining energy from the device object 2 at a rate κ_2. Field amplitudes $s_{\pm 1,2}(t)$ are then defined, so that $|s_{\pm 1,2}(t)|^2$ is equal to the power ingoing to (+) or outgoing from (−) the object 1, 2 respectively, and the CMT equations are modified to [11]

$$\begin{aligned}
\frac{d}{dt}a_1(t) &= -i(\omega_1 - i\Gamma_1)a_1(t) + i\kappa_{11}a_1(t) + i\kappa_{12}a_2(t) - \kappa_1 a_1(t) + \sqrt{2\kappa_1}s_{+1}(t) \\
\frac{d}{dt}a_2(t) &= -i(\omega_2 - i\Gamma_2)a_2(t) + i\kappa_{21}a_1(t) + i\kappa_{22}a_2(t) - \kappa_2 a_2(t) \\
s_{-1}(t) &= \sqrt{2\kappa_1}a_1(t) - s_{+1}(t) \\
s_{-2}(t) &= \sqrt{2\kappa_2}a_2(t),
\end{aligned} \tag{8.7}$$

where again we can set $\omega_{1,2} \to \omega_{1,2} + \kappa_{11,22}$ and $\kappa_{12} = \kappa_{21} \equiv \kappa$.

Assume now that the excitation is at a fixed frequency ω, namely has the form $s_{+1}(t) = S_{+1}e^{-i\omega t}$. Then the response of the linear system will be at the same frequency, namely $a_{1,2}(t) = A_{1,2}e^{-i\omega t}$ and $s_{\pm 1,2}(t) = S_{\pm 1,2}e^{-i\omega t}$. By subsituting these into Eqs.(8.7), using $\delta_{1,2} \equiv \omega - \omega_{1,2}$, and solving the system, we find the field-amplitude transmitted to the load (S_{21} scattering-matrix element)

$$\begin{aligned}
S_{21} \equiv \frac{S_{-2}}{S_{+1}} &= \frac{2i\kappa\sqrt{\kappa_1\kappa_2}}{(\Gamma_1 + \kappa_1 - i\delta_1)(\Gamma_2 + \kappa_2 - i\delta_2) + \kappa^2} \\
&= \frac{2iU\sqrt{U_1U_2}}{(1 + U_1 - iD_1)(1 + U_2 - iD_2) + U^2}
\end{aligned} \tag{8.8}$$

and the field-amplitude reflected to the generator (S_{11} scattering-matrix element)

$$\begin{aligned}
S_{11} \equiv \frac{S_{-1}}{S_{+1}} &= -\frac{(\Gamma_1 - \kappa_1 - i\delta_1)(\Gamma_2 + \kappa_2 - i\delta_2) + \kappa^2}{(\Gamma_1 + \kappa_1 - i\delta_1)(\Gamma_2 + \kappa_2 - i\delta_2) + \kappa^2} \\
&= -\frac{(1 - U_1 - iD_1)(1 + U_2 - iD_2) + U^2}{(1 + U_1 - iD_1)(1 + U_2 - iD_2) + U^2},
\end{aligned} \tag{8.9}$$

where $D_{1,2} \equiv \delta_{1,2}/\Gamma_{1,2}$, $U_{1,2} \equiv \kappa_{1,2}/\Gamma_{1,2}$ and $U \equiv \kappa/\sqrt{\Gamma_1\Gamma_2}$. Similarly, the scattering-matrix elements S_{12}, S_{22} are given by interchanging $1 \leftrightarrow 2$ in Eqs. (8.8),(8.9) and, as expected from reciprocity, $S_{12} = S_{21}$. The coefficients for power transmission (efficiency), reflection and loss are respectively $\eta_P \equiv |S_{21}|^2 = |S_{-2}|^2 / |S_{+1}|^2$, $|S_{11}|^2 = |S_{-1}|^2 / |S_{+1}|^2$ and $1 - |S_{21}|^2 - |S_{11}|^2 = \left(2\Gamma_1 |A_1|^2 + 2\Gamma_2 |A_2|^2\right) / |S_{+1}|^2$.

In practice, the parameters $D_{1,2}$, $U_{1,2}$ can be designed (engineered), since one can adjust the resonant frequencies $\omega_{1,2}$ (compared to the desired operating frequency ω) and the generator/load supply/drain rates $\kappa_{1,2}$. Their choice will target the optimization of the system performance-characteristic of interest:

• In most cases, the goal is to maximize the power transmission (efficiency) $\eta_{\mathrm{P}} = |S_{21}|^2$ of the system, so one would require

$$\eta'_{\mathrm{P}}(D_{1,2}) = \eta'_{\mathrm{P}}(U_{1,2}) = 0. \tag{8.10}$$

Since S_{21} (from Eq. (8.8)) is symmetric upon interchanging $1 \leftrightarrow 2$, the optimal values for $D_{1,2}$ (determined by Eqs. (8.10)) will be equal, namely $D_1 = D_2 \equiv D_{\mathrm{o}}$, and similarly $U_1 = U_2 \equiv U_{\mathrm{o}}$. Then,

$$S_{21} = \frac{2iUU_{\mathrm{o}}}{(1 + U_{\mathrm{o}} - iD_{\mathrm{o}})^2 + U^2} \tag{8.11}$$

and from the condition $\eta'_{\mathrm{P}}(D_{\mathrm{o}}) = 0$ we get that, for fixed values of U and U_{o}, the efficiency is maximized for the following values of the symmetric detuning

$$D_{\mathrm{o}} = \begin{array}{ll} \pm\sqrt{U^2 - (1+U_{\mathrm{o}})^2}, & \text{if} \quad U > 1 + U_{\mathrm{o}} \\ 0, & \text{if} \quad U \leq 1 + U_{\mathrm{o}} \end{array}, \tag{8.12}$$

which, in the case $U > 1+U_{\mathrm{o}}$, can be rewritten for the two frequencies at which the efficiency peaks as

$$\omega_{\pm} = \frac{\omega_1\Gamma_2 + \omega_2\Gamma_1}{\Gamma_1 + \Gamma_2} \pm \frac{2\sqrt{\Gamma_1\Gamma_2}}{\Gamma_1 + \Gamma_2}\sqrt{\kappa^2 - (\Gamma_1 + \kappa_1)(\Gamma_2 + \kappa_2)}, \tag{8.13}$$

whose splitting we denote as $\delta_{\mathrm{P}\pm} \equiv \omega_+ - \omega_-$. (Note that, at exact resonance $\omega_1 = \omega_2 \Rightarrow \Gamma_1 = \Gamma_2 \equiv \Gamma_{\mathrm{o}} \Rightarrow \kappa_1 = \kappa_2 \equiv \kappa_{\mathrm{o}}$, $\delta_{\mathrm{P}\pm} = 2\sqrt{\kappa^2 - (\Gamma_{\mathrm{o}} + \kappa_{\mathrm{o}})^2} < \delta_{\mathrm{E}\pm}$, namely the transmission-peak splitting is smaller than the normal-mode splitting.) Then, by substituting D_{o} into η_{P} from Eq.(8.12), from the condition $\eta'_{\mathrm{P}}(U_{\mathrm{o}}) = 0$ we get that, for fixed value of U, the efficiency is maximized for

$$U_{\mathrm{o}*} = \sqrt{1 + U^2} \qquad \text{and thus from Eq.(8.12)} \qquad D_{\mathrm{o}*} = 0, \tag{8.14}$$

which is known as 'critical coupling' condition, whereas for $U_{\mathrm{o}} < U_{\mathrm{o}*}$ the system is called 'undercoupled' and for $U_{\mathrm{o}} > U_{\mathrm{o}*}$ it is called 'overcoupled'. The dependence of the efficiency

on the frequency detuning D_o for different values of U_o (including the 'critical-coupling' condition) are shown in Figure 8-1(a,b). The overall optimal power efficiency using Eqs.(8.14) is

$$\eta_{P*} \equiv \eta_P\left(D_{o*}, U_{o*}\right) = \frac{U_{o*}-1}{U_{o*}+1} = \left(\frac{U}{1+\sqrt{1+U^2}}\right)^2, \tag{8.15}$$

which is again only a function of the coupling-to-loss ratio $U = \kappa/\sqrt{\Gamma_1\Gamma_2}$ and tends to unity when $U \gg 1$, as depicted in Figure 8-1(c).

• In other cases, the goal is to minimize the power reflection at the side of the generator $|S_{11}|^2$ and the load $|S_{22}|^2$, so one would then require

$$S_{11,22} = 0 \Rightarrow \left(1 \mp U_1 - iD_1\right)\left(1 \pm U_2 - iD_2\right) + U^2 = 0, \tag{8.16}$$

known as 'impedance matching' conditions in electronics. Again, the set of these conditions is symmetric upon interchanging $1 \leftrightarrow 2$, so, by substituting $D_1 = D_2 \equiv D_o$ and $U_1 = U_2 \equiv U_o$ into Eqs.(8.16), we get

$$\left(1 - iD_o\right)^2 - U_o^2 + U^2 = 0 \tag{8.17}$$

from which we easily find that the values of D_o and U_o that cancel all reflections are again exactly those in Eqs.(8.14). It can be seen that, for this particular problem, the two goals and their associated sets of conditions (Eqs.(8.10) and Eqs.(8.16)) result in the same optimized values of the intra-source and intra-device parameters $D_{1,2}$, $U_{1,2}$. Note that for a lossless system this would be an immediate consequence of power conservation (Hermiticity of the scattering matrix), but this is not obvious for a lossy system.

The main conclusion of this section is that, for any temporal energy-transfer scheme, once the parameters specific only to the source or to the device (such as their resonant frequencies and their excitation or loading rates respectively) have been optimally designed, the efficiency is solely a function of and monotonically increases with the ratio of the source-device coupling-rate to their loss rates. Using the definition of a resonance quality factor $Q = \omega/2\Gamma$ and defining by analogy $Q_\kappa \equiv \sqrt{\omega_1\omega_2}/2\kappa$, it is therefore exactly this ratio

$$U = \frac{\kappa}{\sqrt{\Gamma_1\Gamma_2}} = \frac{\sqrt{Q_1Q_2}}{Q_\kappa} \tag{8.18}$$

that we will set as our figure-of-merit for any system under consideration for wireless energy-

transfer, along with the distance over which this ratio can be achieved (clearly, U will be a decreasing function of distance). The desired optimal regime $U > 1$ is called 'strong-coupling' regime and it is a necessary and sufficient condition for efficient energy-transfer. This concept is very general, namely any type of structure and its associated resonant field (e.g. electromagnetic, acoustic, nuclear) satisfying this requirement can be used for the implementation of such efficient energy-transfer.[2] In the following section, we show how 'strong coupling' can be accomplished for particular realistic systems at mid-range distances between two objects, proving thus that a technology for wireless energy-transfer is in fact feasible.

8.2 'Strong coupling' at mid-range distances for realistic systems

Based on the conclusions of the previous Section, our energy-transfer application requires resonant modes of high Q for low (slow) intrinsic-loss rates Γ, and this is why we propose a scheme where the coupling is implemented using the evanescent (non-lossy) stationary near-field, instead of the lossy radiative far-field, which actually needs to be minimized, and this can typically be accomplished, for resonant objects of finite size, by making their sizes subwavelength (known to result in inefficient 'antennas'). Furthermore, small Q_κ for strong (fast) coupling rate κ is required over distances larger than the characteristic sizes of the objects, and therefore, since the extent of the near-field into the air surrounding a finite-sized resonant object is typically smaller than the wavelength (and quantified rigorously by the 'radiation caustic'), this mid-range coupling can only be achieved again using resonant objects of subwavelength size and thus significantly longer evanescent field-tails. This is a regime of operation that has not been studied extensively, since one usually prefers short tails to minimize interference with nearby devices. As can be seen, subwavelength resonances are a key component of our proposed wireless energy-transfer scheme.[3] On the other hand, as the wavelength is increased compared to the size of and the distance between the objects, and the

[2] A typical example in the world of atomic optics is that of cavity Quantum Electrodynamics (QED), where low-loss atomic and photonic resonances interact strongly. [101]

[3] Note that such a resonance will typically be the appropriate choice for the possibly-mobile device-object, however, the resonant source-object will in practice often be immobile and with less stringent restrictions on its allowed geometry and size, which can be therefore chosen large enough that the near-field extent is not limited by the wavelength (using for example waveguides with guided modes tuned close to the 'light line' in air for slow exponential decay therein).

system enters deeply into the quasi-static regime, then the coupling Q_κ is typically constant for fixed object-sizes and distance (determined basically by the static fields), while often the absorption losses are increasing (Q is decreasing). Therefore, identifying the regime, where the 'strong-coupling' figure-of-merit U is maximized, is an optimization problem, in which all of the loss mechanisms must be considered and one of the most important parameters is the operational frequency. Below, we will demonstrate this optimization procedure for a few concrete systems.

As examples and for definiteness, we choose to work with electromagnetic resonant systems. In these systems, resonance occurs by a periodic conversion of the energy W stored in the system from electric to magnetic, so the electric $\mathbf{E}$ and magnetic $\mathbf{H}$ fields for a resonant eigenmode are always $\pi/2$ out of phase in time, and the frequency ω of the fields' oscillation satisfies a variational formula

$$\omega = \frac{\frac{i}{4}\int_V dv\,(\mathbf{E}^* \cdot \nabla \times \mathbf{H} - \mathbf{H}^* \cdot \nabla \times \mathbf{E})}{\frac{1}{4}\int_V dv\left(\epsilon\left|\mathbf{E}\right|^2 + \mu\left|\mathbf{H}\right|^2\right)}. \tag{8.19}$$

The loss mechanisms for an electromagnetic resonance of an open system are: radiation into free space (of impedance $\zeta_o = \sqrt{\mu_o/\epsilon_o}$ and light velocity $c_o = 1/\sqrt{\mu_o\epsilon_o}$), with a rate quantified by the far-field approximation formula [102]

$$Q_{\text{rad}}^{-1} = \frac{2\Gamma_{\text{rad}}}{\omega} = \frac{P_{\text{rad}}}{\omega W} = \frac{\frac{\zeta_o}{2}\left(\frac{\omega}{4\pi c_o}\right)^2 \oint d\Omega\left|\mathbf{f}\right|^2}{\omega\frac{1}{4}\int_V dv\left(\epsilon\left|\mathbf{E}\right|^2 + \mu\left|\mathbf{H}\right|^2\right)} \tag{8.20}$$

where $\mathbf{f} = \int_V dv\,\mathbf{J}\,(\mathbf{r})e^{-i\mathbf{k}\cdot\mathbf{r}}$ is a vector current-moment and $\mathbf{J}$ can be either dielectric-polarization currents ($\mathbf{J}_{\text{p}} = -i\omega\,(\epsilon - \epsilon_o)\,\mathbf{E}$) or electric currents on surfaces of metallic conductors ($\mathbf{J}_{\text{s}} = \hat{\mathbf{n}} \times \mathbf{H}$) [102], and absorption inside the materials [where dielectric materials are described by a complex permittivity function $\epsilon + i\epsilon''$ (and the loss-tangent is defined as $\tan\delta_\epsilon \equiv \epsilon''/\epsilon$), magnetic materials by a complex permeability function $\mu + i\mu''$ (and $\tan\delta_\mu \equiv \mu''/\mu$) and metallic materials by a complex surface impedance ζ_c (and $\zeta_c = 1/\sigma\delta_{\text{s}} = \sqrt{\omega\mu_c/2\sigma}$, where σ is the metal conductivity and δ_{s} the skin-depth at frequency ω)], with a rate quantified, provided it is weak ($\tan\delta_\epsilon$, $\tan\delta_\mu$, $\zeta_c/\zeta_o \ll 1 \Rightarrow$high-$Q_{\text{abs}}$) as is the desired

case for our application, by the perturbative formula

$$Q_{\text{abs}}^{-1} = \frac{2\Gamma_{\text{abs}}}{\omega} = \frac{P_{\text{abs}}}{\omega W} = \frac{\omega \frac{1}{2} \int_V dv \left(\epsilon'' |\mathbf{E}|^2 + \mu'' |\mathbf{H}|^2 \right) + \frac{\zeta_c}{2} \oint_S da |\mathbf{J}_s|^2}{\omega \frac{1}{4} \int_V dv \left(\epsilon |\mathbf{E}|^2 + \mu |\mathbf{H}|^2 \right)}. \tag{8.21}$$

Once two objects 1, 2 with electromagnetic resonant eigenmodes $[\mathbf{E}_{1,2}, \mathbf{H}_{1,2}]$ are brought in proximity, they will interact and the coupling coefficient can be determined from the perturbation formula [see Eq.(12.15) in Appendix]

$$\kappa = \frac{\omega_1 \frac{1}{4} \int_{V_2} dv \left(\mathbf{E}_1^* \cdot \epsilon_2 \mathbf{E}_2 + \mathbf{H}_1^* \cdot \mu_2 \mathbf{H}_2 \right) + \frac{i}{4} \oint_{S_2} da \mathbf{E}_1^* \cdot \mathbf{J}_{s,2}}{\frac{1}{4} \int_V dv \left(\epsilon |\mathbf{E}_1|^2 + \mu |\mathbf{H}_1|^2 \right)} = (1 \leftrightarrow 2) \tag{8.22}$$

where $\epsilon_{1,2}$, $\mu_{1,2}$ are the dielectric, magnetic functions of space that describe only the object $1, 2$ (minus the constant ϵ_o, μ_o background) and $\epsilon = \epsilon_o + \epsilon_1 + \epsilon_2$, $\mu = \mu_o + \mu_1 + \mu_2$ the dielectric, magnetic function of the whole system.

Among the large variety of electromagnetic resonances, we will study two well-known but quite different material systems: dielectric resonators (in the form of two-dimensional disks) and metallic resonators (capacitively-loaded conducting loops, inductively-loaded conducting rods and self-resonant conductive coils). We compute the required CMT parameters $\omega_{1,2}$, $\Gamma_{1,2}$, $\kappa_{11,12,21,22}$ using several independent methods and we show how to obtain for these particular systems the largest possible 'strong-coupling' figure-of-merit U. Despite the simplicity of these systems, all will be found to exhibit acceptably good performance.

8.2.1 Dielectric resonators

8.2.1.1 Dielectric disks

Consider a two-dimensional (2d) dielectric disk object, as shown in Figure 8-2, of radius r and relative permittivity ϵ surrounded by air, that supports 'whispering-gallery' resonant modes. The loss mechanisms for the energy stored inside such a resonant system are radiation into free space and absorption inside the dielectric. Long-tailed subwavelength (and thus high-Q_{rad} from Eq.(8.20)) resonances can be achieved, when the dielectric permittivity ϵ is large and the azimuthal field variations are slow (namely of small principal number m). On the other hand, the loss-tangent is unfortunately typically larger for materials with larger ϵ (and thus Q_{abs} is smaller from Eq.(8.21)). Therefore, how large a total-Q can be achieved

for these systems depends on the availability of dielectric materials with large dielectric constant but small loss tangent. Thankfully, not only are there in the microwave regime (appropriate for approximately meter-range coupling applications) many materials that have these great dielectric properties (e.g. Titania: $\epsilon \approx 96$, $\tan\delta \approx 10^{-3}$; Barium tetratitanate: $\epsilon \approx 37$, $\tan\delta \approx 10^{-4}$; Lithium tantalite: $\epsilon \approx 40$, $\tan\delta \approx 10^{-4}$ etc. [103, 104]), but also $\sqrt{\epsilon}$ could signify instead the effective index of other known subwavelength surface-wave systems, such as photonic modes on surfaces of metallic materials or plasmonic (metal-like, negative-ϵ) materials [17, 18] or metallo-dielectric photonic crystals (SMDPC) [10] or plasmono-dielectric photonic crystals (SPDPC) [65]. In our calculations, we used the arbitrary formula $\tan\delta = 6 \cdot 10^{-6}\epsilon - 2 \cdot 10^{-4}$ for $\epsilon > 35$, which shows the general tendency of the dielectric properties of typical microwave materials and approximately matches some of them, and thus will serve well for a realistic estimation of the achievable performance and will demonstrate the optimization method for this system. To calculate the resonance properties (ω, Q, [$\mathbf{E}$, $\mathbf{H}$]) for this type of disks, two independent methods were employed: numerically, 2d finite-element frequency-domain (FEFD) mode-solving simulations (which solve Maxwell's Equations in frequency domain exactly apart for spatial discretization) were performed [87]; analytically, standard separation of variables (SV) in polar coordinates was used; in both cases, the contributions of absorption and radiation to the losses were separated by turning material losses off to determine Q_{rad} so then $Q_{\text{abs}}^{-1} = Q^{-1} - Q_{\text{rad}}^{-1}$. The results for a dielectric disk with TE-polarized subwavelength modes of $\lambda/r \geq 7$ for three values of m are presented in Figure 8-3. The two methods have excellent agreement and imply that, for a high-ϵ low-$\tan\delta$ dielectric object, the total Q of its resonant modes is maximized at a frequency ω_*, where absorption and radiation losses are balanced and which can be subwavelength as m decreases, while still values of $Q_{\text{rad}} > 1000$ and $Q_{\text{abs}} > 1000$ are achievable. The values for the modes close to this ω_*-peak, for $m = 2$ and $m = 3$, are also shown in Table 8.1.[4]

Consider now two disks 1 and 2 placed at distance D between their centers, as shown in Figure 8-4. To calculate the rate (κ) of energy-transfer between the two disks: numerically, the FEFD mode-solver simulations find the normal modes of the combined system (which are even and odd superpositions of the initial single-disk modes), and then κ can be calculated

[4]Note that for the 3d case the computational complexity would be immensely increased, while the physics would not be significantly different. For example, a spherical object of $\epsilon = 147.7$ has a 'whispering-gallery' mode with $m = 2$, $Q_{\text{rad}} = 13962$, and $\lambda/r = 17$.

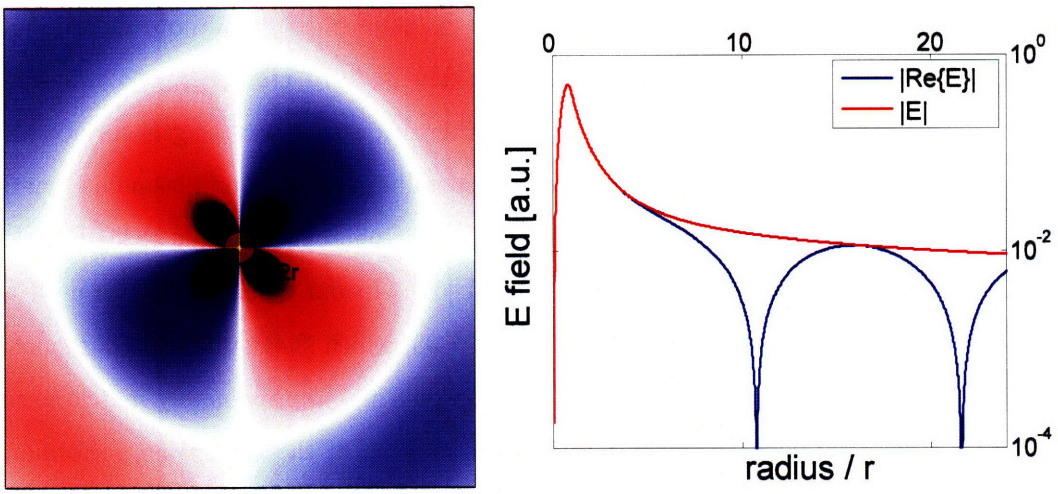


Figure 8-2: *Main plot.* A 2d high-ϵ disk of radius r (shown in yellow) surrounded by air, along with the electric field (with polarization pointing out of the page, from FEFD simulation) of its resonant 'whispering-gallery' mode superimposed (shown in red/white/blue in regions of positive/zero/negative field respectively). *Side plot.* Radial plot of the electric field of the mode shown in the main plot (basically a cross-section of the main plot). Note that in air (radius/$r > 1$) the field follows a Hankel-function form, with an initial exponential-like regime (with long tails compared to the small disk size), followed by the oscillatory/radiation regime (whose presence means that energy is slowly leaking out of the disk).

disk	λ/r	Q_{abs}	Q_{rad}	Q
ϵ=147.7, m = 2	**20.00 (20.00)**	**1468 (1466)**	**1992 (1995)**	**845 (845)**
$\epsilon = 66.3$, $m = 3$	10.00 (10.00)	5098 (5100)	9454 (9455)	3312 (3313)

Table 8.1: Analytical SV and (in parentheses) numerical FEFD results for two of the modes shown in Figure 8-3, close to the frequencies where Q respectively peaks for each m. (The specific disk-mode highlighted with **bold** in the table corresponds to the one plotted in Figure 8-2.)

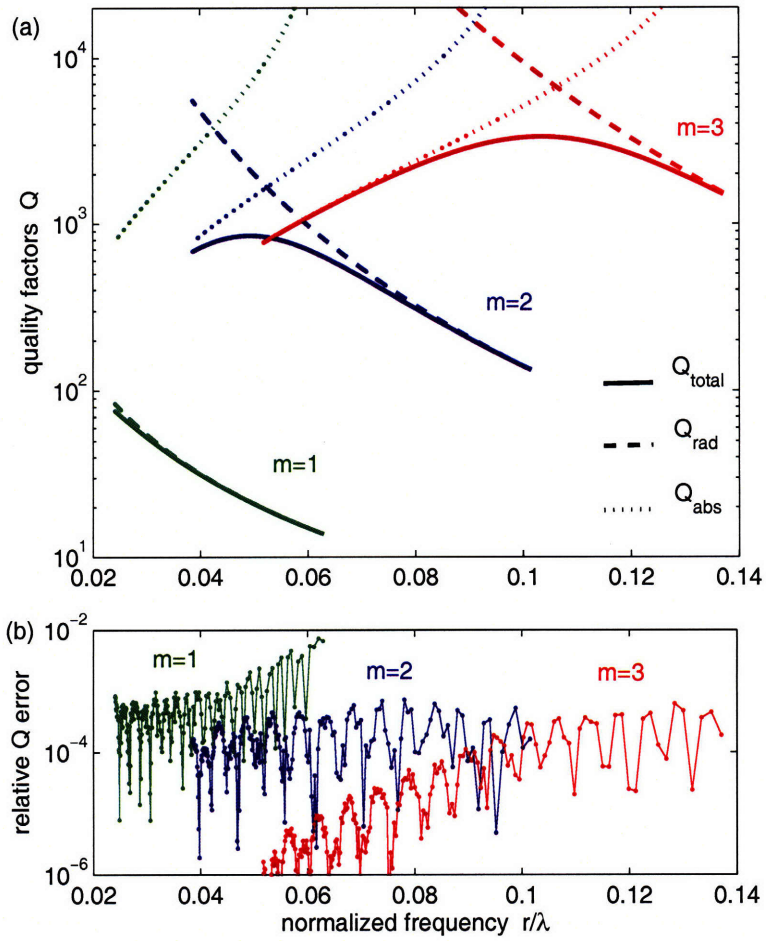


Figure 8-3: (a) Analytical SV results for the wavelength and absorption, radiation and total loss rates Q, for three different m values of subwavelength resonant modes of a dielectric disk, when varying its ϵ in the range $250 \geq \epsilon \geq 35$. Note that disk-material loss-tangent $\tan\delta = 6{\cdot}10^{-6}\epsilon - 2{\cdot}10^{-4}$ was used. (b) Relative Q error between analytical SV and numerical FEFD calculations of part (a).

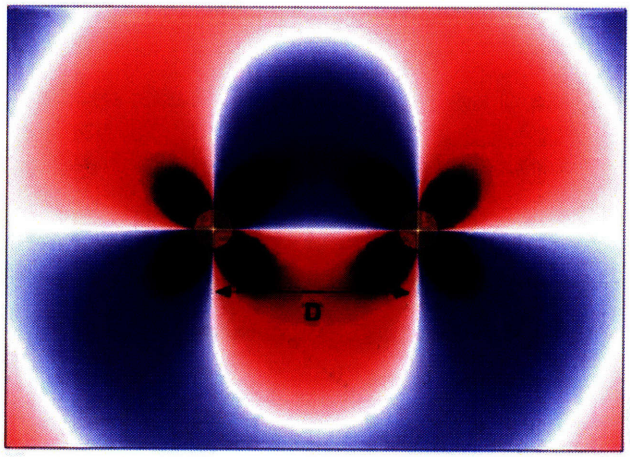


Figure 8-4: System of two same 2d high-ϵ disks of radius r for medium-distance D coupling between them, along with the electric field (from FEFD simulation) of the normal mode, which is an even superposition of the single-disk modes of Figure 8-2, superimposed. Note that there is also a normal mode (not shown), which is an odd superposition of the single-disk modes of Figure 8-2.

by their frequency splitting $\delta_{E\pm}$ and Eq.(8.2); analytically, using the expressions for the SV eigenfields $[\mathbf{E}, \mathbf{H}]_{1,2}$, κ can be calculated by the CMT formula Eq.(8.22). The results for coupling two same disks from those in Figure 8-3 are presented in Figure 8-5 as a function of frequency (due to varying ϵ) at a few fixed distances. The two methods agree well and suggest that: First of all, the performance (U) improves as the dielectric constant increases, for smaller m, and as we move further into the subwavelength regime, because the coupling gets stronger, with ultimate limit the availability of high-ϵ materials. Furthermore, when the distances start falling inside the radiative regime, there are frequencies for which the (already weak) coupling has nulls, however, for non-radiative coupling such that $D < 2r_C$ (where r_C is the radius of the radiation caustic), the coupling is not a strong function of frequency, namely the field is mostly quasi-static, and thus the coupling-to-loss figure-of-merit U peaks at approximately the same frequency as Q peaks, independently of the mid-range distance D. Using then the modes of Table 8.1, close to which the Q peaks for each m, we also plot the coupling as a function of the distance, in Figure 8-6. We find that, for medium-range distances, $U \sim 1 - 40$ is achievable, which is large enough to be useful for typical applications.

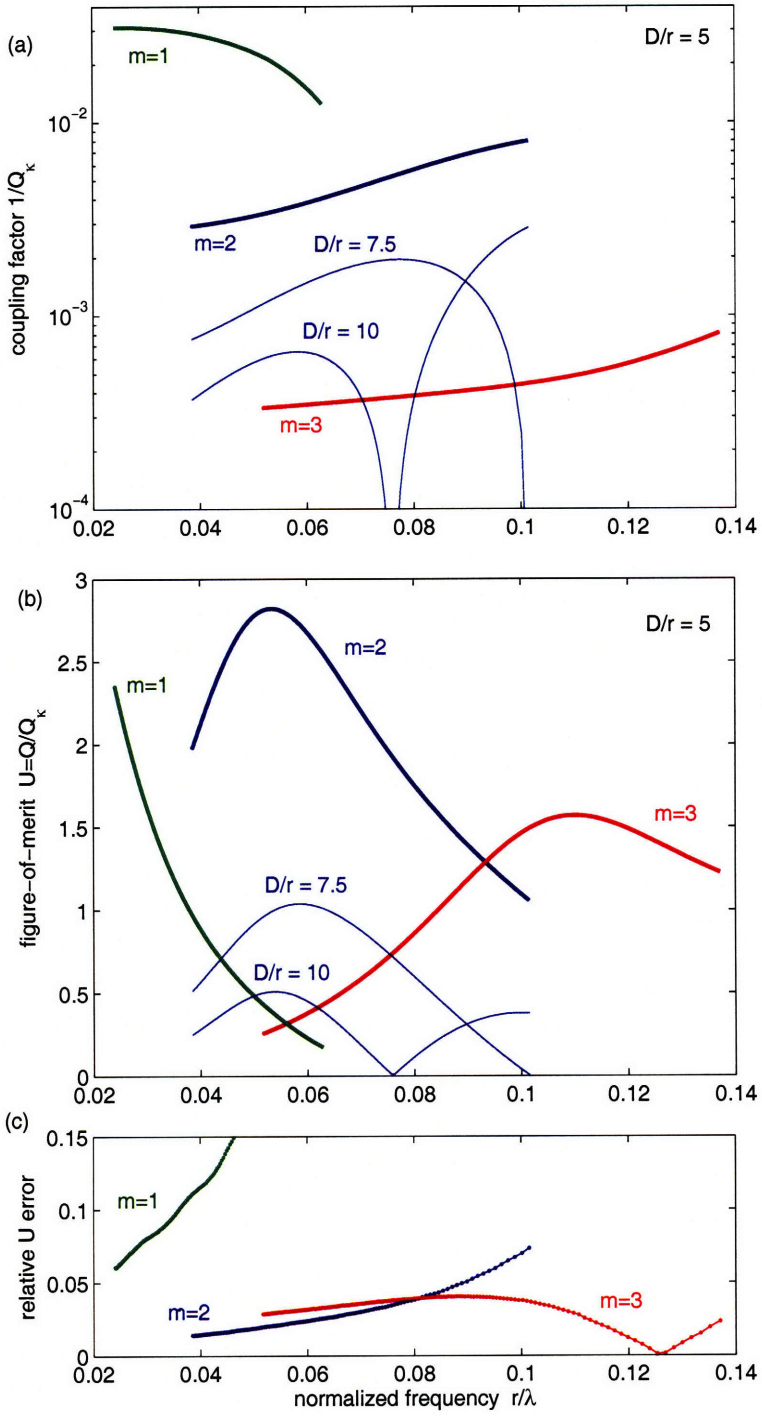


Figure 8-5: CMT results for (a) the coupling rate Q_κ and (b) the coupling-to-loss figure-of-merit U, for three different m values of subwavelength resonant modes of two same dielectric disks at distance $D/r = 5$ (and also a couple more distances for $m = 2$), when varying their ϵ in the range $250 \geq \epsilon \geq 35$. (c) Relative U error between CMT and numerical FEFD calculations of part (b).

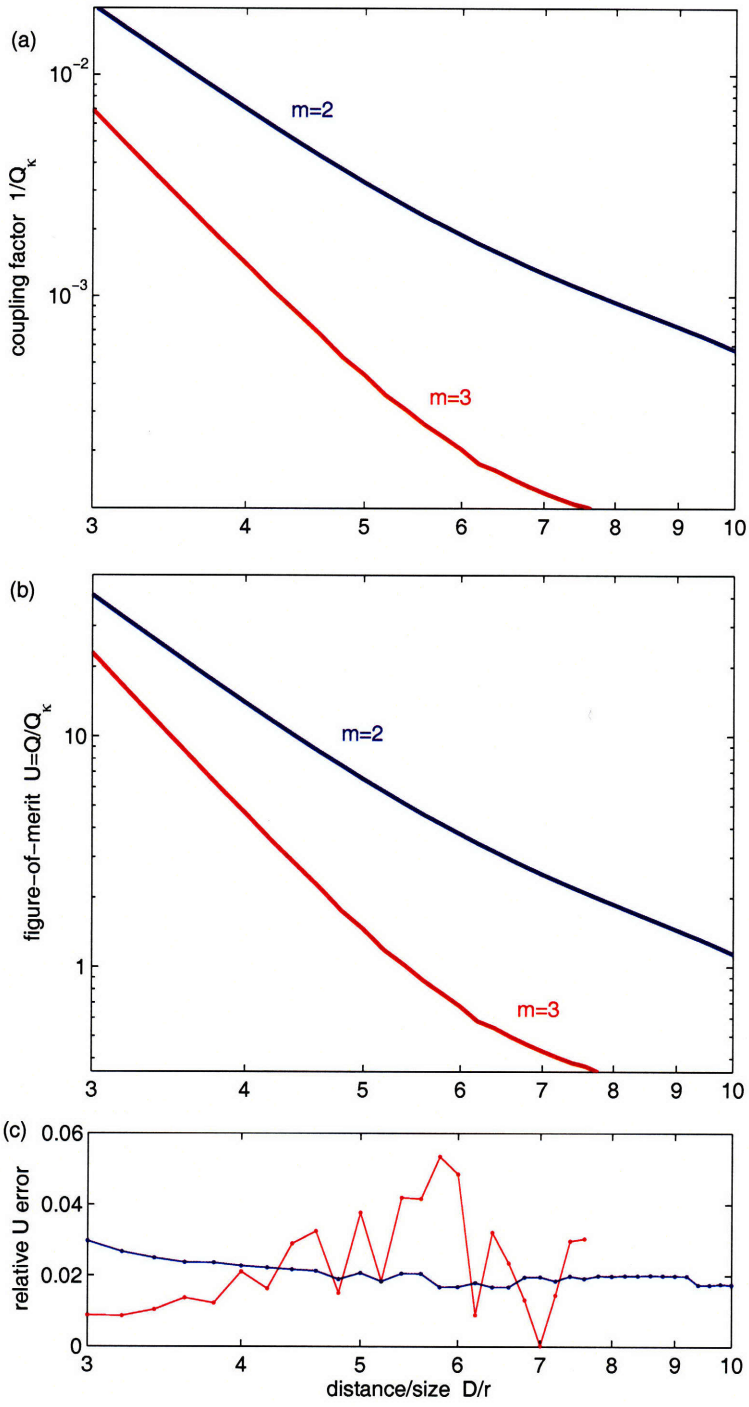


Figure 8-6: CMT results for (a) the coupling rate Q_κ and (b) the coupling-to-loss figure-of-merit U, for the two subwavelength resonant modes shown in Table 8.1 of two same dielectric disks, as a function of their distance D. (c) Relative U error between CMT and numerical FEFD calculations of part (b).

8.2.2 Metallic resonators

Consider a connected metallic structure, which supports a resonant electromagnetic mode of angular frequency ω. In this case, the periodic conversion of energy between electric and magnetic fields, discussed earlier, can be attributed respectively to the surface-charge distribution ρ_s across the structure (which defines then a distributed capacitance throughout) and to the surface-current distribution $\mathbf{J}_s$ across the structure (which similarly defines a distributed inductance). This periodic energy-exchange is accompanied by a $\pi/2$ temporal phase-shift between ρ_s and $\mathbf{J}_s$, in analogy to that between $\mathbf{E}$ and $\mathbf{H}$, namely the energy W contained in the structure is at certain points in time completely due to the charge and at other points in time completely due to the current. In particular, for the subwavelength (but not too much) resonances of current interest (typically the fundamental resonant mode), the charge and current distributions will still be localized on the surface of the metal (within a few skin-depths) but will not vary a lot, rather there will be a positive charge distribution in one part of the structure and a negative on the other part (of equal total amounts to make the object neutral). Then, the charge-conservation equation

$$\nabla \cdot \mathbf{J}_s = i\omega\rho_s \tag{8.23}$$

implies that, if q_o is the maximum amount of the total-charge magnitude accumulated in one side of the capacitance and I_o is the maximum value of the linear-current magnitude crossing any cross-section of the inductance, then $I_o = \omega q_o$. Then, since for these subwavelength resonances, the system operates in the quasi-static regime, one can *define* an effective total capacitance C and an effective total inductance L of the structure through the amount of maximum quasi-static electric and magnetic energy W inside its resonant mode [105]:

$$\frac{1}{C} \equiv \frac{2W}{q_o^2} = \frac{1}{4\pi\epsilon_o q_o^2} \oint_S \oint_S d\mathbf{r}_s d\mathbf{r}'_s \frac{\rho_s^*(\mathbf{r}_s)\,\rho_s(\mathbf{r}'_s)}{|\mathbf{r}_s - \mathbf{r}'_s|}, \tag{8.24}$$

$$L \equiv \frac{2W}{I_o^2} = \frac{\mu_o}{4\pi I_o^2} \oint_S \oint_S d\mathbf{r}_s d\mathbf{r}'_s \frac{\mathbf{J}_s^*(\mathbf{r}_s)\cdot\mathbf{J}_s(\mathbf{r}'_s)}{|\mathbf{r}_s - \mathbf{r}'_s|}. \tag{8.25}$$

With these definitions, the resonant angular frequency and the effective impedance are given by the common formulas $\omega = 1/\sqrt{LC}$ and $Z = \sqrt{L/C}$ respectively. Losses in this resonant system consist of radiative loss into free space and ohmic (material absorption)

loss inside the wire. One can again *define* a total radiation resistance from the amount of power radiated due to the dominant electric-dipole ($\mathbf{p} = \oint_S da \mathbf{r}_s \rho_s$) and magnetic-dipole ($\mathbf{m} = \frac{1}{2}\oint_S da \mathbf{r}_s \times \mathbf{J}_s$) radiation-terms [105] in Eq.(8.20)

$$R_{\rm rad} \equiv \frac{2P_{\rm rad}}{I_o^2} = \frac{\zeta_o}{6\pi}\left[\left(\frac{\omega\left|\mathbf{p}\right|}{c_o q_o}\right)^2 + \left(\frac{\omega}{c_o}\sqrt{\frac{\left|\mathbf{m}\right|}{I_o}}\right)^4\right] \tag{8.26}$$

and a total absorption resistance from the amount of power absorbed inside the wire from Eq.(8.21)

$$R_{\rm abs} \equiv \frac{2P_{\rm rad}}{I_o^2} = \zeta_c \frac{\oint_S da \left|\mathbf{J}_s\right|^2}{I_o^2}. \tag{8.27}$$

With these definitions, the absorption and radiation quality factors of the resonance are given by the common formulas $Q_{\rm rad} = \omega L/R_{\rm rad}$ and $Q_{\rm abs} = \omega L/R_{\rm abs}$ respectively.

Consider now two metallic structures 1 and 2, placed at a distance D between their (e.g. geometric) centers. The electric and magnetic fields are used to couple the resonances of the two resonant conducting structures. Denoting the surface-charge and surface-current distributions of two structures respectively as $\rho_{s1,2}$ and $\mathbf{J}_{s1,2}$, the total peak magnitude charges and currents respectively as $q_{1,2}$ and $I_{1,2}$, and defining, in the same way to the single-object case, capacitances and inductances respectively as $C_{1,2}^{-1} \equiv 2W_{1,2}/q_{1,2}^2$ and $L_{1,2} \equiv 2W_{1,2}/I_{1,2}^2$, we can again *define* the two objects' mutual capacitance M_C and inductance M_L through the total system energy W [105]:

$$W \equiv W_1 + W_2 + \frac{1}{2}\left(q_1^* q_2 + q_1 q_2^*\right)\frac{1}{M_C} + \frac{1}{2}\left(I_1^* I_2 + I_1 I_2^*\right)M_L \Rightarrow$$

$$\frac{1}{M_C} = \frac{1}{4\pi\epsilon_o q_1 q_2}\oint_{S_1}\oint_{S_2} d\mathbf{r}_s d\mathbf{r}_s' \frac{\rho_{s1}^*\left(\mathbf{r}_s\right)\rho_{s2}\left(\mathbf{r}_s'\right)}{\left|\mathbf{r}_s - \mathbf{r}_s'\right|} e^{\frac{i\omega\left|\mathbf{r}_s - \mathbf{r}_s'\right|}{c_o}}, \tag{8.28}$$

$$M_L = \frac{\mu_o}{4\pi I_1 I_2}\oint_{S_1}\oint_{S_2} d\mathbf{r}_s d\mathbf{r}_s' \frac{\mathbf{J}_{s1}^*\left(\mathbf{r}_s\right)\cdot\mathbf{J}_{s2}\left(\mathbf{r}_s'\right)}{\left|\mathbf{r}_s - \mathbf{r}_s'\right|} e^{\frac{i\omega\left|\mathbf{r}_s - \mathbf{r}_s'\right|}{c_o}}. \tag{8.29}$$

and the retardation factor inside the integral can been ignored in the quasi-static regime $D \ll \lambda$ of interest, where each coil is within the near field of the other. With this definition and from Eq.(8.22), the coupling coefficient is given by $Q_\kappa^{-1} = 2\kappa/\sqrt{\omega_1\omega_2} = \left(\sqrt{C_1 C_2}/M_C\right)^{-1} + \left(M_L/\sqrt{L_1 L_2}\right)^{-1}$, and it depends on the frequency only weakly ($\sim \omega D/c_o$), which means that our targeted 'strong-coupling' figure-of-merit U is approximately maximized at the frequency

where $\sqrt{Q_1 Q_2}$ is maximized for these types of metallic quasi-static resonant structures.

From Eqs.(8.23)-(8.29), it follows that to determine the resonance and coupling parameters one simply needs to know the current distributions $\mathbf{J}_s(\mathbf{r}_s)$ in the resonant metallic structures. Solving Maxwell's equations to rigorously find the current distribution of a resonant electromagnetic eigenmode of an arbitrary conducting structure is typically involved, making an exact solution difficult. Here, we will treat only simple structures, where a reasonable guess for the current-distribution can be made: capacitively-loaded conducting loops, inductively-loaded conducting rods and self-resonance conducting coils.

8.2.2.1 Capacitively-loaded conducting loops

Consider a loop of radius r with N turns of conducting wire with circular cross-section of radius a, connected to a pair of conducting parallel plates of area A spaced by distance d via a dielectric material of relative permittivity ϵ, and everything is surrounded by air (as shown in Figure 8-7 for $N = 1$). The loop has inductance L and some self-capacitance C_s and the plates have capacitance C_p, which is added to C_s in parallel, so the loop is resonant at $\omega = 1/\sqrt{L(C_p + C_s)}$. We will examine the simple case $C_p \gg C_s$ (true for $N = 1$ or when the different turns are substantially spaced from each other), which implies we can safely predict that physically all the charge (and thus most of the electric energy) is on the plates of the loading capacitor and thus, from charge conservation, the current distribution is constant along the wire ($|\mathbf{J}_s| = I_o \cdot 2\pi a$). This assumption allows us now to compute analytically from Eq.(8.25) the inductance $L = \mu_o r \left[\ln(8r/a) - 2\right] N^2$ [106, 107] and with the simple capacitance formula $C_p = \epsilon_o A/d$, we have $\omega = 1/\sqrt{LC_p}$. Furthermore, analytical formulas are again available for $\mathbf{p} = 0$ and $|\mathbf{m}| = I_o \pi r^2$ (namely only the magnetic-dipole term is contributing to radiation), so from Eq.(8.26) we have $R_{rad} = \zeta_o 8\pi^5/3 \cdot (r/\lambda)^4 N^2$, and finally from Eq.(8.27) $R_{abs} = \zeta_c (r/a) N^2$, so $Q_{rad} = \omega L/R_{rad} \propto 1/\omega^3$ and $Q_{abs} = \omega L/R_{abs} \propto \sqrt{\omega}$. The external loading capacitance provides the freedom to tune the resonant frequency (for example by tuning A or d), so the calculated Q-factors suggest that the total-Q becomes highest at the optimal frequency

$$\omega_* = \left(\frac{c_o^4}{\pi \zeta_o} \frac{\sqrt{\mu_c/2\sigma}}{aNr^3} \right)^{\frac{2}{7}} \tag{8.30}$$

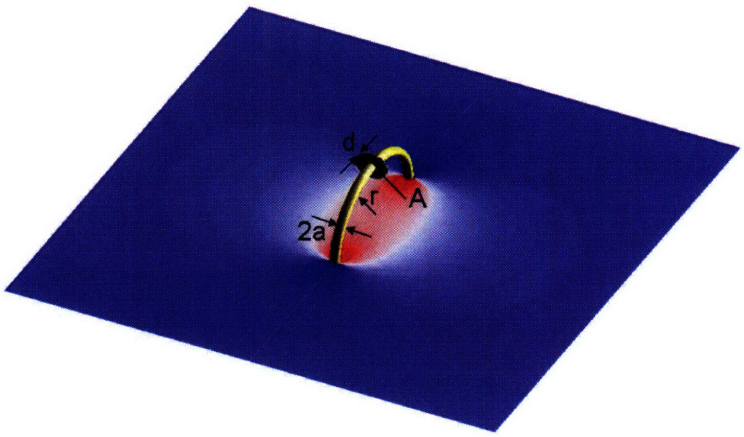


Figure 8-7: A conducting loop of radius r, connected to a pair of d-spaced parallel plates surrounded by air, along with a slice of the magnetic field (component parallel to the axis of the circular loop, from FEFD simulation) of their resonant mode superimposed.

reaching the value

$$Q_* = \frac{6}{7\pi}\left(2\pi^2\zeta_o\frac{\sigma a^2 N^2}{r}\right)^{\frac{3}{7}} \cdot \left(\ln\frac{8r}{a} - 2\right). \tag{8.31}$$

At lower frequencies it is dominated by ohmic loss and at higher frequencies by radiation. Note again, that the formulas above are accurate as long as $C_p \gg C_s$, so, to confirm the validity of our constant-current assumption and the resulting analytical formulas, mode-solving calculations were also performed using another completely independent, computational method: 3d finite-element frequency-domain (FEFD) simulations were conducted, in which the boundaries of the conductor were modeled using a complex-impedance ζ_c boundary condition, valid as long as $\zeta_c/\zeta_o \ll 1$ [105] ($< 10^{-5}$ for copper in the microwave). The results of the above analysis for three $N = 1$ loops with subwavelength modes of $\lambda/r \geq 20$ (namely highly suitable for near-field coupling and well within the quasi-static limit) are presented in Figure 8-8. The two methods (analytical and computational) are in very good agreement and show that, in typical cases of daily-sized objects, the optimal frequency ω_* is in the low-MHz microwave range and the expected quality factors are $Q_{\text{rad}} > 1000$ and $Q_{\text{abs}} > 1000$. The values for the modes at the peak of Q for these three objects are also shown in Table 8.2.

Two capacitively-loaded loops 1 and 2, at distance D between their centers, are coupled only via the magnetic field (the electric field is almost entirely stored inside the capacitor) and, for the rate of energy-transfer between them, the mutual inductance M_L can

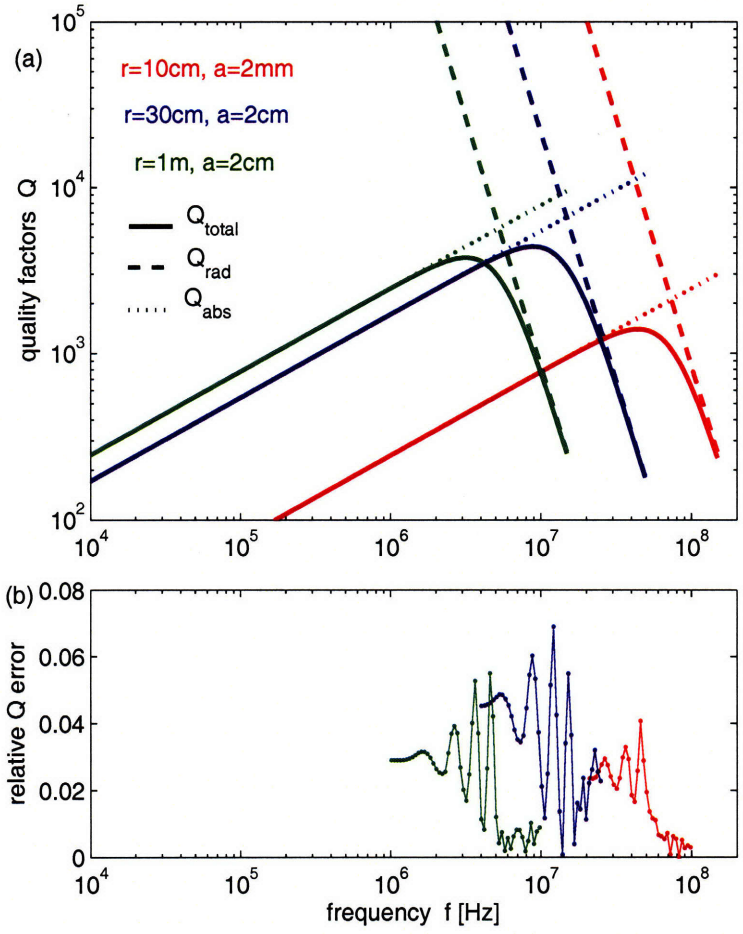


Figure 8-8: (a) Analytical Circuit-theory (CT) results for the frequency and absorption, radiation and total loss rates Q, for the subwavelength modes of three different loops, when varying their loading capacitance. Note that for conducting material copper ($\sigma = 5.998107\text{S/m}$) was used. (b) Relative Q error between the analytical CT and numerical FEFD calculations of part (a).

loop	f [MHz]	Q_{abs}	Q_{rad}	Q
$r = 1\text{m}$, $a = 2\text{cm}$ $\epsilon = 10$, $A = 571\text{cm}^2$, $d = 1\text{cm}$	3.16 (3.18)	4378 (4251)	25918 (27569)	3745 (3683)
$\mathbf{r = 30\text{cm}}$, $\mathbf{a = 2\text{cm}}$ $\boldsymbol{\epsilon = 10}$, $\mathbf{A = 138\text{cm}^2}$, $\mathbf{d = 4\text{mm}}$	**8.89 (8.95)**	**5132 (4896)**	**29956 (25911)**	**4382 (4118)**
$r = 10\text{cm}$, $a = 2\text{mm}$ $\epsilon = 10$, $A = \pi\text{cm}^2$, $d = 1\text{mm}$	42.64 (42.73)	1606 (1567)	10637 (10728)	1395 (1367)

Table 8.2: Analytical CT and (in parentheses) numerical FEFD results for the modes of the three loops shown in Figure 8-8, close to the frequencies where Q respectively peaks. (The specific loop-mode highlighted with **bold** in the table corresponds to the one plotted in Figure 8-2.)

be evaluated numerically from Eq.(8.29) by assuming again constant current-distributions in the case $C_{\text{p1,2}} \gg C_{\text{s1,2}}$. In the quasi-static limit $r \ll D \ll \lambda$ and for the relative optimal orientation shown in Figure 8-9, an approximate analytical formula gives $M_L \approx \mu_o \pi/2 \cdot (r_1 r_2)^2 \,/\, \left(\sqrt{D^2 + r_1^2 + r_2^2}\right)^3 \cdot N_1 N_2 e^{i\omega D/c_o} \approx \mu_o \pi/2 \cdot (r_1 r_2)^2 \,/ D^3 \cdot N_1 N_2$ [105], which means that the coupling factor

$$Q_\kappa \approx \frac{2}{\pi}\left(\frac{D}{\sqrt{r_1 r_2}}\right)^3 \sqrt{\left(\ln\frac{8r_1}{a_1} - 2\right)\left(\ln\frac{8r_2}{a_2} - 2\right)} \tag{8.32}$$

is independent of the number of turns N_1, N_2 and, in this subwavelength limit, the frequency ω, and depends mainly on the $D/\sqrt{r_1 r_2}$ form-factor, where the cubic scaling comes naturally from the cubic dependence of the static near magnetic field generated by a conducting loop.[5] Consequently, the optimal frequency, where the figure-of-merit $U = \sqrt{Q_1 Q_2}/Q_\kappa$ is maximized, is that where $\sqrt{Q_1 Q_2}$ is maximized (given by ω_* of Eq.(8.30) for same loops or lying between ω_{1*} and ω_{2*} for dissimilar loops), and is thus independent of the distance between the two loops, a very useful feature in practice for mobile-object applications. The resulting optimal figure-of-merit is, in the case of same loops,

$$U_* \approx \frac{3}{7}\left(2\pi^2 \zeta_o \frac{\sigma a^2 N^2}{r}\right)^{\frac{3}{7}} \left(\frac{r}{D}\right)^3 \tag{8.33}$$

and suggests that, for a given D/r form-factor, optimizing the energy-transfer efficiency

[5] For a square loop of side $2r$ the analytical formulas, for comparison, are $L = \mu_o 4r/\pi \cdot [\ln(r/a) - 0.08]\, N^2$, $M_L \approx \mu_o 8/\pi \cdot (r_1 r_2)^2 / D^3 \cdot N_1 N_2$ and thus $Q_\kappa \approx 1/2 \cdot (D/\sqrt{r_1 r_2})^3 \cdot \sqrt{[\ln(r_1/a_1) - 0.08]\,[\ln(r_2/a_2) - 0.08]}$, which is slightly better (by $\sim 4/\pi$) than a circular loop, basically due to the increased area crossed by the magnetic flux.

essentially means maximizing Q by:

• increasing the conductivity σ of the conducting material, namely by using good conductors (such as copper or silver) and/or lowering the temperature; at very low temperatures one could use also superconducting materials to achieve extremely good performance.

• increasing the wire radius a, which mainly again helps to reduce the resistive losses in the wire by increasing the cross-sectional area through which the electric current is flowing, so one could alternatively use also a Litz wire or a ribbon instead of a circular wire.

• increasing the number of turns N, which however has an upper limit due to the resulting increased voltage across the capacitor. (Note that Eqs.(8.31) and (8.33) are expected to be accurate only provided the turns are spaced enough from each other so that the assumption $C_{\rm p} \gg C_{\rm s}$ is satisfied, but they qualitatively still provide a good indication that we expect an improvement in the coupling-to-loss ratio with increased N.)

The results of the analytical method, where the integral of Eq.(8.29) was evaluated numerically assuming a constant-current distribution instead of using the approximate analytical formulas, are plotted in Figure 8-10, for the coupling of the loops in Table 8.2 at ω_* as a function of the loops distance. For medium distances the expected coupling-to-loss ratios are in the range $U \sim 1 - 100$, scaling clearly as $(r/D)^3$.

Finally, it is also important to appreciate the difference between the above described resonant-coupling inductive scheme and the well-known non-resonant inductive scheme for energy transfer. Using CMT it is easy to show that, keeping the geometry and the energy stored at the source fixed, the resonant inductive mechanism allows for $\sim Q^2$ ($\sim 10^6$) times more power delivered for work to the load than the traditional non-resonant mechanism. This is why only close-range contact-less medium-power ($\sim W$) transfer is possible with the latter [96, 97], while with resonance either close-range but large-power ($\sim kW$) transfer is allowed [98, 99] or medium-range but small-power ($\sim$ mW) [100] or, as currently proposed, if one also ensures operation in the strongly-coupled regime, medium-range and medium-power transfer is possible. Capacitively-loaded conducting loops are currently used as resonant antennas (for example in cell phones), but those operate in the far-field regime with $D/r \gg 1$, $r/\lambda \sim 1$, and the radiation-Q's are intentionally designed to be small to make the antennas efficient, so they are not appropriate for energy transfer.

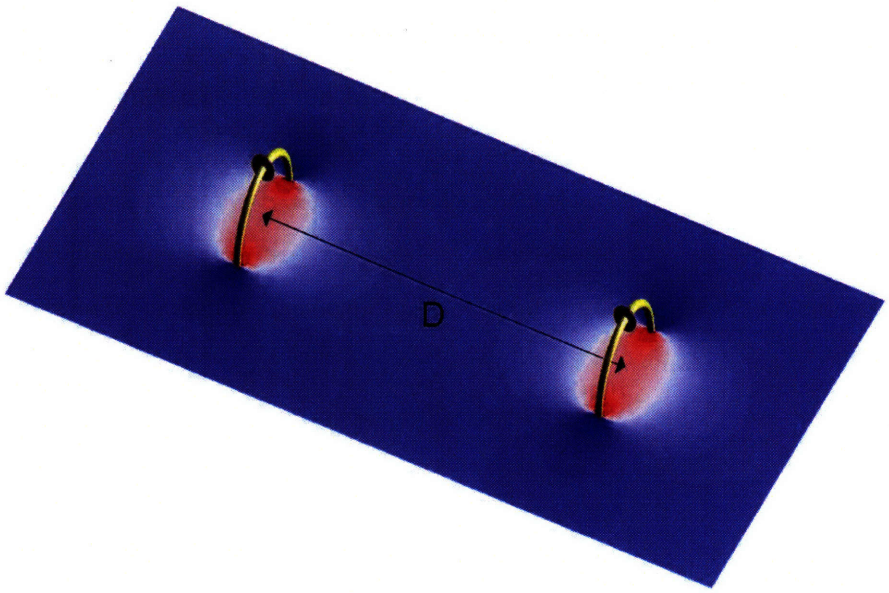


Figure 8-9: System of two same conducting loops, connected to parallel plates for medium-distance D coupling between them, along with a slice of the magnetic field (from FEFD simulation) of the even normal mode superimposed. Note that there is also an odd normal mode (not shown).

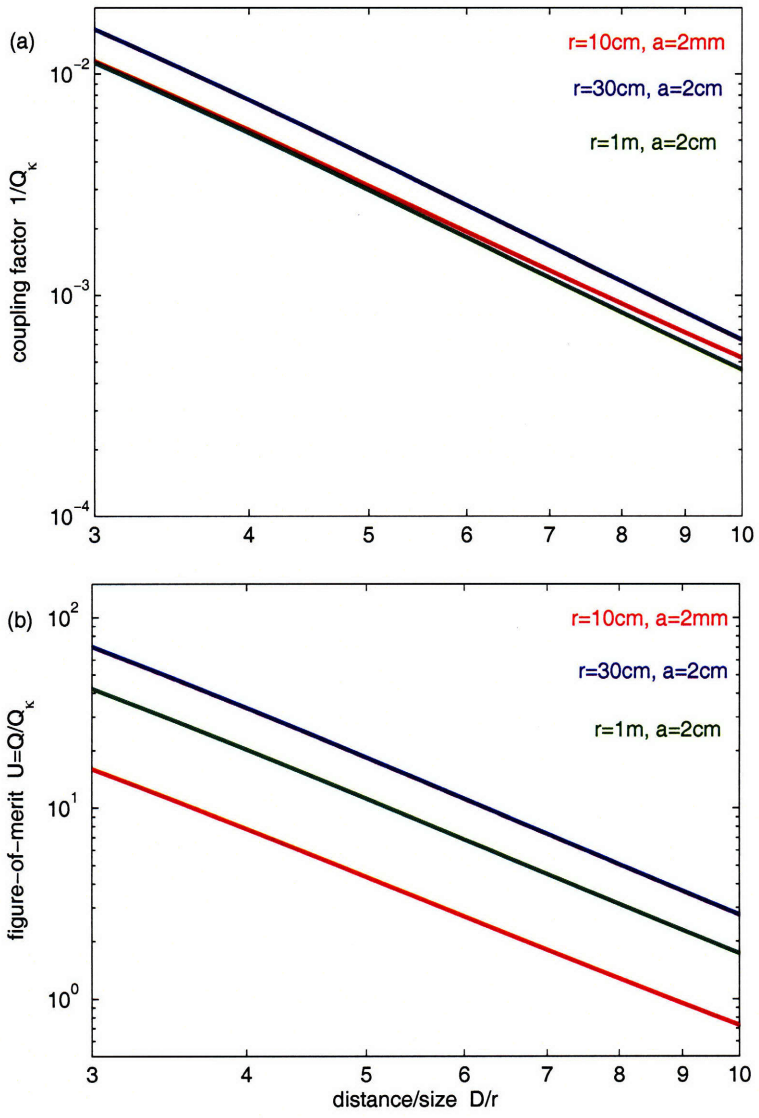


Figure 8-10: Numerical CT results for (a) the coupling rate Q_κ and (b) the coupling-to-loss figure-of-merit U, for the three subwavelength resonant modes shown in Table 8.2 of two same loops, as function of their distance D.

8.2.2.2 Inductively-loaded conducting rods

A straight conducting rod of length $2h$ and cross-sectional radius a is in-series connected at its center to a small coil wrapped around a magnetic material of relative permeability μ, and everything is surrounded by air (as shown in Figure 8-11). The rod has capacitance C and some self-inductance L_s and the coil has an inductance L_c, which is added to L_s in series, so the rod is resonant at $\omega = 1/\sqrt{(L_s + L_c)\,C}$. We will examine the simple case $L_c \gg L_s$ (true when the coil has many turns), which implies that we can safely predict that all the current (and thus most of the magnetic energy) is concentrated inside the coil and varies linearly out to the edges of the rod (where it obviously needs to be zero)[6] and thus, from charge conservation, the charge distribution is positive constant on one half of the rod and negative constant on the other half. This assumption allows us to compute analytically from Eq.(8.24) the capacitance $C^{-1} = 1/(\pi\epsilon_o h) \cdot [\ln(h/a) - 1]$ [108], so then $\omega = 1/\sqrt{L_c C}$. Furthermore, analytical formulas are again available for $|\mathbf{p}| = q_o h$ and $\mathbf{m} = 0$ (namely only the electric-dipole term is contributing to radiation), so from Eq.(8.26) we have $R_{rad} = \zeta_o 2\pi/3 \cdot (r/\lambda)^2$ and from Eq.(8.27) $R_{rad} = \zeta_c (h/3\pi a)$, so $Q_{rad} = 1/\omega C R_{rad} \propto 1/\omega^3$ and $Q_{abs} = 1/\omega C R_{abs} \propto 1/\omega^{3/2}$. These formulas suggest that, as the loading-coil inductance is increased (for example by adding more coil turns) and consequently the frequency is decreased, all the loss terms of the rod are diminishing; clearly, at that point it must be the resistive losses of the inductor itself limiting the structure performance and their scaling should make Q_c decrease as ω decreases. To understand this scaling, a specific inductor design needs to be considered:

[Brooks coil] The coil geometry which, for fixed wire length and thus resistance, demonstrates the highest inductance and thus quality factor is the so-called 'Brooks coil' [106]. This geometry has N_{Bc} turns of conducting wire of cross-sectional radius a_{Bc} wrapped around a cylindrically symmetric coil former, which forms a coil with a square cross-section of side r_{Bc}, where the inner side of the square is also at radius r_{Bc} (and thus the outer side of the square is at radius $2r_{Bc}$), therefore $N_{Bc} \approx (r_{Bc}/2a_{Bc})^2$. The inductance of the coil is then $L_{Bc} = 2.0285\mu r_{Bc} N_{Bc}^2 \approx 2.0285\mu r_{Bc}^5/8a_{Bc}^4$ and its resistance $R_{Bc} \approx (l_{Bc}/\sigma\pi a_{Bc}^2) \cdot \sqrt{1 + \mu_c\omega\sigma a_{Bc}^2/8}$, where the total wire length is $l_{Bc} \approx 2\pi\,(3r_{Bc}/2)\,N_{Bc} \approx 3\pi r_{Bc}^3/4a_{Bc}^2$ and we have used

[6] A transmission-line model of the system would require that the current varies as $\propto \sin[\omega(h - |z|)/c_o]$, where z runs along the rod, but since we will be looking into subwavelength resonances $h \ll \lambda = 2\pi c_o/\omega$, the sinusoidal profile becomes triangular $\propto \omega(h - |z|)/c_o$, as physically predicted.

rod	f [MHz]	Q_{abs}	Q_{rad}	Q
$h = 1\text{m},\ a = 2\text{cm},\ c = 6\text{cm}$	0.62	14287	$7.8 \cdot 10^6$	14253
$h = 30\text{cm},\ a = 2\text{cm},\ c = 2\text{cm}$	2.48	7402	$2.7 \cdot 10^6$	7380
$h = 10\text{cm},\ a = 2\text{mm},\ c = 5\text{mm}$	14.01	3914	$6.9 \cdot 10^5$	3886

Table 8.3: Analytical CT results for the modes of the three rods shown in Figure 8-12, close to the frequencies where Q respectively peaks.

an approximate square-root law for the transition of the resistance from the dc to the ac limit as the skin depth varies with frequency. For this particular Brooks-coil design of the inductor, the tuning procedure of its inductance (and thus of the resonant frequency) involves, e.g. for a fixed inductor size r_{Bc}, increasing the number of turns N_{Bc} by decreasing the wire cross-sectional radius a_{Bc}. Then the desired resonant angular frequency $\omega = 1/\sqrt{L_{\text{Bc}}C}$ is achieved for $a_{\text{Bc}} \approx \left(2.0285\mu r_{\text{Bc}}^5 \omega^2 C\right)^{1/4}$ and the resulting coil quality factor is $Q_{\text{Bc}} \approx 0.169\mu\sigma r_{\text{Bc}}^2 \omega / \sqrt{1 + \omega^2 \mu\sigma \sqrt{2.0285\mu C \left(r_{\text{Bc}}/4\right)^5}}$, which, according to our predictions, indeed is decreasing as frequency decreases. Physically, the coil wire has to become so thin (to fit many turns of it inside a fixed coil-former size) that its cross-section becomes on the order of the skin depth and thus its resistance increases rapidly.

In general, for any inductor design, the total-Q becomes highest at some optimal frequency ω_*, reaching the value Q_* (for a Brooks coil $Q_* \approx Q_{\text{Bc}} \approx 0.8\left(\mu\sigma^2 r_{\text{Bc}}^3/C\right)^{1/4}$). At lower frequencies it is dominated by ohmic loss inside the inductor coil and at higher frequencies by radiation. Note, again, that the above formulas are accurate as long as $L_{\text{c}} \gg L_{\text{s}}$, which, as explained above, is easy to design for by using a large inductance and to the extent that our modelling of the thin-wire losses does not introduce significant errors. The results of the above analysis for three rods, loaded with Brooks coils, with subwavelength modes of $\lambda/h \geq 20$ (namely highly suitable for near-field coupling and well within the quasi-static limit) are presented in Figure 8-12. The optimal frequency ω_* typically lies in lower frequencies than for loops. The values for the modes at the optimal frequency ω_* for these three objects are also shown in Table 8.2.

Two inductively-loaded rods 1 and 2, at distance D between their centers, are coupled only via the electric field (the magnetic field is almost entirely stored inside the inductor) and the mutual capacitance M_C can be evaluated numerically from Eq.(8.28) by assuming again triangular current-distributions in the case $L_{\text{c}1,2} \gg L_{\text{s}1,2}$. In the quasi-static limit $h \ll D \ll \lambda$ and for the optimal relative orientation such that the two rods are aligned on

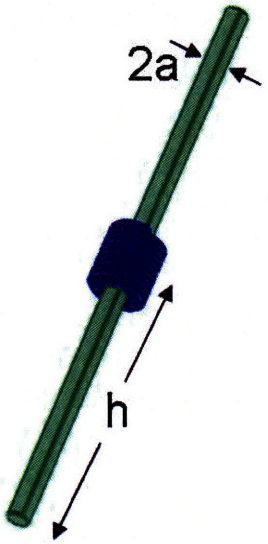


Figure 8-11: A conducting rod of half-length h, connected at its center to a coil and surrounded by air.

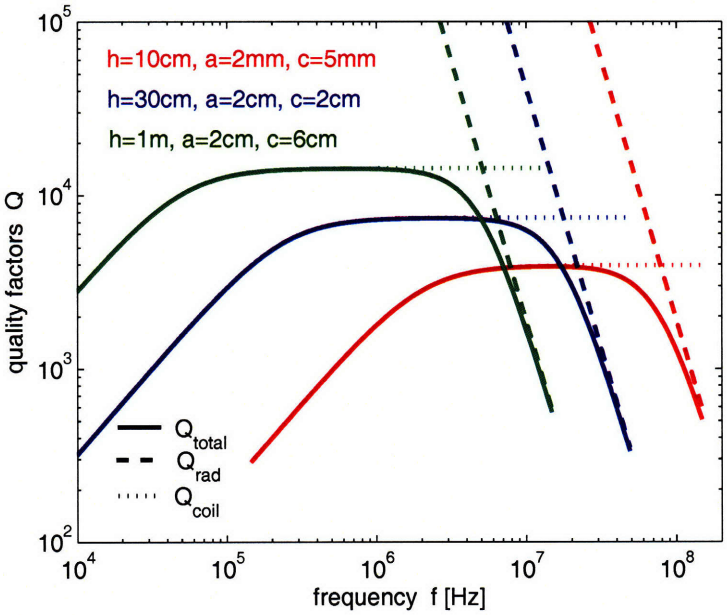


Figure 8-12: Analytical Circuit-Theory (CT) results for the frequency and absorption, radiation and total loss rates Q, for the subwavelength modes of three different rods, when varying their loading inductance. Note that a Brooks inductor was assumed and for conducting material copper ($\sigma = 5.998107\text{S/m}$) was used.

the same axis, an approximate analytical formula gives $M_C^{-1} \approx 1/2\pi\epsilon_o \cdot (h_1 h_2)^2 / D^3$, which means that the coupling factor

$$Q_\kappa \approx 2\left(\frac{D}{\sqrt{h_1 h_2}}\right)^3 \sqrt{\left(\ln\frac{h_1}{a_1} - 1\right)\left(\ln\frac{h_2}{a_2} - 1\right)} \tag{8.34}$$

is again independent of the frequency ω (and so is then U) and depends mainly on the $D/\sqrt{h_1 h_2}$ form-factor, where the cubic scaling comes naturally from the cubic dependence of the static near electric field generated by a conducting rod. Note that this system exhibits slightly weaker coupling than the conducting loops (Q_κ here is smaller), since the effective electrical length of the electric-dipole rod is smaller than its physical length ($h_{\text{eff}} = h/2$) due to the triangular current distribution.[7] To optimize Q and thus U for these rod resonators, focus must be given in increasing the decreasing the losses of the inductor; for example, one should use Litz wire and low-loss high-μ magnetic ferrite cores. The results of this analytical method, where the integral of Eq.(8.28) was evaluated numerically assuming a triangular-current distribution instead of using the approximate analytical formulas, are shown in Figure 8-13, where at ω_* we plot the coupling of the rods in Table 8.3 as a function of the rods distance. The coupling-to-loss ratio for medium distances is again in the range $U \sim 1 - 100$, and scales evidently with $(r/D)^3$.

8.2.2.3 Self-resonant conducting coils [5]

Consider now a conducting wire of length l and cross-sectional radius a, wound into a helical coil of radius r and height h (namely with $N = \sqrt{l^2 - h^2}/2\pi r$ number of turns), surrounded by air, as shown in Figure 8-14. Using intuition from transmission-line theory, we will assume that the resonant mode of the coil is well approximated by a sinusoidal current profile along the length of the conducting wire. Since the finite extent of the conductor forming each coil imposes the boundary condition that the current has to be zero at the ends and we are interested in the lowest resonant mode, then, if we denote by s the coordinate along the wire, such that it runs from $-l/2$ to $l/2$, the surface-current distribution will have the form $\mathbf{J}_s(s) = \hat{\mathbf{s}} I_o/2\pi a \cdot \cos(\pi s/l)$, where we have assumed that the current does not vary significantly along the wire circumference for a particular s, a valid assumption provided $a \ll r$. It

[7] Actually, compared to two square conducting loops of side $2h$, this system couples weaker by exactly a factor of $(h_{\text{eff}}/h)^2 = 4$.

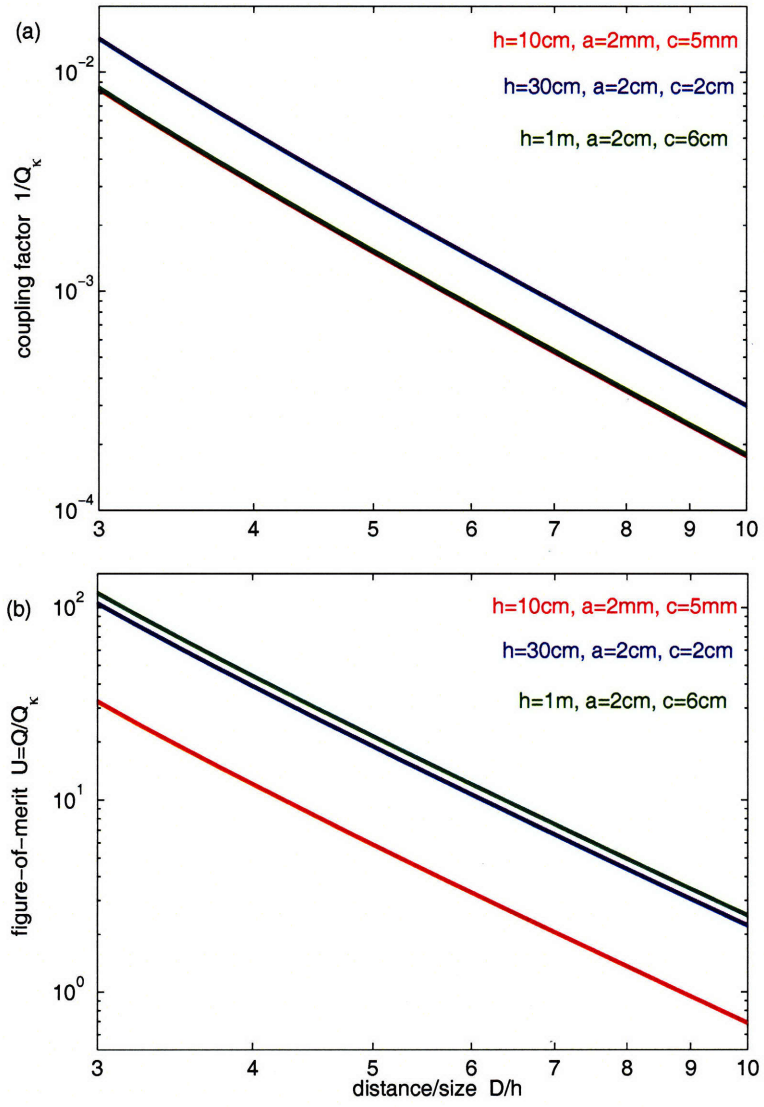


Figure 8-13: Numerical CT results (a) the coupling rate Q_κ and (b) the coupling-to-loss figure-of-merit U, for the three subwavelength resonant modes shown in Table 8.2 of two same rods, as function of their distance D.

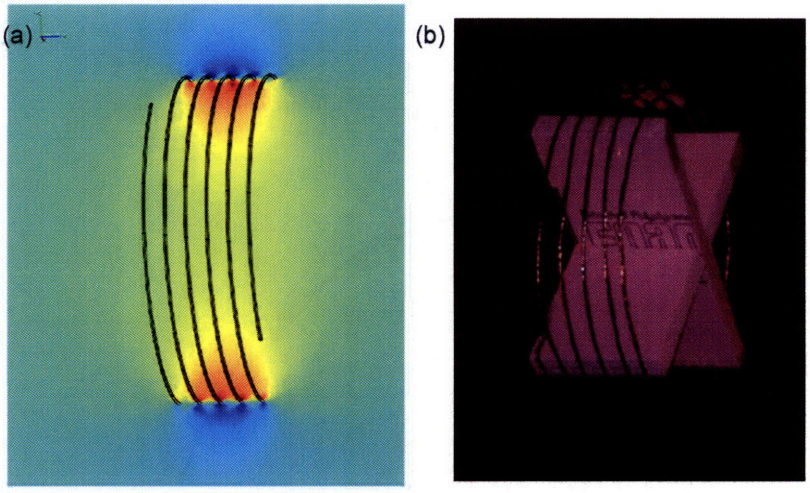


Figure 8-14: A self-resonant coil of radius r and height h with N turns of conducting wire surrounded by air. (a) Shown from a FEFD simulation along with a slice of the magnetic field (component parallel to axis of the coil). (b) Photograph of one of the actual coils built for the experiments, held together by styrofoam blocks and suspended from the ceiling with fishing wire.

immediately follows from the charge-conservation Eq.(8.23) that the surface-charge distribution should be of the form $\rho_s(s) = -iq_o/2\pi a \cdot (\pi/l)\sin(\pi s/l)$, so that $2\pi a \left| \int_0^{l/2} ds \rho_s(s) \right| = q_o$ and $I_o = \omega q_o$. These distributed charge and current profiles result in a distributed capacitance and inductance respectively, and we and find the total so-called 'self-capacitance' C_s and 'self-inductance' L_s of the coil by computing numerically the integrals Eq.(8.24) and (8.25); the associated frequency and effective impedance are $\omega = 1/\sqrt{L_s C_s}$ and $Z_s = \sqrt{L_s/C_s}$ respectively. Analytically we also find $|\mathbf{p}| = q_o \sqrt{\left(\frac{2}{\pi}h\right)^2 + \left[\frac{4N\cos(\pi N)}{(4N^2-1)\pi}r\right]^2}$, $|\mathbf{m}| = I_o \sqrt{\left(\frac{2}{\pi}N\pi r^2\right)^2 + \left[\frac{\cos(\pi N)(12N^2-1)-\sin(\pi N)\pi N(4N^2-1)}{(16N^4-8N^2+1)\pi}hr\right]^2}$, and $\oint_S da\, |\mathbf{J}_s|^2 / I_o^2 = l/4\pi a$, and, with these formulas, the radiation and absorption resistances are calculated analytically by Eq.(8.26) and (8.27) to be $R_{rad} \approx \zeta_o 8/3\pi \cdot \left[(h/\lambda)^2 + 4\pi^4 N^2 (r/\lambda)^2\right]$ and $R_{abs} = \zeta_c l/4\pi a$ respectively, therefore the associated factors Q_{rad} and Q_{abs} may finally be found. The results for two resonant coils of fixed size (radius and height), when varying their number of wire-turns N to tune their frequency, are presented in Figure 8-15, and suggest that quality factors $Q > 1000$ are easily obtainable. Of course, the accuracy of the method decreases for very large N, since then consecutive turns are in very close proximity to each other and induced 'eddy' currents may vary significantly the current distribution along or around the wire.

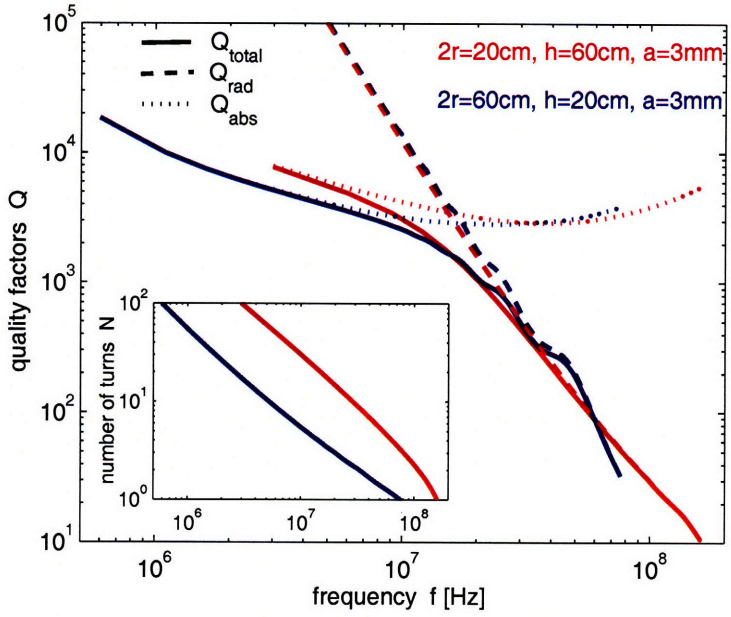


Figure 8-15: Analytical Circuit-Theory (CT) results for the frequency and absorption, radiation and total loss rates Q, for the subwavelength modes of two different self-resonant coils, when varying their number of turns N. Note that for conducting material copper ($\sigma = 5.998107\text{S/m}$) was used. *Inset.* Dependence of self-resonant frequency on N.

To confirm the predictions of the circuit-theory (CT) quasi-static model, we have also performed experimental measurements on such self-resonant conducting coils. Two helical copper coils were built (Figure 8-14(b)) of the same geometric parameters, shown in Table 8.4 (due to imperfections in the construction, seen also in Figure 8-14(b), the spacing between the turns of the helix is not uniform, so we have encapsulated the uncertainty about their uniformity by attributing a 10% uncertainty to h). The resonant frequency and loss rate of each coil were measured by:

1. exciting the coil via a first weakly inductively coupled small loop, connected to a frequency generator,

2. picking up signal from the coil via a second weakly inductively coupled small loop, connected to an oscilloscope,

3. varying the frequency of the generator and monitoring the transmission from the first small excitation coil to the second small pick-up coil,

4. from the Lorentzian-type transmission curve, extracting the resonant f and Q of the coil-mode.

(Note that it is important that the excitation and pickup coils are weakly coupled, so that

coil ($2r = 60$cm, $h = 20 \pm 2$cm, $a = 3$mm, $N = 5.25$)	f [MHz]	Q_{abs}	Q_{rad}	Q
Circuit-theory model	10.56 ± 0.26	3153 ± 50	11453 ± 1633	2472 ± 110
Experimental measurement	≈ 9.90	—	—	950 ± 50

Table 8.4: Numerical CT and experimental results for the resonant mode of the coil shown in Figure 8-14. Note the discrepancy in Q due to the fact that copper ($\sigma = 5.998107$S/m) was assumed for the simulations, while the experimental conductor was measured to have lower conductivity.

they do not significantly load the coil and lower its Q). Given the uncertainty in h, the theoretical prediction for the frequency agrees with the measurement within a good 5%. However, the discrepancy in Q is a large factor of 2.6! After the entire set of experiments had been concluded, we managed to measure the dc resistivity of the copper tubing was substantially smaller than that of copper. Therefore, in all subsequent comparative computations, we will use the experimentally observed value of Q.

Consider now two self-resonant conducting coils at a distance D between their centers. The electric and magnetic fields are used to couple their resonant modes. Usually, the electric coupling highly dominates over the magnetic coupling in the system under consideration for coils with $h \gg 2r$ and, oppositely, the magnetic coupling highly dominates over the electric coupling for coils with $h \ll 2r$. To calculate via CT numerical integration the mutual capacitance and inductance respectively between two self-resonant coils (and thus their coupling rate) from Eqs.(8.28) and (8.29) respectively, again the current profiles are needed and we will assume, as before, a sinusoidal distribution. In Figure 8-17 we show the variation of the coupling rate with frequency (again for fixed size and varying N) for the two coils used previously in Figure 8-15 and at a fixed distance between them. To have a fair comparison, they were placed at the same distance between their edges rather than their centers. It can be seen that indeed the coil form-factor $h/2r$ determines whether the coupling will be mostly magnetic or electric and that, as predicted theoretically, Q_κ is quite independent of frequency (because the retardation factor is small) and the number of turns N (which cancel between L and M_L in the expression for Q_κ), therefore optimizing U essentially entails maximizing Q for given-size coils.

In Figure 8-18(a) we also show how the coupling Q_κ changes with the separation distance D for the coil in Table 8.4, using both numerical computations and experimental measurements. The coupling coefficient is measured by:

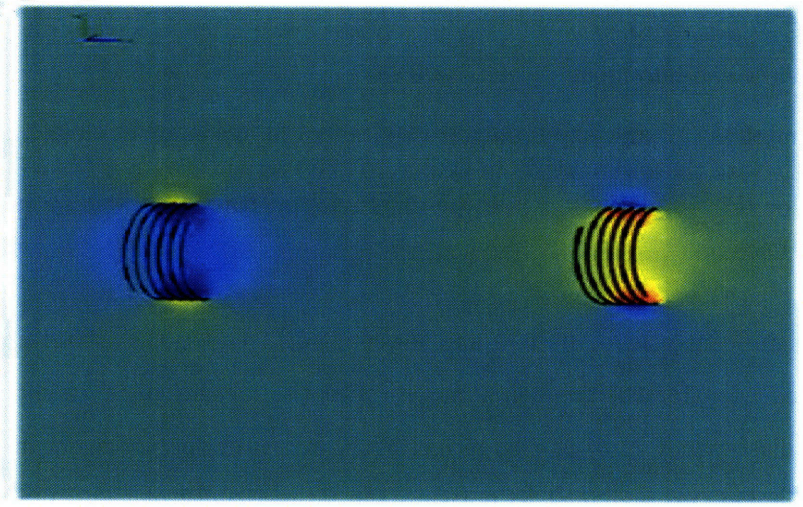


Figure 8-16: System of two self-resonant coils for medium-distance D coupling between them, along with the magnetic field (from FEFD simulation) of the normal mode, which is an odd superposition of the single-coil modes of Figure 8-14.

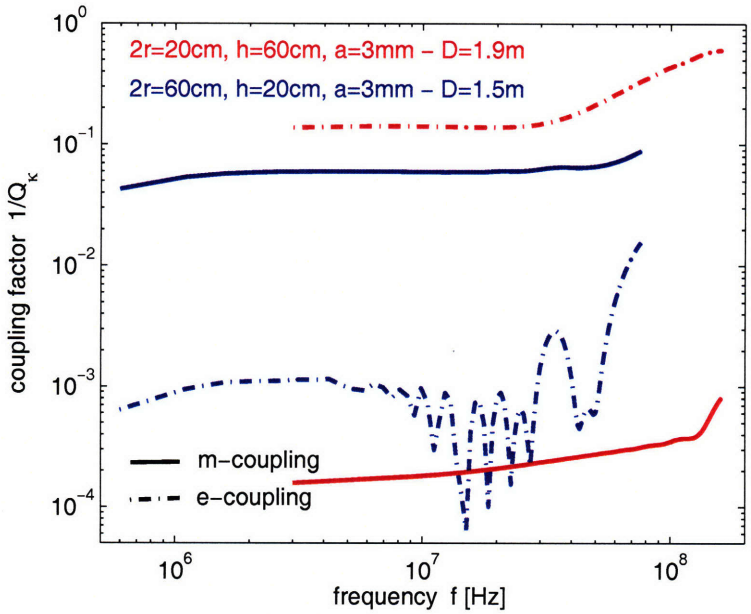


Figure 8-17: Numerical CT results for the electric and magnetic coupling rate Q_κ as a function of the self-resonant frequency (due to variation of N), for the modes shown in Figure 8-15 of two same coils, at the *same* distance $D_e = 1.3$m between their *edges*.

1. fine-tuning both coils to the same resonant frequency when isolated, by slightly adjusting h and/or approaching small metallic objects (aluminum foil),

2. placing the two self-resonant coils at the desired distance and orientation (aligned coaxially here),

3. exciting the first coil via a first weakly inductively coupled small loop, connected to a frequency generator,

4. picking up signal from the second coil via a second weakly inductively coupled small loop, connected to an oscilloscope,

5. varying the frequency of the generator and monitoring the transmission from the first small excitation coil to the second small pick-up coil,

5. from the transmission spectrum, peaked at two frequencies separated by $\delta_{P\pm}$ around the resonant frequency, extracting κ through $\delta_{P\pm} = 2\sqrt{\kappa^2 - \Gamma^2}$ or in general Eq.(8.13).

(Note that it is important that the excitation and pickup coils are weakly coupled, so that they do not significantly load the two coils. If they did, their coupling rate should be added to Γ in the formula above.) The measurements fall in good agreement with theory. In Figure 8-18(b), we then show the figure-of-merit U by simply multiplying all the results of part (a) with the experimental value of $Q = 950$ (where the shaded grey area denotes its ± 50 measurement uncertainty). The coupling-to-loss ratio is $U > 1$ even at $D = 2.4$m (namely at $D/r = 8$), thus the system is in the strongly-coupled regime throughout the entire range of medium distances probed.

8.3 Experimental demonstration of mid-range efficient energy-transfer [5]

The purpose of Section 8.2 was to prove that 'strong coupling' can be achieved for mid-range distances for a variety of electromagnetic systems, purposefully optimized towards this objective. The most convincing demonstration was clearly the experimental measurements of a strong-coupling figure-of-merit $U > 1$ for two self-resonant conducting 60cm-diameter and 20cm-height coils separated by distances a few times their size. With this information at hand, in this Section, we would like to go back and experimentally also confirm the prediction of Section 8.1 that strongly-coupled resonances can lead to efficient mid-range wireless energy-transfer.

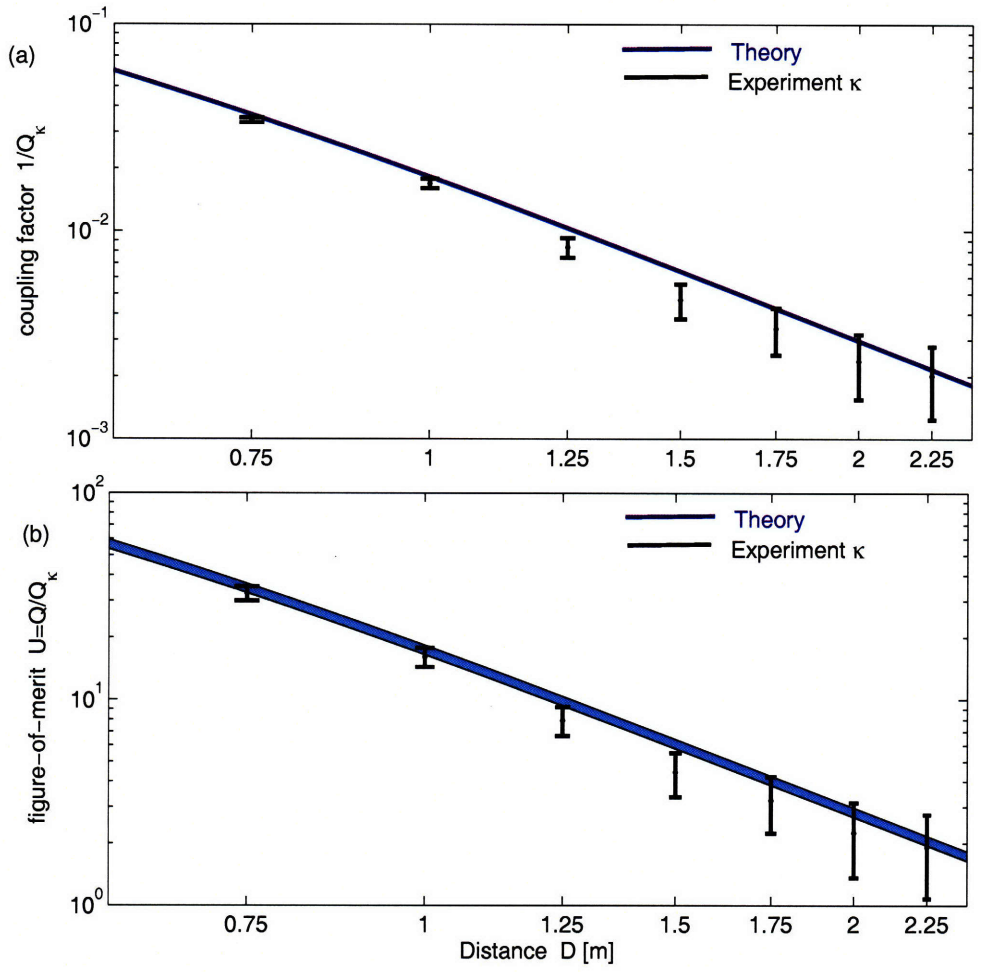


Figure 8-18: Theoretical CT and experimental results (a) the coupling rate Q_κ and (b) the coupling-to-loss figure-of-merit U, for the resonant modes shown in Table 8.4 of the two same self-resonant coils, as function of their distance D.

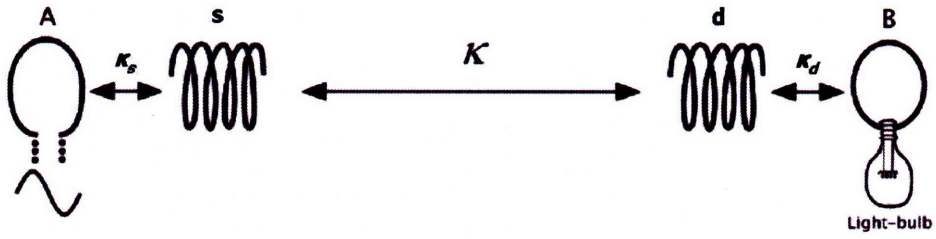


Figure 8-19: Schematic of the experimental setup used for wireless power transmission. s, d are the source, device self-resonant coils, coupled inductively respectively at rate κ_s, κ_d to a power supply circuit (Colpitts oscillator) and to a resistive load (light bulb).

The experimental setup we used consisted of the two same self-resonant coils described above in Table 8.4, through which wireless power transmission was to be achieved, one of which (the source coil denoted s) was coupled inductively (at a rate denoted κ_s) to a power supply circuit, and the other one (the device coil denoted d) was coupled inductively (at a rate denoted κ_d) to a resistive load, as shown schematically in Figure 8-19. The power supply circuit was a standard Colpitts oscillator [109], which was designed to output a sine wave at the resonant frequency 9.9MHz of the coils, driving a single loop of copper wire 25cm in radius (denoted A), via which it was coupled inductively to the source coil s; the rate of energy-feeding κ_s could be adjusted by varying the $A-s$ distance. The resistive load consisted of a previously calibrated incadescent light-bulb, attached to a small loop of insulated wire (denoted B) via which it was coupled inductively to the device coil d; again, the energy-draining rate κ_d could be adjusted by varying the $d-B$ distance. The angle between A and d was adjusted, so that their direct coupling is zero, while the resonator coils s and d were aligned coaxially for optimal coupling. The direct $s-B$ and $A-B$ couplings were negligible due to the distance, non-resonant nature and small size of B. With this experimental setup, we essentially matched the theoretical setup used for the CMT power-transmission analysis in Section 8.1.2.

Having the desired configuration, we proceeded with first optimizing the system parameters for maximum efficiency. In particular, the resonant frequencies of the two coils had to be fine-tuned to match when isolated, by bringing in close proximity to d a metallic object until its frequency matched that of s. Moreover, the rates $\kappa_{s,d}$ had to be adjusted, via the corresponding distances, to satisfy the optimal loading condition $\kappa_s/\Gamma_s = \kappa_d/\Gamma_d = \sqrt{1+(\kappa/\Gamma_s\Gamma_d)^2} \Leftrightarrow U_s = U_d = \sqrt{1+U^2}$ proven in Eq.(8.14). (Note that, because of its inductive nature, the loop B added a small reactive component to the load seen by d, which was compensated for by slightly retuning the coil d.) All the above adjustments were made by supplying a constant power from the Colpitts oscillator and monitoring the brightness of the lit light-bulb, as each adjusting parameter was varied.

Once the maximum possible attainable brightness of the light-bulb had been achieved for fixed supplied power, the efficiency was then measured. To achieve this we now adjusted the power provided by the Colpitts oscillator until the light-bulb was at its full nominal brightness (compared visually to a light-bulb connected to the power line), which meant that we knew the power P_l delivered to the load (Wattage rating of the light-bulb). Then,

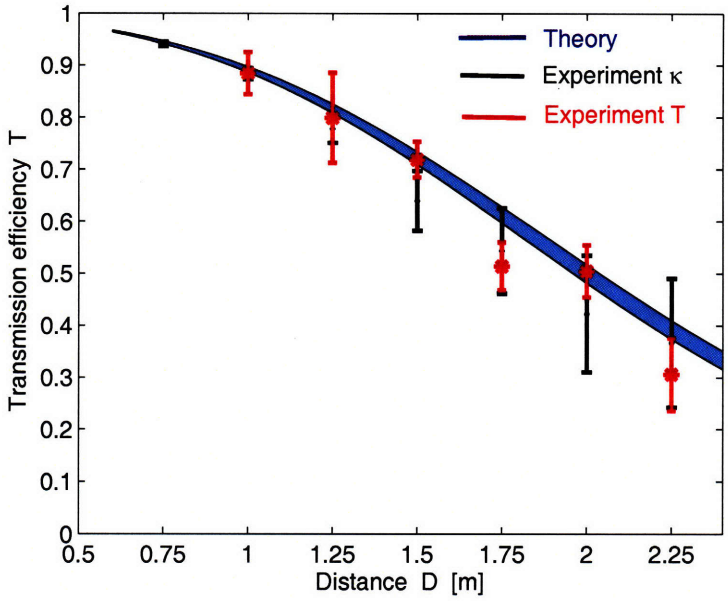


Figure 8-20: Theoretical CT, from experimental measurements of κ and from experimental measurements of currents results for the transmission efficiency T, for the resonant modes shown in Table 8.4 of two same self-resonant coils, as function of their distance D.

in order to isolate the efficiency of the transfer taking place specifically between the source coil and the load, we measured the current at the mid-point of each of the self-resonant coils with a current-probe (which was not found to lower the Q of the coils noticeably). This gave a measurement of the current amplitudes I_s and I_d defined earlier in Section 8.2.2. The power dissipated in each coil was then computed from $P_{s,d} = \Gamma L \left|I_{s,d}\right|^2 = Z \left|I_{s,d}\right|^2 / 2Q$ where $Q \approx 950$ from the measurements and $Z = 690$ from our 5% exact numerical calculation. (Note that also a voltage measurement would have made possible an experimental-only determination of $Z = V_{s,d}/I_{s,d}$, but it was difficult because those probes were loading the coils.) Finally, the efficiency of power transmitted to the load over the power feeding the source coil was directly obtained from $\eta = P_l / \left(P_l + P_s + P_d\right)$.

The entire above procedure had to be repeated at every distance D between the s, d coils. The experimental results as a function of this distance are shown in Figure 8-20, along with the theoretical prediction for maximum efficiency, given by Eq.(8.15), for the numerical and experimental values of U calculated in Figure 8-18. The agreement is apparent given the error bars. Using this setup, we were able to transmit significant amounts of power, for example, fully lighting up a 60W light-bulb from distances more than 2m away, with an

efficiency of more than 40%. Two photographs of this configuration are shown in Figure 8-21. From the second angle, the exact implementation of the schematic in Figure 8-19 is clear. We believe that this is a unique demonstration of the feasibility of mid-range efficient wireless power.

As an additional test, we also measured the total power going into the driving circuit. The efficiency of the wireless transfer itself was hard to estimate in this way, however, as the efficiency of the Colpitts oscillator itself is not precisely known, although it is expected to be far from 100%. Nevertheless, this gave an overly conservative lower bound on the efficiency. When transferring 60W to the load over a distance of 2m, for example, the power flowing into the driving circuit was $\sim$ 400W. This yields an overall wall-to-load efficiency of $\sim$ 15%, which is reasonable given the expected $\sim$ 45% efficiency for the wireless power transfer at that distance and the low efficiency of the driving circuit.

As a final note, we found experimentally that the power transmitted to the load dropped sharply as one of the coils was detuned from resonance. For a fractional detuning $\Delta f/f_0$ of a few times the inverse loaded-Q, the induced current in the device coil was indistinguishable from noise. This confirms that exact resonance is essential for the feasibility of the proposed scheme.

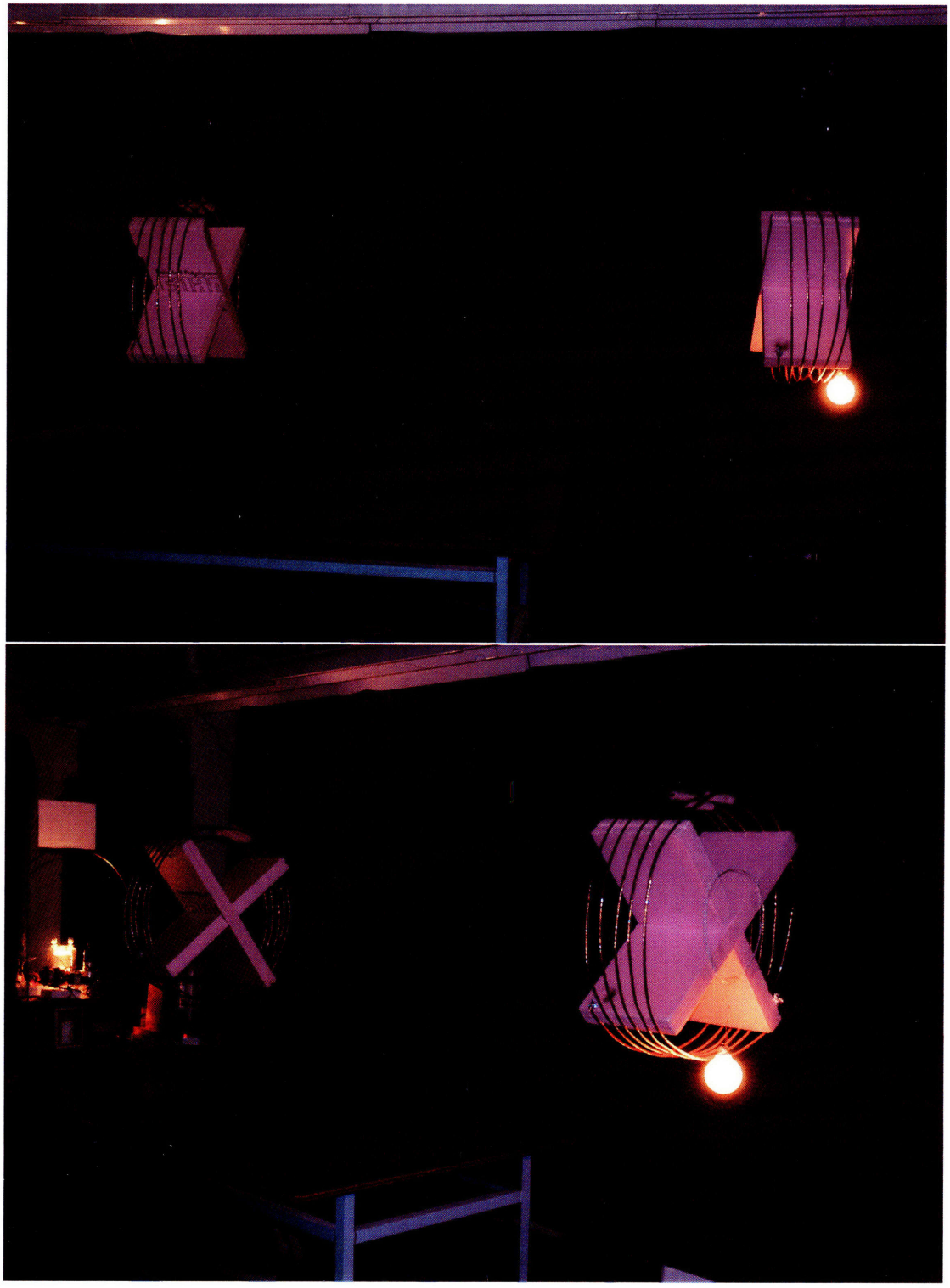


Figure 8-21: Photograph (from two different angles) of the experimental system achieving transmission of 60W with $\sim$ 45% efficiency across 2m distance between two 60cm-diameter self-resonant coils.

Chapter 9

Efficiency enhancement and radiation suppression

9.1 Efficiency enhancement by far-field interference

Our analysis so far has neglected the fact that the radiation generated by the two objects in the energy-transfer system, which can often be a significant part of the instrinsic losses, will typically interfere in the far field. Physically, one can expect that this interference can in principle be engineered to be destructive, resulting in reduced overall radiation losses for the two-object system and thus in enhanced system efficiency. In this section, we show that indeed, in the presence of far-field interference, energy transfer can be more efficient and with less radiated power than what our previous model predicts.

Once more, we will treat the same temporal energy-transfer schemes as before (finite-amount and finite-rate), so that a direct comparison can be made.

9.1.1 Finite-amount energy-transfer efficiency

The inability to predict interference phenomena has often been considered inherent to coupled-mode theory (CMT). Indeed, the coupled-mode equations (Eqs.8.1) failed to predict such a phenomenon in our previous analysis. However, we show here that making only a simple extension to this model, it can actually very successfully predict such interference. The root of the problem stems from the fact that the coupling coefficients were tacitly assumed to be real. This is usually the case when dealing with proper (real) eigenmodes of a

Hermitian (lossless) operator. However, this assumption fails when losses are included, as is for example the current case dealing with generally non-proper (leaky, radiative) eigenmodes of a non-Hermitian (lossy) operator. In this case, the whole coupling-matrix elements $\tilde{\kappa}_{11,22,12,21}$ will generally be complex (denoted with a tilde). The real parts of $\tilde{\kappa}_{11,22}$ will describe, as before, the shift in each object's resonance frequency due to the presence of the other; the imaginary parts of $\tilde{\kappa}_{11,22}$ will describe the change in the losses of each object due to the presence of the other (due to absorption in it or scattering from it, in which latter case losses could be either increased or decreased); both of these are second-order effects and, for the purposes of our mathematical analysis, can again be absorbed into the complex eigenfrequencies by setting $\omega_{1,2} \rightarrow \omega_{1,2} - \mathrm{Re}\{\tilde{\kappa}_{11,22}\}$ and $\Gamma_{1,2} \rightarrow \Gamma_{1,2} + \mathrm{Im}\{\tilde{\kappa}_{11,22}\}$. The real parts of $\tilde{\kappa}_{12,21}$ will denote, as before, the coupling coefficients; the physical interpretation of the imaginary parts of $\tilde{\kappa}_{12,21}$ is yet unclear, but will be shown to be exactly the terms that describe the far-field interference, which we are looking for; again, from reciprocity $\tilde{\kappa}_{12} = \tilde{\kappa}_{21} \equiv \tilde{\kappa} \equiv \kappa + i\Xi$ (note that for a Hermitian problem, the additional requirement $\tilde{\kappa}_{12} = \tilde{\kappa}_{21}^*$ would impose κ to be real). Therefore, for the present analysis, one simply needs to substitute $\kappa \rightarrow \kappa + i\Xi$ in the Equations of Section 8.1.1.

Subsituting $\kappa \rightarrow \kappa + i\Xi$ into Eq.(8.2), the normal modes of the system, at exact resonance $\omega_1 = \omega_2 \equiv \omega_o$ and for $\Gamma_1 = \Gamma_2 \equiv \Gamma_o$, are now found to be

$$\tilde{\omega}_+ = (\omega_o + \kappa) - i\,(\Gamma_o - \Xi) \qquad \text{and} \qquad \tilde{\omega}_- = (\omega_o - \kappa) - i\,(\Gamma_o + \Xi)\,, \tag{9.1}$$

which is exactly the typical case for respectively the odd and even normal modes of a system of two coupled objects, where for the even mode the objects' field-amplitudes have the same sign and thus the frequency is lowered and the radiative far-fields interfere constructively so loss is increased, while for the odd mode the situation is the opposite. Therefore, the coefficient Ξ must be exactly describing the far-field interference phenomenon under examination. In the Appendix, we actually prove, for the particular example of electromagnetic resonances, that Ξ is exactly the change in the radiative loss rates predicted by antenna theory, and this proof can be easily applied to different types of fields too.

To treat now again the problem of energy transfer to object 2 from 1, at exact resonance $\omega_1 = \omega_2$ and in the special case $\Gamma_1 = \Gamma_2 \equiv \Gamma_o$ but in the presence of radiative interference, again simply subsitute $U \rightarrow U + iV$ into Eq.(8.4), where $V \equiv \Xi/\Gamma_o$, and the evolution of

the device field-amplitude becomes

$$\frac{a_2(T)}{|a_1(0)|} = \sin[(U+iV)T]\cdot e^{-T}. \tag{9.2}$$

Now the efficiency $\eta_{\mathrm{E}} = |a_2(T)|^2 / |a_1(0)|^2$ is optimized for the normalized time T_* that is the solution of the transcendental equation

$$\mathrm{Re}\{(U+iV)\cdot\cot[(U+iV)T_*]\} = 1 \tag{9.3}$$

and the resulting optimal energy-transfer efficiency depends only on U, V and is depicted in Figure 9-1(c), evidently increasing with V for a fixed U.

9.1.2 Finite-rate energy-transfer (power) efficiency

Similarly, to treat the problem of continous powering of object 2 by 1, in the presence of radiative interference, simply subsitute $U \rightarrow U+iV$ into all the Equations of Section 8.1.2, where $V \equiv \Xi/\sqrt{\Gamma_1\Gamma_2}$. Either the optimization goal is to maximize efficiency or to minimize reflection, the symmetry upon interchanging $1 \leftrightarrow 2$ is preserved and in each case we have:

• Using Eq.(8.11), the field-amplitude transmission coefficient becomes

$$S_{21} = \frac{2i(U+iV)U_{\mathrm{o}}}{(1+U_{\mathrm{o}}-iD_{\mathrm{o}})^2+(U+iV)^2} \tag{9.4}$$

and from $\eta'_{\mathrm{P}}(D_{\mathrm{o}}) = 0$ we get that, for fixed U, V and U_{o}, the efficiency is maximized for the symmetric detuning

$$D_{\mathrm{o}} = \begin{array}{ll} 2\sqrt{\alpha}\cos\left(\frac{\theta+2\nu\pi}{3}\right);\ \nu=0,1, & \text{if}\quad U^{2/3}-V^{2/3} > (1+U_{\mathrm{o}})^{2/3} \\ \sqrt[3]{\beta+\sqrt{\beta^2-\alpha^3}}+\sqrt[3]{\beta-\sqrt{\beta^2-\alpha^3}}, & \text{if}\quad U^{2/3}-V^{2/3} \leq (1+U_{\mathrm{o}})^{2/3} \end{array}, \tag{9.5}$$

where $\alpha \equiv \left[U^2-V^2-(1+U_{\mathrm{o}})^2\right]/3$, $\beta \equiv UV(1+U_{\mathrm{o}})$, $\theta \equiv \tan^{-1}\sqrt{\alpha^3/\beta^2-1}$ and $U^{2/3}-V^{2/3} > (1+U_{\mathrm{o}})^{2/3} \Leftrightarrow \alpha^3-\beta^2 > 0 \Rightarrow \alpha > 0$. Note that, in the first case, the two peaks of the transmission curve are not equal for $V > 0$, but the one at higher frequencies ($\nu = 0 \Rightarrow$positive detuning) corresponding to the odd system normal mode is higher, as should be expected, since the odd mode is the one that radiates less. Finally, by substituting D_{o} into η_{P} from Eq.(9.5), from $\eta'_{\mathrm{P}}(U_{\mathrm{o}}) = 0$ we get that, for fixed U and V, the efficiency is

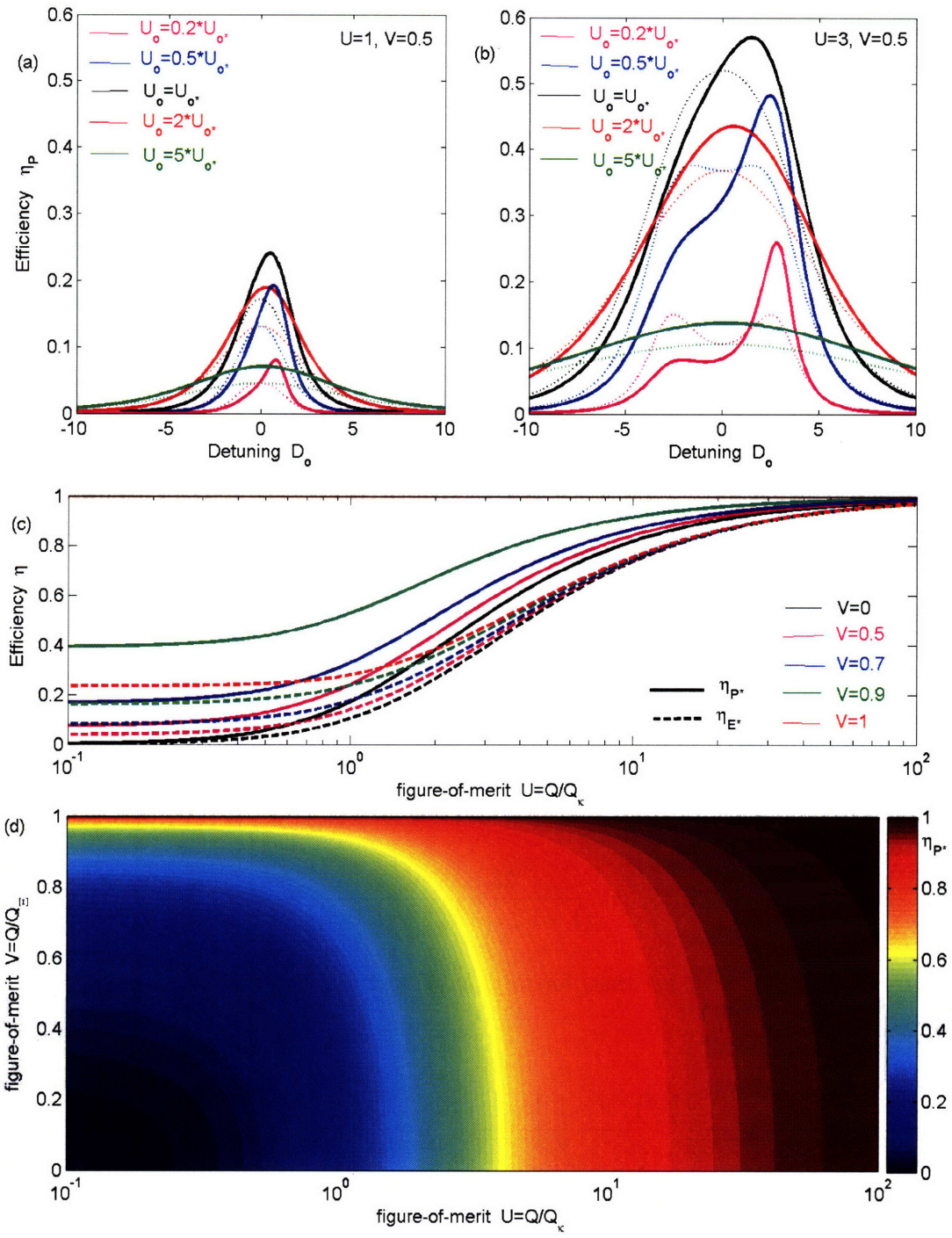


Figure 9-1: (a,b) Efficiency of power transmission η_P for (a) $U = 1$, $V = 0.5$ and (b) $U = 3$, $V = 0.5$, as a function of the frequency detuning D_o and for different values of the loading rate U_o. (The dotted lines show, for comparison, the results when there is no interference, as shown in Figure 8-1(a,b).) (c,d) Optimal (for optimal detuning and under conditions of impedance matching) efficiency for energy transfer (shown only in (c)) and power transmission, as a function of the coupling-to-loss figure-of-merit U and the interference-to-loss figure-of-merit V.

maximized for

$$U_{o*} = \sqrt{(1+U^2)(1-V^2)} \qquad \text{and} \qquad D_{o*} = UV. \tag{9.6}$$

The dependence of the efficiency on D_o for different U_o (including the new 'critical-coupling' condition) are shown in Figure 9-1(a,b). The overall optimal power efficiency using Eqs.(9.6) is

$$\eta_{P*} \equiv \eta_P\left(D_{o*}, U_{o*}\right) = \frac{U^2+V^2}{\left(U_{o*}+1\right)^2+U^2V^2}, \tag{9.7}$$

which again depends only on U, $|V|$ and is depicted in Figures 9-1(c,d), increasing with $|V|$ for a fixed U, and actually $\eta_P \to 1$ as $|V| \to 1$ for all values of U.

• Using Eq.(8.17), the 'impedance matching' condition becomes

$$(1-iD_o)^2 - U_o^2 + (U+iV)^2 = 0 \tag{9.8}$$

from which again we easily find that the values of D_o and U_o that cancel all reflections are exactly those in Eqs.(9.6).

• Often, it may be of most interest to minimize the power radiated from the system, since e.g. it may be a cause of interference to other communication systems, while still maintaining good efficiency. Using Eq.(12.19), we find for two same objects

$$\eta_{rad} \equiv \frac{P_{rad}}{|S_{+1}|^2} = \frac{4U_o\left[\left(|1+U_o-iD_o|^2+|U+iV|^2\right)\frac{Q}{Q_{rad}} - 2V\left(V+VU_o+UD_o\right)\right]}{\left|(1+U_o-iD_o)^2+(U+iV)^2\right|^2}. \tag{9.9}$$

Then, to achieve our goal, we maximize η_P/η_{rad} and find that this is achieved for

$$U_{o**} = \sqrt{1+U^2-V_{rad}^2U^2+V^2-2VV_{rad}} \qquad \text{and} \qquad D_{o**} = UV_{rad}, \tag{9.10}$$

where $V_{rad} \equiv \frac{\Xi}{\sqrt{\Gamma_{rad1}\Gamma_{rad2}}} = \frac{\sqrt{Q_{rad1}Q_{rad2}}}{Q_\Xi}$, as defined in Eq.(12.25) in the Appendix, is the interference the system would experience, if all loss was radiative, namely $V_{rad} = \sqrt{\frac{Q_{rad1}Q_{rad2}}{Q_1Q_2}}V \geq V$. Eq.(9.10) reduces to Eq.(9.6) when $V = V_{rad}$.

The main conclusion of this section is that, for any temporal energy-transfer scheme and given some achieved coupling-to-loss ratio, the efficiency can be enhanced and the radiation can be suppressed by shifting the operational frequency away from exact resonance with each object's eigenfrequency and closer to the frequency of the odd normal-mode, which

suffers less radiation due to destructive far-field interference. Defining $Q_\Xi \equiv \omega/2\Xi$, it is therefore the parameters

$$U = \frac{\kappa}{\sqrt{\Gamma_1\Gamma_2}} = \frac{\sqrt{Q_1Q_2}}{Q_\kappa} \qquad \text{and} \qquad V = \frac{\Xi}{\sqrt{\Gamma_1\Gamma_2}} = \frac{\sqrt{Q_1Q_2}}{Q_\Xi} \tag{9.11}$$

that are the correct figures-of-merit for any system under consideration for wireless energy-transfer, along with the distance over which large U, $|V|$ can be achieved. Clearly, also $|V|$ will be a decreasing function of distance, since two sources of radiation distant by more than a few wavelengths do not interfere substantially. It is important also to keep in mind that the magnitude of V depends on the degree to which radiation dominates the objects' losses, since it is only these radiative losses that can contribute to interference, as expressed from $V_{\text{rad}} \geq V$. Moreover, note that, at some fixed distance between the source and device objects, the figures U, V may not be maximized for the same set of system parameters; in that case, these parameters could be chosen so that the efficiency of Eq.(9.7) is maximized. In the following section, we calculate the magnitude of the efficiency improvement and radiation reduction for realistic systems at mid-range distances between two objects, by employing this frequency detuning and by doing a joint optimization for U,V.

9.2 Far-field interference at mid-range distances for realistic systems

As seen in the previous Section, the problem of maximizing the energy-transfer efficiency may require a modified treatment in the presence of interference. The choice of eigenfrequency for the source and device objects as the one where U is maximum may not be a good one anymore, but also V needs to be considered. Once more, subwavelength resonances will be the preferred choice, because, for a given source-device distance, the interference term V_{rad} will increase as frequency decreases, since naturally the odd mode of two coupled objects, distant much closer than a wavelength, will not radiate at all. On the other hand, as frequency decreases, radiation losses always decrease and typically systems are limited by absorption losses, as discussed earlier; thus, the advantage of interference may be insignificant at some point compared to the deterioration of absorption-Q. Therefore, V will be maximized at some frequency, dependent on the source-device distance, and this optimal

frequency will typically be different than the optimal frequency for U. The optimization of efficiency is then a combined problem, which will be demonstrated below for some of the systems we have been examining so far.

In the case of two objects 1, 2 supporting radiative electromagnetic resonant modes of the same eigenfrequency $\omega_1 = \omega_2 = \omega_o$, placed at distance D so that they couple in the near field and interfere in the far field, the interference coefficient is predicted from antenna theory (AT) [102] to be that in Eq.(12.24)

$$\Xi = \frac{\frac{\zeta_o}{4}\left(\frac{\omega_o}{4\pi c_o}\right)^2 \oint d\Omega \mathbf{f}_1^* \mathbf{f}_2 e^{-i\mathbf{k}\cdot\mathbf{D}}}{\frac{1}{4}\int_V dv \left(\epsilon |\mathbf{E}_1|^2 + \mu |\mathbf{H}_1|^2\right)} = (1 \leftrightarrow 2), \tag{9.12}$$

where $\mathbf{f}_{1,2} = \int_{V_{1,2}} dv\, \mathbf{J}_{1,2}(\mathbf{r})\, e^{-i\mathbf{k}\cdot\mathbf{r}}$ are the vector current-moments of 1, 2 defined earlier too and $\mathbf{D}$ is the distance vector between the arbitrarily-chosen centers of the two objects.

We will demonstrate the efficiency enhancement and the radiation suppression due to interference for the two cases of dielectric disks and capacitively-loaded loops. The degree of improvement will be shown to depend on the nature of the system.

9.2.1 Dielectric resonators

9.2.1.1 Dielectric disks

In the case of 2d dielectric disks, to compute the interference parameter between two coupled disks at distance D, we again use two independent methods to confirm the validity of our results: numerically, the FEFD calculations again give Ξ (and thus V) by the splitting of the loss-rates of the two normal modes; analytically, calculation of the AT prediction of Eq.(9.12) (or equivalently Eq.(12.25) in the Appendix) gives

$$m = 1: \quad V_{\text{rad}} = \frac{2}{(kD)} J_1(kD)$$

$$m = 2: \quad V_{\text{rad}} = \frac{8}{(kD)^3}\left\{3(kD)\cdot J_0(kD) + \left[(kD)^2 - 6\right]\cdot J_1(kD)\right\} \tag{9.13}$$

$$m = 3: \quad V_{\text{rad}} = \frac{6}{(kD)^5}\left\{\left[24(kD)^3 - 320(kD)\right]\cdot J_0(kD) + \left[3(kD)^4 - 128(kD)^2 + 640\right]\cdot J_1(kD)\right\}.$$

The results for the interference of two same disks from those in Figure 8-3 (namely for exactly the same parameters as the coupling was calculated in Figure 8-5) are presented in

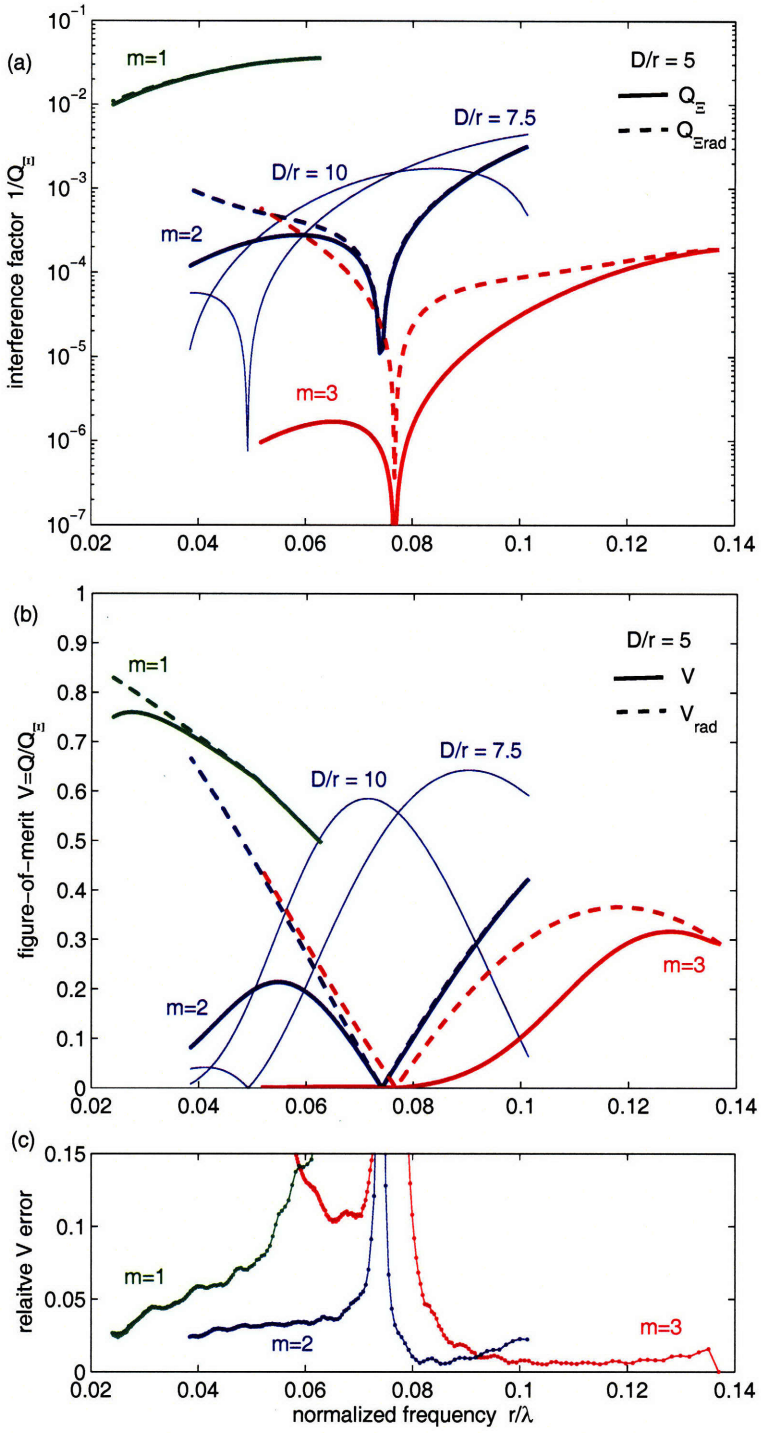


Figure 9-2: Antenna Theory (AT) results for the interference (a) factor Q_Ξ and (b) figure-of-merit $|V|$, as a function of frequency, for the exact same parameters as in Figure 8-5. (c) Relative V error between AT and numerical FEFD calculations of part (b).

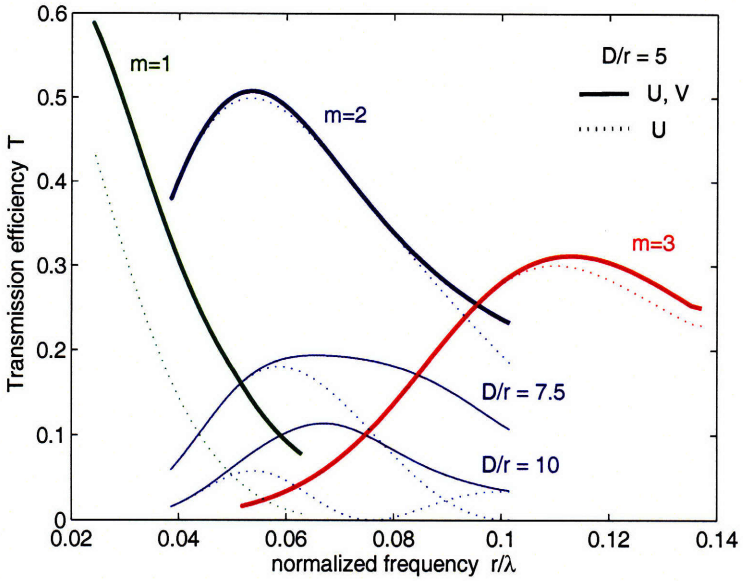


Figure 9-3: Results for the overall power transmission as a function of frequency, for the same set of resonant modes and distances as in Figures 8-5 and 9-2, based on the predictions including interference (solid lines) and without interference just from U (dotted lines).

Figure 9-2, as a function of frequency (due to varying ϵ) at fixed distances. It can be seen that also the interference factor $|V|$ has nulls, which occur even before the system enters the radiative-coupling regime, namely at smaller frequencies than those of U at the same distances, and it decreases with frequency, since then the objects become more and more absorption dominated, so the benefit from radiative interference is suppressed. Both the above effects result into the fact that U (from Figure 8-5(b)) and V (from Figure 9-2(b)) are maximized at different values of the frequency ($\approx \omega_*$ for U) for most distances, and thus different will also be the optimal frequency $\omega_\#$ for the final energy-transfer efficiency of Eq.(9.7), which is shown in Figure 9-3 again for the same set of parameters. From this plot, it is now clear that interference can significantly improve the transfer efficiency, compared to what Eq.(8.15) would predict from the calculated values of the coupling figure-of-merit U.

Furthermore, not only does a given energy-transfer system perform better than what a prediction which ignores interference would predict, but also our optimization design will typically lead to different optimal set of parameters in the presence of interference. For example, for the particular distance $D/r = 5$, it turns out from Figure 9-3 that the $m = 1$ resonant modes can achieve better efficiency than the $m = 2$ modes within the available

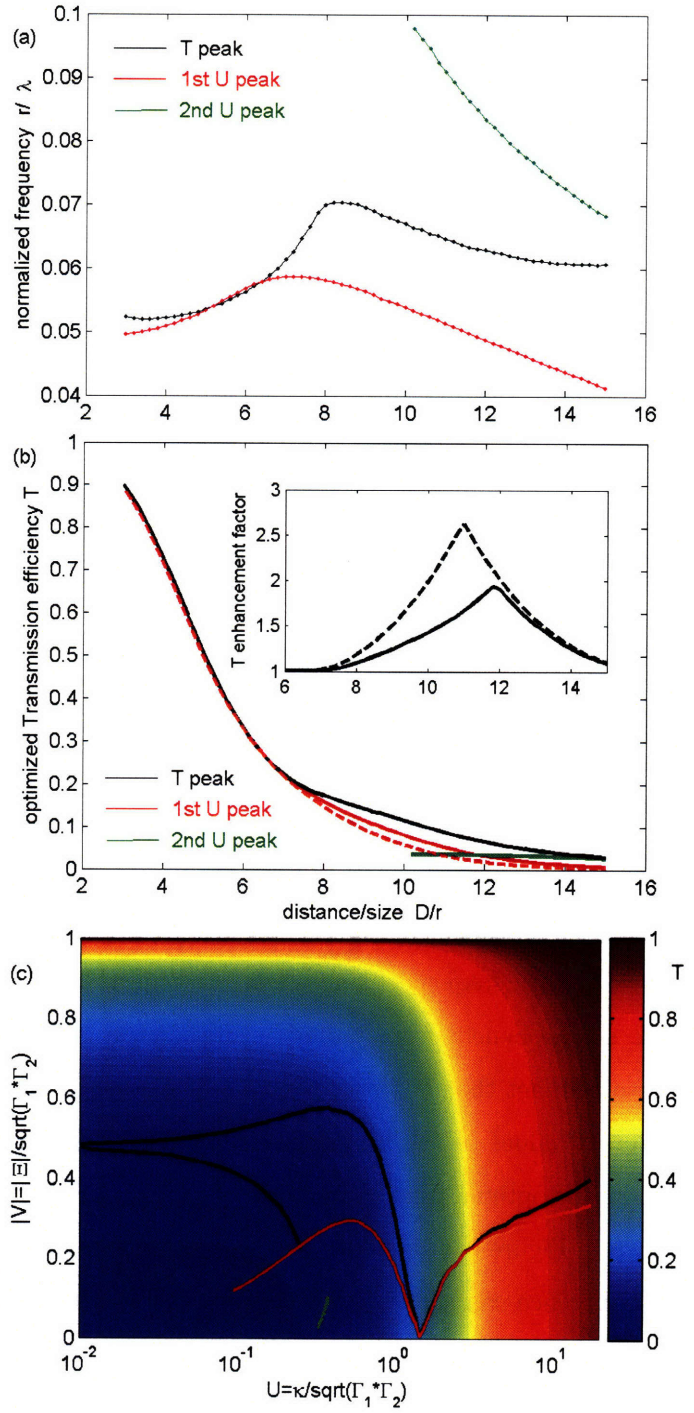


Figure 9-4: (a) Frequencies, where U and T are maximized, as a function of the transfer distance between the disks highlighted in bold in Table 8.1. (b) Efficiencies achieved at the frequencies of (a) and, in inset, the enhancement ratio of the optimal (by definition) for peak frequency of T versus the achievable at the peak frequencies of U. (c) The D-parametrized path of the transmission efficiency for the frequency choices of (a) on the $U - V$ efficiency map.

range of ϵ, by making use of strong interference which counteracts their weaker U, as viewed in Figure 8-5, from which one would have concluded the opposite performance. Moreover, even within the same m-branch, as was discussed in Section 8.2, one would naively design the system to operate at the frequency ω_*, at which Q (and typically U) is maximum. However, the optimization design changes in the presence of interference, since the system should be designed to operate at the different frequency $\omega_\#$, where the overall efficiency T peaks: In Figure 9-4(a), we first calculate those different frequencies where the coupling-to-loss ratio U and the efficiency T (which includes interference) peak, as distance D is changing (again, they peak more than once for distances in the far-field region) for the choice of disk highlighted in bold in Table 8.1, and observe that their difference is actually significant. Then, in 9-4(b) we show the peak efficiency for the various frequency choices. There is not significant improvement for close-enough distances, because the efficiency is basically dominated by the strong coupling, however, for larger distances (on the border to the radiative regime), where efficiency is small and could use a boost, the improvement factor reaches a significant 2 for the particular system under examination. The same result is shown in Figure 9-4(c) as a plot of the path of the efficiency on the $U-V$ map, as distance is changing. Similar results are derived for the modes of different m-order. Physically, moving to higher frequencies increases role of radiative losses compared to absorption and thus interference can have a greater influence. At the optimal frequency $\omega_\#$ radiated power including interference is close to what it is at ω_*, but absorbed power is much less.

Instead of improving efficiency, one might care more about minimizing radiation. In that case, we calculate at the frequency ω_* how much power is radiated when optimized under the conditions Eq.(9.10) compared to the power radiated when simply operating on resonance ($D_o = 0$) in the cases with and without interference (the latter case may be describing a case where the two disks do not interference, because they are dissimilar, or due to decoherence issues etc.). We find in Figure 9-5 that radiation can be suppressed by a factor of 1.6 by detuning the operating frequency towards the odd sub-radiant mode.

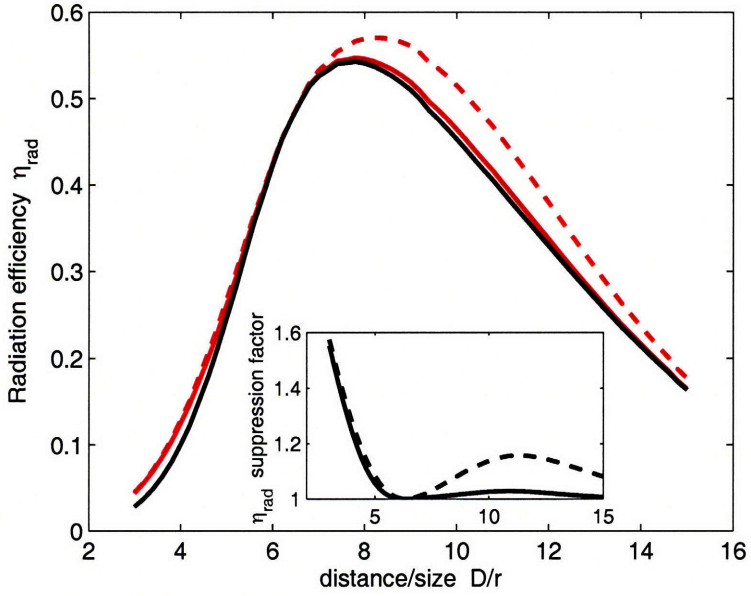


Figure 9-5: Results for the power radiated as a function of the transfer distance at resonant frequency ω_* (red curve of Figure 9-4(a)), when the operating frequency is detuned (solid black line), when it is not (solid red line) and when there is no interference whatsoever (dashed red line). In the inset, we show the corresponing radiation suppression factors.

9.2.2 Metallic resonators

9.2.2.1 Capacitively-loaded conducting loops

For conducting loops, we compute the interference parameter between two coupled loops at distance D, using just the AT analysis (Eq.(9.12) or (12.25)) leading to

$$V_{\text{rad}} = \frac{3}{(kD)^3} \left[\sin(kD) - (kD)\cos(kD)\right], \tag{9.14}$$

for the orientation of optimal coupling, where one loop is above the other. This factor now has nulls only upon reaching the radiative regime, therefore $|V| = (Q/Q_{\text{rad}})\,|V_{\text{rad}}|$ peaks close to U for mid-range very-subwavelength distances. An improvement in the overall efficiency, plotted in Figure 9-6, can still be observed though for the mildly subwavelegth systems (at frequencies higher than ω_*) compared to the predictions in the absence of interference.

By following the same procedure as for dielectric disks, we show in Figure 9-7(a) the optimal frequencies $\approx \omega_*$ of U and $\omega_\#$ of T (with multiple branches), as distance varies and for the loop highlighted with bold in Table 8.2, and in (b) the corresponding maximum

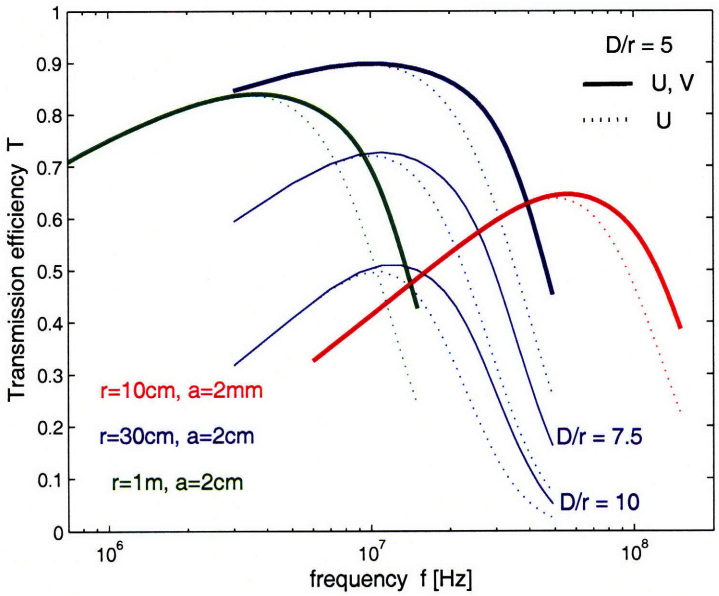


Figure 9-6: Results for the overall power transmission as a function of frequency, for the same set of loop resonant modes and distances as in Figures 8-5 and 9-2, based on the predictions including interference (solid lines) and without interference just from U (dotted lines).

improvement of efficiency upon designing the resonant frequency of the loops to be $\omega_{\#}$ (by definition the optimal choice), as opposed to $\approx \omega_*$ (the dashed line shows the improvement compared to case where interference is not existent). In this case, the improvement again reaches a considerable factor of 2, but this occurs at large relative distances where the efficiency itself is rather small. The D-parametrized path in the $U - V$ plane and the associated improvement are also shown in Figure 9-7(c).

Finally, if we design the system to suppress radiation, again an improvement factor of 2 is achieved when the operating frequency is detuned from the resonant frequency, as shown in Figure 9-8.

As a general conclusion, clearly, far-field interference can be utilized by the system designer to either suppress the total radiation loss or to increase the system efficiency. In the second case, systems operating optimally closer to the radiative regime, benefit more from the presence of far-field interference, which leads to reduced losses for the sub-radiant normal mode of the coupled objects, and this benefit can be substantial.

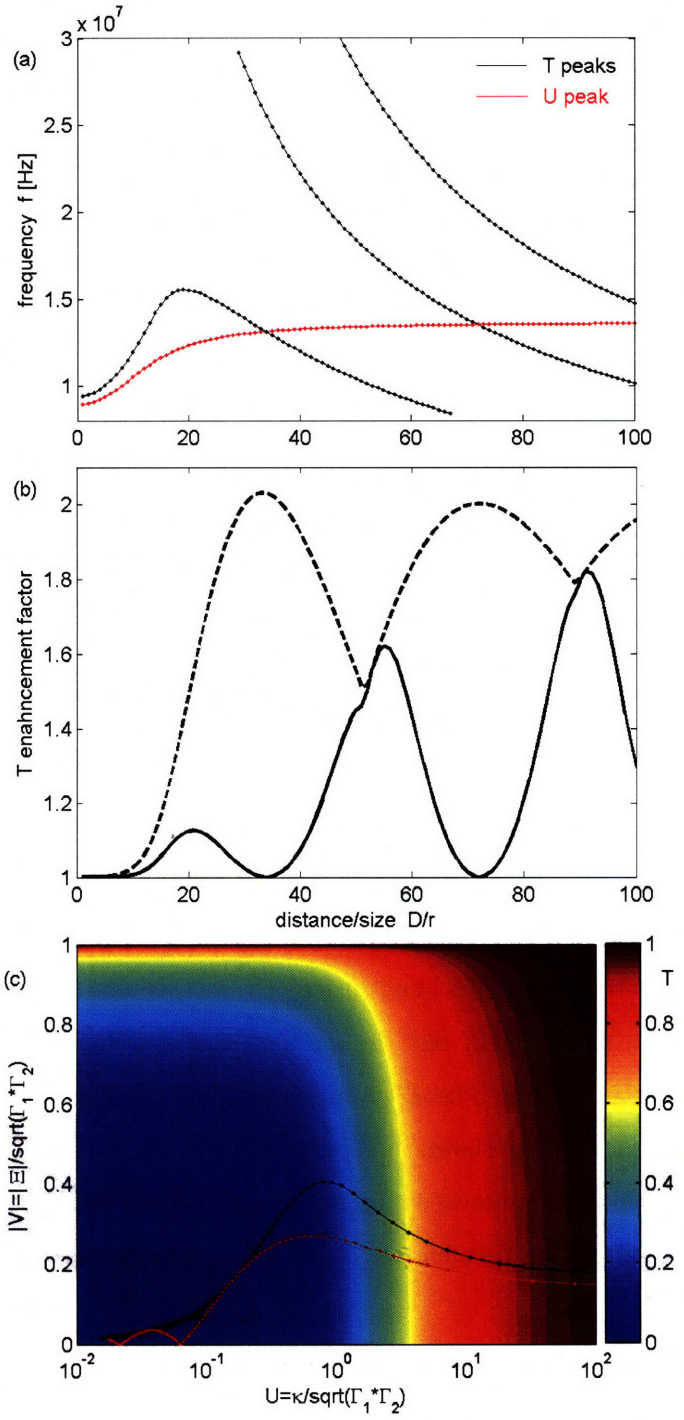


Figure 9-7: (a) Frequencies, where U and T are maximized, as a function of the transfer distance between the loops highlighted in bold in Table 8.2. (b) Efficiencies achieved at the frequencies of (a) and, in inset, the enhancement ratio of the optimal (by definition) for peak frequency of T versus the achievable at the peak frequencies of U. (c) The D-parametrized path of the transmission efficiency for the frequency choices of (a) on the $U - V$ efficiency map.

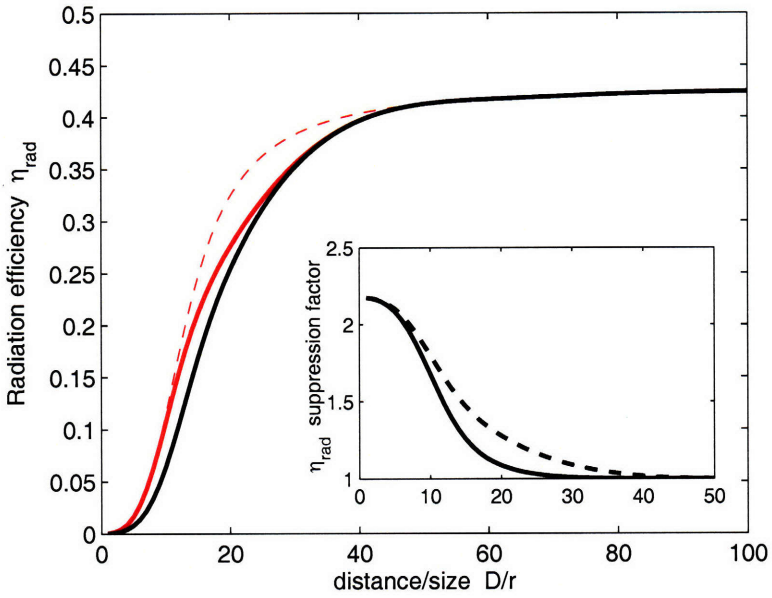


Figure 9-8: Results for the power radiated as a function of the transfer distance at resonant frequency ω_* (red curve of Figure 9-7(a)), when the operating frequency is detuned (solid black line), when it is not (solid red line) and when there is no interference whatsoever (dashed red line). In the inset, we show the corresponing radiation suppression factors.

Chapter 10

Insensitivity to near-presence of extraneous objects

Having established that efficient wireless energy-transfer can be accomplished at mid-range distances with the proposed resonant scheme, the next criterion for estimating its feasibility and applicability is its sensitivity to the near-presence of random and possibly mobile extraneous objects. If the interaction with random objects is strong, it could be deleterious, as seen from two equivalent viewpoints: these objects could affect the system's performance to the extent that it cannot transfer energy efficiently anymore or, reciprocally, the system could affect the random objects to an extent that may be harmful to their performance (in the case of extraneous devices) or their health (in the case of living organisms). What are the necessary requirements for such insensitivity and are they met for realistic material systems and geometries?

10.1 Insensitive energy-transfer by robust lifetime and coupling of resonances

For the proposed coupled-resonance-based wireless energy-transfer scheme, one would physically expect that its viability in the presence of extraneous objects depends strongly on the robustness of the resonant-objects' resonances and interaction. In practice, a random object is expected to detune a resonance, provide an additional loss-channel to it and also reduce its coupling to other resonant objects. We will discuss that the crucial points are the last

ones, namely that the resonance lifetimes and coupling are not substantially decreased.

Let a resonant object 1 have an eigenmode with angular frequency ω_1, frequency-width due to instrinsic (absorption, radiation etc.) losses Γ_1 and vector field $\mathbf{F}_1(\mathbf{r})$, normalized to unity energy. The near-presence of a random object e will perturb the resonance and, if the random object is non-resonant itself, an appropriate analytical framework for modeling this interaction is that of the well-known perturbation theory (PT) [11]. If the field amplitude $a_1(t)$ is defined again so that $|a_1(t)|^2$ is equal to the energy stored inside 1, then, using $e^{-i\omega t}$ time dependence, it can be shown to satisfy, to lowest order:

$$\frac{d}{dt}a_1(t) = -i(\omega_1 - i\Gamma_1)a_1(t) + i\delta\tilde{\omega}_{1(e)}a_1(t), \tag{10.1}$$

where $\delta\tilde{\omega}_{1(e)} \equiv \delta\omega_{1(e)} + i\delta\Gamma_{1(e)}$ is the shift in the complex eigenfrequency of object 1 induced by the presence of object e and will generally be complex (denoted by the tilde), as discussed in Section 9.1. Here, $\delta\omega_{1(e)}$ denotes the (real-)frequency detuning induced and $\delta\Gamma_{1(e)}$ denotes the additional loss-rate induced due to extrinsic (absorption inside e, scattering from e etc.) losses.[1] If 1 is driven by some generator with power $|s_{+1}(t)|^2$ at a rate κ_1, we would similarly get

$$\begin{aligned} \frac{d}{dt}a_1(t) &= -i(\omega_1 - i\Gamma_1)a_1(t) + i\delta\tilde{\omega}_{1(e)}a_1(t) - \kappa_1 a_1(t) + \sqrt{2\kappa_1}s_{+1}(t) \\ s_{-1}(t) &= \sqrt{2\kappa_1}a_1(t) - s_{+1}(t). \end{aligned} \tag{10.2}$$

Note that, if the random object is actually itself a resonant object, then one would have to use the CMT analytical framework to describe the interaction. However, since our energy-transfer scheme is based on extremely sharp resonances, it is essentially improbable that a random resonant object would either have a sharp resonance itself (it is in fact an engineering challenge to design so high-Q resonances for our scheme) or, even in that case, that it would happen to be exactly tuned to our resonant object. Therefore, even in the case of resonant random objects, CMT suggests (through Eqs.(8.3) and (8.8)) that effectively one can ignore the term $+i\kappa_{1e}a_e(t)$ in Eqs.(8.1) and (8.7), which would then reduce respectively to Eqs.(10.1) and (10.2) for object 1 (with $\tilde{\kappa}_{11} \to \delta\tilde{\omega}_{1(e)}$).

When considering an energy-transfer system of two objects 1 and 2, one would simply

[1] The first-order PT model is valid only for small perturbations. Nevertheless, the parameter $\tilde{\kappa}_{11(e)}$, is well defined, even outside that regime, if $a_1(t)$ is taken to be the amplitude of the exact perturbed mode.

have to include the effects of the random objects on both, by appropriately adding the terms $+i\delta\tilde{\omega}_{1,2(e)}a_{1,2}(t)$ in Eqs.(8.1) or (8.7) to denote the frequency shift and the extrinsic losses induced onto both resonant objects. Moreover, also the coupling rate $\tilde{\kappa}$ will be shifted by $\delta\tilde{\kappa}_{(e)}$, for example when the line-of-sight between the two objects is interrupted.

The frequency shift due to mobile random objects is a problem that can be 'fixed' by applying to the one or more resonant objects a feedback mechanism that corrects its frequency and ensures their mutual resonance. Here are some examples, combinations of which could be implemented too:

• Each resonant object could be provided with an oscillator at a fixed reference frequency f_{r} and a monitor, which determines the eigenfrequency of the object; an error signal would then be generated from the difference of the oscillator and monitor frequencies, which would be used to stabilize the eigenfrequency of each resonant object to f_{r} by, for example, adjusting the geometric properties of the object (e.g. the shape of a dielectric disk, the capacitor-plate spacing or area of a capacitively-loaded loop, the dimensions of the inductor of an inductively-loaded rod, the height of a self-resonant coil, etc.) or by changing the position of a non-lossy non-resonant object in the vicinity of each resonant object; this technique assures that all resonant objects operate at the same fixed frequency f_{r}, even in the presence of extraneous objects.

• During energy transfer from a source object fed by fixed power from a generator to device objects feeding loads, each device object could monitor the power delivered to its load and dynamically adjust its resonance frequency (using one of the mechanisms described above) to maximize its output power; this technique allows the source resonance-frequency to vary freely but assures that all devices are in resonance, even in the presence of extraneous objects.

• The frequency of the source object could be monitored and transmitted via communication (information exchange) to the device objects, which are in turn synched to this frequency using frequency adjusters, as described above.

Unlike the frequency shift, extrinsic losses and modified coupling can be detrimental to the functionality of the energy-transfer scheme, because they are difficult to remedy, therefore the new total loss-rates $\Gamma_{1,2(e)} \equiv \Gamma_{1,2} + \delta\Gamma_{1,2(e)}$ and new coupling rate $\tilde{\kappa}_{(e)} = \tilde{\kappa} + \delta\tilde{\kappa}_{(e)} \equiv \kappa_{(e)} + i\Xi_{(e)}$ should be quantified. Then, our perturbed figures-of-merit become

$U_{(e)} = \kappa_{(e)}/\sqrt{\Gamma_{1(e)}\Gamma_{2(e)}} \equiv U \cdot J_\kappa \sqrt{J_1 J_2}$ and $V_{(e)} = \Xi_{(e)}/\sqrt{\Gamma_{1(e)}\Gamma_{2(e)}} \equiv V \cdot J_\Xi \sqrt{J_1 J_2}$, where

$$J_{1,2} \equiv \frac{\Gamma_{1,2}}{\Gamma_{1,2(e)}} = \frac{Q_{1,2(e)}}{Q_{1,2}}, \quad J_\kappa \equiv \frac{\kappa_{(e)}}{\kappa} = \frac{Q_\kappa}{Q_{\kappa(e)}} \quad \text{and} \quad J_\Xi \equiv \frac{\Xi_{(e)}}{\Xi} = \frac{Q_\Xi}{Q_{\Xi(e)}} \tag{10.3}$$

are the perturbation figures-of-merit. In typical situations of random objects, all the above J factors will be less than one, namely the system performance will typically deteriorate in their presence. However, interference effects between the (radiation) far field of an initial resonant-object mode and the field scattered off the extraneous object could, for strong scattering (e.g. off metallic objects), result in reduced individual or system radiation losses, namely $J_{1,2} > 1$ or $J_\Xi > 1$. Similarly, reshaping of the (stationary) near field, which we utilize for the coupling in this proposed energy-transfer scheme, due to the extraneous object could make it more directional towards the device object and thus increase the coupling $J_\kappa > 1$. Therefore, the wireless energy-transfer scheme will be robust provided the J factors are not much less than one, but, even in that case, it could still be viable, if starting from large initial figure-of-merit U (and V). In the following section, we compute some of these perturbation figures-of-merit for realistic systems and placements of the extraneous objects.

10.2 Robust lifetime and coupling of resonances in the near-presence of extraneous objects

Based on the conclusions of the previous Section, the robustness of our energy-transfer method depends on the deterioration factors J, which ideally should be close to one and whose calculation is the task of this Section. However, before undertaking this task, let us note that, as was pointed out, what really matters are the various products UJ, namely the method is still applicable, even if the extrinsic loss-rates are larger than the intrinsic loss-rates, provided that they are still smaller than the coupling rate. In that sense, our sharp-resonance-based scheme is extremely powerful, because, in the presence of a device resonant-object and an extraneous non- or off-resonant object at the same distance from the source resonant-object, the source energy significantly (as discussed earlier, by $\sim Q^2$ times more) favors the resonant object. A simple daily example is how, out of 100 wines glasses, filled up to different levels with wine, only one will break, when a guitar player plays a single tone matching this glass' resonance frequency, while the others will remain intact.

Therefore, this resonant scheme has inherent a transfer selectivity, which contributes greatly to its robustness.

Clearly though, it may be the case that random objects are located much closer to one or more of our system resonators than the other resonators are, so their effect certainly requires estimation and will depend on the objects' particularities in terms of size, materials and placement. An object will typically scatter a field incident on it: when its size is larger than the wavelength, the scattering occurs more in the form of specular reflection of geometric rays, while in the case of a subwavelength object, the incident field will simply reshape itself and wrap around the 'small' object, thus suffering little obstruction. Therefore, not only do resonant objects exchange energy selectively between them, but also subwavelength resonant objects, such as those utilized by our scheme, do not require line-of-sight, when obstructed by similar-sized (subwavelength) objects, as opposed to a radiative energy-transfer method, which would be fatally interrupted. Furthermore, exactly because the near field spreads out from the source, when delivering a certain amount of power to the device, the local power density is typically quite smaller than that of a focused radiated beam; delivering the same power with smaller local fields means that the scheme is less sensitive and, very importantly, much safer. Finally, objects, whose material properties do not differ a lot from those of air (as far as the particular field in use is concerned), or which are located at a region of weak field or distant from the resonant objects or not interrupting their line-of-sight, will obviously have small effects on the system performance and can be considered weak perturbations. In this Section, we want to quantitatively confirm the above arguments based on physical intuition, examine a variety of types of random objects, and consider ways in which their influence can be reduced.

Again, we will investigate electromagnetic resonances. For small perturbations, the frequency detuning induced by the extraneous object e (described by a low-loss complex permittivity function $\epsilon_e + i\epsilon_e''$ and a low-loss complex permeability function $\mu_e + i\mu_e''$) onto the resonant eigenmode [$\mathbf{E}$, $\mathbf{H}$] of an object can be determined by the formula

$$\delta\omega_{(e)} = \frac{\omega \frac{1}{2} \int_{V_e} dv \left[(\epsilon_e - \epsilon_o) |\mathbf{E}|^2 + (\mu_e - \mu_o) |\mathbf{H}|^2 \right] + \frac{1}{2} \oint_{S_e} da \hat{\mathbf{n}}_e \cdot \mathrm{Im} \{\mathbf{E}^* \times \mathbf{H}\}}{2\frac{1}{4} \int_V dv \left(\epsilon |\mathbf{E}|^2 + \mu |\mathbf{H}|^2 \right)} \tag{10.4}$$

where ϵ, μ the dielectric and magnetic functions of the whole system. The extrinsic loss

mechanisms for an electromagnetic resonance are: far-field scattering approximately at a rate

$$(\delta Q)^{-1}_{\mathrm{scat}(e)} \equiv \frac{2\delta\Gamma_{\mathrm{scat}(e)}}{\omega} = \frac{P_{\mathrm{scat}(e)}}{\omega W} = \frac{\frac{\zeta_o}{2}\left(\frac{\omega}{4\pi c_o}\right)^2 \oint d\Omega \left|\mathbf{f}_{(e)}\right|^2}{\omega\frac{1}{4}\int_V dv \left(\epsilon\left|\mathbf{E}\right|^2 + \mu\left|\mathbf{H}\right|^2\right)}, \tag{10.5}$$

where $\mathbf{f}_{(e)} = \int_{V_e} dv \mathbf{J}_{(e)}(\mathbf{r})\, e^{-i\mathbf{k}\cdot\mathbf{r}}$ is a vector current-moment and $\mathbf{J}_{(e)}$ are the induced currents on object e due to the field of the resonant object either in the form of dielectric-polarization currents ($\mathbf{J}_{\mathrm{p}(e)} = -i\omega(\epsilon_e - \epsilon_o)\mathbf{E}$) or electric currents on its surface ($\mathbf{J}_{\mathrm{s}(e)} = \hat{\mathbf{n}}_e \times \mathbf{H}$), if it is a metal, and absorption inside e at a rate, provided it is weak ($\epsilon''_e/\epsilon_e,\ \mu''_e/\mu_e \ll 1$),

$$(\delta Q)^{-1}_{\mathrm{abs}(e)} \equiv \frac{2\delta\Gamma_{\mathrm{abs}(e)}}{\omega} = \frac{P_{\mathrm{abs}(e)}}{\omega W} = \frac{\omega\frac{1}{2}\int_{V_e} dv \left(\epsilon''_e\left|\mathbf{E}\right|^2 + \mu''_e\left|\mathbf{H}\right|^2\right) + \frac{1}{2}\oint_{S_e} da\hat{\mathbf{n}}_e \cdot \mathrm{Re}\left\{\mathbf{E}^* \times \mathbf{H}\right\}}{\omega\frac{1}{4}\int_V dv \left(\epsilon\left|\mathbf{E}\right|^2 + \mu\left|\mathbf{H}\right|^2\right)}. \tag{10.6}$$

When a system of two objects 1, 2 with resonant eigenmodes $[\mathbf{E}_{1,2},\ \mathbf{H}_{1,2}]$ is slightly perturbed by an extraneous object, the shift in the coupling rate $\delta\kappa_{(e)}$ and in the interference parameter $\delta\Xi_{(e)}$ will similarly be a perturbative function of the unperturbed fields and the extraneous object's properties.

Even though Eqs.(10.4)-(10.6) hold only for weak external interactions, they provide very useful physical intuition:

• All perturbations induced on an object 1 by e depend on the square of the small resonant field-tail of 1 at the site of e, while the coupling coefficient between 1, 2 from Eq.(8.22) depends only linearly on the small resonant field-tail of 1 at the site of 2. Therefore, for same distances of e and 2 from 1, and given that the resonant field of 1decays with some exponential or power law, the coupling rate will always be stronger than the extrinsic-loss rates (so $U\sqrt{J_1 J_2} > 1$), confirming analytically our earlier physical intuition that high-Q resonances are highly selective.

• Extraneous objects with sizes much smaller than the wavelength ($\lambda = 2\pi c_o/\omega$) lead, from Eq.(10.5), to very weak scattering, confirming analytically our intuition on the robustness of quasi-static (subwavelength) resonances.

• Most importantly, given that almost all common non-conducting materials are non-magnetic (namely they have $\mu_e \approx \mu_o,\ \mu''_e \approx 0$) but just dielectric, they respond to magnetic fields in the same way as free space, and thus, if our resonators are designed so that the electric field is confined within the resonator, while the magnetic field is the one extending

into free space and utilized for the coupling, then all these common materials irrespectfully of size and placement will disturb our so-called 'magnetic' resonances very little. This separate localization of the electric and magnetic fields, which can deliver the same power ($\mathbf{E} \times \mathbf{H}$) of a radiative plane wave but with a much larger (but safe) $\mathbf{H}$ than $\mathbf{E}$, can happen only in the magneto-quasi-static regime. Only extraneous conducting materials may lead to substantial extrinsic losses due to the eddy currents induced on their surface or to reduced coupling due to the imposed reformation of the magnetic field to be parallel to their surface. An extremely important implication of 'magnetic' resonances relates to safety considerations for human beings. Humans are also non-magnetic and can sustain strong magnetic fields without undergoing any risk. A typical example, where dc magnetic fields $B \sim 1\text{T}$ are safely used on humans, is the Magnetic Resonance Imaging (MRI) technique for medical testing. In contrast, the ac magnetic near-field required in typical microwave energy-transfer systems in order to provide a few Watts of power to devices is only $B \sim 10^{-4}\text{T}$, which is actually comparable to the magnitude of the Earth's dc magnetic field. Since, this scheme is attempting to also minimize the far-field radiation produced, it is reasonable to expect that an energy-transfer method based on 'magnetic' resonances should be safe for living organisms.

Among the examples analyzed earlier, those of dielectric disks (storing the electric energy inside the high-ϵ material), capacitively-loaded loops and self-resonant coils of small h/r-aspect-ratio (storing the electric energy inside the capacitor and distributed capacitance respectively) are predominantly *high-Q magneto-quasi-static resonances* and therefore we will limit our sensitivity analysis to those structures.

Eqs.(10.5) and (10.6), by definition of perturbation theory, hold only for small perturbations. Therefore, even though they provide some useful physical intuition, quantitatively they can only treat easy cases, such as small low-loss and distant extraneous objects, which are not of interest, since we want to test our scheme in more realistic, difficult situations. Therefore, we will use only computational and experimental analyses, and we will investigate the more dangerous cases of either large low-loss objects or small high-loss or conductive objects. We will avoid the extreme cases of both large and highly-lossy or conductive objects, since we cannot expect our scheme to work under *any* condition (for example, if such an object is placed inbetween the source and the device, it would obviously interrupt the energy transfer). In the end, we will find that the wireless energy-transfer scheme can still

be viable for a wide range of extraneous objects and their positionings.

10.2.1 Dielectric resonators

10.2.1.1 Dielectric disks

In the case of dielectric disks, we examine the robustness of their resonances in the presence of one of the following different off-resonance objects: a surface of large extent but of small ϵ, ϵ'' (such as a wall w), as shown in Figures 10-1(a,b), and an object of large ϵ, ϵ'' but of small size (same as the size of the disk but different shape, such as a human muscle m), as shown in Figures 10-1(c,d), where the values of ϵ were found in Ref.[110]. We test their influence as a function of distance with the choice of disk-mode highlighted with bold in Table 8.1 and for the two different placements along the lines where the field eigenmode is minimum (Figures 10-1(a,c)) and maximum (Figures 10-1(b,d)). The results for J of the FEFD simulations are shown in Figure 10-1(e). For distances $D_{(w,m)}$ between the edges of the disk and the 'muscle' or 'wall', the disk resonance seems to be fairly robust, apart for the case of a close-proximity of the 'muscle'.

To examine now the influence of these objects on the entire energy-transfer system, we consider two resonant disks in the close presence of 'walls' and 'muscles', in the configurations shown in Figures 10-2(a-d) (note that due to the symmetry vertical plane, there are twice the random objects than those shown). As can be seen from Figure 10-2(f) the coupling is very robust in the presence of the objects (actually often improved), except when a large-ϵ object is immediately interrupting the field lines, as in (c) the worst possible placement, but still the effect is not strong. The final figure-of-merit is seen to deteriorate by a substantial factor of $5 - 10$ only in the case of the lossy object and because we placed it close to the disks (and again there are twice that many from those shown).

Therefore, we can claim that the energy-transfer scheme is not detrimentally disturbed by the presence of the extraneous objects, with the exception of the very-close proximity of high-loss objects.

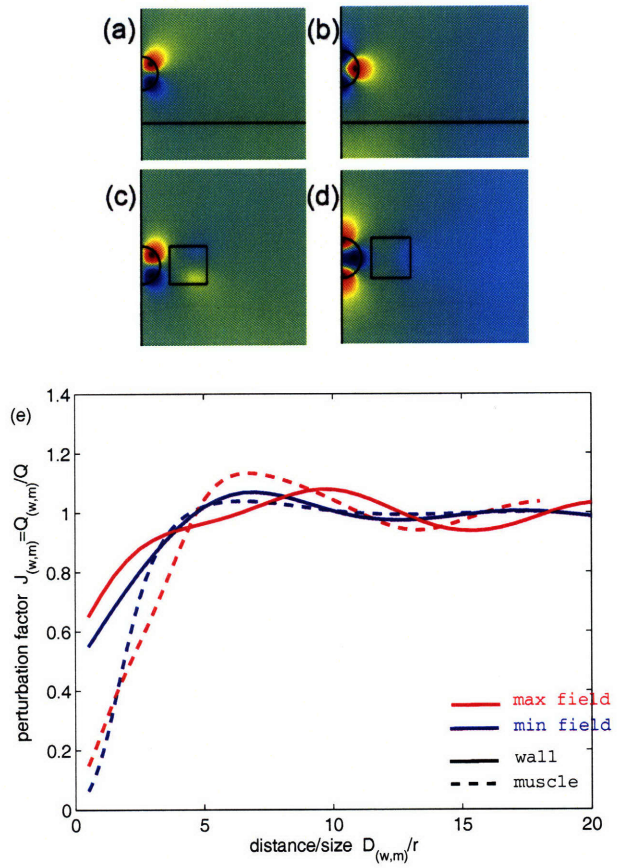


Figure 10-1: (e) Deterioration factor J of Q for a disk mode in the presence of (a,b) a large wall w of $\epsilon = 2.5 + 0.05i$ (typical for daily materials) and (c,d) a small square human muscle m of $\epsilon = 49 + 16i$ (appropriate in the GHz regime) and side $2r$, as a function of the edge-to-edge distance $D_{(w,m)}$ and for two different positionings compared to the disk: (a,c) along the direction of minimum field and (b,d) along the direction of maximum field.

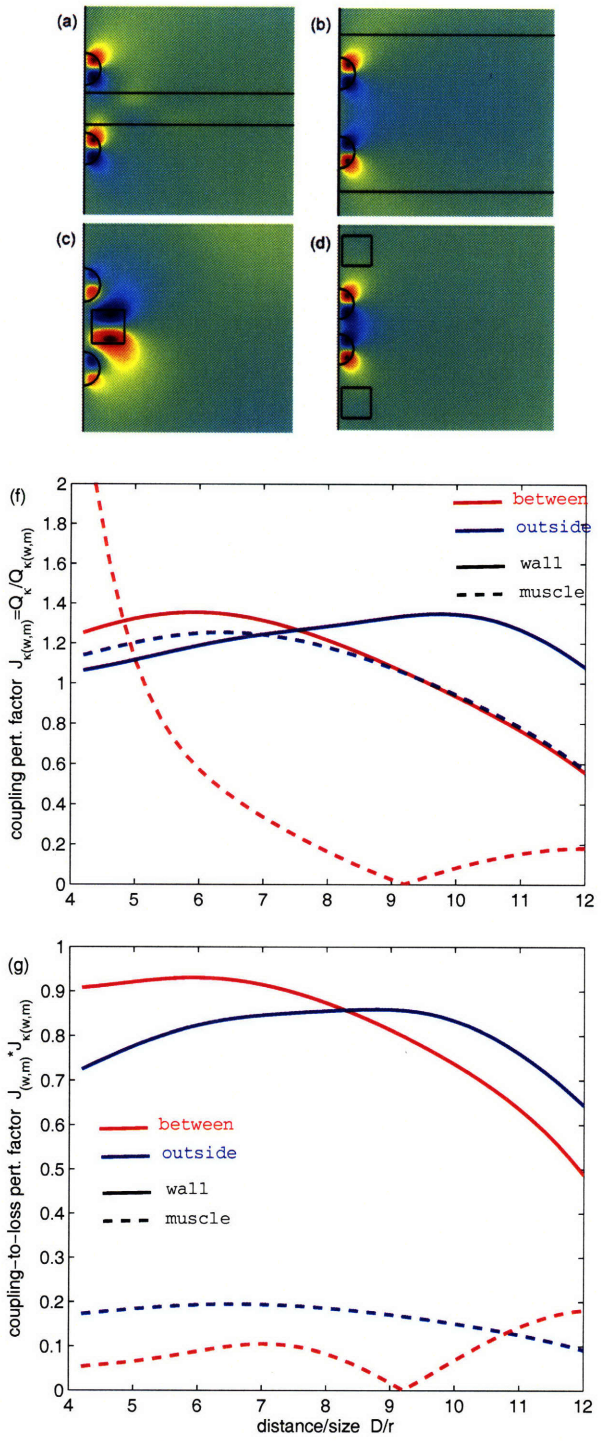


Figure 10-2: Deterioration factors (f) J_κ of Q_κ and (g) $J \cdot J_\kappa$ of U for two coupled disk modes in the presence of (a) a large wall w of $\epsilon = 2.5 + 0.05i$ and thichness $2r$ between the disks, (b) two walls, one behind each disk at distance r , (c) a small square human muscle m of $\epsilon = 49 + 16i$ and side $2r$ between the disks, and (d) two muscles, one behind each disk at distance r.

10.2.2 Metallic resonators

10.2.2.1 Capacitively-loaded conducting loops

For these systems, the subwavelength resonances we have examined are definitely of the magneto-quasi-static type. The dominating field in the space surrounded by the loop is the magnetic field generated by the loop current, accompanied (necessarily from Maxwell Equations) by an electric field proportional to the very small resonant frequency; the additional electric energy required for resonance is that stored (hidden) inside the capacitor. One can estimate the degree to which such a loop has mostly magnetic energy stored in the space surrounding it: if one ignores the fringing electric field from the capacitor, the electric and magnetic energy densities in the space surrounding the loop are given from simple analytical formulas for a subwavelength ($r \ll \lambda$) current loop, so we can calculate their ratio as a function of the distance D_p from the center of the loop (in the limit $r \ll D_p$) and the angle θ with respect to the loop axis [102]

$$\frac{w_e(p)}{w_m(p)} = \frac{\epsilon_o |E(p)|^2}{\mu_o |H(p)|^2} = \frac{\left(1+\frac{1}{p^2}\right)\sin^2\theta}{\left(\frac{1}{p^2}+\frac{1}{p^4}\right)4\cos^2\theta + \left(1-\frac{1}{p^2}+\frac{1}{p^4}\right)\sin^2\theta} \tag{10.7}$$

$$\Rightarrow \frac{\oint_{S_p} da\epsilon_o |E(p)|^2}{\oint_{S_p} da\mu_o |H(p)|^2} = \frac{1+\frac{1}{p^2}}{1+\frac{1}{p^2}+\frac{3}{p^4}},$$

where $p \equiv 2\pi D_p/\lambda$ and the second line is the ratio of averages over all angles by integrating the electric and magnetic energy densities over the surface of a sphere of radius D_p. From Eq.(10.7) it is obvious that indeed for all angles in the near field ($p \ll 1$) the magnetic energy density is dominant, while in the far field ($p \gg 1$) they are equal as should always be for radiative fields. Therefore, this is the criterion that qualifies this class of resonant systems as 'magnetic'.

To provide an estimate of the effect of extraneous objects on the resonance of a capacitively-loaded loop, including the capacitor fringing electric field, we bring a 'human muscle' on top of the capacitor of the loop highlighted with bold in Table 8.2. The computational FEFD results are shown in Figure 10-3 and suggest that this perturbation is weak and thus little power will be imparted onto humans for ordinary distances and placements (not immediately on top of the capacitor). This will be true even better for most ordinary extraneous objects e of much smaller loss-tangent, therefore we conclude that it is indeed fair to say

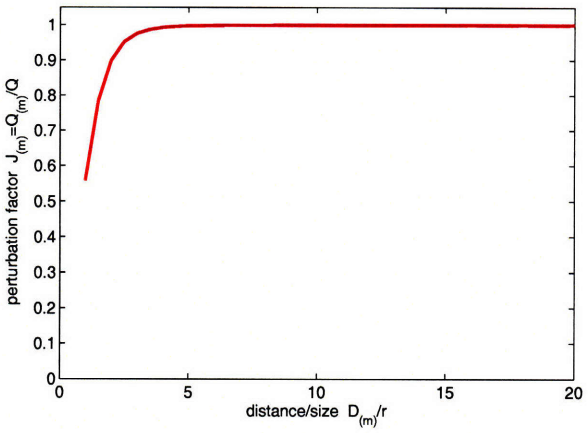


Figure 10-3: Deterioration factor J of Q for a loop mode in the presence of a human muscle m of $\epsilon = 185 + 1230i$ (appropriate in the MHz regime) and dimensions 25cm $\times$ 25cm $\times$ 1.5m, as a function of the edge-to-edge distance $D_{(m)}$ between the muscle and the capacitor.

that our proposed wireless energy-transfer scheme based on magneto-quasistatic resonances is indeed insensitive. The only perturbation that is expected to affect these resonances is a close proximity of large metallic structures.

10.2.2.2 Self-resonant conducting coils [5]

We expect self-resonant coils to be more sensitive to external perturbations than capacitively-loaded loops, as the majority of the electric field is now not confined inside a closed capacitor, but rather distributed across the coil (its capacitance). Since for this class of resonators we performed experiments, it sufficed to test the experimental setup and performance for robustness in the presence of extraneous objects, and did not perform thorough numerical simulations. From our observations, the wireless power-tranmission was not found to be visibly affected, as humans and various everyday objects (such as metallic and wooden furniture, electronic devices large and small etc) were placed between the two coils, even when they drastically obstructed the line of sight between source and device, as can be seen in a photograph in Figure 10-4. External objects were found to have an effect only when they were closer than 10cm from either one of the coils. While some materials (such as aluminum foil, styrofoam and humans) mostly just shifted the resonant frequency (which, as discussed earlier, is not a problem, since it can be easily corrected with a feedback circuit), others (cardboard, wood, and PVC) lowered Q, when placed closer than a few cm from the coil, thereby lowering the efficiency of the wireless powering, but not detrimentally. In summary,

we believe that our setup was fairly robust and thus the method should be viable for a large number of applications.

Reciprocally, we believe that this method of power transmission should be safe for humans. When transferring 60W (more than enough to power a laptop computer) across 2m, we estimated that the magnitude of the ac magnetic field generated is much weaker than the dc Earth's magnetic field for all distances, except for less than about 1cm away from the wires in the coil, an indication of the safety of the scheme even after long-term use. (Comparing ac to dc fields, of course, is not a completely fair comparison, so to be secure that this method is safe, precise tests need to be carried through.) In Figure 10-5, a photograph of the entire reasearch team between the operating wireless energy-transfer is shown.

Finally, the power radiated for these parameters was $\sim$ 5W, which is roughly an order of magnitude higher than cell phones but could be drastically reduced by designing the system to operate at lower frequencies. Therefore, this method should not be a cause of interference in the far-field, namely to communication or surveillance systems, either.

In any case, such a method of wireless energy-transfer would clearly have to abide by international regulations (e.g. by FCC) both for safety and interference, and specific frequency ranges would be allocated to it.

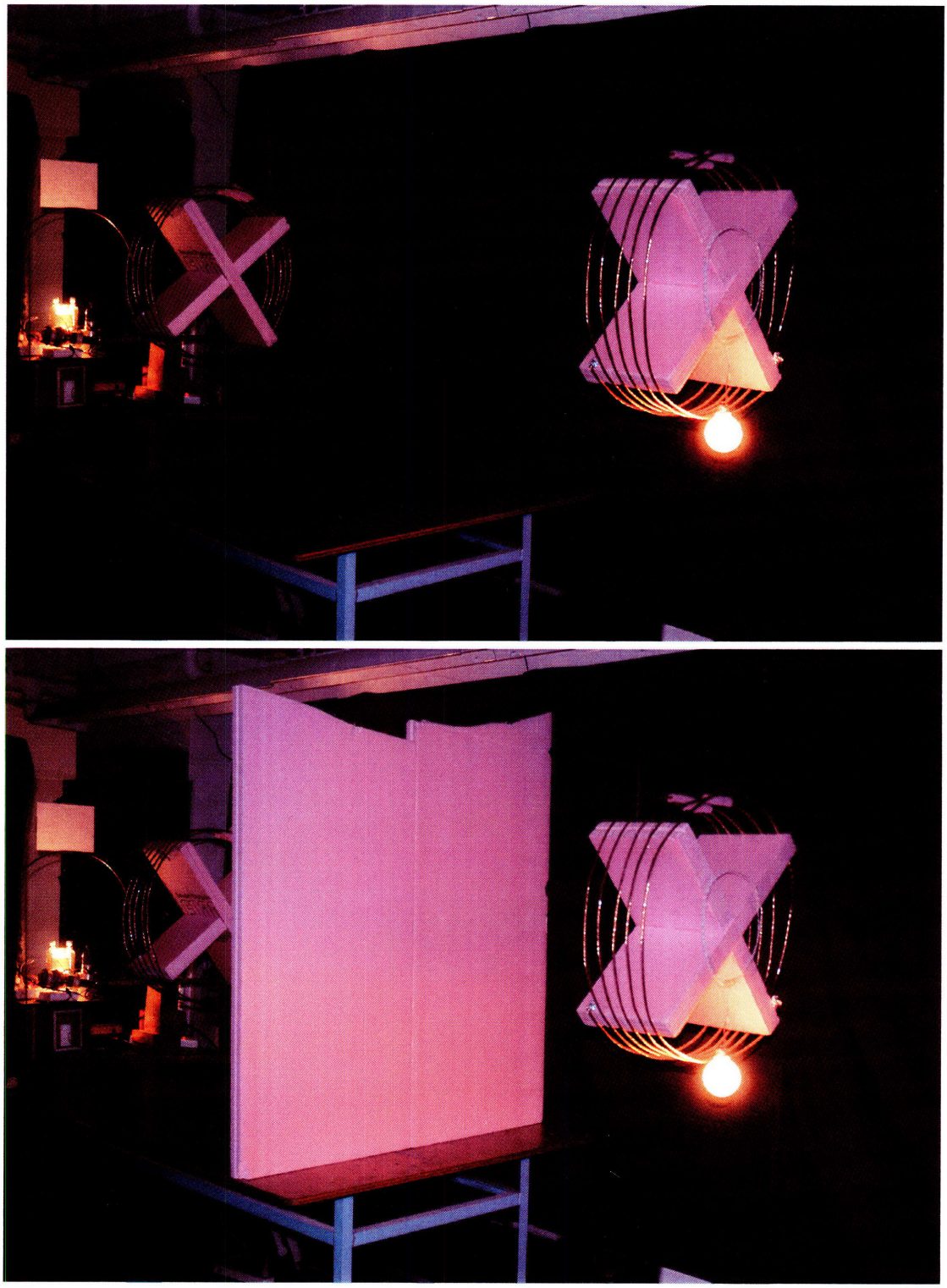


Figure 10-4: Photograph of the experimental system, with and without an obstruction in the line-of-sight of the self-resonator coils, while achieving transmission of 60W across 2m distance. There is no visible difference in the brightness of the light-bulb.



Figure 10-5: Photograph of the experimental system, with the entire research team between the self-resonant coils, while achieving transmission of 60W across 2m distance. All the members of the team are smiling!

Chapter 11

Conclusion

In conclusion, we have described a method based on high-Q and strongly-coupled resonances for mid-range efficient, insensitive wireless energy-transfer. The two performance criteria that were not analyzed in this work are mobility and versatility, so we will comment on those here.

11.1 Mobility and versatility

For a system of wireless energy-transfer to be mobile, the following requirements need to be met:

• omnidirectionality of the fields, which is an inherent feature of the near-fields of our quasi-static resonances (typically, for the metallic resonators the coupling has only a factor of 2 difference between min and max orientations),

• independence from the presence or not of line-of-sight, which we proved both numerically and experimentally and is again due to the subwavelength performance,

• fast dynamic response, which is definitely true since the energy-transfer time is $\sim Q_\kappa$ times smaller than the temporal period (thus $\sim$ 1ms for operation in the MHz) and thus much shorter than any timescale associated with motions of macroscopic objects, and

• fast feedback mechanisms that keep the frequency tuned and achieve impedance matching in real-time, for which some possible implementations were discussed in Section 10.1.

Thus our method seems highly suitable for mobile receivers and minimal additional design would be required to accommodate them.

In order for this system to be versatile, namely to be able to handle simultaneously a

variety of different receivers, different levels of complication can be followed in the approach to meet the specific individual power requirements of each object, while maintaining good overall efficiency: all on resonance but adjusted loading, some frequency- or time-division multiplexing scheme etc. The essence is that the omnidirectionality of the method makes it physically capable to accommodate versatile loading conditions.

Therefore, in total, our proposed wireless energy-transfer scheme is believed to have all the good properties desired. Very simple implementation geometries already provide encouraging performance characteristics, and thus the proposed mechanism is promising for many modern and future applications.

11.2 Applications

The possible applications can be split into three main categories. The first, and perhaps most obvious one, relates to commodity and aesthetics: this wireless powering mechanism could free us from the need to remember to recharge the ubiquitous electronic devices (laptops, cell phones, PDA's, digital cameras) and to eliminate the unappealing mess of entangled wires and cables in our houses and offices. Even though, perhaps the most popular class of applications, this is clearly not a necessity and thus must be considered with precaution in our presently energy-deficient world.

Second, and more important, this method could help improve the performance of already existing technologies: Typically, most mobile devices operating some function and delivering work (such as robots, autonomous vehicles, sensors) nowadays rely on batteries, and thus their operation needs to be interrupted regularly to recharge, their cost is increased and they are loaded with additional unnecessary weight. Instead, placing a wireless-power source (connected to the wired electricity network) under the floor or on the ceiling of a residential or industrial room could enable these devices to roam freely within the room, operating uniterrupted and, depending on the application, perhaps even freeing them completely from the need of a battery. Other mobile devices, predominantly vehicles, receive their power from gas, with the obvious negative results in depletion of existing energy resources and environmental pollution. By switching to electric-powered vehicles, which are much more energy efficient and environmental friendly, one could envision a future, where highways or city streets or traffic lights were equiped with a wireless powering system that would provide

real-time powering or overnight or during-stop recharging. Other types of work-performing mobile devices are wired robotic parts in industrial equipment (such as mechanical arms and joints) that have some degrees of freedom to rotate, but their full mobility is limited by the dependence on the power wire, which is also subject to wear and tear, with the course of time, due to the machine motion. All these problems would be resolved, if the wire was not needed.

Third, and most exciting, the method could enable new technologies: There is a certain class of devices that are hidden or embedded somewhere and are thus difficult or impossible to reach for wired powering or recharging. The most striking examples are implanted medical devices (e.g. artificial hearts, pacemakers, medicine delivery pumps, etc.) and buried underground sensors. In these cases, depending on the importance of the application, one could definitely tolerate a lower efficiency.

All the previous applications were drawn from the daily macroworld. However, since the method is based on general physical scalable principles and not on precise material geometries or even fields, there can be many applications also in the microscopic world, where much smaller wavelengths would be used and smaller powers are needed. For example, one could use it to implement optical inter-connects for CMOS electronics, or to transfer energy to autonomous nano-objects (e.g. MEMS or nano-robots) without worrying much about the relative alignment between the sources and the devices.

11.3 Future directions

Further improvement is expected with serious design optimization and a large number of directions are open for further exploitation. Such work would be focused on improving all aspects of the proposed technology, namely increasing its efficiency and range (or equivalently decreasing the size of the objects), reducing its sensitivity, designing an efficient and compact driving power-supply system, working on the dynamic aspects of the system to handle mobile receivers, designing a protocol to enable and control simultaneous powering of multiple devices, configuring a robust cheap packaging profile and broadening the method's range of applicability.

Some steps have already been taken towards the realization of these goals and we would like to share them as an epilogue. To reduce the size of the device structure so that it

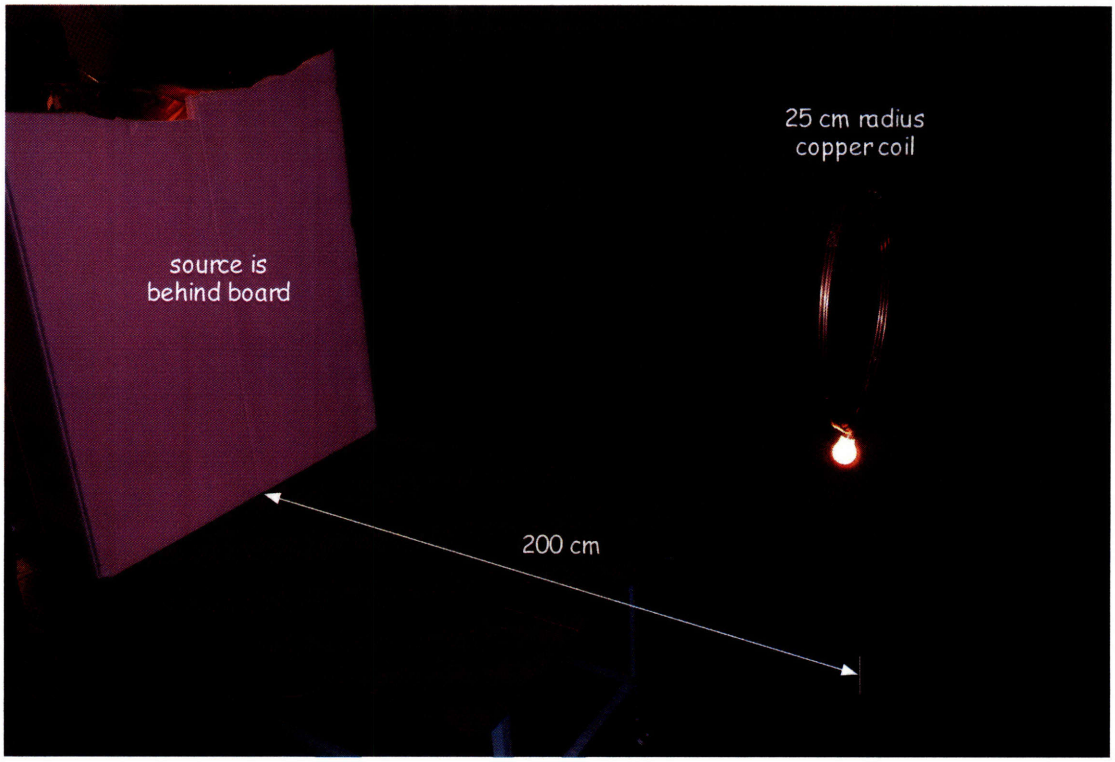


Figure 11-1: Photograph of another experimental setup, where 15W are being delivered to a load on a 50cm-diameter coil across 2m distance, from a source hidden behind a board.

can fit into portable devices, since typically there would not be restrictions on the source size and placement, based on Eq.(8.32), one could, for instance, maintain the product of the characteristic sizes of the source and device objects constant without sacrificing the efficiency. Exactly this approach was realized and is shown in a photograph in Figure 11-1, where a 50cm-diameter but only 4cm-thick coil is delivering 15W to its load, being powered wirelessly across 2m from a source coil of $\sim$ 80cm in diameter hidden behind a styrofoam wall. The setup perhaps starts looking more like what one would expect having in our future homes to power all kinds of devices, namely like what one would perhaps envision as wireless electricity (WiTricity) ...

Part III

Appendices

Chapter 12

Coupled-Mode Theory in electromagnetism

12.1 Derivation of coupled equations and coupling coefficients

Imagine a system of N electromagnetic resonators in proximity to each other. One of the formulations of CMT to predict the coupling-matrix elements is as follows: Let ϵ_n, μ_n be the dielectric, magnetic functions of space that describe only the generally anisotropic, lossy but reciprocal object n (minus the constant ϵ_o, μ_o background) and $\epsilon = \epsilon_o + \sum_n \epsilon_n$, $\mu = \mu_o + \sum_n \mu_n$ the dielectric, magnetic function of the whole system. Each object n, when alone in space, supports a resonant eigenmode of complex frequency ω_n and field profiles $[\mathbf{E}_n, \mathbf{H}_n]$ normalized to unity energy, satisfying the equations

$$\nabla \times \mathbf{E}_n = i\omega_n (\mu_o + \mu_n) \mathbf{H}_n, \qquad \nabla \times \mathbf{H}_n = -i\omega_n (\epsilon_o + \epsilon_n) \mathbf{E}_n \tag{12.1}$$

and the boundary conditions

$$\hat{\mathbf{n}} \times \mathbf{E}_n = 0 \tag{12.2}$$

on the potential metallic surface S_n of object n, while the time-reversed fields $[\mathbf{E}_n^-, \mathbf{H}_n^-]$ satisfy the same equations where $\omega_n \to -\omega_n$. The field of the whole system $[\mathbf{E}, \mathbf{H}]$ satisfies

$$\nabla \times \mathbf{E} = -\mu \frac{\partial}{\partial t} \mathbf{H}, \qquad \nabla \times \mathbf{H} = \epsilon \frac{\partial}{\partial t} \mathbf{E} \tag{12.3}$$

and the boundary condition

$$\hat{\mathbf{n}} \times \mathbf{E} = 0 \tag{12.4}$$

on $S = \sum_{\mathrm{n}} S_{\mathrm{n}}$ accounting for every metallic surface. Consider now the formula

$$\nabla \cdot \left(\mathbf{E} \times \mathbf{H}_{\mathrm{n}}^{-} - \mathbf{E}_{\mathrm{n}}^{-} \times \mathbf{H} \right) = \mathbf{H}_{\mathrm{n}}^{-} \cdot \nabla \times \mathbf{E} - \mathbf{E} \cdot \nabla \times \mathbf{H}_{\mathrm{n}}^{-} + \mathbf{H} \cdot \nabla \times \mathbf{E}_{\mathrm{n}}^{-} - \mathbf{E}_{\mathrm{n}}^{-} \cdot \nabla \times \mathbf{H} =$$

$$= \mathbf{H}_{\mathrm{n}}^{-} \cdot \left(-\mu \frac{\partial}{\partial t} \mathbf{H} \right) - \mathbf{E} \cdot \left[i\omega_{\mathrm{n}} \left(\epsilon_{\mathrm{o}} + \epsilon_{\mathrm{n}} \right) \mathbf{E}_{\mathrm{n}}^{-} \right] + \mathbf{H} \cdot \left[-i\omega_{\mathrm{n}} \left(\mu_{\mathrm{o}} + \mu_{\mathrm{n}} \right) \mathbf{H}_{\mathrm{n}}^{-} \right] - \mathbf{E}_{\mathrm{n}}^{-} \cdot \left(\epsilon \frac{\partial}{\partial t} \mathbf{E} \right) \tag{12.5}$$

using the Eqs.(12.1) and (12.3). Integrating now over the entire space V, excluding the regions enclosed by the closed metallic surfaces S, and applying the divergence theorem, Eq.(12.5) becomes

$$\mathrm{LHS} = \oint_{S} da \hat{\mathbf{n}} \cdot \left(\mathbf{E} \times \mathbf{H}_{\mathrm{n}}^{-} - \mathbf{E}_{\mathrm{n}}^{-} \times \mathbf{H} \right) = \oint_{S} da \hat{\mathbf{n}} \cdot \left(\mathbf{E}_{\mathrm{n}}^{-} \times \mathbf{H} \right) = \sum_{\mathrm{m} \neq \mathrm{n}} \oint_{S_{\mathrm{m}}} da \hat{\mathbf{n}} \cdot \left(\mathbf{E}_{\mathrm{n}}^{-} \times \mathbf{H} \right),$$

$$\mathrm{RHS} = \int_{V} dv \left[-\mathbf{E}_{\mathrm{n}}^{-} \cdot \epsilon \frac{\partial}{\partial t} \mathbf{E} - i\omega_{\mathrm{n}} \mathbf{E} \cdot \left(\epsilon_{\mathrm{o}} + \epsilon_{\mathrm{n}} \right) \mathbf{E}_{\mathrm{n}}^{-} - \mathbf{H}_{\mathrm{n}}^{-} \cdot \mu \frac{\partial}{\partial t} \mathbf{H} - i\omega_{\mathrm{n}} \mathbf{H} \cdot \left(\mu_{\mathrm{o}} + \mu_{\mathrm{n}} \right) \mathbf{H}_{\mathrm{n}}^{-} \right] =$$

$$= -\int_{V} dv \left\{ \mathbf{E}_{\mathrm{n}}^{-} \cdot \left[\epsilon \frac{\partial}{\partial t} + i\omega_{\mathrm{n}} \left(\epsilon_{\mathrm{o}} + \epsilon_{\mathrm{n}} \right) \right] \cdot \mathbf{E} - \mathbf{H}_{\mathrm{n}}^{-} \cdot \left[\mu \frac{\partial}{\partial t} + i\omega_{\mathrm{n}} \left(\mu_{\mathrm{o}} + \mu_{\mathrm{n}} \right) \right] \cdot \mathbf{H} \right\} =$$

$$= -\int_{V} dv \left\{ \mathbf{E}_{\mathrm{n}}^{-} \cdot \left[\epsilon \left(\frac{\partial}{\partial t} + i\omega_{\mathrm{n}} \right) - i\omega_{\mathrm{n}} \sum_{\mathrm{m} \neq \mathrm{n}} \epsilon_{\mathrm{m}} \right] \cdot \mathbf{E} - \mathbf{H}_{\mathrm{n}}^{-} \cdot \left[\mu \left(\frac{\partial}{\partial t} + i\omega_{\mathrm{n}} \right) - i\omega_{\mathrm{n}} \sum_{\mathrm{m} \neq \mathrm{n}} \mu_{\mathrm{m}} \right] \cdot \mathbf{H} \right\} \tag{12.6}$$

where we used the boundary conditions Eqs.(12.4) and (12.2) and the reciprocity of the materials (meaning the ϵ_{n}, μ_{n} tensors are symmetric).

So far the analysis has been exact. Now CMT takes the approach that the field of the total system can be described by a superposition of only those resonant modes that are close in frequency, while ignoring other eigenmodes of the resonators, thus truncating the overcomplete infinite-dimensional Hilbert space to a finite-dimensional one. If $a_{\mathrm{p}}(t)$ is the

field-amplitude of the p^{th} mode in the superposition, so that $|a_p(t)|^2$ is the total energy inside that resonator, then the CMT assumption is

$$\mathbf{E} = \sum_p a_p(t)\,\mathbf{E}_p, \qquad \mathbf{H} = \sum_p a_p(t)\,\mathbf{H}_p, \tag{12.7}$$

which, when plugged into Eq.(12.6), gives

$$\begin{aligned} &-\sum_p \left[\int_V dv\left(\mathbf{E}_n^- \cdot \epsilon \cdot \mathbf{E}_p + \mathbf{H}_n^- \cdot \mu \cdot \mathbf{H}_p\right)\right]\left(\frac{d}{dt} + i\omega_n\right) a_p \\ &+i\omega_n \sum_p \sum_{m\neq n} \left[\int_V dv\left(\mathbf{E}_n^- \cdot \epsilon_m \cdot \mathbf{E}_p + \mathbf{H}_n^- \cdot \mu_m \cdot \mathbf{H}_p\right)\right] a_p \\ &= \sum_p \sum_{m\neq n} \left[\oint_{S_m} da\hat{\mathbf{n}} \cdot \left(\mathbf{E}_n^- \times \mathbf{H}_p\right)\right] a_p. \end{aligned} \tag{12.8}$$

At this point, CMT makes another approximation of perturbative nature. If the objects do not interact strongly (because they are at considerable distance), then the field of one resonator at the site of another will be small. Therefore, one can characterize the terms in Eq.(12.8) by their order in such smallness. Then, it is clear that e.g. the term $\int_V dv \mathbf{E}_n^- \cdot \epsilon_m \cdot \mathbf{E}_p$ for $m \neq n \neq p$ will be 2^{nd}-order-small, much smaller than the 1^{st}-order-small term $\int_V dv \mathbf{E}_n^- \cdot \epsilon_p \cdot \mathbf{E}_p$ and similarly for the surface integrals. Therefore, by ignoring the terms with $m \neq p$, Eq.(12.8) becomes

$$\begin{aligned} &-\sum_p \left[\int_V dv\left(\mathbf{E}_n^- \cdot \epsilon \cdot \mathbf{E}_p + \mathbf{H}_n^- \cdot \mu \cdot \mathbf{H}_p\right)\right]\left(\frac{d}{dt} + i\omega_n\right) a_p \\ &+i\omega_n \sum_p \left[\int_V dv\left(\mathbf{E}_n^- \cdot \epsilon_p \cdot \mathbf{E}_p + \mathbf{H}_n^- \cdot \mu_p \cdot \mathbf{H}_p\right)\right] a_p \\ &= \sum_p \left[\oint_{S_p} da\hat{\mathbf{n}} \cdot \left(\mathbf{E}_n^- \times \mathbf{H}_p\right)\right] a_p. \end{aligned} \tag{12.9}$$

If now we define the quantities

$$W_{\mathrm{np}} = \frac{1}{4}\int_V dv\left(\mathbf{E}_{\mathrm{n}}^{-}\cdot\epsilon\cdot\mathbf{E}_{\mathrm{p}}+\mathbf{H}_{\mathrm{n}}^{-}\cdot\mu\cdot\mathbf{H}_{\mathrm{p}}\right) \tag{12.10}$$

$$C_{\mathrm{np}}=\omega_{\mathrm{n}}\frac{1}{4}\int_V dv\left(\mathbf{E}_{\mathrm{n}}^{-}\cdot\epsilon_{\mathrm{p}}\cdot\mathbf{E}_{\mathrm{p}}+\mathbf{H}_{\mathrm{n}}^{-}\cdot\mu_{\mathrm{p}}\cdot\mathbf{H}_{\mathrm{p}}\right)+\frac{i}{4}\oint_{S_{\mathrm{p}}} da\mathbf{E}_{\mathrm{n}}^{-}\cdot\mathbf{J}_{\mathrm{s,p}}, \tag{12.11}$$

where $\mathbf{J}_{\mathrm{s,p}}=\hat{\mathbf{n}}\times\mathbf{H}_{\mathrm{p}}$ the surface currents on the metallic surfaces, we can write Eq.(12.9) in matrix form

$$\sum_{\mathrm{p}} W_{\mathrm{np}}\frac{d}{dt}a_{\mathrm{p}}=-i\sum_{\mathrm{p}}\omega_{\mathrm{n}}W_{\mathrm{np}}a_{\mathrm{p}}+i\sum_{\mathrm{p}}C_{\mathrm{np}}a_{\mathrm{p}}\Leftrightarrow$$

$$\Leftrightarrow\bar{\mathbf{W}}\cdot\frac{d}{dt}\mathbf{a}=-i\bar{\mathbf{\Omega}}\cdot\bar{\mathbf{W}}\cdot\mathbf{a}+i\bar{\mathbf{C}}\cdot\mathbf{a}\Leftrightarrow$$

$$\Leftrightarrow\frac{d}{dt}\mathbf{a}=-i\left(\bar{\mathbf{W}}^{-1}\cdot\bar{\mathbf{\Omega}}\cdot\bar{\mathbf{W}}\right)\cdot\mathbf{a}+i\left(\bar{\mathbf{W}}^{-1}\cdot\bar{\mathbf{C}}\right)\cdot\mathbf{a}, \tag{12.12}$$

where $\mathbf{a}$ is a vector containing the field-amplitudes and $\bar{\mathbf{\Omega}}$ a diagonal matrix containing the eigenfrequencies. The elements of the matrices in parentheses contain sums of terms of different smallness-orders; if we discard terms that are 2 orders smaller than others in the sum and define $\mathbf{K}\equiv\bar{\mathbf{W}}^{-1}\cdot\bar{\mathbf{C}}$, then we find that $\bar{\mathbf{W}}^{-1}\cdot\bar{\mathbf{\Omega}}\cdot\bar{\mathbf{W}}\approx\bar{\mathbf{\Omega}}$ and we get the known CMT-equations form

$$\frac{d}{dt}\mathbf{a}=-i\bar{\mathbf{\Omega}}\cdot\mathbf{a}+i\mathbf{K}\cdot\mathbf{a}, \tag{12.13}$$

with

$$\kappa_{\mathrm{np}}=\frac{\omega_{\mathrm{n}}\frac{1}{4}\int_{V_{\mathrm{p}}}dv\left(\mathbf{E}_{\mathrm{n}}^{-}\cdot\epsilon_{\mathrm{p}}\mathbf{E}_{\mathrm{p}}+\mathbf{H}_{\mathrm{n}}^{-}\cdot\mu_{\mathrm{p}}\mathbf{H}_{\mathrm{p}}\right)+\frac{i}{4}\oint_{S_{\mathrm{p}}}da\mathbf{E}_{\mathrm{n}}^{-}\cdot\mathbf{J}_{\mathrm{s,p}}}{\frac{1}{4}\int_V dv\left(\mathbf{E}_{\mathrm{n}}^{-}\cdot\epsilon\mathbf{E}_{\mathrm{n}}+\mathbf{H}_{\mathrm{n}}^{-}\cdot\mu\mathbf{H}_{\mathrm{n}}\right)};\quad \mathrm{n}\neq\mathrm{p}, \tag{12.14}$$

while the coefficients κ_{nn} have more complicated forms in general, which may often lead to anomalous coupling-induced frequency shifts [111]. From the reciprocity of the system $\mathbf{K}$ must be a symmetric matrix.

Note that the elements given in Eqs.(12.10), (12.11) (and thus (12.14)) are given in terms of the time-reversed fields rather than the complex-conjugate fields. This was done in purpose, in order to be able to treat lossy systems, which may include both absorption and radiation (so $\mathbf{K}$ is non-Hermitian and thus has complex elements). However, if these losses are weak (namely we are dealing primarily with high-Q resonances), then it is fair to

approximate $[\mathbf{E}_{\mathrm{n}}^{-}, \mathbf{H}_{\mathrm{n}}^{-}] \approx [\mathbf{E}_{\mathrm{n}}^{*}, \mathbf{H}_{\mathrm{n}}^{*}]$. With this assumption and for isotropic materials, the expression (12.11) for the coupling coefficient becomes

$$\kappa_{\mathrm{np}} \approx \frac{\omega_{\mathrm{n}} \frac{1}{4} \int_{V_{\mathrm{p}}} dv \left(\mathbf{E}_{\mathrm{n}}^{*} \cdot \epsilon_{\mathrm{p}} \mathbf{E}_{\mathrm{p}} + \mathbf{H}_{\mathrm{n}}^{*} \cdot \mu_{\mathrm{p}} \mathbf{H}_{\mathrm{p}}\right) + \frac{i}{4} \oint_{S_{\mathrm{p}}} da \mathbf{E}_{\mathrm{n}}^{*} \cdot \mathbf{J}_{\mathrm{s,p}}}{\frac{1}{4} \int_{V} dv \left(\epsilon \left|\mathbf{E}_{\mathrm{n}}\right|^{2} + \mu \left|\mathbf{H}_{\mathrm{n}}\right|^{2}\right)}; \quad \mathrm{n} \neq \mathrm{p}, \tag{12.15}$$

exactly that of Eq.(8.22).

Finally, note that Eqs.(12.10), (12.11) (and thus (12.14)) are integrals of the fields that extend to infinity; however, in the case of radiative (leaky) modes, which are not proper modes and diverge to infinity, these integrals diverge too! The calculation of the coupling-matrix elements requires then some technique to avoid these divergences. One approach is to modify the integration path into the complex space (as done for example in numerical problems with Perfectly Matched Layer (PML) boundary conditions) so that the integrals coverge. Our approach here has been to simply truncate the integrals at the point where the modal energy density starts increasing exponentially due to its leaky nature. Both cases obviously give better results when radiation is weak.

12.2 Prediction of radiative far-field interference

It was noted in the previous Section that the coefficients (12.14) of the CMT coupling matrix will generally be complex, which we denote with a tilde. Even though we understand the physical interpretation of the real part as describing the coupling between the objects, the physical meaning of the imaginary part is not clear, so this will be the investigation topic here.

Let us assume a system of two objects 1, 2, absorb the diagonal coupling-matrix terms $\tilde{\kappa}_{11,22}$ into the frequencies $\tilde{\omega}_{1,2} = \omega_{1,2} - i\Gamma_{1,2}$ and write $\tilde{\kappa}\,(= \tilde{\kappa}_{12} = \tilde{\kappa}_{21}) = \kappa + i\Xi$. Then, in the case of weak losses (so we can use formula (12.15)) and considering that usually $\omega_1 \approx \omega_2 \equiv \omega$ and there are no 'magnetic currents' ($i\omega_2\mu_2\mathbf{H}_2 = 0$) but rather the usual volume-polarization ($\mathbf{J}_{\mathrm{p},2} = -i\omega_2\epsilon_2\mathbf{E}_2$) and surface-electric ($\mathbf{J}_{\mathrm{s},2}$) currents , we can write explicitly for Ξ

$$\Xi \approx \mathrm{Im}\left\{\frac{\omega_1 \frac{1}{4} \int_{V_2} dv \left(\mathbf{E}_1^{*} \cdot \epsilon_2 \mathbf{E}_2 + \mathbf{H}_1^{*} \cdot \mu_2 \mathbf{H}_2\right) + \frac{i}{4} \oint_{S_2} da \mathbf{E}_1^{*} \cdot \mathbf{J}_{\mathrm{s},2}}{\frac{1}{4} \int_{V} dv \left(\epsilon \left|\mathbf{E}_1\right|^{2} + \mu \left|\mathbf{H}_1\right|^{2}\right)}\right\} =$$

$$= \frac{1}{4W_{11}} \mathrm{Im} \left\{ \frac{\omega_1}{\omega_2} \frac{i}{4} \int_{V_2} dv \mathbf{E}_1^* \cdot \mathbf{J}_{\mathrm{p},2} + \frac{i}{4} \oint_{S_2} da \mathbf{E}_1^* \cdot \mathbf{J}_{\mathrm{s},2} \right\} \approx \frac{1}{4W_{11}} \mathrm{Re} \left\{ \int_{V_2} dv \mathbf{E}_1^* \cdot \mathbf{J}_2 \right\} =$$

$$= \frac{1}{4W_{11}} \mathrm{Re} \left\{ \int_{V_2} dv \left[\int_{V_1} dv \, i\omega\mu_{\mathrm{o}} \mathbf{J}_1 \frac{e^{ik|\mathbf{r}_2 - \mathbf{r}_1|}}{4\pi |\mathbf{r}_2 - \mathbf{r}_1|} \right]^* \cdot \mathbf{J}_2 \right\} =$$

$$= \frac{\omega\mu_{\mathrm{o}}}{16\pi W_{11}} \mathrm{Re} \left\{ \int_{V_1} dv \int_{V_2} dv \, \mathbf{J}_1^* \cdot \mathbf{J}_2 \frac{ie^{-ik|\mathbf{r}_2 - \mathbf{r}_1|}}{|\mathbf{r}_2 - \mathbf{r}_1|} \right\} = (1 \leftrightarrow 2) \,, \tag{12.16}$$

and to this formula we need to give some physical meaning.

Towards this goal, let us evaluate from Eqs.(12.13) the total power lost from the system

$$P_{\mathrm{loss}} = -\frac{d}{dt} \left(|a_1|^2 + |a_2|^2 \right) = 2\Gamma_1 |a_1|^2 + 2\Gamma_2 |a_2|^2 + 4\Xi \mathrm{Re} \left\{ a_1^* a_2 \right\} . \tag{12.17}$$

Clearly, the term involving an interaction between the two objects shouuld not include material absorption, since this is a very localized process inside each object. We therefore split this lost power into absorbed and radiated in the folowing way

$$P_{\mathrm{abs}} = 2\Gamma_{\mathrm{abs1}} |a_1|^2 + 2\Gamma_{\mathrm{abs2}} |a_2|^2 \tag{12.18}$$

$$P_{\mathrm{rad}} = 2\Gamma_{\mathrm{rad1}} |a_1|^2 + 2\Gamma_{\mathrm{rad2}} |a_2|^2 + 4\Xi \mathrm{Re} \left\{ a_1^* a_2 \right\} , \tag{12.19}$$

so the mysterious term is associated with the radiation from the two-object system. However, we have a tool to compute this radiated power separately: antenna theory.

Assume the total field is oscillating at a fixed frequency ω (as is the case for example when it is in one of the two normal modes or when it is externally excited). The power radiated from the 'array' of the two objects 1, 2 at vector-distance $\mathbf{D}$ between their centers, when $\mathbf{f}_{1,2} = \int_{V_{1,2}} dv \, \mathbf{J}_{1,2} \left(\mathbf{r}'_{1,2} \right) e^{-i\mathbf{k} \cdot \mathbf{r}'_{1,2}}$ is the vector current-moment of each one around its individual center and there is $W_{1,2} = |a_{1,2}|^2$ energy inside each one, is

$$P_{\mathrm{rad}} = \frac{\zeta_{\mathrm{o}}}{2} \left(\frac{\omega}{4\pi c_{\mathrm{o}}} \right)^2 \oint d\Omega \, |\mathbf{f}|^2 = \frac{\zeta_{\mathrm{o}}}{2} \left(\frac{\omega}{4\pi c_{\mathrm{o}}} \right)^2 \oint d\Omega \left| \frac{a_1 \mathbf{f}_1}{\sqrt{W_1}} + \frac{a_2 \mathbf{f}_2}{\sqrt{W_2}} e^{-i\mathbf{k} \cdot \mathbf{D}} \right|^2 =$$

$$= \frac{\zeta_{\mathrm{o}}}{2} \left(\frac{k}{4\pi} \right)^2 \left[\frac{\oint d\Omega \, |\mathbf{f}_1|^2}{W_1} |a_1|^2 + \frac{\oint d\Omega \, |\mathbf{f}_2|^2}{W_2} |a_2|^2 + 2\mathrm{Re} \left\{ \frac{\oint d\Omega \mathbf{f}_1^* \cdot \mathbf{f}_2 e^{-i\mathbf{k} \cdot \mathbf{D}}}{\sqrt{W_1 W_2}} a_1^* a_2 \right\} \right] =$$

$$= 2\Gamma_{\mathrm{rad1}} |a_1|^2 + 2\Gamma_{\mathrm{rad2}} |a_2|^2 + \zeta_{\mathrm{o}} \left(\frac{k}{4\pi} \right)^2 \mathrm{Re} \left\{ \frac{\oint d\Omega \mathbf{f}_1^* \cdot \mathbf{f}_2 e^{-i\mathbf{k} \cdot \mathbf{D}}}{\sqrt{W_1 W_2}} a_1^* a_2 \right\} , \tag{12.20}$$

where we used Eq.(8.20), and thus by comparing Eqs.(12.19) and (12.20), we infer

$$\Xi = \frac{\zeta_o \left(\frac{k}{4\pi}\right)^2}{4\sqrt{W_1 W_2}} \frac{\mathrm{Re}\left\{\oint d\Omega \mathbf{f}_1^* \cdot \mathbf{f}_2 e^{-i\mathbf{k}\cdot\mathbf{D}} a_1^* a_2\right\}}{\mathrm{Re}\left\{a_1^* a_2\right\}}, \tag{12.21}$$

namely Ξ is exactly the interference term in antenna theory. By substituting for the vector current-moments, this becomes

$$\Xi = \frac{\zeta_o \left(\frac{k}{4\pi}\right)^2}{4\sqrt{W_1 W_2}} \frac{\mathrm{Re}\left\{\oint d\Omega \left[\int_{V_1} dv \mathbf{J}_1 e^{-i\mathbf{k}\cdot\mathbf{r}_1'}\right]^* \cdot \left[\int_{V_2} dv \mathbf{J}_2 e^{-i\mathbf{k}\cdot\mathbf{r}_2'}\right] e^{-i\mathbf{k}\cdot\mathbf{D}} a_1^* a_2\right\}}{\mathrm{Re}\left\{a_1^* a_2\right\}} =$$

$$= \frac{\zeta_o \left(\frac{k}{4\pi}\right)^2}{4\sqrt{W_1 W_2}} \frac{\mathrm{Re}\left\{\int_{V_1} dv \int_{V_2} dv \mathbf{J}_1^* \cdot \mathbf{J}_2 \oint d\Omega e^{-i\mathbf{k}\cdot(\mathbf{r}_2-\mathbf{r}_1)} a_1^* a_2\right\}}{\mathrm{Re}\left\{a_1^* a_2\right\}} =$$

$$= \frac{\zeta_o \left(\frac{k}{4\pi}\right)^2}{4\sqrt{W_1 W_2}} \frac{\mathrm{Re}\left\{\int_{V_1} dv \int_{V_2} dv \mathbf{J}_1^* \cdot \mathbf{J}_2 \frac{4\pi \sin(k|\mathbf{r}_2-\mathbf{r}_1|)}{k|\mathbf{r}_2-\mathbf{r}_1|} a_1^* a_2\right\}}{\mathrm{Re}\left\{a_1^* a_2\right\}} =$$

$$= \frac{\omega\mu_o}{16\pi\sqrt{W_1 W_2}} \frac{\mathrm{Re}\left\{\int_{V_1} dv \int_{V_2} dv \mathbf{J}_1^* \cdot \mathbf{J}_2 \frac{\sin(k|\mathbf{r}_2-\mathbf{r}_1|)}{|\mathbf{r}_2-\mathbf{r}_1|} a_1^* a_2\right\}}{\mathrm{Re}\left\{a_1^* a_2\right\}}, \tag{12.22}$$

where we wrote with respect to a global coordinate system $\mathbf{r}_2 - \mathbf{r}_1 = \mathbf{D} + \mathbf{r}_2' - \mathbf{r}_1'$ and evaluated the integral over the angles of $\mathbf{k}$.

Note now that $W_1 \approx W_2 \approx W_{11} \approx W_{22}$ since all modes are by definition in CMT normalized to have unity energy, and therefore Eqs.(12.16) and (12.22) will become identical, if we can take the currents $\mathbf{J}_{1,2}$ to be real. This is indeed the case for eigenmodes, where the field solution in bounded regions (such as those where the currents are flowing) is always stationary (in contrast to the leaky part of the eigenmode, which is radiative) and for high enough Q it can be chosen so that it is real in the entire bounded region. Therefore, from either one of Eqs.(12.16) and (12.22) we can write

$$\Xi = \frac{\omega\mu_o}{16\pi\sqrt{W_1 W_2}} \int_{V_1} dv \int_{V_2} dv \mathbf{J}_1 \cdot \mathbf{J}_2 \frac{\sin\left(k\left|\mathbf{r}_2 - \mathbf{r}_1\right|\right)}{\left|\mathbf{r}_2 - \mathbf{r}_1\right|}. \tag{12.23}$$

Another useful form can be written now from Eq.(12.21)

$$\Xi = \frac{\frac{\zeta_o}{4}\left(\frac{k}{4\pi}\right)^2 \oint d\Omega \mathbf{f}_1^* \cdot \mathbf{f}_2 e^{-i\mathbf{k}\cdot\mathbf{D}}}{\sqrt{W_1 W_2}}, \tag{12.24}$$

single disk	λ/r	Q_{abs}	Q_{rad}	Q
$\epsilon_1 = 147.7,\ r_1 = 1,\ m = 2$	20.00 (20.00)	1468 (1466)	1992 (1995)	845 (845)
$\epsilon_2 = 102.22,\ r_2 = 1.2,\ m = 2$	16.67 (16.67)	2444 (2451)	977 (976)	698 (698)

Table 12.1: Analytical SV (and in parentheses numerical FEFD) results for the wavelength and absorption, radiation and total loss rates, for two different subwavelength-disk resonant modes. Note that disk-material loss-tangent $\tan\delta = 6 \cdot 10^{-6}\epsilon - 2 \cdot 10^{-4}$ was used.

and finally, using once more Eq.(8.20), we can define the interference parameter

$$V_{\text{rad}} \equiv \frac{\Xi}{\sqrt{\Gamma_{\text{rad1}}\Gamma_{\text{rad2}}}} = \frac{\oint d\Omega \mathbf{f}_1^* \cdot \mathbf{f}_2 e^{-i\mathbf{k}\cdot\mathbf{D}}}{\sqrt{\oint d\Omega \left|\mathbf{f}_1\right|^2 \oint d\Omega \left|\mathbf{f}_2\right|^2}}. \tag{12.25}$$

We have proven that, in electromagnetism, CMT can predict far-field interference phenomena between coupled leaky (but high-Q) resonances by the imaginary part of the coupling coefficient, since it was shown to be exactly the contribution to the interference predicted by antenna theory. In the following paragraph, we also implement numerical calculations to prove this point.

12.2.1 Coupled and interfering dielectric disks

Our goal here to confirm our analytical predictions of the previous Section with an actual implementation on a realistic system and numerical calculations. The system will be that of two dielectric disks, each one supporting a subwavelength resonant mode that is intrinsically leaky. The modal properties for each one were calculated using both an analytical method (separation of variables (SV)) and a numerical method (finite-element frequency-domain (FEFD) calculations), and they are shown in Table 12.1; the two disks were chosen so that their eigenfrequencies are slightly different (not absolutely exact resonance) and their loss-rates substantialy different, so that we can treat a complicated and general case.

To test the ability of CMT to sucessfully predict the coupling and the interference of the two disks at varying distance D, we will compare three different calculations of the normal modes of the combined two-disk system as a function of distance, with special attention to the radiation-Q of these normal modes (imaginary part of frequency), which should have explicit interference effects by being lower for the even and higher for the odd mode. First, we use the CMT result for the split normal modes from Eq.(8.2) with $\kappa \to \tilde{\kappa} = \kappa + i\Xi$, where $\tilde{\kappa}$ (κ and Ξ) is calculated from the CMT formula (12.15), so this is the prediction of solely

CMT. Second, we use the same CMT formula Eq.(8.2) for the normal modes, only this time we will use the CMT result for κ and the antenna theory result for Ξ from Eq.(12.25), which for two 2d 'whispering-gallery' modes of $m = 2$ finds

$$V_{\text{rad}} = \frac{8}{(kD)^3}\left\{3\,(kD)\cdot J_0\,(kD) + \left[(kD)^2 - 6\right]\cdot J_1\,(kD)\right\}, \tag{12.26}$$

where J_{n} is the Bessel function of n^{th} order. Third, we perform exact FEFD calculations. The results for the real and imaginary part of the splitting of the complex normal-mode frequencies are shown in Figure . The agreement between them is very good, even though quite dissimilar objects were chosen and the result has a nonconventional form. In particular, as we predicted analytically in the previous Section, the CMT and the antenna theory results agree very well for the entire range of distances, and ironically, they both fail to be correct (assuming FEFD is the most exact method) for close distances, which is expected, as at that point the interaction between the objects is not small anymore and the perturbative arguments fail. For example, more resonant modes need to be considered to make a good prediction for the field of the coupled system, which is starting to be localized inbetween the disks (basically the gap between the disks starts being the 'small perturbation' on a solid object) and thus its radiation behavior changes. Finally, note that we only plot the complex frequency splitting and not also the average complex frequency, because the frequency shifts induced between the two objects are second-order effects and thus CMT cannot provide a good description [111].

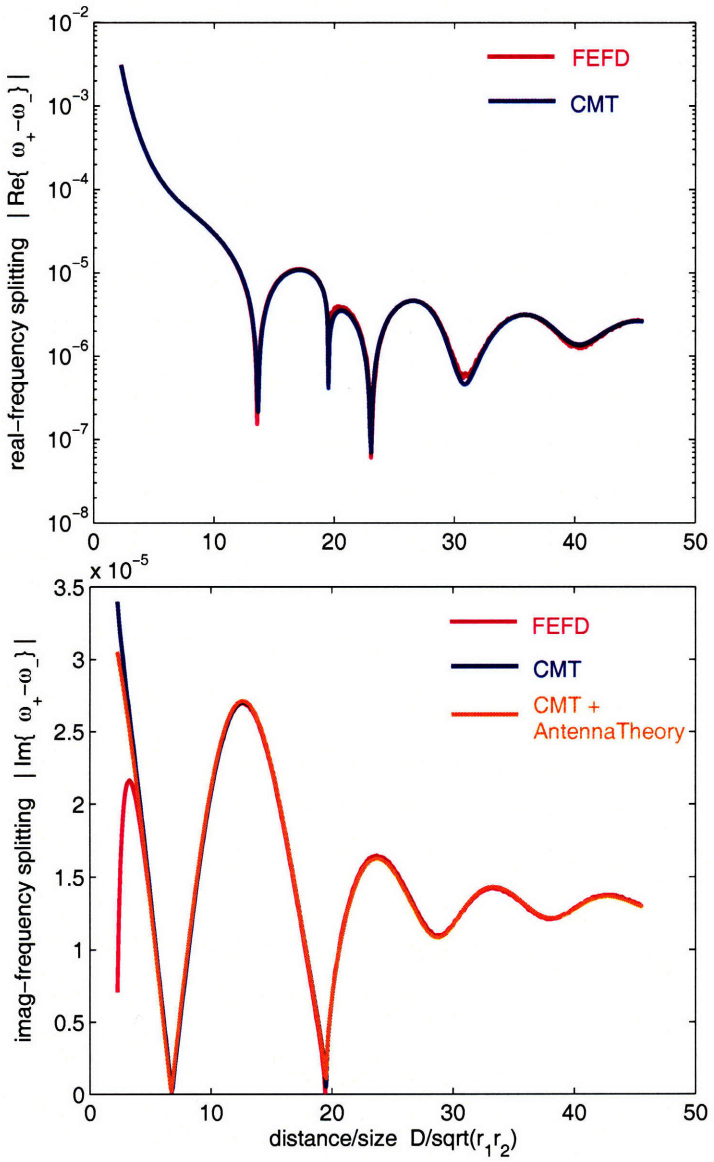


Figure 12-1: Results for the real and imaginary parts of the complex frequency splitting of the two normal modes of the system of two coupled 2d disks with the properties in Table 12.1 as a function of their distance D, using three methods: CMT calculation for κ and Ξ, CMT calculation for κ and analytical antenna-theory prediction for Ξ, and numerical FEFD calculations.

Bibliography

[1] A. Karalis, S. G. Johnson, and J. D. Joannopoulos, "Discrete-mode cancellation mechanism for high-Q integrated optical cavities with small modal volume," Opt. Lett. **29,** 2309–2311 (2004).

[2] A. Karalis, E. Lidorikis, M. Ibanescu, J. D. Joannopoulos, and M. Soljačić, "Surface-Plasmon-assisted guiding of broadband slow and subwavelength light in air," Phys. Rev. Lett. **95,** 063901 (2005).

[3] A. Karalis, J. D. Joannopoulos, and M. Soljačić, under review in Nature Physics (unpublished).

[4] A. Karalis, J. D. Joannopoulos, and M. Soljačić, "Efficient wireless non-radiative mid-range energy transfer," Annals of Physics **323,** 34–48 (2008).

[5] A. Kurs, A. Karalis, R. Moffatt, J. D. Joannopoulos, P. Fisher, and M. Soljačić, "Wireless power transfer via strongly coupled magnetic resonances," Science **317,** 83–86 (2007).

[6] J. T. Mok and B. J. Eggleton, "Expect more delays," Nature **433,** 811–812 (2005).

[7] G. P. Agrawal, *Nonlinear Fiber Optics*, 3rd ed. (Academic Press, San Diego, CA, 2001).

[8] E. Yablonovitch, "Inhibited spontaneous emission in solid-state physics and electronics," Phys. Rev. Lett. **58,** 2059–2062 (1987).

[9] S. John, "Strong localization of photons in certain disordered dielectric superlattices," Phys. Rev. Lett. **58,** 2486–2489 (1987).

[10] D. F. Sievenpiper, E. Yablonovitch, J. N. Winn, S. Fan, P. R. Villeneuve, and J. D. Joannopoulos, "3D metallo-dielectric photonic crystals with strong capacitive coupling between metallic islands," Phys. Rev. Lett. **80,** 2829–2832 (1998).

[11] H. A. Haus, *Waves and Fields in Optoelectronics* (Prentice-Hall, Englewood Cliffs, NJ, 1984).

[12] J. D. Joannopoulos, R. D. Meade, and J. N. Winn, *Photonic Crystals: Molding the Flow of Light* (Princeton Univ. Press, 1995).

[13] S. G. Johnson and J. D. Joannopoulos, *Photonic Crystals: The Road from Theory to Practice* (Kluwer, Boston, MA, 2002).

[14] S. Noda, "Recent Progresses and Future Prospects of Two- and Three-Dimensional Photonic Crystals," J. Lightwave Tech. **24,** 4554–4567 (2006).

[15] M. Soljačić, S. G. Johnson, S. Fan, M. Ibanescu, E. Ippen, and J. D. Joannopoulos, "Photonic-crystal slow-light enhancement of non-linear phase sensitivity," J. Opt. Soc. Am. B **19,** 2052–2059 (2002).

[16] G. Lenz, B. J. Eggleton, C. K. Madsen, and R. E. Slusher, "Optical delay lines based on optical filters," IEEE J. Quantum Electron. **37,** 525–532 (2001).

[17] H. Raether, *Surface Plasmons* (Springer-Verlag, Berlin, 1988).

[18] S. A. Maier, *Plasmonics: Fundamentals and applications* (Springer, 2007).

[19] N. Ocelic and R. Hillenbrand, "Subwavelength-scale tailoring of surface phonon polaritons by focused ion-beam implantation," Nature Materials **3,** 606–609 (2004).

[20] T. Taubner, D. Korobkin, Y. Urzhumov, G. Shvets, and R. Hillenbrand, "Near-field microscopy through a SiC superlens," Science **313,** 1595 (2006).

[21] S. E. Harris, J. E. Field, and A. Imamoğlu, "Nonlinear optical processes using Electromagnetically Induced Transparency," Phys. Rev. Lett. **64,** 1107–1110 (1990).

[22] L. V. Hau, S. E. Harris, Z. Dutton, and C. H. Behroozi, "Light speed reduction to 17 metres per second in an ultracold atomic gas," Nature **397,** 594–598 (1999).

[23] A. V. Turukhin, V. S. Sudarshanam, M. S. Shahriar, J. A. Musser, B. S. Ham, and P. R. Hemmer, "Observation of ultraslow and stored light pulses in a solid," Phys. Rev. Lett. **88,** 023602 (2002).

[24] M. S. Bigelow, N. N. Lepeshkin, and R. W. Boyd, "Observation of ultraslow light propagation in a Ruby crystal at room temperature," Phys. Rev. Lett. **90,** 113903 (2003).

[25] Y. A. Vlasov, M. O'Boyle, H. F. Hamann, and S. J. McNab, "Active control of slow light on a chip with photonic crystal waveguides," Nature **438,** 65–69 (2005).

[26] C. Liu, Z. Dutton, C. H. Behroozi, and L. V. Hau, "Observation of coherent optical information storage in an atomic medium using halted light pulses," Nature **409,** 490–493 (2001).

[27] D. F. Phillips, A. Fleischhauer, A. Mair, R. L. Walsworth, and M. D. Lukin, "Storage of light in atomic vapor," Phys. Rev. Lett. **86,** 783–786 (2001).

[28] M. F. Yanik and S. Fan, "Stopping light all optically," Phys. Rev. Lett. **92,** 083901 (2004).

[29] S. G. Johnson, A. Mekis, S. Fan, and J. D. Joannopoulos, "Molding the flow of light," Comp. Sci. Eng. **3,** 38–47 (2001).

[30] S. G. Johnson, S. Fan, A. Mekis, and J. D. Joannopoulos, "Multipole-cancellation mechanism for high-Q cavities in the absence of a complete photonic band gap," Appl. Phys. Lett. **78,** 3388–3390 (2001).

[31] J. Čtyroký, "Photonic bandgap structures in planar waveguides," J. Opt. Soc. Am. A **18,** 435–441 (2001).

[32] M. R. Watts, S. G. Johnson, H. A. Haus, and J. D. Joannopoulos, "Electromagnetic cavity with arbitrary Q and small modal volume without a complete photonic bandgap," Opt. Lett. **27,** 1785–1787 (2002).

[33] H. Benisty, D. Labilloy, C. Weisbuch, C. J. M. Smith, T. F. Krauss, D. Cassagne, A. Béraud, and C. Jouanin, "Radiation losses of waveguide-based two-dimensional photonic crystals: Positive role of the substrate," Appl. Phys. Lett. **76,** 532–534 (2000).

[34] W. Bogaerts, P. Bienstman, D. Taillaert, R. Baets, and D. De Zutter, "Out-of-Plane Scattering in Photonic Crystal Slabs," IEEE Photon. Technol. Lett. **13,** 565–567 (2001).

[35] B. D'Urso, O. Painter, J. O'Brien, T. Tombrello, A. Yariv, and A. Scherer, "Modal reflectivity in finite-depth two-dimensional photonic-crystal microcavities," J. Opt. Soc. Am. B **15,** 1155–1159 (1998).

[36] R. Ferrini, R. Houdré, H. Benisty, M. Qiu, and J. Moosburger, "Radiation losses in planar photonic crystals: two-dimensional representation of hole depth and shape by an imaginary dielectric constant," J. Opt. Soc. Am. B **20,** 469–478 (2003).

[37] J. Takahara, S. Yamagishi, H. Taki, A. Morimoto, and T. Kobayashi, "Guiding of a one-dimensional optical beam with nanometer diameter," Opt. Lett. **22,** 475–477 (1997).

[38] P. Berini, "Plasmon-polariton modes guided by a metal film of finite width bounded by different dielectrics," Opt. Express **7,** 329–335 (2000).

[39] J.-C. Weeber, A. Dereux, C. Girard, J. R. Krenn, and J.-P. Goudonnet, "Plasmon polaritons of metallic nanowires for controlling submicron propagation of light," Phys. Rev. B **60,** 9061–9068 (1999).

[40] J. R. Krenn, B. Lamprecht, H. Ditlbacher, G. Schider, M. Salerno, A. Leitner, and F. R. Aussenegg, "Non-diffraction-limited light transport by gold nanowires," Euro-Phys. Lett. **60,** 663–669 (2002).

[41] T. Nikolajsen, K. Leosson, I. Salakhutdinov, and S. I. Bozhevolnyi, "Polymer-based surface-plasmon-polariton stripe waveguides at telecommunication wavelengths," Appl. Phys. Lett. **82,** 668–670 (2003).

[42] I. V. Novikov and A. A. Maradudin, "Channel polaritons," Phys. Rev. B **66,** 035403 (2002).

[43] S. I. Bozhevolnyi, V. S. Volkov, E. Devaux, and T. W. Ebbesen, "Channel Plasmon-Polariton guiding by subwavelength metal grooves," Phys. Rev. Lett. **95,** 046802 (2005).

[44] P. R. Villeneuve, S. Fan, J. D. Joannopoulos, K.-Y. Lim, G. S. Petrich, L. A. Kolodziejski, and R. Reif, "Air-bridge microcavities," Appl. Phys. Lett. **67,** 167–169 (1995).

[45] J. Vučković, M. Lončar, H. Mabuchi, and A. Scherer, "Design of photonic crystal microcavities for cavity QED," Phys. Rev. E **65,** 016608 (2002).

[46] K. Srinivasan and O. Painter, "Fourier space design of high-Q cavities in standard and compressed hexagonal lattice photonic crystals," Opt. Express **11,** 579–593 (2003).

[47] H.-Y. Ryu, M. Notomi, and Y.-H. Lee, "High-quality-factor and small-mode-volume hexapole modes in photonic-crystal-slab nanocavities," Appl. Phys. Lett. **83,** 4294–4296 (2003).

[48] Y. Akahane, T. Asano, B.-S. Song, and S. Noda, "High-Q photonic nanocavity in a two-dimensional photonic crystal," Nature **425,** 944–946 (2003).

[49] H. Benisty, P. Lalanne, S. Olivier, M. Rattier, C. Weisbuch, C. J. M. Smith, T. F. Krauss, C. Jouanin, and D. Cassagne, "Finite-depth and intrinsic losses in vertically etched two-dimensional photonic crystals," Optical and Quantum Electron. **34,** 205–215 (2002).

[50] D. Marcuse, *Theory of Dielectric Optical Waveguides*, 2nd ed. (Academic Press, San Diego, 1991).

[51] E. M. Purcell, "Spontaneous emission probabilities at radio frequencies," Phys. Rev. **69,** 681 (1946).

[52] T. Tamir and A. A. Oliner, "Guided complex waves," Proc. IEE **110,** 310–334 (1963).

[53] P. Bienstman and R. Baets, "Optical modelling of photonic crystals and VCSELs using eigenmode expansion and perfectly matched layers," Optical and Quantum Electron. **33,** 327–341 (2001).

[54] Y. Akahane, T. Asano, B.-S. Song, and S. Noda, "Fine-tuned high-Q photonic-crystal nanocavity," Opt. Express **13,** 1202–1214 (2005).

[55] T. Asano, B.-S. Song, and S. Noda, "Analysis of the experimental Q factors (1 million) of photonic crystal nanocavities," Opt. Express **14,** 1996–2002 (2006).

[56] E. Kuramochi, M. Notomi, S. Mitsugi, A. Shinya, and T. Tanabe, "Ultrahigh-Q photonic crystal nanocavities realized by the local width modulation of a line defect," Appl. Phys. Lett. **88,** 041112 (2006).

[57] Y. Sugimoto, N. Ikeda, N. Carlsson, K. Asakawa, N. Kawai, and K. Inoue, "Fabrication and characterization of different types of two-dimensional AlGaAs photonic crystal slabs," J. Appl. Phys. **91,** 922–929 (2002).

[58] D. J. Ripin, K.-Y. Lim, G. S. Petrich, P. R. Villeneuve, S. Fan, E. R. Thoen, J. D. Joannopoulos, E. P. Ippen, and L. A. Kolodziejski, "One-Dimensional Photonic Bandgap Microcavities for Strong Optical Confinement in GaAs and GaAs/AlxOy Semiconductor Waveguides," J. Lightwave Tech. **17,** 2152–2160 (1999).

[59] A. Yariv and P. Yeh, *Optical waves in crystals: Propagation and control of laser radiation* (Wiley, New York, NY, 1984).

[60] R. E. Collin and F. J. Zucker, in *Antenna Theory* (McGraw-Hill, 1969), Chap. 13: General characteristics of traveling-wave antennas by A. Hessel, pp. 184–235.

[61] C. Sauvan, G. Lecamp, P. Lalanne, and J. P. Hugonin, "Modal-reflectivity enhancement by geometry tuning in Photonic Crystal microcavities," Opt. Express **13,** 245–255 (2005).

[62] J. Čtyroký *et al.*, "Bragg waveguide grating as a 1D photonic band gap structure: COST 268 modelling task," Optical and Quantum Electron. **34,** 455–470 (2002).

[63] J.-C. Weeber, Y. Lacroute, and A. Dereux, "Optical near-field distributions of surface plasmon waveguide modes," Phys. Rev. B **68,** 115401 (2003).

[64] M. Hochberg, T. Baehr-Jones, C. Walker, and A. Scherer, "Integrated plasmon and dielectric waveguides," Opt. Express **12,** 5481–5486 (2004).

[65] S. I. Bozhevolnyi, J. Erland, K. Leosson, P. M. W. Skovgaard, and J. M. Hvam, "Waveguiding in surface plasmon polariton band gap structures," Phys. Rev. Lett. **86,** 3008–3011 (2001).

[66] M. Quinten, A. Leitner, J. R. Krenn, and F. R. Aussenegg, "Electromagnetic energy transport via linear chains of silver nanoparticles," Opt. Lett. **23,** 1331–1333 (1998).

[67] S. A. Maier, P. G. Kik, H. A. Atwater, S. Meltzer, E. Harel, B. E. Koel, and A. A. G. Requicha, "Local detection of electromagnetic energy transport below the diffraction limit in metal nanoparticle plasmon waveguides," Nature Materials **2,** 229–232 (2003).

[68] Q. Xu, V. R. Almeida, R. R. Panepucci, and M. Lipson, "Experimental demonstration of guiding and confining light in nanometer-size low-refractive-index material," Opt. Lett. **29,** 1626–1628 (2004).

[69] P. Palinginis, F. Sedgwick, S. Crankshaw, M. Moewe, and C. J. Chang-Hasnain, "Room temperature slow light in a quantum-well waveguide via coherent population oscillation," Opt. Express **13,** 9909–9915 (2005).

[70] K. Y. Song, M. G. Herráez, and L. Thévenaz, "Observation of pulse delaying and advancement in optical fibers using stimulated Brillouin scattering," Opt. Express **13,** 82–88 (2004).

[71] D. Dahan and G. Eisenstein, "Tunable all optical delay via slow and fast light propagation in a Raman assisted fiber optical parametric amplifier: a route to all optical buffering," Opt. Express **13,** 6234–6249 (2005).

[72] J. K. S. Poon, L. Zhu, G. A. DeRose, and A. Yariv, "Transmission and group delay of microring coupled-resonator optical waveguides," Opt. Lett. **31,** 456–458 (2006).

[73] H. Gersen, T. J. Karle, R. J. P. Engelen, W. Bogaerts, J. P. Korterik, N. F. van Hulst, T. F. Krauss, and L. Kuipers, "Real-space observation of ultraslow light in photonic crystal waveguides," Phys. Rev. Lett. **94,** 073903 (2005).

[74] D. A. B. Miller, "Fundamental limit to linear one-dimensional slow light structures," Phys. Rev. Lett. **99,** 203903 (2007).

[75] J. B. Khurgin, "Performance limits of delay lines based on optical amplifiers," Opt. Lett. **31,** 948–950 (2006).

[76] R. S. Tucker, P.-C. Ku, and C. J. Chang-Hasnain, "Slow-light optical buffers: Capabilities and fundamental limitations," J. Lightwave Tech. **23,** 4046–4066 (2005).

[77] J. B. Khurgin, "Optical buffers based on slow light in electromagnetically induced transparent media and coupled resonator structures: comparative analysis," J. Opt. Soc. Am. B **22,** 1062–1074 (2005).

[78] R. W. Boyd, D. J. Gauthier, A. L. Gaeta, and A. E. Willner, "Maximum time delay achievable on propagation through a slow-light medium," Phys. Rev. A **71,** 023801 (2005), and erratum: Phys. Rev. A, vol. 72, no. 5, pp. 059903, 2005.

[79] J. B. Khurgin, "Adiabatically tunable optical delay lines and their performance limitations," Opt. Lett. **30,** 2778–2780 (2005).

[80] J. B. Khurgin, "Expanding the bandwidth of slow-light photonic devices based on coupled resonators," Opt. Lett. **30,** 513–515 (2005).

[81] B. Macke and B. Ségard, "Propagation of light-pulses at a negative group-velocity," Eur. Phys. J. D **23,** 125–141 (2003).

[82] J. T. Mok, C. M. De Sterke, I. M. C. Littler, and B. J. Eggleton, "Dispersionless slow light using gap solitons," Nature Physics (2006).

[83] E. N. Economou, "Surface Plasmons in thin films," Phys. Rev. **182,** 539–554 (1969).

[84] J. J. Burke, G. I. Stegeman, and T. Tamir, "Surface-polariton-like waves guided by thin, lossy metal films," Phys. Rev. B **33,** 5186–5201 (1986).

[85] M. Ibanescu, S. G. Johnson, D. Roundy, Y. Fink, and J. D. Joannopoulos, "Microcavity confinement based on an anomalous zero group-velocity waveguide mode," Opt. Lett. **30,** 552–554 (2005).

[86] B. Maes, M. Ibanescu, and J. D. Joannopoulos, "Microcavities based on multimodal interference," Opt. Express **15,** 6268–6278 (2007).

[87] COMSOL, <http://www.comsol.com>.

[88] M. Soljačić and J. D. Joannopoulos, "Enhancement of nonlinear effects using photonic crystals," Nature Materials **3,** 211–219 (2004).

[89] C. Cohen-Tannoudji, J. Dupont-Roc, and G. Grynberg, *Atom-Photon interactions* (Wiley, 2004).

[90] L. van Hove, "The occurence of singularities in the elastic frequency distribution of a crystal," Phys. Rev. **89,** 1189–1193 (1953).

[91] O. Svelto, *Principles of lasers*, 4th ed. (Springer, 1998).

[92] S. G. Johnson, M. L. Povinelli, M. Soljačić, A. Karalis, S. Jacobs, and J. D. Joannopoulos, "Roughness losses and volume-current methods in photonic-crystal waveguides," Appl. Phys. B **81,** 283–293 (2005).

[93] C. Kittel, *Introduction to Solid State Physics*, 7th ed. (Wiley, New York, NY, 1996).

[94] N. Tesla, "Apparatus for transmitting electrical energy,", US patent number 1,119,732, 1914.

[95] T. A. Vanderelli, J. G. Shearer, and J. R. Shearer, "Method and apparatus for a wireless power supply,", US patent number 7,027,311, 2006.

[96] J. M. Fernandez and J. A. Borras, "Contactless battery charger with wireless control link,", US patent number 6,184,651, 2001.

[97] L. Ka-Lai, J. W. Hay, and P. G. W. Beart, "Contact-less power transfer,", US patent number 7,042,196, 2006, (SplashPower Ltd., <www.splashpower.com>).

[98] A. Esser and H.-C. Skudelny, "A new approach to power supplies for robots," IEEE Trans. on Industry Appl. **27,** 872–875 (1991).

[99] J. Hirai, T.-W. Kim, and A. Kawamura, "Wireless transmission of power and information for cableless linear motor drive," IEEE Trans. on Power Electronics **15,** 21–27 (2000).

[100] G. Scheible, B. Smailus, M. Klaus, K. Garrels, and L. Heinemann, "System for wirelessly supplying a large number of actuators of a machine with electrical power,", US patent number 6,597,076, 2003, (ABB, <www.abb.com>).

[101] A. Takao, D. Barak, E. Wilcut, W. P. Bowen, A. S. Parkins, T. J. Kippenberg, K. J. Vahala, and H. J. Kimble, "Observation of strong coupling between one atom and a monolithic microresonator," Nature **443,** 671–674 (2006).

[102] J. A. Kong, *Electromagnetic Wave Theory* (EMW Publishing, 2000).

[103] D. M. Pozar, *Microwave Engineering* (Wiley, New Jersey, 2005).

[104] M. V. Jacob, J. G. Hartnett, J. Mazierska, J. Krupka, and M. E. Tobar, "Lithium Tantalate - A high permittivity dielectric material for microwave communication systems," In *IEEE TENCON*, pp. 1362–1366 (2003).

[105] J. D. Jackson, *Classical Electrodynamics*, 3rd ed. (Wiley, New York, 1998).

[106] F. W. Grover, *Inductance calculations* (Dover, Mineola, New York, 1973).

[107] C. A. Balanis, *Antenna Theory: analysis and design* (Wiley, New Jersey, 2005).

[108] W. Geyi, "A method for the evaluation of small antenna Q," IEEE Trans. Antennnas and Propagation pp. 2124–2129 (2003).

[109] W. A. Edson, *Vacuum-Tube Oscillators* (Wiley, New York, 1953).

[110] K. Fenske and D. Misra, "Dielectric materials at microwave frequencies," Applied Microwave and Wireless **12,** 92–100 (2000).

[111] C. Popović, Miloš A.and Manolatou and M. R. Watts, "Coupling-induced resonance frequency shifts in coupled dielectric multi-cavity filters," Opt. Express **14,** 1208–1222 (2006).